Investigating the Influences on Substorm Signatures and their Identification

Christian John Lao

A dissertation submitted in partial fulfillment

of the requirements for the degree of

Doctor of Philosophy

of

University College London.

Department of Space and Climate Physics

University College London

August 28, 2025

I, Christian John Lao, confirm that the work presented in this thesis is my own. Where information has been derived from other sources, I confirm that this has been indicated in the work.

Abstract

Substorms are a rapid release of energy that is redistributed throughout the magnetosphere-ionosphere system, resulting in many observable signals, such as enhancements in the aurora, energetic particle injections, and ground magnetic field perturbations. Numerous substorm identification techniques based on each of these signals have been provided in the literature, but often with no cross-calibration. Since the signals produced are not necessarily unique to substorms and may not be sufficiently similar to be identified for each and every substorm, individual event lists may misidentify events, hindering our understanding of the phenomenon.

To gauge the scale of this problem, we quantify the association between lists of substorms derived from SuperMAG SML/SMU indices, midlatitude magnetometer data, particle injections, and auroral enhancements. Overall, although some degree of pairwise association is found between the lists, even lists generated by applying conceptually similar identification techniques to ground magnetometer data achieve an association with fewer than 50% event coincidence.

The poor event agreement between different ground magnetometer-based methods is hypothesised to be due to the poor differentiation between magnetic perturbations due to substorms and magnetospheric convection enhancements. Unlike other substorm identification methods, the SOPHIE technique (Forsyth et al., 2015) attempts to distinguish between negative SML bays produced by a substorm or magnetospheric convection enhancement by examining the SMU index. Despite this, we find evidence that up to 50% of the events originally identified as substorms are misidentified and that the auroral indices alone are insufficient to distinguish between the phenomena.

Finally, four event studies are presented. These show a classical substorm, a "classical" magnetospheric convection enhancement, an atypical substorm - from the location of the auroral onset and ground magnetic signature - and a magnetospheric convection enhancement occurring in a location that we would expect only substorms to occur. Even when integrating further geomagnetic indices, there appears to be no differentiator apart from coupled changes in SMU and SML in identifying the convection enhancements from substorms. Furthermore, there seems to be no difference in the driving of the magnetosphere prior to substorms or convection enhancements.

Impact Statement

The substorm is one of the most energetic phenomena in the Earth's magnetosphere and thus presents a space weather risk. Space weather poses a significant threat to infrastructure that society relies on and was added to the UK National Risk Register in 2012. This thesis investigated the quality of our current methods for identifying substorm intervals. Our understanding of the phenomena depends on the quality of the catalogues against which we verify our theories and models.

The research in this thesis presents a rigorous evaluation of the temporal association between different catalogues of substorms from the various signatures it is capable of producing. The techniques used to complete this are used in the verification of both terrestrial weather and space weather models, but have not seen widespread use in solar terrestrial physics. The completed analysis showed that our current methods of identifying substorms have a poor agreement with each other, with the level of agreement even falling to that of random chance. This research has been published in the Journal of Geophysical Research: Space Physics.

Another finding was that our best methods for identifying a single manifestation of the substorm showed critical flaws. We showed that $>50\%$ of the events identified from the ground magnetic signature of the substorm were, in fact, related to another phenomenon. The results of the analysis indicated that relying on this single signature of the substorm for identification was not satisfactory for robust identification of events, and further datasets are required for correct identification. This research has also been published in Journal of Geophysical Research: Space Physics.

The findings presented in this thesis have been disseminated within the wider

scientific community through presentations at several national and international meetings. This has been achieved in both science-focused meetings and workshops supporting specific upcoming missions. This has increased awareness about issues around substorm identification and current conclusions regarding the phenomenon.

Ultimately, this research will provide a foundation for the implementation and evaluation of a community-driven quantitative description of the substorm, from which we can further delve into the specifics of the phenomenon.

Acknowledgements

I owe many thanks to the Science and Technology Facilities Council for the funding of this research, and to the many people and institutions who have provided data used to complete this thesis. I would also like to acknowledge the contributions of Chris Owen and Jim Wild in examining this thesis.

On this journey of completing this PhD, I owe the biggest thanks to my co-supervisors, Colin Forsyth and Mervyn Freeman. I'm grateful for the time you both took to speak to me about this incredible project on 2 July 2021 and for picking me as your student. I know that I have not made it an easy supervision for either of you with my escapades to the US and Scotland. It truly has been a privilege to have you as my supervisors. Thank you both for your patience, support, and guidance over the past 3 and a half years and for everything you have taught me about the magnetosphere and beyond. Your faith and encouragement kept me going when I couldn't see the forest for the trees.

I am grateful to have met so many remarkable people during my PhD. A big thank you to the members of "AR CL NN": Nawin - you have always been the best student and I appreciate you, Abid - I hope this message finds you well, thank you both for the countless adventures while at MSSL and beyond, you made the office a fun and vibrant place, all the best with all your future endeavours! Thank you to all the students of the Plasma group past - *Mayur, Sam, Caoimhe, Jefferson, Seong-Yeop, Joel, Sachin, Simon, Camille, Gabriel*, I have learnt so much from all of you and not just about plasma physics - and present - *Chiara, Harry, Jingting, Tom, Bhagyashri, Xiangyu, Hao*, you all inspire me and I know you will all go on to do great things! I would also like to thank the academics, post-docs and engineers

of the Plasma group, without your insights and dedication I would not be half the researcher I am today. There are too many students - all of whom have made my time at MSSL memorable - to mention - just to say a thank you for all the lunchtime walks and game nights during my time there. I am also grateful for all the past and present staff at MSSL who have provided both insightful conversations and distractions, such as football on sunny Surrey days. In particular, I would like to thank the general office, especially Philippa and Sam, for all your help in all non-academic aspects of PhD life. In addition to the community at MSSL, I have had the fortune to travel across the world to meet some truly inspiring people. I'd like to thank Andy Smith for the endless advice and always answering my emails within the hour. Thank you to Gian Luca and Joe for being my mentors at the LANL summer school, I learnt so much from both of you in just a few weeks. I'd like to also thank Megan Mark for getting Dovile and I to the lab and making sure we survived that summer, you made it such a blast.

I owe a lot to science outreach and the lessons, opportunities, and inspiration it has provided me during my PhD. I would like to thank *Will, Abbie, Michaela*, and the rest of the Orbyts team for encouraging me to get involved in Orbyts. Thank you for letting me be part of an incredible program, and I wish it and each one of you success in the future!

On a personal level, my gratitude goes to my friends and family who have endlessly supported and encouraged me through this PhD and long before. My biggest thanks go to my mum, my auntie Catalina, and my uncle John for all their support over the years, without it, this PhD would have stayed just a dream. To my dear uncle, look what that boy you taught how to divide on that living room table all those years ago went on to do, he couldn't have done it without you.

Finally, to Dovile, my partner-in-crime, thank you for everything.

UCL Research Paper Declaration Form

UCL Research Paper Declaration Form: referencing the doctoral candidate's own published work(s)

1. **For a research manuscript that has already been published** (if not yet published, please skip to section 2)**:**

   (a) **What is the title of the manuscript?**
   On the Association of Substorm Identification Methods

   (b) **Please include a link to or doi for the work:**
   https://doi.org/10.1029/2024JA032762

   (c) **Where was the work published?**
   Journal of Geophysical Research: Space Physics

   (d) **Who published the work?**
   Wiley

   (e) **When was the work published?**
   September 2024

   (f) **List the manuscript's authors in the order they appear on the publication:**
   Christian J. Lao, Colin Forsyth, Mervyn P. Freeman, Andy W. Smith, Michaela K. Mooney

   (g) **Was the work peer reviewed?**

Yes

(h) **Have you retained the copyright?**

Yes

(i) **Was an earlier form of the manuscript uploaded to a preprint server (e.g. medRxiv)? If 'Yes', please give a link or doi**

No

If 'No', please seek permission from the relevant publisher and check the box next to the below statement:

☒ *I acknowledge permission of the publisher named under 1d to include in this thesis portions of the publication named as included in 1c.*

2. **For a research manuscript prepared for publication but that has not yet been published** (if already published, please skip to section 3)**:**

   (a) **What is the current title of the manuscript?**

   (b) **Has the manuscript been uploaded to a preprint server 'e.g. medRxiv'?**
   If 'Yes', please give a link or doi:

   (c) **Where is the work intended to be published?**

   (d) **List the manuscript's authors in the intended authorship order:**

   (e) **Stage of publication:**

3. **For multi-authored work, please give a statement of contribution covering all authors** (if single-author, please skip to section 4)**:**
   C.J. Lao analysed and produced the results in this article. C.J. Lao, C. Forsyth and M.P. Freeman edited the main manuscript text. All co-authors provided insightful comments and contributions to the manuscript and reviewed it before publication.

4. **In which chapter(s) of your thesis can this material be found?**
   Chapter 4

e-Signatures confirming that the information above is accurate (this form should be co-signed by the supervisor/ senior author unless this is not appropriate, e.g. if the paper was a single-author work)**:**

Candidate:

Christian John Lao

Date:

06 May 2025

Supervisor/Senior Author signature (where appropriate)**:**

Colin Forsyth

Date:

06 May 2025

1. **For a research manuscript that has already been published** (if not yet published, please skip to section 2)**:**

   (a) **What is the title of the manuscript?**
   Separating DP1 and DP2 Current Pattern Contributions to Substorm-Like Intensifications in SML

   (b) **Please include a link to or doi for the work:**
   https://doi.org/10.1029/2024JA033592

   (c) **Where was the work published?**
   Journal of Geophysical Research: Space Physics

   (d) **Who published the work?**
   Wiley

   (e) **When was the work published?**
   April 2025

   (f) **List the manuscript's authors in the order they appear on the publication:**
   Christian J. Lao, Colin Forsyth, Mervyn P. Freeman, Jesper W. Gjerloev

(g) **Was the work peer reviewed?**

Yes

(h) **Have you retained the copyright?**

Yes

(i) **Was an earlier form of the manuscript uploaded to a preprint server (e.g. medRxiv)? If 'Yes', please give a link or doi.**

https://doi.org/10.22541/essoar.173386078.84405314/v2

If 'No', please seek permission from the relevant publisher and check the box next to the below statement:

☒ *I acknowledge permission of the publisher named under 1d to include in this thesis portions of the publication named as included in 1c.*

2. **For a research manuscript prepared for publication but that has not yet been published** (if already published, please skip to section 3)**:**

(a) **What is the current title of the manuscript?**

(b) **Has the manuscript been uploaded to a preprint server 'e.g. medRxiv'?**

If 'Yes', please give a link or doi:

(c) **Where is the work intended to be published?**

(d) **List the manuscript's authors in the intended authorship order:**

(e) **Stage of publication:**

3. **For multi-authored work, please give a statement of contribution covering all authors** (if single-author, please skip to section 4)**:**

C.J. Lao analysed and produced the results in this article. C.J. Lao, C. Forsyth and M.P. Freeman edited the main manuscript text. J.W. Gjerloev provided the geomagnetic indices and ground magnetometer data via the SuperMAG initiative. All co-authors provided insightful comments and contributions to the manuscript and reviewed it before publication.

4. **In which chapter(s) of your thesis can this material be found?**
   Chapter 5

e-Signatures confirming that the information above is accurate (this form should be co-signed by the supervisor/ senior author unless this is not appropriate, e.g. if the paper was a single-author work)**:**

Candidate:

Christian John Lao

Date:

06 May 2025

Supervisor/Senior Author signature (where appropriate)**:**

Colin Forsyth

Date:

06 May 2025

Contents

List of Figures

List of Tables

Chapter 1

Introduction

1.1 Motivation

The subject of this thesis is the terrestrial magnetospheric substorm. The substorm is a result of the coupling between the plasma and interplanetary magnetic field coming from the Sun, and the Earth's magnetic field and the plasma trapped within its confines. In this chapter, the physics that governs the interactions between plasmas and electromagnetic fields is introduced. Furthermore, an overview of the "geography" of the Earth's magnetosphere is briefly introduced with its various unique plasma populations. Finally, the large-scale processes that govern the dynamics of the magnetosphere and the coupling between regions and to the ionosphere are described.

1.2 Plasma Physics

Plasmas have been coined the 'fourth state of matter' (Piel, 2010). One nonmathematical description of plasma is that it is a gas consisting of electrons and ions that demonstrate collective behaviour (simply, it acts as a fluid would), interacts with electromagnetic fields, and has no net charge (Chen, 2013). This description is greatly simplified and ignores many of the unique properties of plasmas. For example, the property of a plasma looking electrically neutral to the outside in a steady state despite being composed of electrically charged particles is termed *quasi-neutrality* and is discussed in full in the following section.

1.2.1 Quasi-neutrality and collective behaviour of plasmas

For a plasma to appear quasineutral, the Coulomb potential of every charged particle within it is shielded by the other charged particles in the plasma. The Coulomb potential is defined as the electric potential experienced by a test charge due to a single point charge in a vacuum, given by

$$\phi_C = \frac{q}{4\pi\varepsilon_0 r} \tag{1.1}$$

where q is the charge, ε_0 is the permittivity of free space and r is the distance to the potential source. If a localised charge imbalance occurs in a plasma, the electrons and ions in the immediate vicinity of the charge imbalance reconfigure. This results in the test charge experiencing a Debye potential given by

$$\phi_D = \frac{q}{4\pi\varepsilon_0 r}\exp\left(-\frac{r}{\lambda_D}\right) \tag{1.2}$$

where λ_D is the Debye length, the distance at which the Coulomb potential is reduced by a factor of e due to the presence of shielding charged particles. The Debye length is given by

$$\lambda_D = \sqrt{\frac{\varepsilon_0 k_b T_e}{n q_e^2}} \tag{1.3}$$

where k_B is the Boltzmann constant, T_e is the electron temperature, q_e is the electron charge and assuming a proton-electron plasma ($n = n_i = n_e$), n is the plasma number density. The electron temperature and charge are used instead of the ion values because electrons exhibit greater mobility. If the characteristic length scale of plasmas is much larger than the Debye length, i.e. $L \gg \lambda_D$, it is described as quasi-neutral. Otherwise, there is not enough space for the shielding effect to occur, and it is simply an ionised gas. This requirement is often called the first plasma criterion.

The process described above is termed *Debye shielding*, and is an example of the collective behaviour of a plasma. For a plasma to exhibit collective behaviour, there must be a high enough number density of plasma particles within a Debye

sphere (a sphere with radius equal to the Debye length) to shield a charge disturbance and return the plasma to quasi-neutrality. The number of particles in a Debye sphere is given by

$$N_D = \frac{4\pi}{3} n\lambda_D^3. \tag{1.4}$$

The term $n\lambda_D^3$ is called the plasma parameter, Λ, and the second plasma criterion requires that $\Lambda \gg 1$, such that there are enough particles for a plasma to display collective behaviour.

When the quasi-neutrality of a plasma is disturbed, such as when a perturbation field is applied, the electrons within it will move to correct the imbalance in the charge density because they are more mobile (to first approximation). This involves accelerating toward relatively static ions and oscillating around them due to the inertia of the electrons. The frequency of electron oscillation is known as the electron plasma frequency, and it characterises the fundamental mode of oscillation of the plasma. This frequency is given by

$$\omega_{pe} = \sqrt{\frac{n_e q_e^2}{m_e \varepsilon_0}} \tag{1.5}$$

where m_e is the mass of the electron.

Not all plasmas are fully ionised. An example of this is the Earth's ionosphere. In this scenario, we have a significant number of neutral particles, and if collisions between charged particles and neutrals occur too often, the electrons will be forced into equilibrium with the neutrals, and the medium will no longer behave as a plasma, but simply like a neutral gas. For electrons to remain unaffected by collisions with neutral particles, the collision frequency between electrons and neutral particles must be much lower than the electron plasma frequency, $\omega_{pe} \gg \nu_n$. This is the third criterion for an ionised medium to behave as a plasma.

Now that the concept of a plasma has been introduced, to understand the dynamics of the magnetosphere, we must cover the interactions of plasmas with electric and magnetic fields. In the following sections, two different treatments of plasma physics are described to highlight various properties of magnetised plasmas.

Concepts from these two different approaches are used throughout this thesis to describe and explain the dynamical processes of the magnetosphere and the substorm.

1.2.2 Single Particle Motion

Since the primary constituents of a plasma are electrically charged particles, single-particle dynamics is the simplest method to describe a plasma. This involves considering each particle individually and solving its equation of motion. This method only considers the effects of magnetic and electric fields on the motion of a particle, disregarding interactions between particles.

The particle motions are governed by the Lorentz force, given by

$$\vec{F}_L = q(\vec{E} + \vec{v} \times \vec{B}) \tag{1.6}$$

where $\vec{E}$ and $\vec{B}$ are the electric and magnetic field vectors, respectively, and $\vec{v}$ is the particle velocity vector, and Maxwell's equations, given by

$$\nabla \cdot \vec{B} = 0 \tag{1.7}$$

$$\nabla \cdot \vec{E} = \frac{\rho}{\varepsilon_0} \tag{1.8}$$

$$\nabla \times \vec{B} = \mu_0 \vec{j} + \mu_0 \varepsilon_0 \frac{\partial \vec{E}}{\partial t} \tag{1.9}$$

$$\nabla \times \vec{E} = -\frac{\partial \vec{B}}{\partial t} \tag{1.10}$$

with the space charge density ρ given by $\rho = q_e(n_i - n_e)$, μ_0 the permeability of free space and $\vec{j}$ the electric current density. In order, equations (1.7)-(1.10) are termed Gauss's law for magnetism, Gauss's law, Ampère-Maxwell law, and Faraday's law. Moreover, since $\mu_0 \varepsilon_0 = c^{-2}$, the inverse square of the speed of light, the second term on the right-hand side of the Ampère-Maxwell law will be negligible in a plasma as long as the variations in the electric field occur over long periods. In space plasmas, this is generally assumed if we do not consider propagation of electromagnetic waves.

In the simplest scenario, considering a particle moving with velocity $\vec{v}$ in an

environment with zero electric field ($\vec{E} = 0$) and constant magnetic field $\vec{B}$, the equation of motion for such a particle from equation (1.6) is

$$\begin{aligned} F &= q(\vec{v} \times \vec{B}) \quad \text{or} \\ m\frac{\mathrm{d}\vec{v}}{\mathrm{d}t} &= q(\vec{v} \times \vec{B}) \end{aligned} \tag{1.11}$$

where m is the particle mass. Taking the dot product of equation (1.11) with $\vec{v}$ gives

$$m\frac{\mathrm{d}\vec{v}}{\mathrm{d}t} \cdot \vec{v} = \frac{\mathrm{d}}{\mathrm{d}t}\left(\frac{mv^2}{2}\right) = 0 \tag{1.12}$$

which shows that the particle kinetic energy remains constant under a static magnetic field.

If a uniform magnetic field is directed along the z axis, $\vec{B} = B\hat{\mathbf{e}}_z$, we obtain the components

$$\begin{aligned} m\dot{v}_x &= qBv_y \\ m\dot{v}_y &= -qBv_x \\ m\dot{v}_z &= 0 \end{aligned} \tag{1.13}$$

The velocity component parallel to the magnetic field, $v_{\|} = v_z$, is constant. Taking the second derivative of equation (1.13) , we obtain

$$\begin{aligned} \ddot{v}_x &= -\omega_g^2 v_x \\ \ddot{v}_y &= -\omega_g^2 v_y \end{aligned} \tag{1.14}$$

where ω_g is known as the gyrofrequency (additionally as the cyclotron or Larmor frequency), and is defined as

$$\omega_g = \frac{qB}{m} \tag{1.15}$$

The solutions to Equations (1.14) describe a circular motion of the particle around the magnetic field, with the direction of rotation dependent on the sign of the particle charge. The radius of orbit is termed the gyroradius, r_g (also the Larmor

radius), and it is given by

$$r_g = \frac{v_\perp}{\omega_g} \tag{1.16}$$

where $v_\perp = \sqrt{v_x^2 + v_y^2}$ is the velocity of the particle perpendicular to the direction of the magnetic field. Thus in the presence of a constant, uniform, magnetic field, charged particles with no component of velocity parallel to the field move in circular orbits in the plane perpendicular to the magnetic field with the size of the orbit proportional to the particle velocity and inversely proportional to magnitude of the magnetic field, with direction of orbit opposite for electrons and ions. The centre of the particle's orbit is known as the guiding centre.

The angle between a particle's total velocity vector, $v_\parallel + v_\perp$, and the magnetic field direction is referred to as the pitch angle, α, and is given by

$$\alpha = \arctan\left(\frac{v_\perp}{v_\parallel}\right) \tag{1.17}$$

The motion of a particle with a pitch angle of 0° will be entirely along the magnetic field (a field-aligned particle) while a particle with a pitch angle of 90° will move only perpendicular to the magnetic field (a trapped particle). Particles with pitch angles between 0° and 90° travel in a helical motion around their guiding centre.

If an electrostatic field is also present, then $\vec{E} \neq 0$. In most cases of geophysical plasmas, the parallel component (to the magnetic field) of an electrostatic field, $E_\parallel$, is not sustained because it is cancelled out by the movement of electrons, which are highly mobile along field lines. Considering a constant, uniform, electric field component perpendicular to the magnetic field and directed along the x-axis, i.e. $\vec{E}_\perp = E\hat{\mathbf{e}}_x$. The perpendicular components from equation (1.6) are

$$\begin{aligned} \dot{v}_x &= \omega_g v_y + \frac{q}{m} E_x \\ \dot{v}_y &= -\omega_g v_x \end{aligned} \tag{1.18}$$

Taking the derivative of the equation (1.18), we obtain

$$\begin{aligned} \ddot{v}_x &= -\omega_g^2 v_x \\ \ddot{v}_y &= -\omega_g^2 \left(v_y + \frac{E_x}{B} \right) \end{aligned} \tag{1.19}$$

The electrostatic field's perpendicular component to the magnetic field direction accelerates the charged particle in the direction perpendicular to the static electric and magnetic fields. This increases the particle's velocity (and gyroradius) on one side of the gyration and decreases its velocity on the other side. This is equivalent to superposing a further velocity component onto the particle's gyromotion in the $-y$ direction. As we have arbitrarily chosen the directions of the magnetic and electric fields, the generalisation of this motion, the drift of the guiding centre, is given by

$$\vec{v}_E = \frac{\vec{E} \times \vec{B}}{B^2} \tag{1.20}$$

and is termed the ExB drift. It is independent of a particle's charge and mass, therefore electrons and ions move in the same direction and with the same velocity.

The superposition of drift velocities to the gyromotion of a particle can be extended to any force, so that a more general form of guiding centre drift is obtained. This general force drift is given by

$$\vec{v}_F = \frac{1}{q} \frac{\vec{F} \times \vec{B}}{B^2} \tag{1.21}$$

which implies that any force that does not depend on charge will impart a charge-dependent drift velocity to the particles and, conversely, any charge-dependent force will result in a charge-independent drift velocity. Examples of some relevant drifts in the magnetosphere in addition to the $E \times B$ drift and their "force" equations are given in Table 1.1[1][2].

[1] $\mu = \frac{mv_\perp^2}{2B} = \frac{W_\perp}{B}$ is the magnetic moment, i.e. the ratio between perpendicular particle energy and magnetic field strength.

[2] R_c is the local radius of curvature.

Name	Force equation
Gradient drift	$\vec{F}_{\nabla} = -\mu \nabla \vec{B}$
Curvature drift	$\vec{F}_R = m v_{\parallel}^2 \frac{\vec{R}_c}{R_c^2}$
Polarisation drift	$\vec{F}_P = -m \frac{\mathrm{d}\vec{E}}{\mathrm{d}t}$

Table 1.1: Single particle drifts in magnetosphere.

1.2.3 Magnetohydrodynamics

The theory of single-particle motion is useful in describing the dynamics of a few particles exposed to electromagnetic fields. However, when a large number of particles need to be considered, it is not always appropriate. Unlike single-particle dynamics, which evaluates the motions of individual particles, magnetohydrodynamics (MHD) considers the bulk properties of the plasma, treating it as an electrically conducting fluid. Plasmas that have scale sizes much larger than the Larmor radius, r_g, and variations on timescales much longer than the inverse of the gyrofrequency, ω_g, are well described by the theory of MHD (Alfvén, 1942). MHD can be used to describe either one fluid (single-fluid, MHD which is presented in this section) or one fluid per particle species (multi-fluid MHD), though quasi-neutrality is assumed in all cases.

Assuming there are no sources or sinks, then the plasma will follow the continuity equation given by

$$\frac{\partial n}{\partial t} + \nabla \cdot (n\vec{v}) = 0 \tag{1.22}$$

with n being the plasma fluid number density and $\vec{v}$ the plasma fluid velocity. Equation (1.22) states that the number density, mass, and charge density are conserved during the plasma's motion in the absence of any interaction processes that can create or annihilate particles (Baumjohann and Treumann, 1996).

The momentum equation for the single-fluid MHD plasma is given by

$$\frac{\partial}{\partial t}(nm\vec{v}) + \nabla \cdot (nm\vec{v}\vec{v}) + \nabla \cdot \mathbf{P} - \rho\vec{E} - \vec{j} \times \vec{B} = 0 \tag{1.23}$$

where $\mathbf{P}$ is the total pressure tensor, ρ is the space charge density and m the plasma

fluid mass.

The density and pressure of a plasma be related by an equation of state, which if we assume that the pressure is isotropic, can be written in the form given by

$$p \propto n^{\gamma} \tag{1.24}$$

where γ is the polytropic index, which can take values from 0, which represents the isobaric case or constant pressure, to ∞, which represents the isometric case or constant density. It is often assumed that a plasma behaves adiabatically, and therefore we use $\gamma = \frac{5}{3}$.

Using Ampère's law, (1.9) the $\vec{j} \times \vec{B}$ term in equation (1.23) can be written as

$$\vec{j} \times \vec{B} = \frac{1}{\mu_0}\Big(\nabla \times \vec{B}\Big) \times \vec{B} = \frac{1}{\mu_0}\Big(\vec{B} \cdot \nabla\Big)\vec{B} - \nabla\left(\frac{B^2}{2\mu_0}\right) \tag{1.25}$$

which can be interpreted as the $\vec{j} \times \vec{B}$ term having two components of force. The first term on the right side of equation (1.25) represents the magnetic tension force, which opposes the bending of the field lines. The second term on the right-hand side of equation (1.25) represents the force resulting from the gradient in magnetic flux density. It is dimensionally a pressure, p_B, and for the isotropic case it is given by

$$p_B = \frac{B^2}{2\mu_0} \tag{1.26}$$

The ratio of plasma pressure to magnetic pressure is termed the plasma beta, it is given by

$$\beta = \frac{p}{p_B} = \frac{2\mu_0 n k_b T}{B^2} \tag{1.27}$$

In a high beta plasma, $\beta > 1$, the plasma pressure dominates. Whereas in a low beta plasma, $\beta < 1$, magnetic forces dominate.

For a single-fluid MHD plasma, the momentum conservation equation contains the electric current density, $\vec{j}$, as a new variable. To be able to close the system of equations, an additional expression is required for the evolution of $\vec{j}$, this is the

Generalised Ohm's law for a single-fluid MHD plasma given by

$$\vec{E} + \vec{v} \times \vec{B} = \eta \vec{j} + \frac{1}{nq_e} \vec{j} \times \vec{B} - \frac{1}{nq_e} \nabla \cdot \mathbf{P}_e + \frac{m_e}{nq_e^2} \frac{\partial \vec{j}}{\partial t} \tag{1.28}$$

where η is the plasma resistivity, and $\mathbf{P}_e$ is the electron pressure tensor. In order, the terms on the right-hand side of equation (1.28) are named the resistive or Hall term, the Lorentz force term, the electron pressure term and the electron inertia term.

Moreover, further assumptions can be made to simplify the MHD equations to the ideal MHD case. In an ideal MHD plasma, it assumed that the fluid has infinite conductivity, $\eta = 0$, and therefore the first term on the right-hand side of equation (1.28) disappears. At the length and timescales for which ideal MHD is valid, i.e. large time and length scales, the electron pressure, electron inertia and Lorentz force terms can also be neglected. These assumptions are generally valid when considering plasmas in the solar wind and Earth's magnetosphere. Applying these assumptions to the Generalised Ohm's law results in the simplified form

$$\vec{E} + \vec{v} \times \vec{B} = 0 \tag{1.29}$$

which is Ohm's law in ideal MHD conditions.

If we consider a plasma with finite conductivity while retaining the other assumptions from above, then the first term on the right-hand side of equation (1.28) is retained. If we also replace the resistivity, η, with the conductivity of the plasma, $\sigma = 1/\eta$, the Generalised Ohm's law is then given by

$$\vec{j} = \sigma \left(\vec{E} + \vec{v} \times \vec{B} \right) \tag{1.30}$$

Taking the curl of equation (1.30) and substituting for $\vec{j}$ with Ampère's law, equation (1.9), and for $\vec{E}$ with Faraday's law, equation (1.10), followed by applying vector identities results in

$$\frac{\partial \vec{B}}{\partial t} = \nabla \times \left(\vec{v} \times \vec{B} \right) + \frac{1}{\sigma \mu_0} \nabla^2 \vec{B} \tag{1.31}$$

which is termed the MHD induction equation. The first term on the right-hand side of equation (1.31) describes the changes of the magnetic field through convection with the plasma, termed the convective term, while the second term describes the effect of the diffusion of the magnetic field through the plasma, namely the diffusive term. From equation (1.31), it is clear that in the limit of a perfectly conducting plasma, $\sigma = \infty$, the field moves with the plasma as the diffusive term disappears. If the conductivity of a plasma is finite, i.e. the plasma is collisional, then the magnetic field will diffuse through the plasma to some extent. The extent to which the plasma is convective or diffusive can be expressed as the magnetic Reynolds number, given by

$$R_m = \frac{\left|\nabla \times \left(\vec{v} \times \vec{B}\right)\right|}{\left|\mu_0^{-1}\sigma^{-1}\nabla^2\vec{B}\right|} \tag{1.32}$$

Using simple dimensional terms, where $\nabla \to 1/L$, equation (1.32) can also be written as

$$R_m = \mu_0 \sigma L V \tag{1.33}$$

where L is the length scale over which the magnetic field varies and V is the convective velocity of the plasma. When $R_m \gg 1$, the plasma is well described by ideal MHD, where convection dominates diffusion. This is also known as the frozen-in flow approximation, where the plasma is frozen to the magnetic field (or similarly, the magnetic field is frozen into the plasma), i.e. when the particles move, the magnetic field changes shape such that the particles remain frozen to the same field line, and vice versa. This is also known as Alfvén's theorem, named after Hannes Alfvén. For the opposite case, $R_m \ll 1$ diffusion dominates over convection, where the magnetic field readily diffuses through the plasma and vice versa.

1.2.4 Magnetic Reconnection

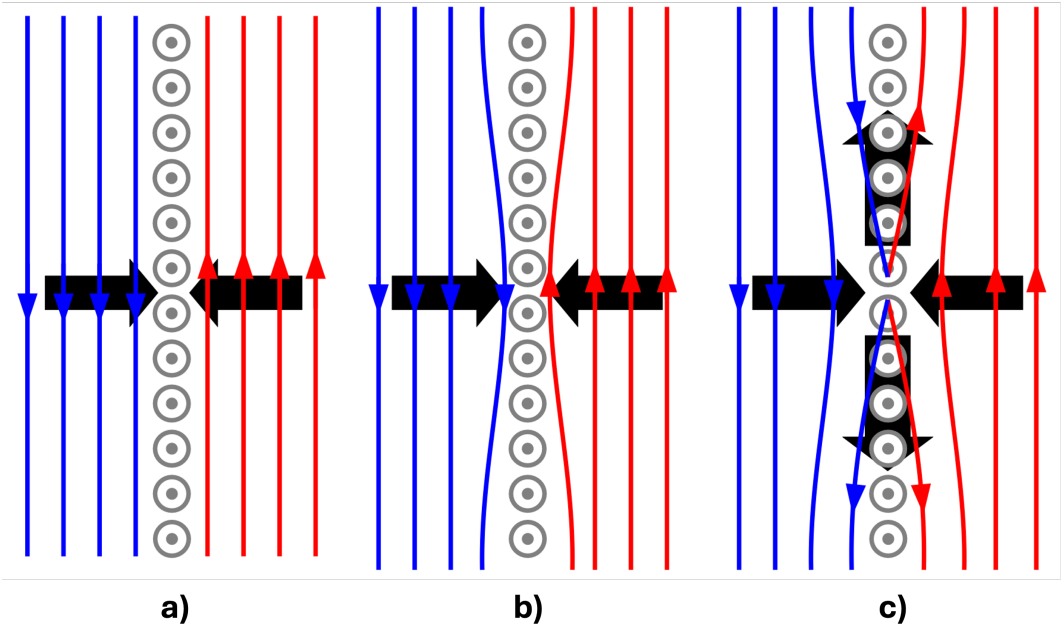

Figure 1.1: An illustration of a basic reconnection geometry. The blue and red lines are magnetic field lines, the grey circles represent a thin current sheet directed out of the page and the black arrows show the direction of the bending of the field lines (adapted from Walsh (2009)).

The magnetic Reynolds number, R_m, provides an indicator of the accuracy of the ideal MHD approximation for a given plasma (Baumjohann and Treumann, 1996). When it is large, i.e. $R_m \gg 1$, and ideal MHD holds, magnetic field lines from different sources and the particle populations frozen-in to them cannot mix. However, when the magnetic Reynold's number approaches unity, for example on small length scales, such as in thin current sheets, the frozen-in flux theorem breaks down allowing the plasma particles to diffuse across the magnetic field as both diffusion and convection processes become important (Parker, 1957; Nakamura et al., 2006; Hesse and Cassak, 2020).

When the magnetic fields diffuse through a plasma, they can merge and undergo a topological change. This process is known as magnetic reconnection. During magnetic reconnection, the magnetic field lines 'break' and 'reconnect' (Parker, 1957; Paschmann, 2008). Figure 1.1 shows a magnetic topology with antiparallel field lines frozen into the plasma, for which magnetic reconnection is most efficient.

If the field lines on each side are stagnant and do not move, this configuration can be stable over long periods, as illustrated in Figure 1.1a. However, when field lines on both sides move toward the current sheet as a result of the flow of plasma, as displayed in Figure 1.1b, the pairs of magnetic field lines will eventually reconnect, i.e. change their topology such that two new, highly bent field lines are created, illustrated in Figure 1.1c. An X-type configuration is shown in Figures 1.1b and c, with the magnetic field being zero in the centre of the X, the magnetic neutral point. The field lines that form the X and pass through the neutral point are called the separatrix (Baumjohann and Treumann, 1996).

Magnetic tension will act to straighten these newly formed lines, which results in them being expelled from the reconnection site, and thus allowing the next pair of field lines to reconnect. This whole process transfers magnetic energy to particle kinetic energy, as the particles frozen in to the newly formed bent field lines will accelerate as these field lines straighten (Paschmann, 2008). The two plasma populations which were associated with each separate magnetic field regime now coexist on the new magnetic field line and are essentially mixed (Paschmann, 2008). Magnetic reconnection is important to this thesis, as it controls the flow of energy and mass from the solar wind and interplanetary magnetic field to the Earth's magnetosphere, as well as its transport within the magnetosphere.

1.3 Solar system plasmas

Plasma exists throughout the solar system in largely distinct regimes. However, as noted above, processes such as reconnection (Dungey, 1961) and viscous interactions (Axford, 1962) allow mass and energy to be transferred between these regimes, leading to the phenomena that we study in this thesis.

1.3.1 The Solar Wind

The solar wind is the term given to the continuous radial outflow of plasma from the Sun into interplanetary space. Parker (1958) postulated that because of the high temperatures and significant pressure difference between the solar corona and the surrounding interstellar medium, the plasma on the Sun's surface should stream

away from it, overcoming the force of gravity. Due to the high conductivity of the outflowing plasma, the solar magnetic field is frozen-in to it and is therefore carried out by the solar wind. The footpoints of this interplanetary magnetic field (IMF) are considered to be fixed to the Sun's photosphere and, therefore, rotate as the Sun's surface rotates (Fisk, 1996). The radial expansion of the solar wind in addition to solar rotation results in the IMF approximating an Archimedean spiral structure in interplanetary space, known as the Parker spiral (Parker, 1959).

The solar wind and IMF are highly variable, although the solar wind is often classified as slow solar wind when it has a velocity of less than 500 km/s or fast solar wind when it has a velocity in excess of 600 km/s (Neugebauer and Snyder, 1966; Zirker, 1977; Feldman et al., 2005). The fast solar wind is thought to originate from coronal holes, which are regions of open magnetic field lines, whereas the slow solar wind is thought to originate near areas of closed coronal magnetic field. Typical solar wind properties at the radial distance of the Earth (known as 1 Astronomical Unit or AU $\approx 1.5 \times 10^{11}$ m) are shown in Table 1.2.

Table 1.2: Typical values for the Solar Wind near Earth (values taken from Borovsky (2020) average of OMNI2 measurements at L1 from 1995-2018).

Quantity	Mean Value (unit)
Flow Speed	430 (km/s)
Number density	6.3 (cm^{-3})
Magnetic field magnitude	5.8 (nT)
Proton Temperature	8.2 (eV)
Electron Temperature	14.8 (eV)
Ion gyroradius	53 (km)
Alfvén speed	58 (km/s)

1.3.2 The Earth's Magnetosphere

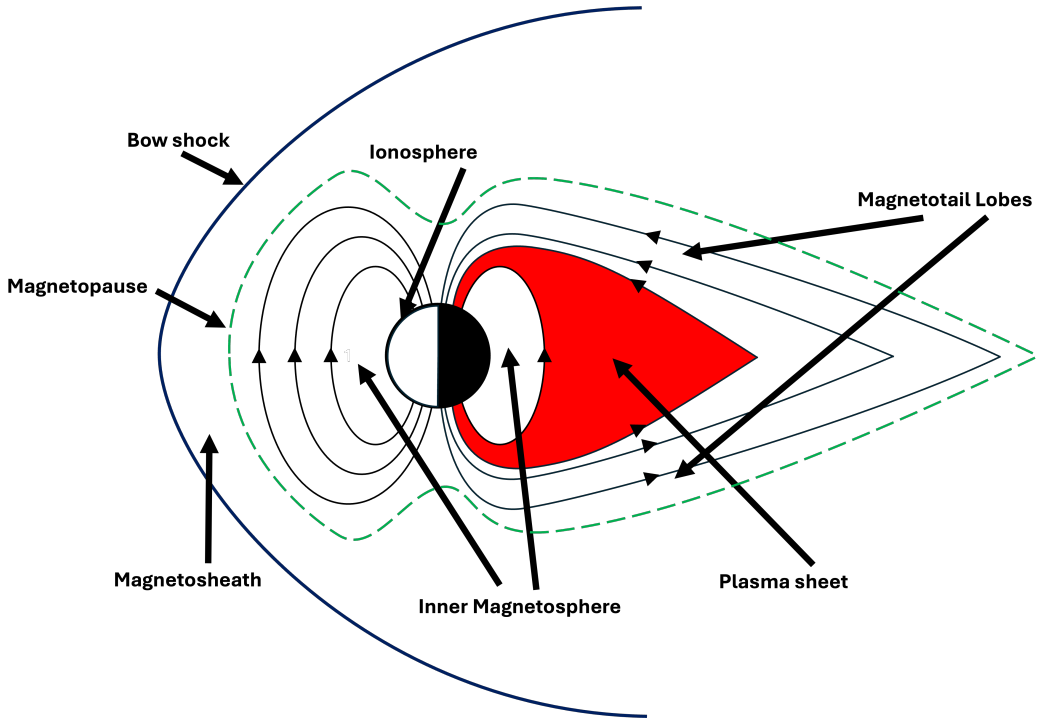

Figure 1.2: Schematic of the Earth's magnetosphere in the closed configuration, highlighting some key regions (not to scale).

Magnetised bodies in the solar system, such as the Earth, have a magnetosphere in which the magnetic field of the body is the dominant force acting on the plasma. Figure 1.2 shows a schematic along the noon-midnight meridian of the Earth's magnetosphere, with several key regions labelled. In the "closed magnetosphere" configuration displayed, as a first approximation reconnection does not occur (e.g. during periods when the IMF directed northward, i.e. perfectly parallel to the terrestrial magnetic field across the dayside magnetosphere) and the solar wind plasma is unable to enter the magnetosphere because of the frozen-in condition. This static magnetosphere forms because of the pressure balance between the solar wind particle pressure and the internal magnetic and particle pressure. In the absence of external forces, the intrinsic field of the Earth is well represented by a magnetic dipole with a field strength of $\approx 3.1 \times 10^{-5}$ T at the surface equator. However, this approximation progressively breaks down away from the Earth due to the forces exerted by the solar wind and the IMF, compressing it on the sunward side

of the terminator (the dayside, left on Figure 1.2) and stretching it into a long tail, the magnetotail, anti-sunward of the terminator (the nightside, right on Figure 1.2) as a result of tangential drag from the solar wind in the closed model of the magnetosphere. The magnetosphere is filled with plasma, originating both from upper atmospheric particles which are ionised and solar wind particles captured when reconnection does occur and the frozen-in approximation breaks down, described in Section 1.4.1.

1.3.2.1 The Bow Shock and Magnetosheath

The bow shock was first postulated by Axford (1962) and Kellogg (1962). As the solar wind propagates towards the magnetosphere, it is travelling at super-Alfvénic speeds. Therefore, when it encounters an impenetrable object, such as the Earth's magnetic field, due to Alfvén's theorem it is forced to slow down and divert around it. Due to its super-Alfvénic nature, it is not possible for any pressure waves to divert its flow around the Earth, thus a fast magnetosonic shock front is formed upstream of the magnetosphere (Slavin and Holzer, 1981). This is known as the bow shock and is found at approximately 14 R_E from Earth, where the super-Alfvénic solar wind flow slows to sub-Alfvénic speeds (Montgomery et al., 1970; Fairfield, 1992).

The solar wind is deflected around the terrestrial field between the bow shock and the magnetopause, with the solar wind downstream of the shock front slowed down to sub-Alfvénic speeds. As a consequence of this slowing down at the shock front, the solar wind kinetic energy is converted to magnetic and thermal energy, resulting in the increase in magnetic field strength, plasma pressure and density downstream of the shock. This region of hot, dense, and slowed solar-wind plasma is called the magnetosheath (Formisano et al., 1973; Dessler and Fejer, 1963). The plasma within the magnetosheath has a density and magnetic field strength up to four times that in the unshocked solar wind (Phan et al., 1994).

1.3.2.2 The Magnetopause

Within the magnetosheath region, the frozen-in approximation still holds, and thus the solar wind-originating magnetosheath and terrestrial plasma populations do not mix (Dessler and Fejer, 1963). This results in a discontinuity between the magnetic fields frozen into these plasma populations. By Ampère's law, thin current sheets exist where there are gradients in the magnetic field. The current sheet at the boundary between the magnetosheath and magnetosphere is known as the magnetopause, or also as the Chapman-Ferraro current (Chapman and Ferraro, 1931). On the dayside magnetopause, this current circulates duskward at low latitudes and dawnward at higher latitudes. On the nightside magnetopause, it flows dawnward and is closed duskward through the nightside plasma sheet. Under typical conditions, the position on the Earth-Sun line of the magnetopause, or "stand-off distance", at the subsolar point is $\approx 10\ R_E$ (Fairfield, 1971). The magnetopause current sheet is where the two distinct plasma populations are able to mix via magnetic reconnection in the open model of the magnetosphere, discussed in Section 1.4.1.

1.3.2.3 The Inner Magnetosphere

The inner magnetosphere (within $\approx 10\ R_E$) includes but is not limited to 3 distinct plasma populations: the plasmasphere (Lemaire and Gringauz, 1998); the ring current (Daglis et al., 1999); and the radiation belts (Van Allen et al., 1958; Li and Hudson, 2019). The 3 populations are differentiated by their particle energies.

The plasmasphere is a toroidal region which co-rotates with Earth and extends up to $\approx 4\ R_E$ that consists of dense, cold plasma ($\approx 10^3\ cm^{-3}$ and ≈ 1 eV, Lemaire and Gringauz, 1998; Delzanno et al., 2021) of ionospheric origin. The outer boundary of the plasmasphere, the plasmapause, is identified by a sharp particle number density gradient, often dropping sharply to $\approx 1\ cm^{-3}$ over $\approx 2500\ km$ (Watanabe et al., 2025).

The ring current is a westward directed current located between $\approx 4-9\ R_E$ as a result of trapped particles with energies of 1 to 100s keV that gradient-curvature drift in the equatorial plane dominated by the proton population, as the ring current electrons have negligible energy density (Singer, 1957; Daglis et al., 1999). Trapped

electrons drift towards east and the ions toward west, and thus there is a net flow of charge and an electric current. The ring current consists of both ionospheric- and plasma sheet-origin plasma. In particular, during periods of strong magnetospheric convection and substorms particles from the plasma sheet are injected into the inner magnetosphere some of which contribute to the ring current (Sandhu et al., 2018, 2019).

Also within the inner magnetosphere are the radiation belts (Van Allen et al., 1958), which are separated into an inner radiation belt and an outer radiation belt by the slot region located approximately at $2-4\ R_E$ (Li and Hudson, 2019). The radiation belt plasma population has a lower density ($\approx 1\ cm^{-3}$), compared to the plasmaspheric plasma, but the radiation belt particles have much higher energies. The inner radiation belt is relatively stable and primarily contains protons with energies of 10s to 100s MeV (Li and Hudson, 2019). The outer radiation belt is highly dynamic in time, space, and intensity, containing mainly 10s keV to 10s MeV electrons, with its outer boundary being highly variable but on average located at $8\ R_E$ (Bloch et al., 2021). These dynamics result from the injections of electrons during substorms which are then accelerated to high energies via wave-particle interactions (e.g., Jaynes et al., 2015; Rasinskaite et al., 2025).

1.3.2.4 The Magnetotail

Whilst the dayside magnetosphere is compressed by the incoming solar wind and the IMF, on the nightside the solar wind flow acts to stretch the terrestrial field via viscous interactions into a long tail-like configuration. The magnetotail acts as a reservoir of plasma and energy deposited to the magnetosphere from its interaction with the solar wind. The diameter of the tail is around $\approx 50\ R_E$, while its length can exceed $1000\ R_E$ (Ness, 1965; Hones Jr. et al., 1986), and is commonly split into three different regions: the plasma sheet (Bame et al., 1967), the tail lobes (Crooker, 1977), and the plasma sheet boundary layer (Eastman et al., 1984).

At the centre of the magnetotail is a region of hot, relatively dense plasma ($\approx 1\ cm^{-3}$) with low magnetic field strength called the plasma sheet (Bame et al., 1967; Baumjohann et al., 1989). The plasma sheet magnetically maps down to the

nightside auroral oval in the ionosphere. Within the plasma sheet, is a region named the neutral sheet located at the centre: a thin layer where the magnetic field strength becomes near-zero as the field switches direction from sunward in the Northern Hemisphere to anti-sunward in the Southern Hemisphere. The associated cross-tail current, which flows from dawn to dusk, closes through the magnetopause current on the flanks of the magnetotail (Lui, 1984). On either side of the plasma sheet are the northern and southern magnetotail lobes (Crooker, 1977; Cowley, 1980). These are regions of open magnetic field that map down to the northern and southern polar caps and are characterised by a strong magnetic field and low plasma density. The plasma sheet boundary layer is the transition region between the lower density tail lobe and higher density plasma sheet plasma populations, and is characterised by plasma densities and temperatures between those of the tail lobe and central plasma sheet (Eastman et al., 1984) . As will be discussed in Section 1.4.1, in the open model of the magnetosphere magnetic reconnection can occur in the neutral sheet which acts to remove some of the stored energy and plasma in the magnetotail as well as inject particles into the inner magnetosphere and along field lines into the ionosphere.

1.3.2.5 The Ionosphere

The ionosphere is an upper region of the atmosphere where the particle population transitions from the neutral atmosphere to the ionised plasma of the magnetosphere. The base of the ionosphere is located at approximately 60 km and extends to more than 1000 km in altitude (Hargreaves, 1992; Schunk and Nagy, 2009). The density and temperature of the ionospheric plasma vary significantly with height. However, the plasma temperature of the ionosphere is typically low and generally less than 1 eV, and the plasma density ranges from $\approx 10^3 - 10^6\ cm^{-3}$.

The ionosphere is formed primarily by the ionisation of neutral particles by solar UV radiation (Hargreaves, 1992; Schunk and Nagy, 2009). The precipitation of energetic particles of magnetospheric and solar origin also contributes, though the rate of ionisation by these methods is more variable. Precipitating particles impact with ions and neutrals, causing ionising collisions. The released electrons

then undergo further ionising collisions until the electron energy is insufficient to ionise particles. Instead, the further collisions cause electron excitation in neutrals which, as they de-excite, emit electromagnetic radiation that is observable as the aurora (Hargreaves, 1992; Schunk and Nagy, 2009).

The ionosphere has a significant population of neutral particles (Hargreaves, 1992; Schunk and Nagy, 2009). This results in a higher neutral collision rate that decouples the ions from the magnetic field. Above about 250 km the plasma is frozen in. Below this, ions collide with neutrals to produce an electrical current that has components both parallel to the electric field (Pedersen current) and antiparallel to the $\vec{E} \times \vec{B}$ motion (Hall current). The ionosphere is therefore not a fully ionised plasma, and the ideal MHD framework cannot be applied to the ionospheric plasma. Ion outflows from the ionosphere are a major source of magnetospheric plasma.

1.4 Solar Wind-Magnetospheric Coupling

1.4.1 The Dungey Cycle

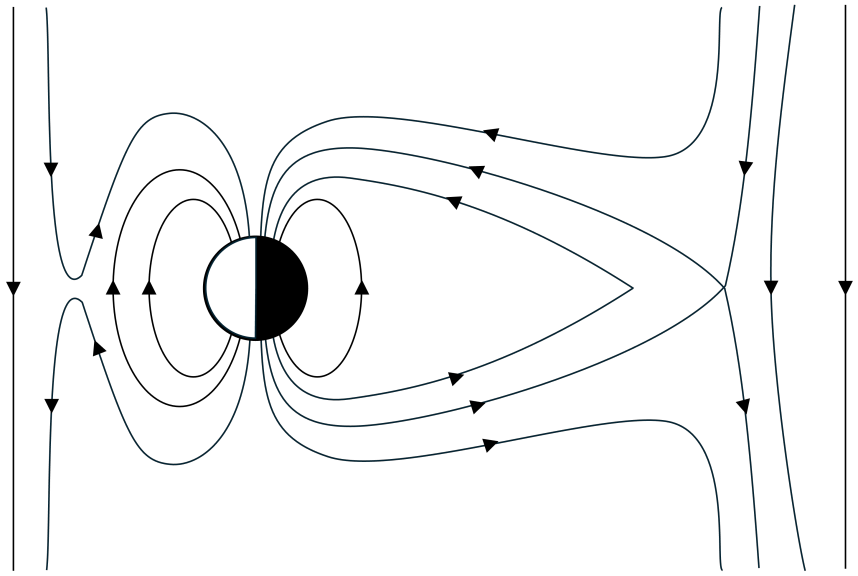

Figure 1.3: Schematic of the magnetic field line reconfiguration during the Dungey cycle. Reconnection on the dayside magnetopause opens up magnetic field lines to solar wind magnetic field. They are then dragged anti-sunward into the magnetotail where they form the tail lobes. Another reconnection site at the distant neutral line in the tail closes the open flux, allowing them to return to a more dipolar configuration before convecting back round to the dayside to complete the cycle (not to scale).

The Dungey cycle (Dungey, 1961) describes the interaction between the frozen-in magnetic field of the solar wind and the terrestrial magnetosphere during southward directed IMF. It is also described as the open model of the magnetosphere and illustrates a process in which mass and energy from the solar wind is transferred to the magnetosphere. A schematic of the field configuration is shown in Figure 1.3. At the heart of the Dungey cycle is the concept of magnetic reconnection, where the frozen-in flux approximation breaks down at thin current sheets, allowing for the reconnection of sheared magnetic fields and change in magnetic topology. During southward IMF, the magnetic field of the solar wind reconnects with the closed terrestrial magnetic field on the dayside to create open magnetic field lines, with one end at Earth and the other in interplanetary space. These newly reconnected, highly kinked field lines will straighten through the magnetic tension force. Far away from the reconnection site, the frozen-in condition still holds, so these open field lines are frozen to the solar wind flow and are thus dragged anti-sunward towards the nightside magnetosphere.

The addition of open magnetic flux into the lobes increases the magnetic pressure, causing the magnetopause to flare outward and the cross-tail current to strengthen and thin. This causes the terrestrial field, which is directed oppositely in the tail region, to reconnect in the distant neutral line. Reconnection at this distant neutral line results in a new closed field line, albeit one that is still stretched and distorted, and another field line connected only to the IMF which travels with the solar wind away from the Earth. The newly closed field lines are forced to relax back to a dipole-like configuration by shrinking and convecting earthward from the tail, resulting in earthward flows of plasma frozen-in to the field lines. The field lines then propagate back to the dayside, where the cycle repeats. This cycle of magnetospheric convection, described by the Dungey cycle, is the idealised case in which it is assumed that the IMF is steady and purely southward directed but is the framework from which more complex modes are derived (Partamies et al., 2009).

1.4.2 Substorms

The description in Dungey (1961) is a simplified case, where the energy input and release, the dayside and nightside reconnection rates, are steady and well-matched (Cowley, 2000; Milan et al., 2007) . However, this is not often the case, as the IMF conditions are highly variable. During southward-oriented IMF, magnetic flux can build up in the magnetotail lobes if the dayside reconnection rate exceeds the nightside (Cowley, 2000; Milan et al., 2007). This is likely because there is no instantaneous communication process between the reconnection regions on the dayside and on the nightside (Axford, 1969). This accumulation and storage of flux in the magnetotail lobes is termed the substorm growth phase (McPherron, 1970).

The term substorm was first published by Akasofu and Chapman (1961) in the context of its auroral manifestation. The onset of the expansion phase of the auroral substorm is described as a brightening of the equatormost auroral arc followed by a poleward and westward and eastward expansion of the aurora. This was later related to magnetic energy release and plasma energisation (e.g., Hones Jr., 1976). Although the exact timing and role of various physical processes remain debated, reconnection (Baker et al., 1996) and plasma instabilities (Lui, 1991) are key components. Globally, stored magnetic energy can only be released via the closure of the open magnetic field in the tail with reconnection at the Near-Earth Neutral Line (NENL) around $20-25\ R_E$ (Hones Jr., 1976) before it convects back towards the dayside. During this phase, the rate of reconnection at the NENL generally exceeds that at the dayside. Moreover, various localised phenomena occur throughout the magnetosphere, which will be described in the following chapter (Akasofu, 1964; Heppner, 1954; Lezniak et al., 1968; Angelopoulos et al., 1992; Smith et al., 2020).

The substorm recovery phase is often described as the relaxation of the magnetosphere to its initial quiescent state, with the rate of reconnection in the tail reducing to match the dayside. However, often significant magnetospheric and auroral dynamics are still ongoing during this period (Opgenoorth et al., 1994; Pulkkinen et al., 1994) and there is an indication that the flux continues to close (Mooney et al., 2020).

The substorm can be thought of as a magnetospheric loading-unloading process consisting of three phases: growth (energy addition), expansion (energy release), and recovery (return to quiet state). Despite being a fundamental magnetospheric process, the substorm is still not fully understood. Indeed, fundamental questions such as "What are the unique identifiers of substorms?" and "How do substorms differ from other modes of SW-M-I coupling?" still persist. This thesis tackles questions regarding the occurrence and identification of substorms in order to advance our understanding of this phenomenon.

Chapter 2

Literature Review

2.1 Introduction to Substorms

The term substorm was first published in Akasofu and Chapman (1961), where it was defined as a magnetic disturbance in the auroral zone caused by currents flowing in the ionosphere characterised by fluctuations faster than those of a geomagnetic storm. Akasofu (1964) defined the auroral substorm, providing much of the framework we use to study substorm dynamics, describing its onset, as well as the expansion and recovery phases of evolving auroral morphology that coincide with the polar magnetic disturbance. The auroral and magnetic observations were joined by Akasofu (1968) in a framework called the magnetospheric substorm, although previous studies had noted a link between changes in auroral activity and magnetic disturbances (Heppner, 1954), including Birkeland (1908) who referred to them as 'polar elementary storms'. Subsequent studies have further developed the concept of substorms to include the addition of magnetic energy and flux prior to onset, known as the growth phase of the substorm (McPherron, 1970), and during the expansion phase the injections of energetic particles into the inner magnetosphere (Lezniak et al., 1968; Kamide and McIlwain, 1974), the rapid reconfiguration of the nightside magnetic field to one that is more dipolar (Cummings and Coleman Jr., 1968), and the formation and ejection of a plasmoid (Hones Jr., 1976; Hones Jr. et al., 1986). These events coincide with the reduction of magnetic flux in the magnetotail lobes and the diversion of the tail current along magnetic field lines into

the auroral ionosphere to form a field-aligned current system known as the substorm current wedge (SCW) (McPherron et al., 1973; Kepko et al., 2015). The field-aligned currents of the SCW cause a characteristic ground magnetic perturbation at midlatitudes (McPherron et al., 1973; Clauer and McPherron, 1974b), and the closure of the SCW in the westward auroral electrojet results in the Disturbance Polar type 1 (DP1) ground magnetic deflection at higher latitudes (Heppner, 1954; Akasofu et al., 1965; Forsyth et al., 2018; Murphy et al., 2022). The waiting time between successive substorms is on average 3 hours (Borovsky et al., 1993; Freeman and Morley, 2004; Forsyth et al., 2015). However, the distribution of waiting times is highly skewed and varies depending on the signature of the substorm used (McPherron and Chu, 2018; Borovsky and Yakymenko, 2017). In the following subsections, the phases of the substorm are discussed in further detail and other magnetospheric modes (Partamies et al., 2009; Huang et al., 2009; Pulkkinen et al., 2010) that may be misidentified as substorms are introduced.

2.1.1 The Growth Phase

The first stage of the substorm is called the growth phase, first inferred from observation by McPherron (1970), and usually starts after a southward turning of the interplanetary magnetic field (IMF). After the southward turning, the entire polar ionosphere responds within 2 minutes (Ridley et al., 1997; Ruohoniemi and Greenwald, 1998) or at the latest, after 15 minutes (Cowley and Lockwood, 1992). The growth phase has been shown to last on the order of tens of minutes, usually within the range of 20 - 160 minutes (Li et al., 2013; Iyemori, 1980; Kamide et al., 1996). Li et al. (2013) showed that solar wind conditions controlled the length of the growth phase, with a larger solar wind electric field correlated with shorter growth phases. Furthermore, they found lower bounds for the solar wind electric field and flow speeds of 0.6 mV/m and 280 km/s for substorm occurrence, as well as a weak correlation between the intensity of a given substorm and the intensity of the solar wind electric field during its growth phase.

Figure 2.1 shows some of the typical features observed throughout the magnetosphere during the growth phase of the substorm. Under southward IMF, recon-

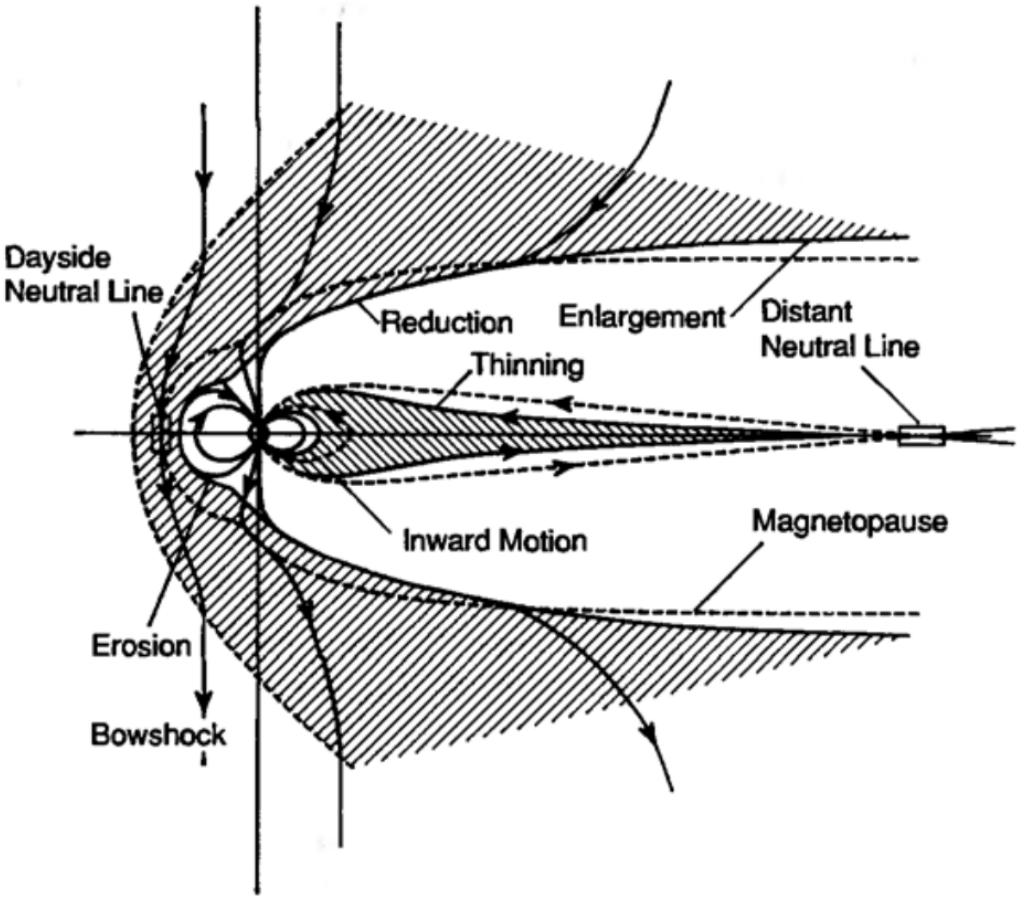

Figure 2.1: Schematic of the typical features of the substorm growth phase (from Kivelson and Russell, 1995).

nection occurs at the dayside subsolar point, opening previously closed terrestrial magnetic field lines to the solar wind. The newly opened field lines are swept back over the polar cap and into the magnetotail by the solar wind flow, leading to the accumulation of open magnetic flux in the tail. Mishin and Karavaev (2017) estimated that the maximum possible open flux in the magnetosphere is ≈ 1.2 GWb.

The convection of closed tail magnetic field lines to the dayside is not fast enough to replenish the flux opened on the dayside, leading to the erosion of the dayside magnetopause, which moves inwards by 10–20% (Aubry et al., 1970; Holzer and Slavin, 1978; Sibeck et al., 1991). The addition of open magnetic flux to the tail lobes increases the magnetic field pressure within the lobes (Coroniti and Kennel, 1972a) which causes the magnetotail to flare outwards in order that the impinging shocked solar wind exerts a greater pressure on the magnetopause to balance

the higher lobe magnetic pressure within it (Petrinec and Russell, 1996; Shue et al., 1997). The increase in tail lobe flux also causes the lobe field to become less dipolar and more 'tail-like'.

As a consequence of increased lobe pressure, the plasma sheet thins (Pytte et al., 1978; Asano et al., 2004), causing the inner edge of the plasma sheet to move earthward and the cross-tail current to increase (Pulkkinen et al., 1992). In the aurora, this is observed as an equatorward motion of the auroral oval, in addition to an increased polar cap area due to the increased open flux in the magnetosphere (Cheng, 2004; Coumans et al., 2007). Additionally, Forsyth et al. (2014b), showed that the plasma sheet pressure and temperature are higher during growth phases with stronger solar wind driving, though the plasma sheet density remains approximately constant. They also observed a weak correlation between plasma sheet temperature during the substorm growth phase and the minimum SML index observed in the subsequent substorm.

The expansion of the polar cap creates equatorward and sunward flow (Cowley and Lockwood, 1992) that enhance electrical currents in the auroral oval, known as electrojets. This is observed as a gradual increase in magnetic activity in ground-based magnetometers (Troshichev et al., 1974; Kokubun and Iijima, 1975; Nishida and Kamide, 1983; Kamide et al., 1996). In particular, magnetic perturbations of the two-cell Disturbance Polar type 2 (DP2) current pattern (Nishida and Kokubun, 1971) are observed in which both the eastward and westward electrojets are enhanced.

The substorm growth phase is a necessary condition of the substorm process, in which $\approx 10^{15}$ J of energy is extracted from the solar wind by dayside reconnection and stored in the magnetotail (Tanskanen et al., 2002). This increase in energy and pressure in the tail cannot continue indefinitely and must be released. The energy release is achieved during the substorm expansion phase.

2.1.2 The Expansion Phase and Onset Signatures

The beginning of the substorm expansion phase is called substorm onset, and its occurrence has traditionally been defined as a sudden brightening in one of the equatorward arcs in the nightside auroral oval (Akasofu, 1964). The expansion phase represents the rapid release of the energy stored in the magnetotail lobes, stored during the growth phase. During the expansion phase, there is the reconfiguration of the whole nightside magnetosphere, resulting in the observables described below. Other magnetospheric and ionospheric observables to those described in the following sections are present at substorm onset and during the expansion phase, such as the excitation of Pi2 pulsations (Saito et al., 1976; Sakurai and Saito, 1976; Yeoman et al., 1994; Smith et al., 2020) and the formation and release of a plasmoid in the magnetotail (Hones Jr., 1984; Rostoker, 1999).

2.1.2.1 The Auroral Substorm

Methods using the aurora as a proxy for substorms still rely on the Akasofu (1964) definition of the onset of the expansion phase as a sudden brightening of the equatorward edge of a quiet auroral arc, followed by a rapid poleward and azimuthal expansion of this arc over the course of approximately 30 minutes, before auroral intensity subsides over the course of approximately 2 hours. The original schematic of the auroral substorm evolution is shown in Figure 2.2, where the darkness of the line indicates the intensity of the aurora. Using variations of this definition, many authors have visually identified substorm onsets from successive auroral images, whether for individual case studies or statistical analyses (Liou et al., 2001; Frey et al., 2004; Nishimura et al., 2010; Gabrielse et al., 2021). This relies on the observer's judgment, introducing a degree of subjectivity and lack of reproducibility to the lists created. A variety of instruments have also been used including spacecraft imagers such as the Imager for Magnetopause-to-Aurora Global Exploration (IMAGE) Far Ultraviolet Imager (FUV) instrument suite (which is further discussed in Section 3.2) and the ground-based Time History of Events and Macroscale Interactions during Substorms (THEMIS) All-Sky Imager (ASI) array (Mende et al., 2008). For example, Nishimura et al. (2010) used the THEMIS ASI array, in which

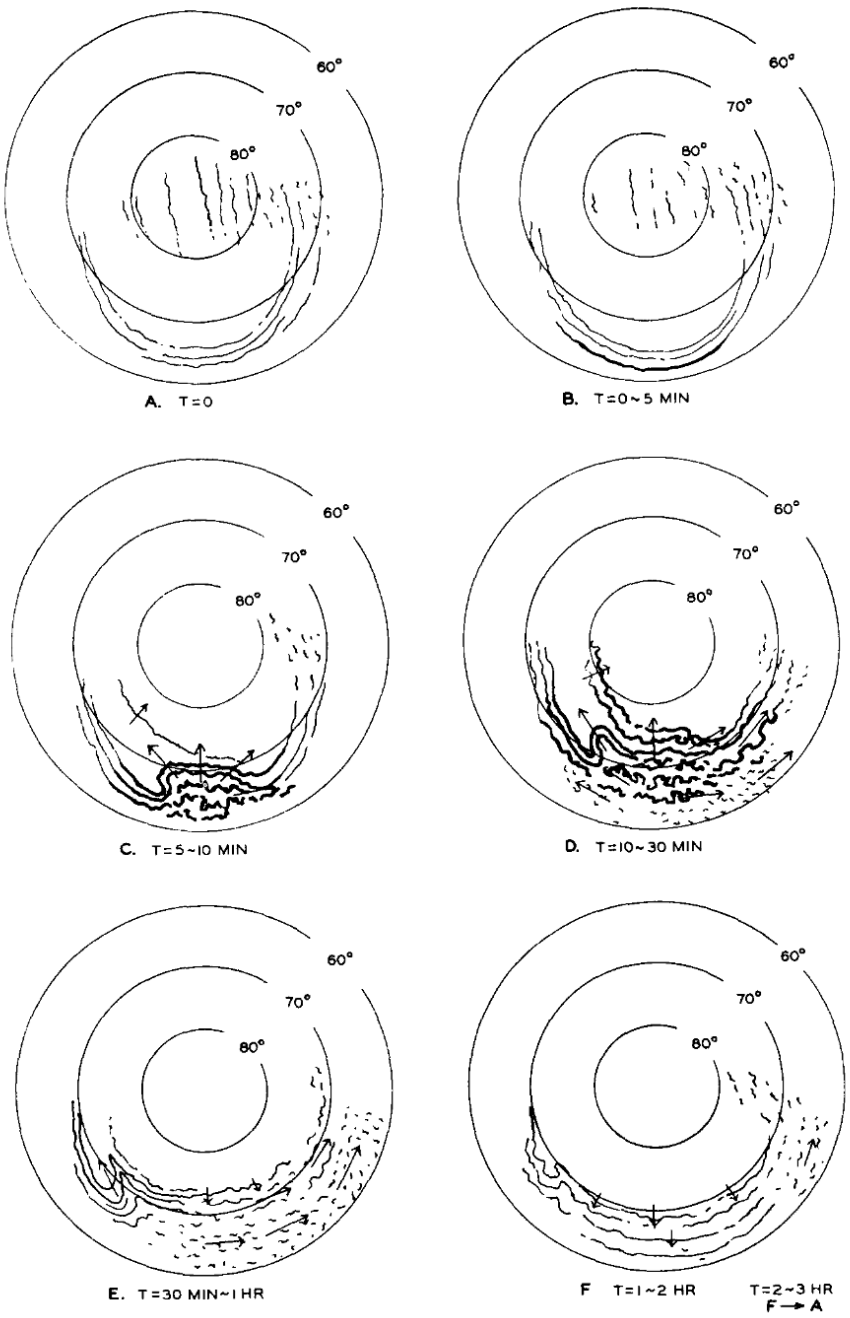

Figure 2.2: Schematic of the evolution of the auroral substorm from onset to its expansion poleward and azimuthally over the course of ≈ 30 minutes, before the "recovery" of auroral intensity to the background level and the poleward edge's retreat to lower latitudes ≈ 2 hours after onset (from Akasofu, 1964)

each imager takes an image every 3 seconds with a spatial resolution of 1 km per pixel over an all-sky field of view. Using ground-based all-sky imagers means that the aurora can only be observed in the absence of clouds, in addition to the limi-

tation that the array only covers a limited portion of the auroral oval. Space-based imagers were also widely used in the era of the IMAGE and Polar spacecraft. These were not bound by the cloud restriction or geographical constraint of only observing a specific portion of the sky, like a single ASI is. In fact, both spacecraft had the capability of observing a whole auroral oval, but were limited in terms of their observation window due to their orbit and lifetime. For example, Frey et al. (2004) used the space-based IMAGE FUV instrument suite, (Mende et al., 2000b) which can view the entire northern auroral oval at a spatial resolution of up to 50 km per pixel every 2 minutes. However, its viewing period was limited due to orbital constraints at $\approx$ 8 hours of observations for every $\approx$ 14 hour spacecraft orbit, with "good" observations of the northern auroral oval only available for the first 2.5 years of the mission. Since the end of the Polar mission in 2008, there has not been a global auroral imager. However, the long wait for this beneficial view of the aurora will soon be ended with the imminent launch of the ESA Solar wind Magnetosphere Ionosphere Link Explorer (SMILE) spacecraft.

2.1.2.2 The Substorm Current Wedge

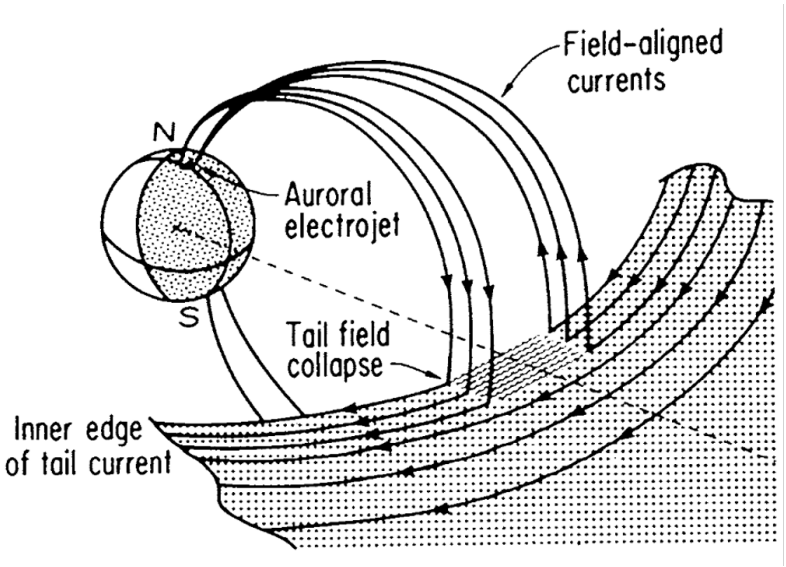

Figure 2.3: Schematic of the Substorm Current Wedge (from McPherron et al., 1973)

Coincident with the sudden brightening of the aurora, there is the formation of a large-scale current system known as the Substorm Current Wedge (SCW) in the

inner magnetotail. The cross-tail current that was intensified in the growth phase is disrupted and diverted via a pair of field-aligned currents into the ionosphere (McPherron et al., 1973; Kepko et al., 2015), as shown in Figure 2.3. Gjerloev et al. (2007) showed that the most probable width of the SCW by the end of the expansion phase is $\approx$ 6 hours of MLT (90°). The circuit typically contains $\approx$ 300 kA total current, with up to $\approx$ 1 MA for large substorms (Sergeev et al., 1996c; Gjerloev et al., 2007; Newell and Gjerloev, 2011; Chu et al., 2014, 2015).

The closure of the SCW in the ionosphere is observed as an enhancement of the westward auroral electrojet centred around local midnight (Heppner, 1954; Akasofu et al., 1965; Weimer, 1994). The strength of the enhancement depends on the background conductivity of the ionosphere and is strongest in the dark winter ionosphere (Newell et al., 1996; Wang et al., 2005; El-Alaoui et al., 2023) due to the formation of a Cowling current channel (Cowling, 1932; Boström, 1964; Amm and Fujii, 2008).

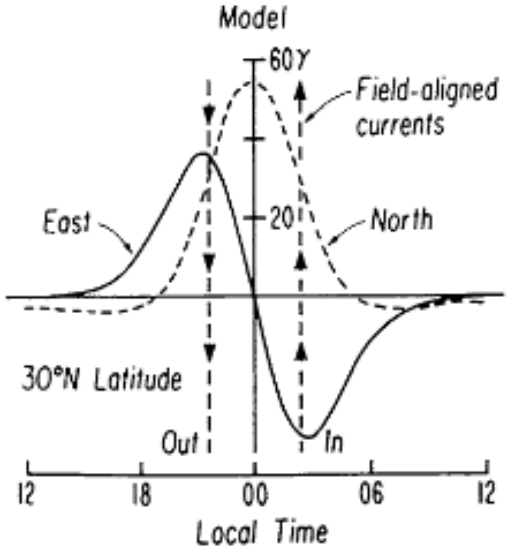

Figure 2.4: Schematic of the midlatitude perturbations observed on the ground due to the substorm current wedge (from McPherron et al., 1973)

The formation of the SCW also produces a distinctive pattern of changes in the midlatitude magnetic field, shown in Figure 2.4 (McPherron et al., 1973; Caan et al., 1975; Chu et al., 2015). Assuming a simple wedge structure, everywhere within the wedge, and additionally some distance on either side, the north component of the

magnetic field is positive and symmetric about the central meridian of the wedge. The east component of the magnetic field perturbation is antisymmetric about the central meridian. In the Northern Hemisphere the east component is positive west of the central meridian and negative east of the central meridian, with extremes at the locations of the upward and downward field-aligned currents (Clauer and McPherron, 1974a). In the Southern Hemisphere, the northern component is also positive, but the signs of the magnetic perturbations in the east component are reversed.

The structure of the substorm current wedge continues to be a much debated topic within substorm research. Specifically, whether the wedge is a singular large-scale current loop (McPherron et al., 1973; Sergeev et al., 2011), a double-wedge system (Gjerloev and Hoffman, 2014), or a series of "wedgelets" (Zhang et al., 2011; Liu et al., 2013, 2015). However, Forsyth et al. (2014a) showed using in situ measurements that the structure of the SCW during the expansion phase was inconsistent with the model that the SCW is formed by a series of wedgelets that become a coherent structure. Furthermore, Walker et al. (2024) showed that, when using a grid spacing of 100 km in their inversion technique, there were no clear signs that the substorm current wedge was composed of wedgelets.

2.1.2.3 Particle Injections

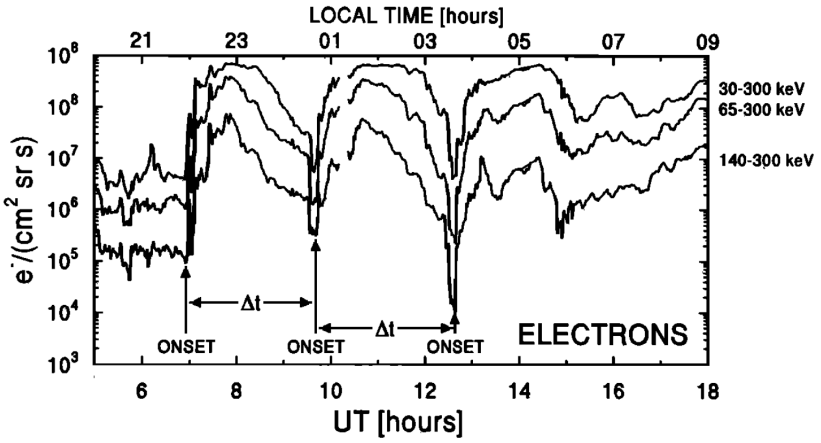

Figure 2.5: Example timeseries from one of the Los Alamos National Laboratory (LANL) geosynchronous satellites from 02 March 1983. Three substorms are observed as three sharp increases in the particle flux at all energies with Δt indicating the time between successive onsets (from Borovsky et al., 1993)

Another signature used for the identification of substorms is the Earthward injection of energetic electrons and protons observed in geosynchronous orbit (Lezniak et al., 1968), which previous studies have temporally associated with the auroral and ground magnetic signatures of substorms (Arnoldy and Chan, 1969; Kamide and McIlwain, 1974; Yeoman et al., 1994; Weygand et al., 2008). Injections are most visible in particle energies in the 10s of keV (e.g. Baker et al., 1978; Belian et al., 1978). However, impulsive increases in particle fluxes during substorms are also observed at lower energies (DeForest and McIlwain, 1971; Parks et al., 1980). Figure 2.5 shows an example time interval from one of the LANL probes in which three substorm onsets are observed, exhibited by rapid increases in particle flux at all energies before a gradual decrease to background levels. It should be noted that for a substorm, there is usually the requirement that the injection is dispersionless (i.e. particle fluxes peaking simultaneously rather than sequentially with decreasing particle energy) as this indicates observation within the injection region (usually 1 - 2 MLT from 24 MLT) (Reeves et al., 2003; Henderson, 2022). However, studies have also included dispersed injections when there are no spacecraft available within the injection region, with the dispersion being used to map back to potential injection locations (Yeoman et al., 1994; Reeves et al., 1996; Mauk and Meng, 1983). Borovsky et al. (1993) visually identified substorm onsets as the sudden increase in energetic particle flux after a "drop-out" that is associated with the growth phase observed by at least two geosynchronous satellites located nearest to magnetic midnight. The Borovsky et al. (1993) set of observations was one of the first substantial catalogues of substorm events created that allowed for the study of the statistical effects of the substorm and any obvious drivers of its onset. Various models and theories have been proposed to explain the simultaneous enhancement of particles of all energies (e.g., McIlwain, 1974; Moore et al., 1981; Mauk and Meng, 1983; Birn et al., 1997; Li et al., 1998; Sergeev et al., 2005; Gabrielse et al., 2012), but the mechanism and its causal relationship with the other substorm signatures are still not well understood.

2.1.2.4 Substorm onset models

There are two major phenomenological models for substorm onset - the Near-Earth Neutral Line model (NENL) and the Current Disruption model (CD) - which differ with respect to the nature and location of the substorm onset mechanism and the causal order of events.

The NENL model of substorms was first developed by Hones Jr. (1976), who suggested that magnetic reconnection in the magnetotail was the triggering process for the onset of the substorm. Hones Jr. et al. (1986) postulated that the reconnection site initially forms in the near-Earth plasma sheet at roughly $20-30\ R_E$, causing the tailward release of a plasmoid and a brightening and poleward expansion of the aurora at the ionospheric footpoint of the reconnection site. However, this initial formulation of the NENL model was inconsistent with the fact that the substorm onset arc rarely mapped beyond $10-15\ R_E$.

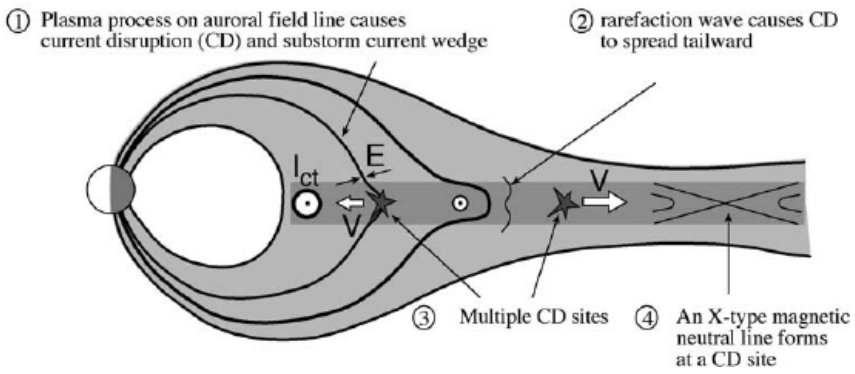

Figure 2.6: Schematic of Current Disruption model of the substorm (from Lui, 2004).

To explain this discrepancy, an alternative substorm model was proposed called the Current Disruption (CD) model (Lui, 1996). In the CD model framework, shown in Figure 2.6, the expansion onset is believed to start with a sudden reduction of the cross-tail current and formation of the SCW due to one of several possible plasma instabilities at the earthward edge of the plasma sheet (Roux et al., 1991; Lui et al., 1991; Cheng and Lui, 1998; Voronkov et al., 2003; Cheng, 2004). The current disruption and dipolarisation of the tail field launches a rarefaction wave down the tail as a result of the depletion of plasma in the CD region. This rarefaction wave acts to thin the midtail plasma sheet, triggering reconnection at the NENL.

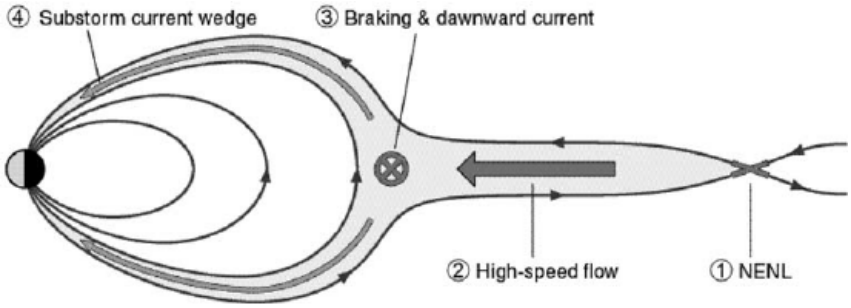

Figure 2.7: Schematic of the adjusted NENL model (from Lui, 2004).

The discrepancy between the substorm onset arc and the NENL locations also led to a modification of the NENL model by Baker et al. (1996) as shown in Figure 2.7. They proposed that NENL reconnection caused earthward and tailward propagating flows within the plasma sheet, known as Bursty Bulk Flows (BBFs) (Angelopoulos et al., 1992), which carried magnetic flux. The increasing magnetic field strength and plasma pressure as the BBF's travel earthward act to slow down or break the flows, and the flux they carry builds up in the Current Disruption region ($8-10\ R_E$). This has the effect of disturbing the cross-tail current and creating the substorm current wedge.

Therefore, the Near-Earth Neutral Line and Current Disruption Models disagree on the causal sequence of events that constitute a substorm. However, whether a current disruption in the near-Earth region of the plasma sheet triggers reconnection or vice versa, both models agree that a plasma instability causes a disturbance of the cross-tail current in the plasma sheet, causing it to divert and form the substorm current wedge.

2.1.3 The Recovery Phase

The recovery phase of the substorm was also defined in the seminal study by Akasofu (1964). The beginning of the recovery phase in the aurora is identified as the end of the poleward motion of the auroral oval. If dayside reconnection is still ongoing, the poleward edge of the auroral oval retreats to lower latitudes, as displayed in the Figure 2.2 panels E and F. Auroral intensity decreases during the substorm recovery phase (Frank and Craven, 1988), although complex displays are still visible (Opgenoorth et al., 1994; Forsyth et al., 2020a). There is also a decrease in

magnitude in the magnetic perturbations observed on the ground as the magnetosphere returns to its quiet-time configuration, with the decline of reconnection in the magnetotail at the Near-Earth neutral line and the decay of the SCW (Pulkkinen et al., 1994). The substorm recovery phase has a typical duration of 30 - 40 minutes (Forsyth et al., 2015; Chu et al., 2015), but in certain cases it can last longer.

2.1.4 Substorm-like activity

2.1.4.1 Steady Magnetospheric Convection

Periods of steady magnetospheric convection (SMCs) are extended periods of time (at least 90 minutes, longer than a typical substorm recovery phase, and have been observed to last up to 10 hours) when the magnetosphere is driven by southward IMF, but typically none of the features of the substorm are observed. The aurora is active compared to quiet time levels, but there is no substorm-like activity, i.e. sudden brightening of an equatorward arc (Pytte et al., 1978; Sergeev et al., 1996a; O'Brien et al., 2002; McPherron et al., 2005; Walach and Milan, 2015). SMC events are characterised by the appearance of a double auroral oval, where the diffuse equatorward boundary is split from the poleward boundary by a dark region (Elphinstone et al., 1995; Pulkkinen et al., 1995). However, during these intervals there are no sudden intensifications of the westward electrojet near midnight, no midlatitude positive bays, and no dipolarisations at synchronous orbit (McPherron et al., 2008). During SMC periods, the nightside and dayside reconnection rates are steady and roughly equal, and as such they are also known as "balanced reconnection intervals" or BRIs (DeJong et al., 2009).

There are many similarities in the features observed during SMCs and the recovery phases of a substorm (Sergeev et al., 1996a). Therefore, for an event identified to qualify as an SMC, it must have a duration longer than 90 minutes of a typical substorm recovery phase. It is thought that SMC intervals transition directly from substorms or at least substorm onset and expansion phases. Sergeev et al. (1996a) suggested that the magnetic field configuration required for steady magnetospheric convection to occur could only arise after the unloading of tail flux in a substorm expansion. Moreover, DeJong et al. (2009) found that only one of 51 BRI cases

identified did not occur after a substorm. This was further supported by Kissinger et al. (2012), where they found that 92% of their 2924 SMC events between January 1997 and May 2011 occurred after a well-defined substorm onset identified from the AL index. In contrast to these results, Walach and Milan (2015), argued that a significant portion of SMC events, using criteria similar to those in the above studies, are part of a prolonged version of substorms due to continued driving on the dayside during expansion phases.

2.1.4.2 Pseudobreakups

The term pseudobreakup was originally introduced by Akasofu (1964) to describe events in which an auroral arc initially brightened similar to a substorm onset, but then the auroral intensity decreased a few minutes later without any major expansion. These events are identified during quiet times and during substorm growth phases, with growth phase pseudobreakups often occurring at more poleward arcs than substorm breakups (Pulkkinen et al., 1998). In addition to the term pseudobreakup, Ohtani et al. (1993), introduced the term pseudosubstorm to refer to magnetospheric changes related to the phenomena, as well as the auroral manifestation. In this thesis, the term pseudobreakup is used; however, the terms have been used interchangeably in the literature.

Nakamura et al. (1994) studied these events further, showing that pseudobreakups show many of the signatures of substorm onset, including the formation of a SCW, magnetic field dipolarisation, and energetic particle injections. This is in addition to pseudobreakups that show brightening of the most equatorward auroral arc, enhancement of the westward auroral electrojet, and ejection of a plasmoid (Aikio et al., 1999). It is often difficult to distinguish between small substorms and pseudobreakups, with Rostoker (1998) suggesting that all auroral breakup activations are controlled by the same physics, regardless of size, and that substorm expansions are built up of a series of small-scale current systems, one of which could show up as a pseudo-breakup. The defining feature of the pseudobreakup is the lack of poleward and azimuthal expansion of the aurora and its short lifetime. The mechanism preventing a pseudobreakup developing into a substorm is still under debate, whether

it is a lack of stored energy in the tail (Nakamura et al., 1994; Ohtani et al., 1993), or too low ionospheric conductivity to close the substorm current wedge (Koskinen et al., 1993).

2.1.4.3 Global Sawtooth Oscillations

Global sawtooth oscillations or sawtooth events are identified by the quasi-periodic enhancement of energetic electron and proton fluxes at geosynchronous orbit (Belian et al., 1995; Huang, 2002; Huang et al., 2003; Reeves et al., 2003; Henderson, 2004). Similar to substorm-related particle injections, they are observed as sudden increases in particle fluxes (i.e. a dispersionless injection) of both electrons and protons at geosynchronous orbit, before a steady decrease to background levels. A key differentiator is that these impulsive increases in particle flux typically occur in trains of 3 - 8, with the wave-like pattern, similar to the teeth of a saw, giving them their namesake. Each "tooth" in a sawtooth event occurs quasi-periodically, with a typical recurrence period of 2 - 4 hours. However, compared to substorm-related injections, sawtooth events have the added criterion that the dispersionless injections have to be observed by two spacecraft, one on the dayside (near noon local time) and one on the nightside (near local midnight) (Cai and Clauer, 2009; Henderson et al., 2006b).

Sawtooth events typically occur during geomagnetic storm intervals, particularly when solar wind driving is strong and steady (Cai et al., 2011). Moreover, the solar wind driving conditions prior to and during sawtooth events are typically stronger than those during typical substorm intervals (Partamies et al., 2009). Typically, the phenomena associated with a single tooth are similar to those of a single isolated substorm, with the exception of a double auroral oval as observed during SMC events (Henderson et al., 2006b). Henderson (2004), showed that a previously well-studied substorm interval was actually a sawtooth event if modern definitions were applied, raising the question of whether there was a physical distinction between the two modes.

2.2 Ionospheric Current Systems

As one of the primary topics of this thesis is the ground magnetic signature of the substorm, it is important to introduce the morphology and dynamics of the electrical current systems of the terrestrial magnetosphere and ionosphere. It is the variations in these current systems that are observed by ground magnetometers via Ampere's law. In this Section, a quick introduction to various current systems in the magnetosphere is presented, before a focus on the equivalent ionospheric current systems, namely the Disturbance Polar (DP) systems (Nishida, 1968b).

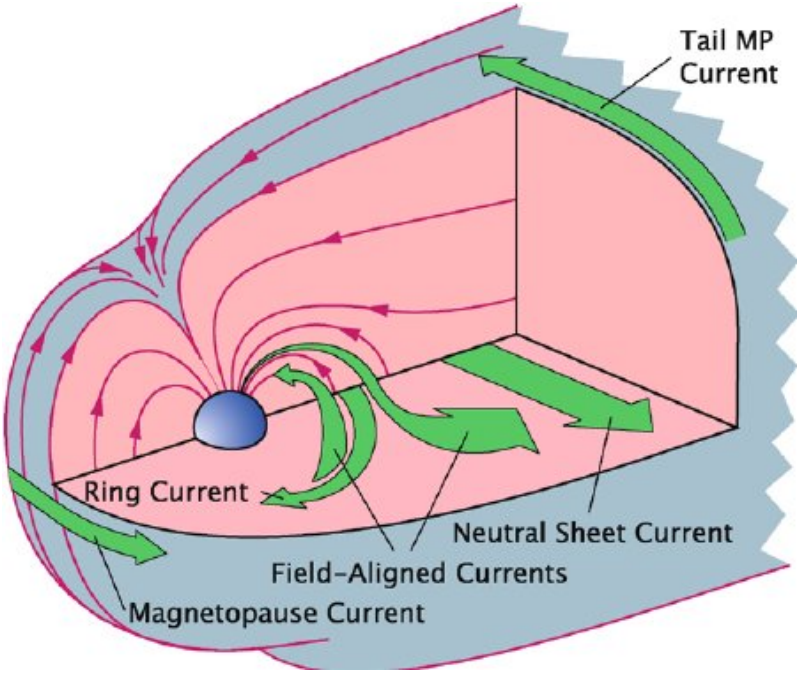

Figure 2.8: Schematic of Magnetospheric Currents (original figure from Baumjohann and Treumann (1996), taken from Baumjohann et al. (2010)

Figure 2.8 displays a schematic that highlights the regions of the magnetosphere in which the currents that we are about to discuss flow. On the dayside, Chapman and Ferraro (1931) were the first to suggest that the Earth's magnetosphere carves out a cavity in the solar wind that neither solar wind plasma nor its magnetic field can penetrate. The thin boundary that separates the magnetosphere from the solar wind is a current sheet, known as the magnetopause, with its existence confirmed by Explorer 10 and 12 measurements in the early 1960s (e.g., Cahill and Amazeen, 1963). This current is directed from dawn to dusk across the equatorial

magnetopause, and dusk to dawn across the high-latitude magnetopause tailward of the magnetospheric cusps. Changes in solar wind dynamic pressure affect the size of the magnetosphere and the strength of the magnetopause currents.

In the nightside magnetosphere, in situ observations by the IMP-1 satellite revealed that the nightside geomagnetic field was dragged out far behind Earth in the anti-sunward direction, with a thin current sheet flowing where the magnetic field changes direction in the equatorial plane (Ness, 1965; Speiser and Ness, 1967; Bame et al., 1967). This magnetotail (or also often named neutral sheet) current is directed from dawn to dusk in the equatorial plane and is closed through two different loops, one above and below on the tail magnetopause, both flowing dusk to dawn.

The magnetospheric ring current is a result of the gradient and curvature drift motion of warm ($\sim$keV) trapped charged particles in the inhomogeneous terrestrial magnetic field, which gyrate and bounce along magnetic field lines and drift around the Earth on the order of a few hours. The westward drift of ions and eastward drift of electrons results in net charge transport and the corresponding westward ring current flowing around the Earth. Substorms are an important phenomenon in creating the ring current, with Sandhu et al. (2018) evaluating that approximately 9% of the energy released by the substorm is transferred onto the ring current.

There also exist currents that flow along magnetic field lines, named Birkeland or field-aligned currents, whose existence was first proposed by Birkeland (1908) to explain the variations of the magnetic field measured on the ground in the polar regions. These currents, which are mainly carried by electrons, connect the magnetospheric currents with ionospheric currents. Their large-scale morphology was first deduced using observations from the TRIAD satellite (Iijima and Potemra, 1976a,b), of which a schematic is shown in Figure 2.9. The current system forms two concentric rings above the auroral ionosphere: the poleward (Region 1) currents and the equatorward (Region 2) currents. The Region 1 currents connect the ionosphere to the currents in the magnetopause and the magnetotail, while the Region 2 currents connect to the partial ring current in the inner magnetosphere (Iijima and

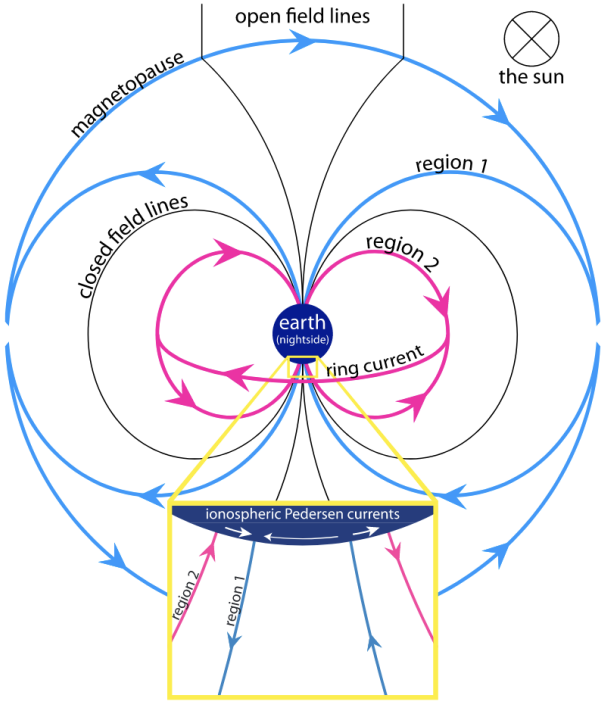

Figure 2.9: Schematic of the Region 1 and Region 2 Birkeland and their closure in the ionosphere and magnetosphere (from Coxon et al., 2014a).

Potemra, 1978; Cowley, 2000). The Region 1 and 2 currents are closed through the ionosphere by horizontal Pedersen currents and so their current strength depends on the conductance of the ionosphere that depends on solar illumination, which varies daily, seasonally and with the solar cycle, and on particle precipitation into the ionosphere from space. Coxon et al. (2014a) showed that at current magnitudes greater than ≈ 1.5 MA the Region 1 currents tend to be stronger than the Region 2 currents, peaking at a ratio of ≈ 1.15 at ≈ 4 MA. Moreover, the work of Coxon et al. (2014b) showed that while the magnitude of both Region 1 and Region 2 increases after the onset of the substorm, the diverted current of the SCW preferentially flows through the more poleward Region 1 currents.

The Disturbance Polar (DP) current systems (Nishida, 1968b) are specified from equivalent ionospheric currents, i.e. the ionospheric current confined within a spherical surface at around 100 km altitude that would create the magnetic perturbation observed on the ground, i.e. the equivalent current direction is evaluated by rotating the surface magnetic perturbation by 90° clockwise. They do not have a

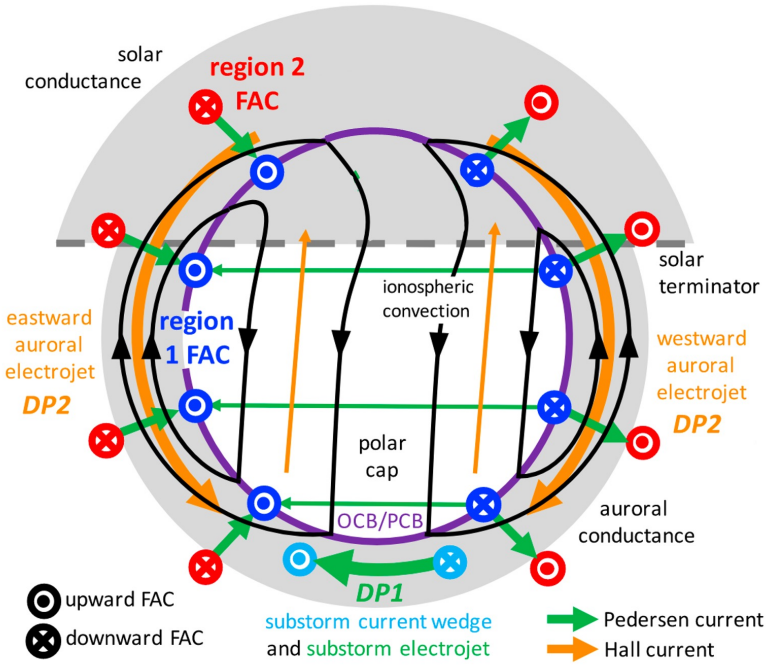

Figure 2.10: Schematic of the primary equivalent current systems in the polar ionosphere of the Northern Hemisphere (adapted from Milan et al. (2017).

unique relationship to the distribution of the true Hall, Pedersen, and field-aligned currents that flow in the magnetosphere-ionosphere system. There must be a degree of care when interpreting these equivalent currents, since conductance gradients and the contribution of distant currents also affect the resulting pattern (Milan et al., 2017). To a first approximation, ground magnetic perturbations are due to Hall currents only because, for a uniformly conductive ionosphere with field-aligned currents perpendicular to the ground, the magnetic perturbations from field-aligned currents and their corresponding Pedersen currents exactly cancel (Fukushima, 1969).

Figure 2.10 shows a schematic of the polar ionosphere of the Northern Hemisphere, with plasma and current flows highlighted. The Pedersen currents (shown in green) act to close upward and downward field-aligned currents, the Region 1 (blue) and Region 2 (red) currents, while Hall currents (orange) flow in the direction opposite to the flow streamlines of the ionospheric convection pattern (black). The "convection" of charged particles in the ionosphere is the result of the solar wind electric field imposed on open field lines, causing the ionospheric particles to drift with velocity $\vec{E} \times \vec{B}/B^2$ over the polar cap. This motion can also be thought of as the

motion of plasma frozen to the magnetic field as it circulates with the Dungey cycle of magnetospheric convection under steady southward IMF conditions (Dungey, 1963). As discussed earlier, magnetic perturbations on the ground are to a first approximation due to Hall currents only (Fukushima, 1969, 1994), which are directed in the $-\vec{E} \times \vec{B}$ direction.

The Hall currents related to ionospheric convection are strongest in the auroral zones because of the enhanced conductivity in this region compared to the polar cap, and are directed eastward in the dusk sector and westward in the dawn sector. These currents are also known as eastward and westward auroral electrojets. The magnetic perturbations associated with the auroral electrojets, as well as those over the polar cap, have been termed the Disturbance Polar 2 (DP2) pattern, which was first identified by Obayashi (1967) and Nishida (1968b) who described their morphology and relationship with variations in the solar wind and the IMF. Nishida (1968a) showed that fluctuations in the DP2 pattern are highly correlated with the southward component of the IMF (B_z) with a short (approximately 10 minute) time lag. Shore et al. (2018) used data-driven methods to evaluate the spatial modes that contribute the most to ground magnetic variations to show that the mode representing the DP2 pattern was the dominant source of variance in any given month, for any season throughout a complete solar cycle. They also showed that the "DP2 mode" consistently had the highest correlation with the IMF B_z at a delay of 30 minutes of the modes evaluated by their method, although this level of correlation varied from $\sim 0.3 - \sim 0.8$.

Since plasma from the magnetotail flows both dawnward and duskward around the Earth in the Dungey cycle, then one might expect the auroral electrojet magnitudes to be similar, this is not often the case. Substorm-related electron precipitation can result in elevated dawn MLT conductance (e.g Wallis and Budzinski, 1981; Stepanov et al., 2021). This results in a stronger westward DP2 electrojet and dawn-dusk asymmetry to the DP2 pattern, which is observed statistically (Shore et al., 2018). The case of a symmetric auroral electrojet pair approximates the summertime scenario, where the morning and afternoon MLT sectors are mostly and

similarly illuminated by the Sun and thus have similar levels of conductance in the auroral zone.

The Disturbance Polar 1 (DP1) pattern is the set of magnetic perturbations related to the closure of the field-aligned currents of the substorm current wedge (see Section 2.1.2.2). During the expansion phase of the substorm a pair of upward and downward FACs typically to the west and east of the midnight meridian are closed by the substorm electrojet across the nightside auroral ionosphere. It is indicated in Figure 2.10 as a Pedersen current, although the substorm electrojet may be amplified by a secondary Hall current flowing parallel to the Pedersen current that is caused by the generation of a Cowling current channel (Cowling, 1932; Boström, 1964; Coroniti and Kennel, 1972b) due to substorm-related electron precipitation. Therefore, the magnitude of the substorm (or DP1) electrojet is modulated by the conductivity difference between the current channel and the background ionosphere (Amm and Fujii, 2008), introducing a seasonality to the magnitude of substorm-related magnetic perturbations. As discussed in Section 2.1.2.2, although it is possible to show that on average, the SCW has this simple single upward and downward FAC structure closed by a westward ionospheric current (Clausen et al., 2013), substorm FACs can be highly azimuthally structured on a case by case basis (Forsyth et al., 2014a), with the true nature of the wedge still an active topic of research. For example, Forsyth et al. (2018) showed evidence for a two-loop structure for the SCW, using the AMPERE FAC dataset, thus avoiding attempting to account for the Cowling conductance channel created in the ionosphere. Shore et al. (2018) also resolved a spatial mode that represents the DP1 current system with a strong westward current over the midnight sector at auroral latitudes. In contrast to the DP2 mode, this DP1 mode was not resolved for every month of the solar cycle analysis, showing a seasonal trend of being resolved less often during summer and when it was resolved, being the third or fourth dominant mode to contribute to monthly geomagnetic variance. Moreover, Shore et al. (2019) showed that this spatial mode was largely uncorrelated with the IMF, with only 17% of the DP1 mode variance explainable by the IMF. This is due to the DP1 pattern's relationship with the sub-

storm, which has a nonlinear and time-integrated relationship with variations in the IMF (Freeman and Morley, 2009; Morley and Freeman, 2007).

In the schematic picture of ionospheric electrodynamics, DP1 and DP2 are discussed as appearing separately and due to distinctly different reasons. That is, DP1 is related to the loading-unloading phenomenon, the substorm, and DP2 corresponds to periods of steady southward IMF, when the magnetosphere is directly driven and there is increased magnetospheric convection. In reality, the pattern of magnetic perturbations on the ground is, in fact, a superposition of the DP1 and DP2 current patterns, along with those discussed further below, and the dominance of which is constantly varying. This was first discussed in Kamide (1982), where they noted that the location of the contributing station to AL was often at 03 MLT, however, during the substorm expansion phases the location of the contributing station would change to pre-midnight MLTs (22-23), before shifting again towards dawn MLTs during the substorm recovery phases. They suggested that the substorm-associated westward electrojet consists of two components, which have different characteristic times. One is mainly produced by Hall conductivity enhancements that dominate in the midnight sector, and the other by southward electric fields in the morning sector (Kamide, 1982). Clauer and Kamide (1985) expanded on the concept, showing that both DP1 and DP2 current patterns are enhanced over the course of the substorm. They showed that the DP2 pattern is elevated and dominant during the growth phase of the substorm, while DP1 is dominant during the expansion phase. Additionally, after the decay of the DP1 system, a strong DP2 system continues to exist during what they call “the enhanced convection phase of the substorm”.

Kamide et al. (1996) expanded on this further, proposing the “two-component auroral electrojet model”. With this model, they show that substorm time variations of current patterns in the polar region consist of two basic components, the signatures of which are shown in Figure 2.11. The two components result from the relative strength of electric fields and conductivities in the intensification of the auroral electrojet and are identified as the signatures for directly driven and

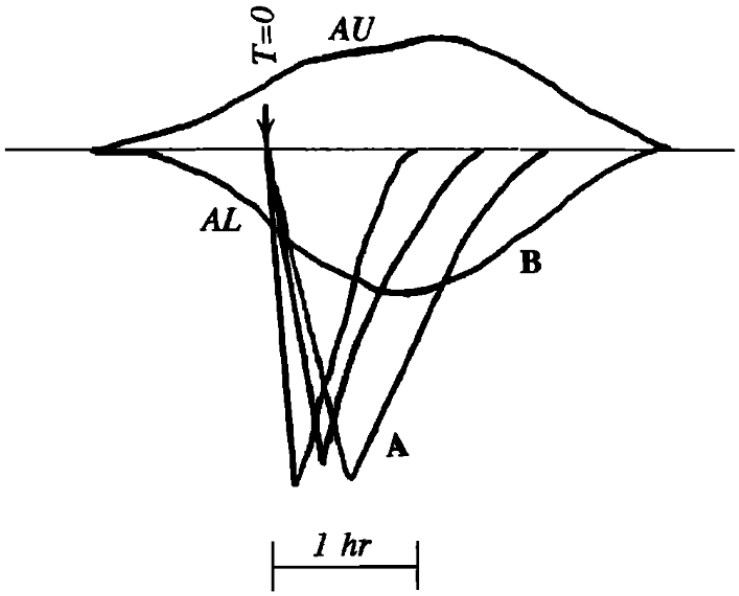

Figure 2.11: Sketch of the variations in the AU and AL indices due to the two components of the electrojet. (from Kamide and Kokubun, 1996).

the loading-unloading components in solar wind-magnetosphere interactions. They also discuss that not every geomagnetically disturbed interval indicates the presence of a substorm expansion phase (Kamide and Kokubun, 1996). In Figure 2.11, component A is the result of the rapid release of energy of the substorm expansion phase, which causes only deviations of AL and occurs at faster timescales compared to component B. Component B is related to the steadier increase in both the AU and AL indices when magnetospheric convection is increased. Kamide et al. (1996) highlight that the time series of these auroral indices is therefore a superposition of these components. It should be noted that Shore et al. (2017) found that their resolved DP2 and DP1 modes were both intensified at auroral substorm onset, showing that this two-component decomposition still does not provide a complete view of the polar ionospheric electrodynamics.

Beyond the DP1 and DP2 equivalent current systems that correspond to the magnetosphere's response to the substorm and convection, other equivalent current systems have been proposed in the literature. An example is the DPY pattern (Friis-Christensen and Wilhjelm, 1975) which is associated with the east-west component of the IMF (B_y). The DPY system consists of a single vortex, which is

approximately centred on the geomagnetic pole and whose polarity and strength are controlled by the IMF B_y. This vortex controls the relative strength of the two vortices of the DP2 pattern when added to its symmetric component (Friis-Christensen et al., 1985). It is strongest in the region of the ionospheric footprints of the dayside cusp, where ionospheric currents close the Region 0 (R0) FACs. Like the DPY current system, the polarity of the R0 currents depends on the IMF B_y (Svalgaard, 1973; Feldstein, 1976; Wilhjelm et al., 1978). There is also the NBZ pattern in the polar cap associated with periods of strong northward directed IMF B_z (Maezawa, 1976; Iijima et al., 1984). The NBZ pattern manifests as twin reversed lobe convection cells on the dayside polar cap, related to sunward convection that occurs in the middle of the polar cap during northward IMF Bz, as a result of high-latitude reconnection between the IMF and the lobe magnetic field (Maezawa, 1976). It can be envisioned as part of a four-cell pattern along with two conventional convection cells farther equatorward (Burch et al., 1985).

2.3 Summary of solar wind and ionospheric influences on substorms

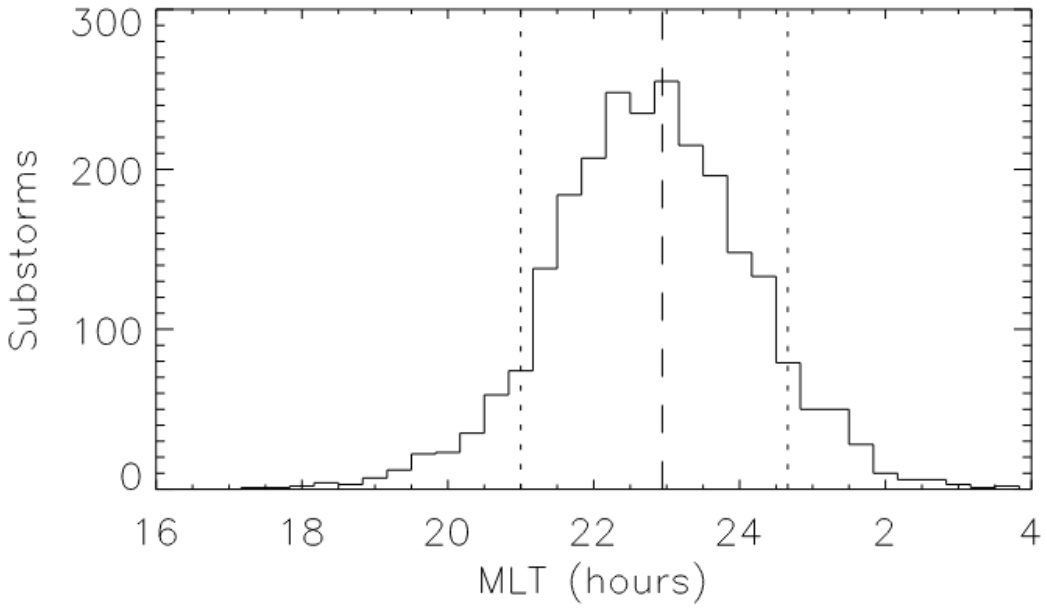

Figure 2.12: Histogram of onset location (MLT) of 2437 auroral substorms (from Frey et al., 2004).

Frey et al. (2004) observed that 80% (between the 10th and 90th percentiles) of auroral substorm onsets they identified using IMAGE observations between May 2000 and December 2002 occurred in a ≈ 3.2 hour MLT window centred on ≈ 23.00 MLT, shown in Figure 2.12. A similar result was found by Liou (2010) using Polar UVI, who showed that a Gaussian fit to the 2003 substorms they identified had a mean location of 22.60 MLT with a standard deviation of 1.10. The fact that substorm onset auroras predominantly take place at pre-midnight MLTs is somewhat expected, as the upward current at the duskward edge of the SCW is supported by downward-streaming electrons. However, beyond these statistical means, the location of substorm onset is largely unpredictable, particularly in the other signatures of substorms.

The distribution of Frey et al. (2004) and Liou (2010) differs from the findings of Yeoman et al. (1994). In their study using 10 days of data from LANL satellites and the UK Sub-Auroral Magnetometer Network (SAMNET) midlatitude magne-

tometer network, they found that substorm-related Pi2 pulsations occurred at a wide range of local times, from 15.00 MLT to 10.00 MLT, although this was still centred in the midnight sector. Furthermore, they found that substorm-related particle injections, although still centred at midnight, were observed at all local times. They also showed a systematic difference between proton and electron injections, where the proton distribution was shifted slightly before pre-midnight and, conversely, for the electrons, a slight shift towards post-midnight. They explained this difference as the effect of the gradient-curvature drifts of the different injected particle species.

The effect of the IMF on the location of substorm onset is a well-studied topic, especially by correlation studies, though some of the physical mechanisms behind these effects still remain ambiguous. In terms of the location of onset in magnetic latitude (MLat), Liou et al. (2001) showed using 648 "well-defined" auroral substorms from Polar UVI that the onset latitudes were correlated with IMF B_z, i.e. for more strongly southward IMF, the MLat of onset decreases, while being anticorrelated with IMF B_x, i.e. the onset MLat decreased for increasing B_x. The effect of IMF B_x is thought to be due to the anti-sunward shift of the auroral oval in the Northern Hemisphere for $B_x > 0$ and the sunward shift when $B_x < 0$, which has also been observed in convective flows over the polar cap (Cowley et al., 1991; Meng, 1980). This acts to decrease the MLat of onset, as the auroral oval near the midnight sector has shifted equatorward.

Liou et al. (2001) noted that the relationship between onset MLat and the IMF B_z, was stronger than that with the IMF B_x. Furthermore, Gérard et al. (2004) using 78 substorms in the 2000-2001 winter solstice showed that for larger IMF magnitudes, the MLat of onset decreased. They also showed that the latitudes of substorm onsets were located at a variable distance from the poleward auroral boundary but occur at a relatively constant displacement from the equatorward boundary, regardless of auroral excitation species. Moreover, an anti-correlation between the 1-hour averaged solar wind dynamic pressure and the onset MLat was observed. Both effects are likely the result of a more strongly driven magnetosphere, which contains more open flux, resulting in the auroral oval moving equatorward (Milan et al.,

2009).

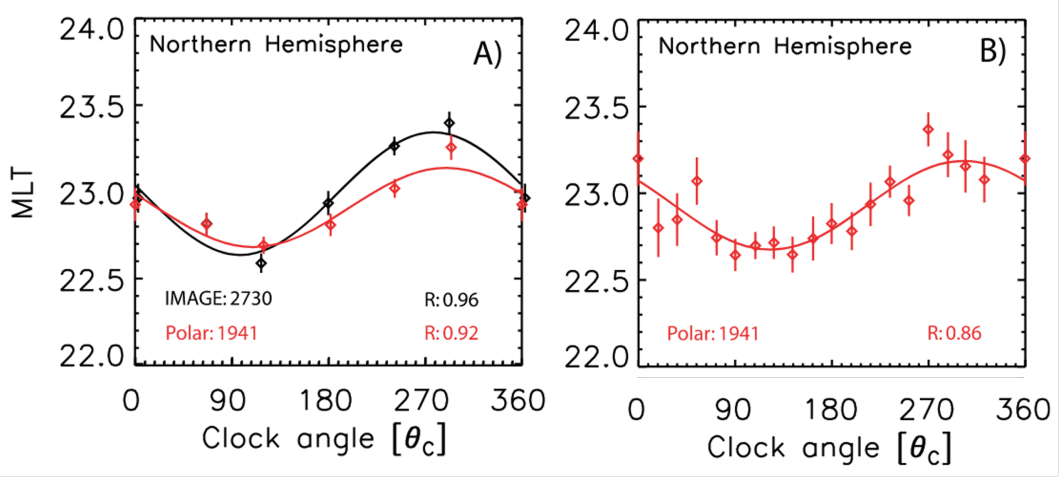

Figure 2.13: A) Substorm MLT locations for 60° bins of IMF clock angle in the Northern Hemisphere. Substorms identified from IMAGE (Polar) data are shown in black (red). B) Average substorm MLT locations for 18° bins of IMF clock angle for substorms identified from Polar data in the Northern Hemisphere. The number in the bottom left is the number of events and R the Spearman correlation coefficient between the data and a fitted sine function (from Østgaard et al., 2011).

Various studies have shown that the location of the onset of the substorm in MLT has a stronger relationship with the IMF B_y than with the other components of the IMF (Østgaard et al., 2004, 2005; Wang et al., 2007; Liou and Newell, 2010; Østgaard et al., 2011). In particular, Østgaard et al. (2011) used the substorm onset lists curated by Frey et al. (2004) and Liou (2010) to show that the substorm onset MLT and a sine function fit to the IMF clock angle are well correlated, as shown in Figure 2.13. They also showed that the average onset MLT showed a greater dependence on the clock angle than the value of B_y itself, with a saturation in the westward shift of onset MLT in the Northern Hemisphere for positive B_y values > 4 nT also observed. The effect of IMF B_y can be explained by considering how magnetic flux is added dawn-dusk asymmetrically to the magnetotail for negative and positive values and assuming that this non-uniform penetration of IMF B_y extends into the closed magnetosphere, which in turn can lead to changes in the observed projection of the substorm onset on the ionosphere (Tenfjord et al., 2015; Khurana et al., 1996). An asymmetry can also be observed between hemispheres under dif-

ferent clock angles, with the Northern Hemisphere onset westward of the Southern Hemisphere onset for clock angles $< 180^\circ$ and eastward for clock angles $> 180^\circ$ Østgaard et al. (2005); Liou and Newell (2010); Østgaard et al. (2011).

In addition to IMF B_y, the Earth's dipole tilt also displays an effect on the azimuthal location of substorm onset. A positive dipole tilt angle will lead to an added positive By component on closed field-lines in the magnetotail at dusk, and an added negative By component at dawn (as shown in Figure 3 of Liou and Newell (2010)), due to the warping of the tail associated with non-zero dipole tilt (Tsyganenko, 1998). This results in phenomena in the dusk magnetotail projecting to earlier MLTs in the ionosphere in the Northern Hemisphere. The results of Liou and Newell (2010) and Østgaard et al. (2011) are consistent with this hypothesis, under the assumption that the location of substorm onset in the magnetotail is predominantly shifted duskward. We see some evidence of this with the observed distribution of tail reconnection signatures showing a duskward shift (Angelopoulos et al., 1994; Walsh et al., 2014).

Recently, Elhawary et al. (2022) using substorm onsets by Frey et al. (2004) and Liou (2010) showed that there is also an ionospheric influence on the azimuthal location of substorm onset. In their study, they showed that the magnitude of ground magnetic perturbations is generally higher during the 20 minutes preceding duskward substorm onsets than during the 20 minutes preceding dawnward substorm onsets. They suggested that this effect on the substorm onset location is due to a higher ionospheric conductance related to the elevated levels of geomagnetic activity, leading to a duskward shift in magnetospheric substorm onset.

2.4 Summary

The magnetospheric substorm has been the subject of a significant amount of research for over 60 years since the first definition of its expansion and recovery phase (Akasofu, 1964). However, despite being a fundamental magnetospheric process, it is still not fully understood. In particular to this thesis, it remains unclear what the "true" signature (or signatures) of the substorm is (are), with many authors declar-

ing their own set of conditions on what constitutes a substorm without a community consensus. Moreover, the external (solar wind) and internal (magnetospheric and ionospheric) influences on its signatures are also ambiguous.

The primary aim of this thesis is to understand the various signatures of the substorm and their relationship to each other, as well as to detach the false identification of other phenomena capable of producing them. In order to do so, in Chapter 4 we evaluate the temporal relationship between different substorm lists that have been provided for community use. Following this, in Chapter 5, we attempt to understand and decompose the substorm contribution to high-latitude magnetic perturbations from another phenomena capable of doing so. Finally, in Chapter 6, we discuss a set of four events selected using the framework presented in Chapter 5.

Chapter 3

Instrumentation, Datasets and Methods

3.1 Ground-based Magnetometers and Geomagnetic Indices

Ground-based magnetometers have been one of the most widely used types of instrument for inferring the state of the magnetosphere by measuring geomagnetic disturbances. These instruments on the ground measure deflections in the magnetic field caused by currents flowing in the ionosphere and magnetosphere by Ampere's law, similar to the magnetic deviations created by a current flowing in a wire. Ground magnetometers have three major strengths that support their widespread usage in studying the Magnetosphere-Ionosphere system, as they provide (1) near global coverage, via the use of individual magnetometers within networks discussed further below, (2) near-continuous uninterrupted monitoring of the system, and (3) multiple decades of observations.

The measurements from individual magnetometers can be integrated into a wider network to evaluate large-scale phenomena ongoing in the Magnetosphere-Ionosphere system. To increase the practicality of these multiple measurements, various geomagnetic indices have been developed that combine these data sources into a single time series rather than interpreting a large number of magnetograms. In addition, the SuperMAG initiative (Gjerloev, 2012) integrates data from multiple

networks, acting as a super-network of sorts, applying their own data cleaning and preprocessing methods to single station data. In this thesis, we make use of the Auroral Upper (AU), Auroral Lower (AL), Midlatitude Positive Bay (MPB) and Polar Cap (PC) indices, which are discussed below and used in the following chapters, but other commonly used geomagnetic indices in the literature include the planetary K index (Kp) and ring-current indices (Dst and Sym-H).

3.1.1 Coordinate systems

Before outlining the geomagnetic indices used in this thesis, it is important to discuss the coordinate systems used in the recording of data and computation of the indices. Variations in the magnetic field are typically recorded in either a cartesian geographic coordinate system (X, Y, Z) a dipole coordinate system (H, D, Z) or a compass-type coordinate system (confusingly also H, D, Z). In the geographic and dipole coordinate systems, X and H are the surface horizontal component directed toward north, Y and D horizontal eastward and Z downward. Where they differ is that for the geographic system the X direction is aligned with a great circle that passes through the point of observation and the north geographic pole, whereas in the dipole system the H direction is aligned with a great circle that passes through the point of observation and the north geomagnetic pole. In the H, D, Z compass-type system, H is the horizontal field strength, D is the declination angle in degrees (angle with geographic north, positive eastward), and Z is the vertical component. It should be noted that the dipole coordinate system is time-varying in the reference frame of Earth, due to the position of the dipole pole changing slowly as the main magnetic field of Earth varies, while the other two systems are fixed. For SuperMAG, all data, which are collected in various coordinate systems by different organisations and agencies, are rotated onto a time-varying local magnetic coordinate system, before the calculation of any indices. Here, their self-labelled NEZ coordinate system is defined as N toward local magnetic north, Z directed vertically downward toward the centre of the Earth, and E directed in the Z$\times$N direction, toward local magnetic east. For each station, the local NEZ coordinates are evaluated using a 17-day running window on its magnetic measurements (Gjerloev, 2012)

3.1.2 The Auroral Indices AU and AL, SuperMAG and and SuperMAG derived substorm lists

The Auroral Electrojet (AE) indices Auroral Upper (AU) and Auroral Lower (AL) indices were proposed by Davis and Sugiura (1966) and endorsed by IAGA to provide a measure of the strength of the auroral electrojet currents, which is minimally contaminated by the strength of the ring current (Rostoker, 1972). The auroral electrojet currents flow in the ionosphere above the polar region, and variations in their strength are observed as deviations in the southward (westward electrojet) or northward (eastward electrojet) component of the Earth's magnetic field in the Northern Hemisphere. The original AU and AL indices are derived from approximately 12 magnetic observatories at high latitude, specifically between 60.44° magnetic latitude (MLat) and 71.21°, approximately equally spaced in magnetic local time (MLT). To evaluate the indices, the H component of the magnetic field at each station is produced, then the monthly mean from all stations is subtracted from the corresponding dataset such that they are placed onto a common baseline. The maximum and minimum envelopes of the combined dataset defined as the AU and AL indices, respectively. Therefore, the AU and AL indices measure the maximum and minimum magnetic deviation at aurora latitudes at any specific time. Note that another commonly used index in the study of space physics and also endorsed by IAGA, the AE index, is derived from AU and AL. It is simply the difference between the AU and AL indices, i.e. $\mathrm{AE} = \mathrm{AU} - \mathrm{AL}$. However, in this thesis the AE index is not used.

SuperMAG is the result of a worldwide collaboration of organisations that have operated and maintained nearly 600 magnetometers to date. In the time period analysed in this thesis (1997 - 2019), there are between ~ 80 and ~ 160 stations at auroral latitudes. The yearly variation in stations is shown in Figure 3.1, with snapshots of the network that data is taken from on 12th September 1997 and 12th September 2019 shown in Figure 3.2. It should be noted that although the general trend is a greater number of stations, during the interval certain stations may have been switched off. For example, the lowest latitude station on the east coast of

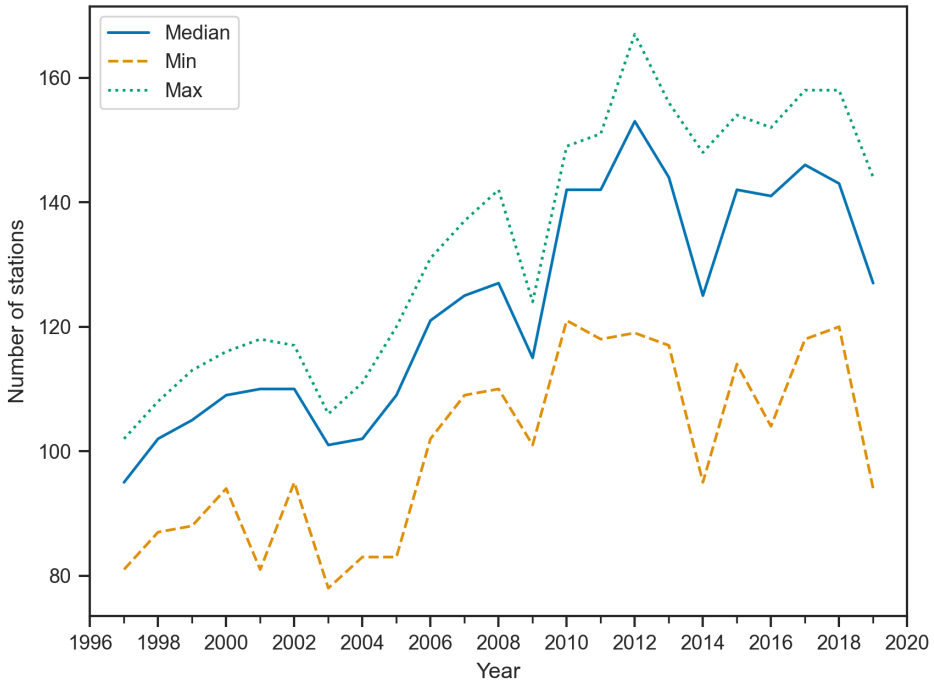

Figure 3.1: The number of stations contributing to SuperMAG's derivation of auroral indices. The yearly maximum, median and minimum number of stations are shown.

Greenland that is contributing data in September 1997 observed as a green dot on Figure 3.2a, does not contribute data in September 2019, as no green dot present in that location in Figure 3.2b.

In order to robustly integrate these multiple datasets, the measurements of individual stations are first re-sampled to a regular 1-minute temporal resolution before being transformed onto a common coordinate system (NEZ) as described above, then a common baseline is removed from each measurement, similar to the original AU and AL indices. However, a more complex routine is applied to determine this baseline than for the original AU/AL stations. '*Typical*' variations of the data at two selected timescales, the diurnal and yearly cycles, are removed as well as any remaining offset in the data. The '*typical*' values at these two timescales are evaluated as either the mode of the data or the centre of a Gaussian fitted to the probability distribution. These two values are normally similar, and the '*typical*' is defined as the mode unless it is affected by a single-point spike where instead the centre of the Gaussian is used (Gjerloev, 2012).

(a)

(b)

Figure 3.2: The contributing stations to the SuperMAG collaboration in the Northern Hemisphere in (a) 1997 (92 stations) and (b) 2019 (122 stations) in MLat vs MLT coordinates, here each concentric ring is 10° of MLat and each radial line indicates 6 hours of MLT. Note that while generally the number of stations increased, some stations were removed, for example, see the lowest latitude station on the east coast of Greenland present in (a) but not in (b).

The SuperMAG Auroral Upper (SMU) and Auroral Lower (SML) index values are evaluated in the exact same manner as the AU and AL and are their generalisation to many stations, leveraging the SuperMAG amalgamation of magnetometer arrays managed by different institutions. This allows for a much higher density of station coverage, especially in the latitudinal direction. SML and SMU are viewed as better substorm activity indicators than the original AU and AL, as the likelihood of the substorm onset location being overhead a ground magnetometer in the SuperMAG network is much higher. Furthermore, Bergin et al. (2020) showed that the magnitude of the SME index is systematically greater than the AE index, especially so for large disturbances, another indicator that the original AU and AL indices used an insufficient station density to fully resolve magnetosphere-ionosphere dynamics. However, there are still large geographic gaps in the derivation of SMU and SML, particularly over Siberia and the Atlantic.

There is no generally accepted method for identifying substorms from the auroral electrojet indices, and different sets of criteria are used in different studies. In the following sections, we briefly describe some selected algorithms available in the literature.

3.1.2.1 Forsyth et al. (2015) Substorm Onsets and PHases from Indices of the Electrojet

Substorm Onsets and PHases from Indices of the Electrojets (SOPHIE) is a non-parametric method applied to the auroral indices SML and SMU to identify phases of the substorm cycle at a temporal resolution of 1 minute (Forsyth et al., 2015). Precisely, SOPHIE identifies substorm expansion phase onsets using a threshold based on the yearly percentiles of rates of decrease of the SML index. For example, using the SOPHIE list with an Expansion Percentile Threshold of 90 or EPT 90 means that for an SML-bay to be considered a candidate substorm onset, the gradient of its decrease must surpass the 90th percentile of negative gradients observed in that calendar year. The substorm recovery phase is identified similarly for increases in SML, however the Recovery Percentile Threshold (RPT) is set automatically so that the difference in the number of expansion phases and recovery phases is min-

imised. Forsyth et al. (2015) then argue that any period that is not part of an ongoing expansion or recovery phase can be labelled as a potential growth phase, in which magnetic flux and energy is stored in the magnetotail.

In addition, Forsyth et al. (2015) considered that not all decreases and recoveries of SML are driven by substorms and that similar signatures may arise due to enhancements in magnetospheric convection. SOPHIE uses the SMU index for information to filter out events that are not due to substorm activity. The method accomplishes this by flagging expansion phases in the time series where the change in SMU is similar to what is observed in SML. Specifically, in previously published phase series identified by the SOPHIE method, expansion phases that have an absolute change of SML less than twice that of the absolute change of SMU, i.e. $\left|dSML_{expansion\ phase}\right| / \left|dSMU_{expansion\ phase}\right| < 2$, are flagged as potentially misidentified substorms due to enhancements in convection. The following recovery phase after the expansion is also flagged. However, in the process of completing this thesis, we found that the SOPHIE method mislabelled certain substorm cases as convection enhancement intervals. These cases were when a negative SML bay formed, and a decrease was also observed in SMU that met the criteria above. If we consider that SMU is generally reflective of the strength of convection, a plausible explanation that a decrease in SMU can be observed during an expansion phase is the scenario that the substorm occurs in the period following a northward turning in the IMF, such that the dayside reconnection rate and therefore the strength of the convection decreases. Recent studies (Dai et al., 2024) have shown variations in dayside convection and driving of the Dungey cycle from changes in the IMF. As we would normally expect SMU to increase, rather than decrease, during convection enhancements, we have revised the criteria for a Convection Enhancement to be as follows:

1. $\Delta SMU > 0$ over the expansion interval.

2. $\Delta SML < 0$ over the expansion interval.

3. $\frac{-\Delta SML}{\Delta SMU} < 2$ over the expansion interval.

If these three criteria are satisfied, then the expansion phase and the following recovery are flagged as a convection enhancement. The study completed in Chapter 4 was carried out using a SOPHIE version with the previous convection enhancement filtering logic, as this misidentification of convection enhancements from substorms was found during the analysis of Chapter 5. The rest of the analysis from Chapter 5 onwards was completed using SOPHIE with the new corrected logic of SOPHIE when filtering convection enhancements from substorms. In the period between 1997 and 2019, 32956 intervals met the criteria to be a candidate substorm event, with the updated logic of SOPHIE this was split into 30329 substorms and 2627 convection enhancements. With the original SOPHIE logic, approximately 4% of the 30329 substorms were misclassified as convection enhancements.

In the original SOPHIE paper (Forsyth et al., 2015), the factor of two used in the convection enhancement criterion 3 above was not fully explored but rather based on expert judgement, which is not uncommon in solar-terrestrial physics (e.g., the Newell and Gjerloev (2011) identification of substorm onset as being when dSML/dt is less than -15 nT/min or the identification of geomagnetic storms as when Dst drops below -50 nT). For symmetric DP2 electrojets, then the convection enhancement factor in criterion 3 would be unity, which might approximate a summertime case where the morning and afternoon MLT sectors are similarly illuminated by the Sun and have similar conductances. However, electron precipitation from substorm injections can sustain an enhanced morning MLT conductance (e.g., Wallis and Budzinski, 1981) and create a relatively stronger westward DP2 electrojet, as is statistically observed (Shore et al., 2018). Thus, a factor of two is again chosen in criterion 3 to take account of this, but we shall later explore the effect of varying this factor in Chapter 5.

3.1.2.2 The Newell and Gjerloev (2011) Substorm Onset List

Another algorithm utilising the SML index for the identification of substorm events was developed by Newell and Gjerloev (2011). Here, they considered the SML index using a 30-minute running window and defining a substorm onset that occurs at time t_0 when four conditions were satisfied:

1. $SML(t_0+1) - SML(t_0) < -15$ nT
2. $SML(t_0+2) - SML(t_0) < -30$ nT
3. $SML(t_0+3) - SML(t_0) < -45$ nT
4. $\sum_{i=4}^{i=30} SML(t_0+i)/26 - SML(t_0) < -100$ nT.

where $SML(t_0)$ was the value of SML at time t_0 measured in nanoteslas. These criteria were selected such that the negative bay created in SML had a sharp drop (15 nT per min for 3 consecutive minutes) and was sustained (the mean value of SML must be at least 100 nT below the initial value for the rest of the 30-minute running window). Furthermore, once an event is identified at time t_0, the method progresses in time 20 minutes, so the algorithm hard-codes the minimum waiting time between events. In their study, Newell and Gjerloev (2011) compares the algorithm's ability to find onsets using both the AL and SML indices and found that, using time delay analysis, the time difference between a POLAR UVI auroral onset and a geomagnetic index was minimized when using SML over AL and was, on average, 394 seconds after the UVI onset compared to 626 seconds. In the period between 1997 and 2019, the Newell and Gjerloev (2011) method identifies 39256 substorm onsets from the SML index.

3.1.2.3 The Borovsky and Yakymenko (2017) Substorm Onset List

Borovsky and Yakymenko (2017) developed another algorithm to identify substorm events from the SML index in their study of substorm occurrence rates, where they also compared with events identified from particle injections. The algorithm identifies a substorm event and onset in the following manner:

- Periods where there is at least a decrease of 150 nT in 15 minutes are identified as potential substorm events.
- Within these periods, potential onset times are identified as times when the decrease in SML from minute to minute is more negative than -10 nT.
- For each potential onset time in a period, the time integrals of the magnitude of the SML index for the 45 minutes before and after the potential onset are

evaluated. If the ratio of the "after" to "before" integral is less than 1.5 then that potential onset time is rejected.

- The earliest remaining potential onset time within each -150 nT in 15-minute period is accepted as the onset time of the substorm.
- The final criterion is that if a "150 nT-in-15 min" period occurs within 15 minutes of a prior "150 nT-in-15 min" period, the second interval is voided and the onset time in that second interval is not used. Therefore, the theoretical minimum waiting time is 16 minutes.

In their study Borovsky and Yakymenko (2017), the algorithm they developed identified 28,464 substorms between 1979 and 2015 using the SML index with a minimum waiting time of 27 minutes between substorm onsets.

3.1.2.4 The Ohtani and Gjerloev (2020) Substorm Onset List

The Ohtani and Gjerloev (2020) method for identification using the SML index was developed in their study of the substorm current wedge, particularly if it is composed of wedgelets. The method they developed "is not meant to identify every substorm onset, but rather to identify the onsets of isolated substorms" (Ohtani and Gjerloev, 2020). Similarly to the method by Forsyth et al. (2015), before any criterion was applied to the SML index, it was first smoothed using a 9-minute wide boxcar filter. Then a potential onset time, t_0, is identified using the following criteria:

1. That it is an isolated substorm, $(t_0 - 40\text{ min} < t < t_0 - 1\text{ min} : SML \geq -100\text{nT})$
2. That there is an observable gradual growth phase slope, $(t_0 - 40\text{ min} < t < t_0 - 1\text{ min} : |\Delta SML/\Delta t| \leq 1.5\text{nT})$
3. There is a clear break or "elbow" in SML to define the onset, $(t_0 - 10\text{ min} \leq t \leq t_0 + 10\text{ min} : \Delta SML^2/\Delta t^2 \leq -1.5\text{nT/min}^2)$
4. The sudden decrease in SML surpasses a given slope, $(t_0 + 1\text{ min} < t < t_0 + 10\text{ min} : \Delta SML/\Delta t \leq -3\text{nT/min}$

5. The substorm is sustained over a long duration, i.e. longer than 30 minutes, $(t_0 + 1 \text{ min} < t < t_0 + 30 \text{ min} : SML \leq 1.1 \times SML(t_0)$

6. The substorm is sufficiently intense, $min(SML) - SML(t_0) \leq -100\text{nT})$

To minimise the impact of single-point spikes in SML, a linear least squares fit is made to SML in the period $t_0 - 40$ min $< t < t_0 - 1$ min, with the first criterion that this period is greater than -100 nT, ensuring that the identified substorm is an isolated event. The threshold was selected to be consistent with previous studies of the substorm growth phase (Gjerloev et al., 2007). Criterion 3 and 4 also use linear fits for robustness, with two fits used in Criterion 3, before and after the onset break, to calculate $\Delta SML^2/\Delta t^2$ and a single fit for Criterion 4 to calculate $\Delta SML/\Delta t$. As there may be multiple candidate onset times per SML bay identified, the onset time, t_0, is selected to be the candidate that has the minimum value of its second derivative. Finally, this method requires that the onset is identified in the midnight MLT sector, 20 to 03 MLT. More specifically, they require that in the preceding 15 minutes after a candidate onset time, the contributing station to SML has to be within the 20 to 03 MLT region, otherwise the event is rejected. The method typically identifies 500 - 700 substorms per year.

3.1.2.5 The McPherron and Chu (2018) SML Substorm Onset List

McPherron and Chu (2018) developed another algorithm to identify substorm events using the SML index. This method, which standardises the index before applying any criterion, was first developed on the Midlatitude Positive Bay (MPB) index. The formal procedure on the SML index is not explicit in the literature, other than the MPB procedure, described in full in the next section, was reapplied to the SML index. In the period between January 1982 and December 2012, the McPherron and Chu (2018) method identified 94,396 substorm onsets from the SML index.

3.1.3 The Midlatitude Positive Bay index and derived substorm lists

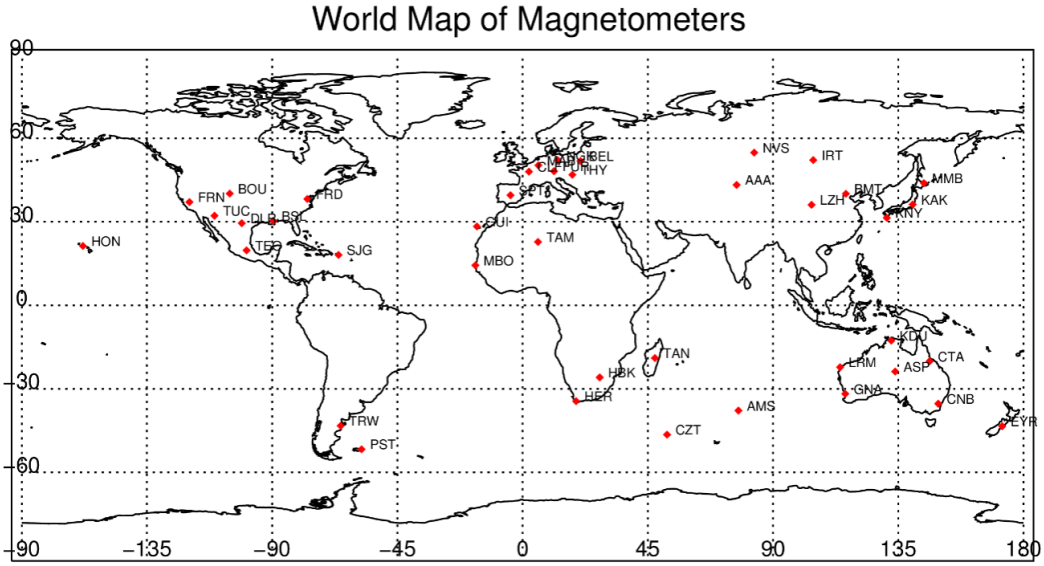

Figure 3.3: Map of magnetometer stations used to create the MPB index.

When the Substorm Current Wedge forms, its midlatitude signature is a positive perturbation in the northward H component of the ground magnetic field, symmetric about the central meridian (the perturbation is maximal at this central meridian) of the wedge and a weak negative perturbation outside of the structure. The perturbation to the eastward component of the magnetic field D is antisymmetric about the central meridian of the wedge, with a positive perturbation west to the centre of the wedge and a negative perturbation to the east. The midlatitude ground magnetic signature of the substorm has also been used extensively for the identification of events and various studies of the properties of the substorm (Clauer and McPherron, 1974b,a; Caan et al., 1975, 1978). In their study of the statistical lobe signature of substorms, Caan et al. (1978), developed a formal quantitative method to identify the onsets of the substorms. This method, named the “bay finder” was included in the appendix of Caan et al. (1978). The MPB index studied in this thesis was developed by Chu et al. (2015) as an extension to the “bay finder” concept and using stations from the INTERMAGNET network of observatories, particularly the

stations that are positioned between 20° and 52° latitude in both the Northern and Southern Hemispheres. Figure 3.3 shows a map of the stations used for the calculation of the MPB index, and Table 3.1 lists the 41 stations used and their locations. These stations are positioned farther away from the auroral oval at midlatitudes to detect disturbances caused by large-scale field-aligned currents of the substorm current wedge (McPherron et al., 1973; Caan et al., 1978).

There exist two distinct methods to derive the modern MPB index from magnetometer data from stations at midlatitudes. In the method of Chu et al. (2015), the data from each station that contributes to the index, seen in Table 3.1 was first transformed to geomagnetic HDZ coordinates. The secular trend, defined as the running monthly average, and solar quiet variations were removed from the raw data. This was further de-trended using a 12-hour low-pass filter to remove any effect of long-duration geomagnetic activity. The MPB index was calculated as the average moving variance of the changes in the H and D components, $\Delta H^2 + \Delta D^2$ from stations within 5 hours of 23.5 MLT. The MPB index is a measure of the magnetic field differential from background at midlatitudes. Its unit, nT^2, is proportional to the power of the magnetic perturbations rather than the amplitude of them. An alternate method has been set out by McPherron and Chu (2017) which used a smaller set of magnetometer stations, a wider MLT acceptance and different methodologies to remove the background signal.

3.1.3.1 The Chu et al. (2015) Substorm Onset List

In addition to the MPB index, Chu et al. (2015) additionally developed a substorm identification algorithm for their study of the substorm waiting time dependence on the solar cycle. Substorm events and onsets at t_0 were identified using the following criteria:

1. For a substorm to be identified, the MPB index must cross a threshold of 25 nT^2.

2. The time at which the MPB index reaches its maximum for a substorm, t_{max}, is also defined as the end of the expansion phase and the beginning of the

Table 3.1: Magnetometer stations used to provide magnetic field data to create the MPB index (Chu et al., 2015).

IAGA ID	NAME	Geographic Longitude	Geographic Latitude	Magnetic Longitude	Magnetic Latitude
AAA	Alma-Ata	76.92	43.25	152.7	34.3
AMS	Martin de Vivies	77.57	-37.8	144.3	-46.4
ASP	Alice Spring	133.88	-23.76	208.2	-32.9
BEL	Belsk	20.79	51.84	105.2	50.2
BMT	Beijing Ming Tombs	116.18	40.06	187	30.1
BOU	Boulder	-105.24	40.14	320.6	48.4
BSL	Bay St. Louis	-89.64	30.35	339.8	40.1
CLF	Chambon la Forêt	2.27	48.02	85.7	49.8
CNB	Canberra	149.36	-35.32	226.9	-42.7
CTA	Charters Towers	146.25	-20.08	221	-28
CZT	Port Alfred	51.9	-46.44	113.3	-51.4
DLR	Del Rio	-100.92	29.5	327.3	38.3
EYR	Eyrewell	172.35	-43.42	253.8	-47.1
FRD	Fredericksburg	-77.37	38.2	353.4	48.4
FRN	Fresno	-119.72	37.09	305.3	43.5
FUR	Furstenfeldbruck	11.28	48.17	94.6	48.4
GNA	Gnangara	115.95	-31.78	188.9	-41.9
GUI	Guimar-Tenerife	-16.43	28.32	60.6	33.8
HBK	Hartebeesthoek	27.71	-25.88	94.4	-27.1
HER	Hermanus	19.23	-34.43	84	-34
HON	Honolulu	-158	21.32	269.7	21.6
IRT	Irkutsk	104.45	52.17	176.9	41.9
KAK	Kakioka	140.18	36.23	208.8	27.4
KDU	KAKADU	132.47	-12.69	205.6	-22
KNY	Kanoya	130.88	31.42	200.8	21.9
LRM	Learmonth	114.1	-22.22	186.5	-32.4
LZH	Lanzhou	103.84	36.1	176.1	25.9
MAB	Manhay	5.68	50.3	90.1	51.4
MBO	Mbour	-16.97	14.38	57.5	20.1
MMB	Memembetsu	144.2	43.9	211.3	35.4
NGK	Niemegk	12.68	52.07	97.6	51.9
NVS	Novosibirsk	83.23	54.85	159.5	45.6
PST	Port Stanley	302.11	-51.7	11.5	-41.7
SJG	San Juan	-66.15	18.11	6.1	28.6
SPT	San Pablo-Toledo	-4.35	39.55	76	42.8
TAM	Tamanrasset	5.52	22.79	81.8	24.7
TAN	Antananarivo	47.55	-18.92	115.8	-23.7
TEO	Teoloyucan	260.81	19.75	330.4	28.8
THY	Tihany	17.89	46.9	100.5	46
TRW	Trelew	-65.38	-43.26	5.6	-33.1
TUC	Tucson	-110.73	32.18	316	39.9

recovery phase.

3. A minimum waiting time is enforced so that there must be at least 30 minutes between successive MPB maxima. If there were two peaks identified within 30 minutes, the largest peak was selected to be the substorm.

4. The preliminary onset time, t_0, is defined as the maxima of the second derivative of the MPB index prior to the peak.

5. The onset time, t_0, is refined using the original magnetic field data, specifically the point of the elbow of the slope of a combination of stations

within 5 hours of 23.5 MLT that showed large magnetic perturbations ($>$ Δ10 nT in 20 min).

6. The end of an MPB event, t_{end}, is defined as the minima of the second derivative of the MPB index after the peak.

In the period 1982 to 2012, the Chu et al. (2015) algorithm identified 40,562 substorm events or approximately 1300 onsets per year. In their time delay analysis comparison with Frey et al. (2004) auroral substorm onsets, Chu et al. (2015) found that the MPB substorm onsets were near simultaneous to their counterparts in the aurora.

3.1.3.2 The McPherron and Chu (2018) MPB Substorm Onset List

Another method was developed in McPherron and Chu (2017) to identify substorms using the MPB index. Before any criterion is applied, they first standardise the index by subtracting the 4-hour running mean of MPB, followed by dividing the difference by the 4-hour running standard deviation. This acts to shrink large peaks and enhance small peaks in the original index timeseries. After the MPB index is transformed, a substorm event and onset time, t_0, is identified from the standardised index when the following criteria are met:

1. A substorm event is defined as periods during which the standardised index exceeds a threshold of 1.0.

2. A smooth spline fit is then applied to the raw MPB index. To determine the onset time, t_0, the analytic derivative of this smooth spline fit is evaluated.

3. Zero crossings of this analytic derivative that correspond to minima of the standardised index are considered as possible onset times for the substorm event. The difference from each minimum or candidate onset time, to the peak value of the standardised index is then calculated; earlier minima are accepted as the onset time only if their difference to the peak is 1.25$\times$ greater than the later minima. Otherwise, successful later minima are compared until an onset time is accepted.

4. To evaluate the end of the substorm event, a similar zero crossing logic is used in reverse, accepting the later end times only if their difference to the peak is $1.25\times$ than earlier candidate end times.

This was applied to the Chu et al. (2015) derivation of the MPB index, which identified 100,687 substorms between January 1982 and December 2012. In the processing of the algorithm, other properties of identified events were also evaluated, including event duration, standardised peak value, original peak value, the change in MPB from onset to peak, and area under the original peak from onset to end. In a follow up study, McPherron and Chu (2018) compared the waiting time distributions of various onset lists, showing that their method of identifying substorms (both in MPB and SML) found events that displayed a double-peaked distribution in contrast to the other onset lists from magnetic indices studied in this thesis.

3.1.4 PC Index

Table 3.2: Magnetometer stations used to derive the PC index.

IAGA ID	Station Name	Geographic Longitude	Geographic Latitude
THL	Qaanaaq	290.77	77.47
VOS	Vostok	106.87	-78.46

The Polar Cap (PC) index is a historically 15-minute (now 1-minute) index designed to be a measure of the strength of the cross-polar-cap ionospheric current. It is related to the anti-sunward ionospheric plasma convection in the polar cap driven by the dawn-dusk electric field generated by the solar wind. It has units of mV/m. The idea for the measure originates from Troshichev and Andrezen (1985). The concept was further developed by Troshichev et al. (1988) and Vennerstrøm et al. (1991). Two indices are derived: a PC North (PCN) index calculated using data from the Qaanaaq station, formerly Thule station, and a PC South (PCS) index calculated from the Vostok magnetic data. The method for the derivation of these indices is detailed in Troshichev et al. (2006, 2009). Geographic coordinates for the two magnetic observatories are shown in Table 3.2. The PC indices have been used widely in geomagnetic studies in the literature, particularly when exploring the coupling between the solar wind and the Earth's magnetosphere (McCreadie and Menvielle, 2010). In this thesis, only the PCN index is used and is referred to as the PC index.

3.2 IMAGE FUV

Imager for Magnetopause-to-Aurora Global Exploration (IMAGE) was a NASA medium-class explorer (MIDEX) mission developed to study the global response of the Earth's magnetosphere to changes in the Solar Wind as part of NASA's Sun-Earth Connections Program. It carried a suite of instruments focused on the imaging of the different coupled plasma regions of the Earth's magnetosphere, including the magnetopause, the auroral zone, the plasmasphere, as well as the inner plasma sheet and the ring current (Gibson et al., 2000; Burch, 2000). In order to study the aurora, IMAGE carried a far-ultraviolet (FUV) imager suite (Mende et al., 2000b) capable of imaging the aurora at 120 - 190 nm.

The IMAGE satellite was launched on 25 March 2000, and was operational between May 2000 and December 2005, when communication with the satellite was lost[1]. During its operational period, IMAGE was placed into a precessing polar orbit with a perigee of 1,000 km and an apogee of 45,600 km ($\sim 7\ R_E$) with an orbital period of 14.14 hours (Burch, 2000). For its first two-year prime mission operations, IMAGE's orbital apogee was placed over the Northern Hemisphere, with its inclination precessing from 40° to 90° and back to 40°, completing two sweeps in local time around the Earth (Fuselier et al., 2000). The satellite was spin-stabilised, with a nominal rotation period of ≈ 2 minutes, with the spin axis aligned perpendicular to the orbital plane such that each instrument pointed towards Earth once per spin. Following its 2-year nominal mission lifetime, the mission duration was extended with the orbit precessing so that apogee was instead over the Southern Hemisphere. In this thesis, only data and a derived product, the Frey et al. (2004) substorm onset list, taken from the prime science mission (2000 - 2002) of the FUV instrument suite are used.

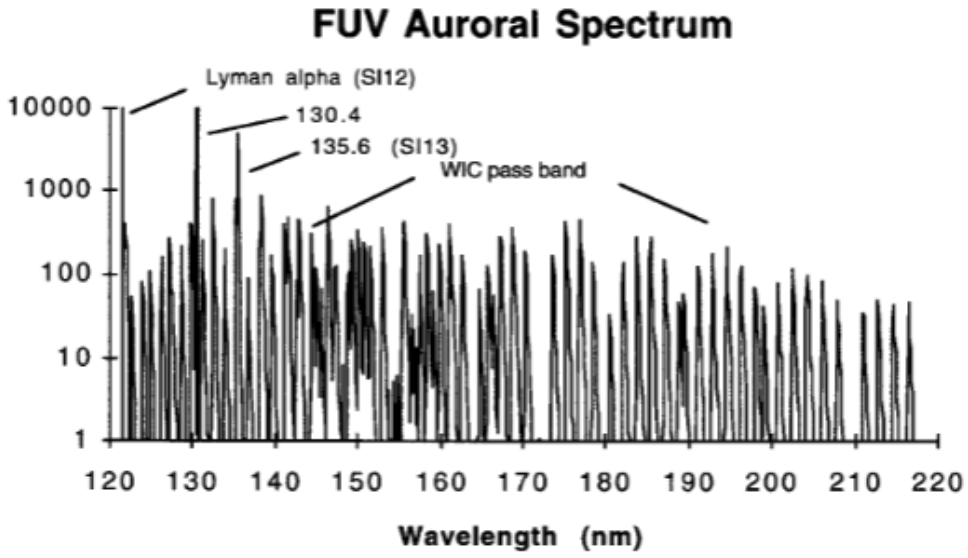

Figure 3.4: FUV Auroral Spectrum with the band passes of instruments onboard IMAGE indicated (from Mende et al., 2000b).

3.2.1 The Wideband Imaging Camera and Spectrographic Imagers

The FUV instrument consisted of three cameras: the Wideband Imaging Camera (WIC) Mende et al. (2000a) and two spectral imagers (SI-12 and SI-13) Mende et al. (2000b). The Wideband Imaging Camera (WIC, Mende et al. (2000a)) was designed to observe broad band ultraviolet emissions (140 - 190nm). To provide global imagery of the auroral oval, WIC had a $17^\circ \times 17^\circ$ field-of-view (FOV), with a dectector resolution of 256×256, corresponding to a 52km $\times$ 52km nominal pixel projection at apogee and 1.2km $\times$ 1.2km at perigee, thus able to distinguish the desirable auroral features of the order of 100 km in size.

The Spectrographic Imager (SI, Mende et al. (2000c)) was designed to observe specific proton and electron excited aurora: 121.8 nm Lyman-α proton emission and 135.6 nm atomic Oxygen (OI) emission from electron precipitation. SI had a $15^\circ \times 15^\circ$ FOV with a 128×128 pixel density, resulting in a 92km $\times$ 92km nominal pixel projection at apogee and 2km $\times$ 2km at perigee.

[1] In 2018, IMAGE was rediscovered by an amateur astronomer; however, communications with the satellite were unable to be re-established.

3.2.2 The Frey et al. (2004) Auroral Onset List

During the nominal mission phase of IMAGE, Frey et al. (2004) searched through the data collected by the FUV suite to determine substorm onsets. They used WIC as their primary data source, due to its higher spatial resolution, and using SI-13 when images from WIC were not of high enough quality to determine an onset. In this method of identifying from images of the aurora they defined a substorm onset if the following criteria were met:

1. There was a clear local brightening of the aurora,
2. The brightening of the aurora had to expand to the poleward boundary of the auroral oval and spread azimuthally for at least 20 minutes,
3. A substorm onset was only accepted as a separate event if at least 30 minutes had passed after the previously identified onset.

This leveraged the original definition of the auroral substorm by Akasofu (1964). The third criteria imposed a minimum waiting time of 30 minutes between substorm events, while 2 eliminated possible false identifications which were like pseudobreakups rather than true substorm events. In addition to the onset time of the substorm, Frey et al. (2004) also evaluated the location of the auroral onset using a brightest pixel search algorithm on the onset image of the event. Frey et al. (2004) also state in their study that extremely active auroral intervals were ignored as during these intervals it is ambiguous to locate a clear local brightening of the aurora. The Frey et al. (2004) list used in this thesis was accessed from the SuperMAG website rather than from the auxiliary material of the original study, with the only difference being that the SuperMAG version dropped some information, such as the spacecraft geocentric distance, the brightness of the brightest pixel, etc..

3.3 LANL geosynchronous spacecraft

The Los Alamos National Laboratory (LANL) spacecraft are a set of satellites located at geosynchronous orbit ($6.6R_E$), that are approximately evenly spaced in longitude around the Earth. In the period May 2000 to December 2002, there were between 2 and 6 spacecraft operating at any one time. Onboard they have the Magnetospheric Plasma Analyzer (MPA) (Bame et al., 1993), which measures the low-energy plasma $1eV - 40keV$, the Synchronous Orbit Particle Analyzer (SOPA) (Belian et al., 1992) that measures the energy range between $50keV - < 2MeV$ for electrons and ions between $50eV - 50MeV$, and the Energy Spectrometer for Particles (ESP) (Meier et al., 1996) that measures from $1MeV$ to several MeV particles. The SOPA instrument consists of three, nearly identical, silicon solid-state detector telescopes that accept particles from three different angles relative to the spacecraft spin axis (30°, 90°, and 120°), each with a field of view of 11°. For SOPA, electron fluxes are measured in 10 energy channels from 50 keV to above 1.6 MeV, and proton fluxes are measured in 12 channels measuring particles of 50 keV to 50 MeV. In this thesis, only data products derived from the SOPA instrument are used, and in particular only the electron measurements.

3.3.1 The Borovsky and Yakymenko (2017) Particle Injection List

Recently, Borovsky and Yakymenko (2017) developed an automated method to identify substorm-related energetic electron injections where they used the SOPA instrument onboard the LANL satellites to determine the specific entropy of the electron population at geosynchronous orbit. This was achieved by evaluating a density-temperature description of the plasma from spin-averaged electron energy spectra measured by the SOPA instruments (Cayton et al., 1989; Denton et al., 2010). These were calculated for each spacecraft at a 10-second cadence before calculating median values for the density and temperature every 30 minutes. These density and temperature values are used to calculate the specific entropy given by $S = T/n^{2/3}$ for each LANL spacecraft operating. To identify a substorm event

window from the occurrence of an electron injection in geosynchronous orbit, the minimum value of the quantity $log(S)$ is calculated every 30 minutes for all spacecraft operating at that time. When this multispacecraft minimum value of $log(S)$ decreases by 1.0 or more in a subsequent window, an injection is declared at the beginning of that 30-minute window. If two subsequent half-hour windows meet the criteria for a substorm identification, only the first onset time is accepted. Therefore, the minimum waiting time between substorm injections is 60 minutes.

The reasoning for using an entropy measure to identify substorm injections is that during a substorm injection, one would expect a simultaneous increase of the hot-electron number density and a decrease of the hot-electron temperature (hardness of the energy spectrum) at geosynchronous orbit. However, when there are no new substorm injections, the population of substorm-injected electrons at geosynchronous orbit ages and the specific entropy of the population steadily increases with time. During this ageing, the number density of the electrons is expected to decrease with time, while the mean energy of the electrons increases with time.

It should be noted that the time at which a substorm is detected in situ (such as these particle injections) depends on the positions of the geosynchronous spacecraft at the time of the actual substorm onset. If no satellite is present in the vicinity of the injection region, then the freshly injected electrons must drift toward dawn and then into the dayside until a satellite is encountered. Hence, the onset times identified from the substorm electron injections may be systematically delayed from the onset times identified by other measures.

3.4 Solar Wind Data

In addition to the substorm onset lists and ground magnetometer data, observations of the solar wind and interplanetary magnetic field (IMF) are also used in this thesis. In particular, the OMNI High Resolution OMNI (OMNI HRO) 1-minute dataset from 1 January 1997 to 31st December 2019 is used. The dataset is a combination of observations taken by the Wind and ACE (Advanced Composition Explorer) spacecraft which orbit around the first Lagrange Point (L1). The dataset is preprocessed for ease of use in the studies of solar wind-magnetospheric coupling (King and Papitashvili, 2005). This preprocessing includes an aberration correction of the solar wind velocity values to account for Earth's rotation around the sun, before all the parameters are time shifted to the approximate location of the Bow Shock nose location approximated by empirical techniques (Farris and Russell, 1994; Shue et al., 1997). The data is then averaged from the various data cadences of the instruments onboard either Wind or ACE to provide a 1-minute dataset. In addition to solar wind and IMF parameters, various geomagnetic indices are also included in the OMNI HRO dataset including the AL, AU and the PC index. The dataset is provided by NASA Goddard Space Flight Centre, Space Physics Data Facility is publicly available from Coordinated Data Analysis Web or OMNIWeb.

3.5 The 2 x 2 contingency table and derived metrics

In order to evaluate the association between the different substorm onset lists in this thesis, we use methods which have predominantly been used in the verification of dichotomous meteorological forecasts. In recent years, these techniques have been used more regularly in the field of space physics, particularly in the forecasting of space weather events and the evaluation of space weather models (Forsyth et al., 2020b; Haiducek et al., 2020; Mooney et al., 2021; Smith et al., 2021). This method of analysis is conducted with the use of a two-by-two contingency table, an example of which is shown in Table 3.3, from which various metrics can be derived from combinations of its elements A, B, C and D.

It is common to see contingency tables with the labels Forecast and Ground Truth in the literature. This is because it is usually used in the case of binary forecast verification, where a forecast that returns a positive or negative prediction of a feature (an event, or crossing of a threshold value or not) is compared to the ground truth or observation of that feature. However, in the study of substorms, there is currently no ground truth or observation of true occurrence of substorms, only proxies for occurrence from the various resulting effects of the phenomenon. As such, we use the terms Reference and Comparison lists to compare between different substorm identification methods. There are 4 possible outcomes to fill in the 2×2 contingency table:

- **True Positive (A)**: a substorm is observed in the Reference list and a substorm is observed to occur in the Comparison list
- **False Positive (B)**: a substorm is not observed in the Reference list and a substorm is observed to occur in the Comparison list
- **False Negative (C)**: a substorm is observed in the Reference list and a substorm is not observed to occur in the Comparison list
- **True Negative (A)**: a substorm is not observed in the Reference list and a substorm is not observed to occur in the Comparison list

Table 3.3: 2x2 contingency table for binary forecasts (Hogan and Mason, 2011).

		Reference	
		Yes	No
Comparison	Yes	*A* (True Positive)	*B* (False Positive)
	No	*C* (False Negative)	*D* (True Negative)

although we use the terms Reference and Comparison list or method in this thesis, we retain the common convention of the terms for the elements of the truth table.

From the elements of the contingency table, it is possible to construct several metrics that summarise the level of association between the two lists that are compared. This includes the Heidke Skill Score (HSS) (Equation 3.5), also known as Cohen's Kappa outside the meteorology literature (Cohen, 1960), to quantify the association between the onset lists analysed. This metric is derived from the Proportion Correct (PC), a measure of the correct predictions compared to the total number of predictions, given by

$$\begin{aligned} PC &= \frac{A+D}{A+B+C+D} \text{ or} \\ PC &= \frac{A}{A+B+C+D} + \frac{D}{A+B+C+D}. \end{aligned} \tag{3.1}$$

A proportion correct of 1 indicates a perfect association between two onset lists. The HSS is derived from PC by comparing PC to a reference value, PC_{ref}, such that PC_{ref} is the Proportion Correct that would be obtained by random coincidence of the events populating each list if they were statistically independent of each other, and is given by:

$$\begin{aligned} PC_{ref} &= p(\text{True Positive}) + p(\text{True Negative}) \\ PC_{ref} &= p(\text{Yes}_{\text{Reference}}) \cdot p(\text{Yes}_{\text{Comparison}}) + p(\text{No}_{\text{Reference}}) \cdot p(\text{No}_{\text{Comparison}}). \end{aligned} \tag{3.2}$$

The maximum likelihood estimate of Proportion Correct from the elements of the contingency table is:

$$PC_{ref} = \left(\frac{A+B}{n}\right)\left(\frac{A+C}{n}\right) + \left(\frac{B+D}{n}\right)\left(\frac{C+D}{n}\right), \tag{3.3}$$

where $n = A+B+C+D$, is the sum of the elements of a given contingency table.

The Heidke Skill Score is then formulated as:

$$\text{HSS} = \frac{PC - PC_{ref}}{PC_{perfect} - PC_{ref}} = \frac{PC - PC_{ref}}{1 - PC_{ref}}, \tag{3.4}$$

which after inputting our expressions for PC and PC_{ref} gives:

$$\text{HSS} = \frac{2(A \times D - B \times C)}{(A+B)(B+D) + (A+C)(C+D)}. \tag{3.5}$$

The Heidke Skill Score has a range of -1 to 1, with 1 indicating a perfect association, 0 equivalent to random or no association, and -1 anti-association between two onset lists (where the Comparison list is populated singularly with events when the Reference list does not observe events). Note that the Heidke Skill Score is the same no matter which of the two lists is the reference or comparison, i.e. the score is the same when B and C are swapped in Equation 3.5.

It is possible to construct other skill scores from elements of the contingency table, however in this thesis the Heidke Skill Score is used as it has many desirable features (Hogan and Mason, 2011). First, it makes use of all elements of the contingency table such that it considers the correct co-identification of events and co-identification of non-events equally. It is truly equitable, meaning that a substorm list full of random events and constant identification (either always identifying or never identifying) will have a score of zero. It is bounded, described earlier as a perfect event association of two event lists achieves a score of 1. It is linear such that the same change in score is observed when adding 1 to the True Positives or True Negatives as when 1 is subtracted from the False Positives or False Negatives. Another desirable feature is that it is transpose symmetric such that the same score

is achieved when alternating which list is used as the Reference onset list and the Comparison onset list. Finally, it is defined as such that onset lists with different numbers of events identified are unable to achieve a perfect score.

In addition to the Heidke Skill Score, we also make use of the True Positive Rate (TPR), also called Sensitivity in other contexts. The TPR is the probability that the Comparison list also observes an Reference list event when an event is observed in the Comparison list. In terms of the elements of the contingency table, it is given by:

$$\mathrm{TPR} = \frac{A}{A+C}. \tag{3.6}$$

The True Positive Rate is used in addition to the Heidke Skill Score in this thesis, as it is a more interpretable metric, indicating the ratio of observed events in one substorm identification method that were also observed in another. Additionally, Liemohn et al. (2021) highlight that due to metrics prioritising different features of data-model comparison (or in the case of this thesis data-data), it is best practice to conduct analyses using more than a single metric.

Chapter 4

Evaluating the association between Substorm onset signatures and the techniques applied to them

This work has been published in C. J. Lao, C. Forsyth, M. P. Freeman, A. W. Smith, and M. K. Mooney. On the Association of Substorm Identification Methods. Journal of Geophysical Research: Space Physics*, 129(9):e2024JA032762, 2024. ISSN 2169-9402. doi: 10.1029/2024JA032762*

4.1 Introduction

As with any natural phenomenon, the success of a substorm theory or model lies in its ability to describe not only its characteristic features but also its variability. Although considerable progress has been made in identifying and understanding the characteristic features of a substorm (see section 2.1), the quantitative explanation or prediction of substorm variability, such as size or timing, is more limited (see e.g., Freeman and Morley, 2004; Morley et al., 2007; Maimaiti et al., 2019).

One necessary requirement in developing a model to explain or predict substorm variability is a sufficiently extensive catalogue of substorms to validate the model over the widest possible range of circumstances. The first substantial catalogue of 1373 substorm onset times was produced by Borovsky et al. (1993) based on visual inspection of energetic particle data at geostationary orbit and was used

to examine the variability of waiting times between substorm onsets. Subsequently, another major catalogue of 2437 substorm onsets was produced by Frey et al. (2004) based on visual inspection of auroral imaging data and used to analyse the variability in substorm onset location in the ionosphere. The data for the two catalogues were not contemporaneous and therefore could not be directly compared; however, they both identified substorms at a rate of ~ 1500 onsets per year. In the last decade many more catalogues of substorm onset times have been produced based on a variety of data sources and using both visual inspection and automated detection methods. Notably, however, they differ significantly with the number of substorms differing by a factor of five over a common 2.5-year time interval (see Table 4.1) and with very different distributions of waiting times between onsets (Forsyth et al., 2015; McPherron and Chu, 2018).

Consequently, those seeking to validate their models and theories of substorms using such catalogues are left with the open question of whether any validation is quantifying the model's ability to replicate the substorm phenomenon or its ability to replicate a property of a catalogue of events that may or may not all be substorms (Haiducek et al., 2020). Any conclusions could turn out to be specific to the catalogue being analysed. As an example, Forsyth et al. (2015) showed distinct differences both in the average evolution of an auroral magnetic index using different onset lists as the reference and in the distribution of waiting times between onsets, which might support or contradict corresponding models such as Weimer (1994), Doxas et al. (2004) and Freeman and Morley (2004), respectively.

Although the signature used for each substorm catalogue may be considered to be a plausible identifier of substorm onset, and the substorm concept suggests that the various signatures should all occur close to onset, there are various practical and physical reasons why the catalogues may nevertheless differ. Firstly, instruments may not be available or in the right place to observe a substorm signature, which itself may be relatively localised. For example, spacecraft are continually moving, the spatial distribution of ground magnetometers is not uniform (Shore et al., 2018), an auroral brightening might not be visible in the sunlit summer hemisphere, or a par-

ticle injection might not reach geostationary orbit (Boakes et al., 2011). Secondly, signatures may not be sufficiently similar from substorm to substorm to be uniquely defined. For example, substorm identification based on an amplitude and/or rate of change threshold of some measure will generally be affected by the variability of substorm energy loss (Tanskanen et al., 2002), and ground magnetic perturbations will be affected by variable ionospheric conductance from seasonally dependent solar illumination (Forsyth et al., 2018). Third, some substorm identification methods focus solely on the onset of the substorm (Newell and Gjerloev, 2011; Chu et al., 2015; Borovsky and Yakymenko, 2017; Ohtani and Gjerloev, 2020) rather than the whole substorm cycle (Forsyth et al., 2015). Fourthly, the observational features that are leveraged for substorm identification may also be attributed to other magnetospheric phenomena. For example, sudden changes in the ground magnetic field may be caused by enhanced magnetospheric convection (Sergeev et al., 1996a; Kissinger et al., 2011; Walach and Milan, 2015), pseudobreakups (Pulkkinen et al., 1998; Kullen and Karlsson, 2004), and global sawtooth oscillations (Belian et al., 1995; Lee et al., 2004; Cai et al., 2006; Henderson et al., 2006a).

In summary, the absence of an onset in one signature may not indicate the absence of a substorm, and conversely, a singular occurrence may not truly indicate a substorm. However, the validity of any study of the physics of substorms or the effect of substorms on the magnetosphere-ionosphere-thermosphere system requires consensus on what constitutes a substorm event and a consistent catalogue of events. To make progress towards this, in this study, we examine the extent to which various substorm onset lists identify events at similar times by quantifying the level of temporal association between pairs of onset lists. Binary forecast verification methods are used, as described in Section 3.5, applying pairwise comparisons to onset lists based on a wide variety of instrumentation, including ground-based magnetometers (Newell and Gjerloev, 2011; Chu et al., 2015; Forsyth et al., 2015; Borovsky and Yakymenko, 2017; McPherron and Chu, 2018; Ohtani and Gjerloev, 2020), spacecraft auroral imagers (Frey et al., 2004), and in situ spacecraft (Borovsky and Yakymenko, 2017) between 18 May 2000 and 31 December 2002, a common time

period in which onset lists based on different substorm signatures are available. We used the Heidke Skill Score to examine the extent to which events in one list have a corresponding event in another within a conservative estimate of the lifetime of a substorm expansion phase.

4.2 Data and method

4.2.1 Substorm onset lists

We studied the association between the different substorm onset signatures by applying dichotomous forecast verification techniques to substorm onset lists available between the dates of 18 May 2000 and 31 December 2002, which is the interval of the Frey et al. (2004) auroral onset list. The substorm onset lists we analysed were the Frey et al. (2004) auroral onset list, the Newell and Gjerloev (2011); Forsyth et al. (2015); Borovsky and Yakymenko (2017); McPherron and Chu (2018) SuperMAG SML lists, the Chu et al. (2015); McPherron and Chu (2018) MPB index lists and the Borovsky and Yakymenko (2017) particle injection list. The number of substorms in each list and their source is summarised in Table 4.1.

Table 4.1: Onset lists used for analysis.

Substorm Identification Phenomena	Onset Identification Method	Dataset	Number of Substorms
Auroral Enhancements	Frey et al. (2004)	Fr2004 IMAGE	2437
Auroral Zone Ground Magnetic Perturbations	Forsyth et al. (2015)	SOPHIE SML	1724 - 10035
	Newell and Gjerloev (2011)	NG2011 SML	4793
	Borovsky and Yakymenko (2017)	BY2017 SML	1960
	McPherron and Chu (2018)	MC2018 SML	7908
	Ohtani and Gjerloev (2020)	OG2020 SML	2265
Midlatitude Ground Magnetic Perturbations	Chu et al. (2015)	C2015 MPB	3418
	McPherron and Chu (2018)	MC2018 MPB	8601
Geosyncronous Particle Injections	Borovsky and Yakymenko (2017)	BY2017 PI	2149

For the Forsyth et al. (2015) Substorm Onsets and Phases From Indices of the Electrojet (SOPHIE) technique, onset lists were originally published for three different Expansion Percentile Threshold (EPT) values - 50%, 75%, and 90%. In this study, we extended the range of EPTs to between 5% and 95%, to (1) evaluate the EPT value for which the SOPHIE onsets are best associated with events in each of the other onset lists and (2) infer the relative sensitivity of the other methods.

The discrete EPT thresholds used for this study are shown in Table 4.2, with the corresponding number of onsets ranging from 1724 to 10035. For the non-SOPHIE substorm lists analysed, there are also a wide range of onsets observed for the period analysed, from 1960 (BY2017 SML) to 8601 (MC2018 MPB) events, as can be seen in Table 4.1.

Table 4.2: Number of onsets identified using different thresholds of the SOPHIE technique.

Expansion Percentile Threshold	Number of Onsets
05	10035
10	10141
15	10094
20	10073
25	9943
30	9769
35	9608
40	9349
45	9160
50	8738
55	8404
60	7986
65	7433
70	6754
75	6012
80	5306
85	4343
90	3245
95	1724

4.2.2 Windowing event lists for contingency table analysis

The analysis carried out in this study made use of contingency tables, as described in Section 3.5 to evaluate the coincidence between events identified by different substorm identification techniques. To create the contingency tables, we divided our analysis period into consecutive windows, 30 minutes in length. The 30-minute timescale was chosen because 1) it is the identification cadence of the slowest method analysed, the particle injections identified using the Borovsky and Yakymenko (2017) technique, and 2) is a conservative estimate for a substorm expansion phase to develop and the various onset signatures to spread through the magneto-

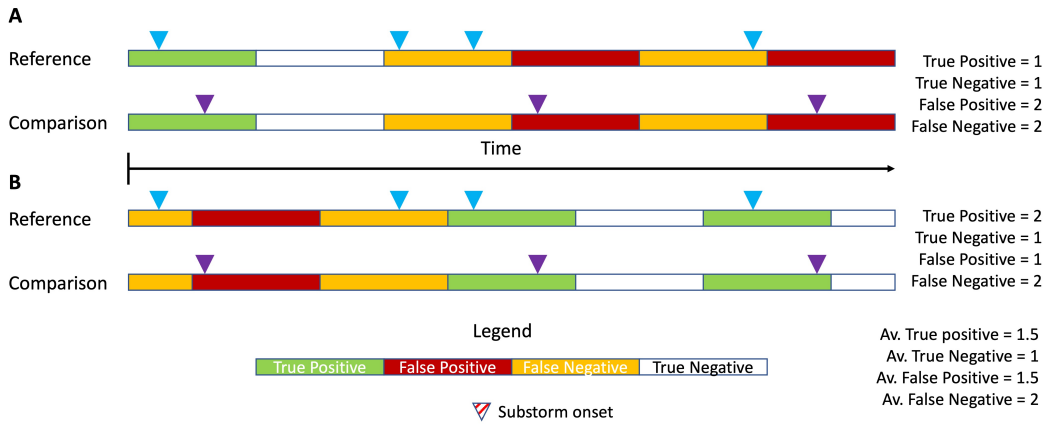

Figure 4.1: Schematic of time series windowing method used to populate the contingency tables of the pairwise comparisons of association. The blue triangles indicate an event in the Reference "time series" and purple an event in the Comparison "time series". In the pairwise comparison shown by (A), we see the classification of the windows dependent on whether an event from either is observed in them or not. The rows denoted by (B) shows our bootstrap method to account for events that coincide within 30 minutes but may have been classed in different windows by the segmentation of the time series. The median of the 30-minute stepped window labellings are what are used as the elements of the contingency tables.

sphere. This setup is shown in Figure 4.1A, where two example time series of events are displayed, one labelled the Reference list and another the Comparison list, with events from each highlighted as triangles (light blue for the Reference and purple for the Comparison). We populated a contingency table for a pairwise comparison by noting whether an event was seen only in a Reference list, only in a Comparison list, in neither, or in both within each 30-minute time window.

Since the position in time of our windows is arbitrary, it is possible for events that are within 30 minutes of each other to appear in different windows (see, for example, the last events in both lists in Figure 4.1A). This will result in close events coming up as misses, returning windows as false positives and false negatives. To mitigate this, we applied a pseudo-bootstrap method. We implemented this by incrementing the start time by 1 minute steps up to the 30 minute length of our windows. Figure 4.1B shows an example of pseudo-bootstrap method applied to the procedure set up in Figure 4.1B, where we have stepped by half of the comparison window length. As can be seen from the figure, the resultant window labelling varies. As

a result of this method, there will be 30 versions of the contingency table created, since we use a window length of 30 minutes. To apply the metrics described in Section 3.5, we take the median values of the contingency tables for the final pairwise comparison. We evaluated the median numbers of true positives, false positives, false negatives and true negatives of the 30 realisations to be used in the metrics describing event association rather than simply summing them to avoid multiple counting event coincidence or disagreement between the lists. Note that the values for true positives, false positives, false negatives and true negatives may come from different time shifts as a result of taking their median values. However, this results in an equivalent Heidke Skill Score up to the 5th decimal point, as calculating the Heidke Skill Score first and then its median. As will be discussed in Section 4.4, this within the error value of the HSS and thus we can take the two calculations as equivalent.

For comparisons with the Fr2004 IMAGE list, adjustments of the analysis were made to compensate for IMAGE having sight of the entire northern auroral oval for only 8 - 10 hours of every orbit (Frey et al., 2004). The time windows in the pairwise comparison when IMAGE was unable to observe the northern auroral oval were filtered out, this was achieved by removing any windows without an IMAGE observation available within it, as IMAGE was only capturing images of the Northern Hemisphere during the period analysed. Filtering out for when IMAGE could not observe the auroral oval. still left $\sim$32,000 of the $\sim$46,000 30-minute windows. Additionally, the BY2017 PI list indicates a 30 minute interval in which an injection is observed, where they have marked the beginning of the interval as their epoch times (Borovsky and Yakymenko, 2017), this was compensated for by adding 15 minutes to the epoch times to not bias towards the beginning or end of their identified intervals.

4.3 Results

4.3.1 Intercalibration of the SOPHIE technique with other substorm onset identification methods

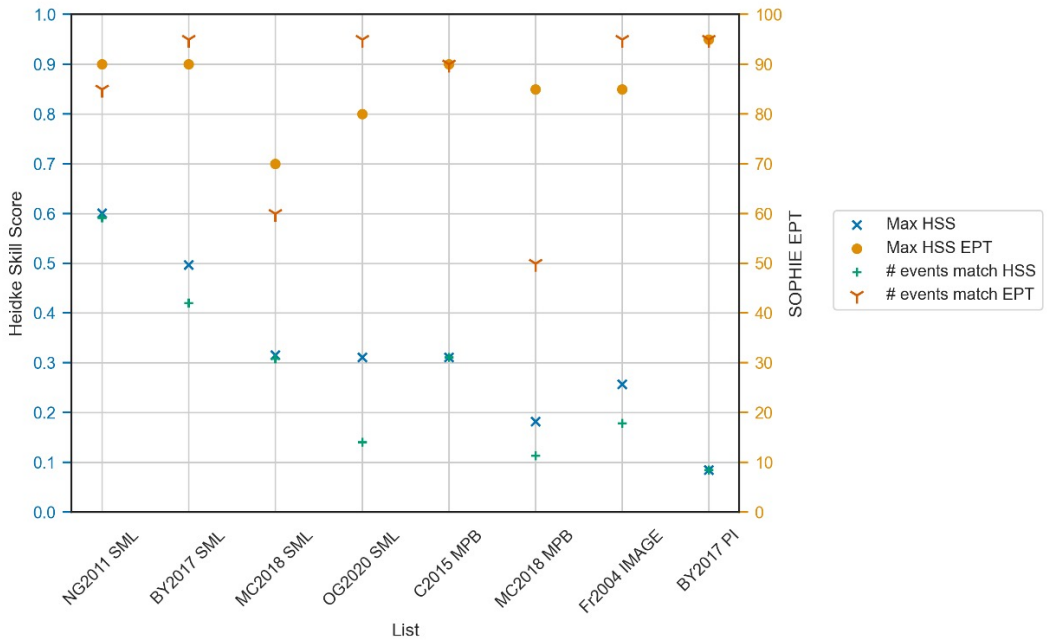

Figure 4.2: The results of comparing various onset lists against various sensitivities of the SOPHIE technique. The blue crosses indicate the maximum Heidke Skill Score achieved by the SOPHIE technique, and light orange dots indicate which tuning of the technique achieved this maximum score. The dark orange tri-markers denote the EPT that has the closest correspondence to the event count of the compared list, with the green pluses being the score achieved by that EPT.

We first examine the effect of SOPHIE detection sensitivity on the association between the SOPHIE technique and other lists. Figure 4.2 shows the results of this analysis, where we have plotted the maximum Heidke skill score achieved by the SOPHIE technique against the other event lists, as well as the Expansion Percentile Threshold (EPT) that achieves this score. As explained in Section 3.5, the Heidke skill score quantifies the improvement over the random chance that events in two lists coincide, with a score of 1 indicating the perfect event association of two lists (within 30 minutes).

Figure 4.2 shows that the SOPHIE technique is able to identify substorm onsets associated with those observed by different methods with some degree of skill,

achieving Heidke skill scores ranging from 0.08 with BY2017 PI to 0.60 with NG2011 SML. The best associations are obtained with detection methods using the same SML dataset as SOPHIE, obtaining scores of 0.31 to 0.60. The associations of SOPHIE with MPB and auroral images are lower, with scores between 0.18 and 0.31, whereas the association of SOPHIE with BY2017 PI is only marginally better than random chance. For the methods that use either the SML index or the MPB index, SOPHIE generally scores poorer when compared with the MC2018 method that applies a normalisation procedure, presumably because SOPHIE is based on the unnormalised SML index.

The value of SOPHIE EPT that provides the maximal HSS (orange dots in Figure 4.2) is mostly relatively high at 80 - 95%. This implies that non-SOPHIE onsets associate best with the largest changes in the lowpass-filtered SML used by SOPHIE, and specifically in the upper 20% of all such changes. This is true for all but the MC2018 SML onset list, where a Heidke Skill Score of 0.32 is achieved with a lower EPT = 70%. The MC2018 SML list has the second-highest number (7908) of identified events, and so it may be thought that in this case the best associating EPT is low in order that the number of SOPHIE events matches the high number of MC2018 SML events. By comparing Table 4.1 and Table 4.2, we see that within the 5% EPT resolution, the closest number of SOPHIE events (7986) to that of MC2018 SML (7908) is indeed found for a low EPT = 60%, but this is still lower than the EPT = 70% that maximises the Heidke skill score, for which SOPHIE identifies 6754 events, some 1154 or 15% fewer events than MC2018 SML. To investigate this further, we plot in Figure 4.2 the EPT that has the closest number of events to each of the other compared lists, and the Heidke Skill Score this EPT achieved. We see that, in general, the Heidke Skill Score is not simply maximised by minimising the difference in the number of events between the two lists, as for five of the seven list comparisons the EPT that scores best does not have the most similar number of events. That is, it is not only the number of events in each list, but also their relative timing, that matters. Indeed, if the reference and comparison lists had the same number of events but the events in one of the lists were purely random in time,

then the events would be statistically independent of each other and the HSS would be zero by definition.

4.3.2 Relationship between different onset methods

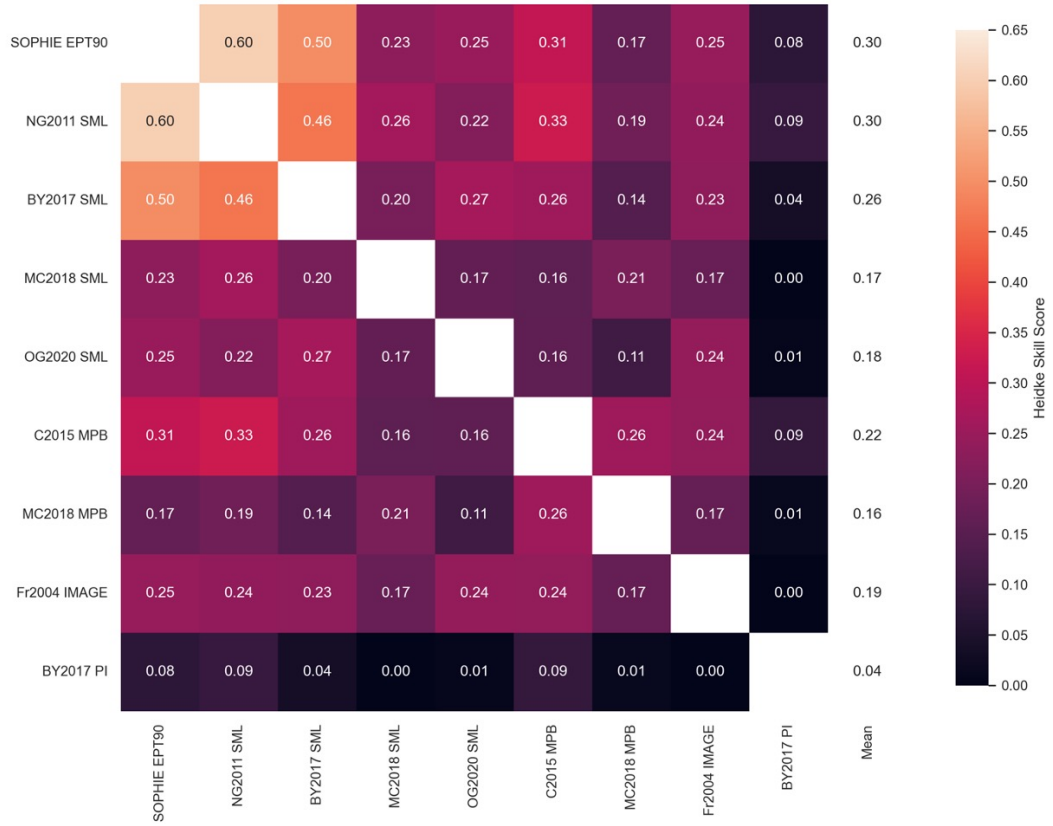

Figure 4.3: A heatmap of the Heidke Skill Scores achieved by every cross-comparison. Lighter colours indicate a higher level of event coincidence between the two onset lists. It is symmetric along the main diagonal by a property of the Heidke Skill Score formulation. The last column is the mean Heidke Skill Score achieved by that onset lists for all its comparisons.

Figure 4.3 shows a "heatmap" of the Heidke skill scores obtained by comparing all the onset lists with each other. It should be noted that this analysis now uses a single SOPHIE sensitivity in order not to bias the results towards the SOPHIE technique by including multiple SOPHIE onset lists with different EPTs. EPT 90 was selected as it was the version that scored highest on average when compared against the other non-SOPHIE onset lists. We have quoted the metrics here to the second significant figure, as the uncertainty in the Heidke skill scores shown is on the order of 10^{-3}, assuming that event occurrence is approximately independent,

stationary, and rare such that the standard error of the count in each element of the truth table is the square root of the count based on Poisson counting statistics. As the Heidke skill score is invariant to which event list is used as the comparison or reference list, the heatmap produced is symmetric about the main diagonal. The mean of the Heidke Skill Scores achieved by one onset list with each of the others is shown on the rightmost column of the heatmap.

The highest scores are obtained when comparing the SML gradient lists that do not filter out events by MLT (SOPHIE EPT90, NG2011 SML and BY2017 SML) with one another (0.46 - 0.60) although none of them are an exact match due to the differing nuances of each algorithm, e.g., smoothing of the raw SML signal, gradient threshold, hard-coded delay between identification of successive onsets, etc. Furthermore, these SML gradient lists that do not filter by MLT also achieve the highest mean scores of 0.26 to 0.31, although these means are biased because they contain cross-comparisons with other SML gradient lists, a problem that we address in Section 4.3.4.

The next highest mean HSS of 0.22 is achieved by the C2015 MPB method, which is another gradient method, but based on the MPB index. It performs particularly well when compared with the SOPHIE technique and NG2011 SML, with scores of 0.31 and 0.33 respectively. The comparison of C2015 MPB with NG2011 is the highest score achieved outside of comparisons between gradient-SML lists.

The normalised method lists of MC2018 show a weaker association with other lists than gradient-based methods, for both the SML and MPB indices. The average HSS is 0.17 for MC2018 SML and 0.18 for MC2018 MPB.

A similar mean HSS of 0.19 is found for the Fr2004 IMAGE event list based on visual identification of auroral onset. Notably, Fr2004 IMAGE performs better when compared against the gradient-based methods.

The OG2020 SML list performs similarly to the other SML gradient methods when compared with Fr2004 IMAGE achieving a HSS of 0.24. However, it achieves a lower mean score compared to the other SML gradient methods, 0.18, similar to the performance of the MC2018 normalised index method. This reduction could be

due to the filtering of this method for isolated onsets occurring within 20 - 03 MLT only. We applied an MLT filter to the NG2011 SML onset list, resulting in a reduced mean Heidke skill score, although achieving the same score when compared with Fr2004 and BY2017 PI (results not shown).

The BY2017 PI list obtains the lowest average score with an average HSS of 0.04, with no comparison with the BY2017 PI events achieving an HSS greater than 0.09. This implies that coincidence between BY2017 PI and other lists shows very little improvement over random chance coincidence of events within 30 minutes. Indeed, comparisons between BY2017 PI and both MC2018 SML or Fr2004 IMAGE obtain a score of 0.00 implying a purely random association. We note that this is despite the fact that BY2017 PI and Fr2004 IMAGE identify a similar number of onsets (= 2149 and 2437, respectively).

4.3.3 Relationship between common index methods and other methods

As SML-based onset lists tend to perform well against each other, including multiple SML-based lists in Figure 4.3 biases their overall mean skill score compared to that of the other lists. Figure 4.4 shows a heatmap of the Heidke skill scores achieved by each SML-based list compared to the other non-SML lists. The SML-based lists achieve the best scores with the C2015 MPB list, followed by the Fr2004 IMAGE list. MC2018 MPB achieves its highest score when compared to its equivalent algorithm on the SML dataset, MC2018 SML. The BY2017 PI achieves a mean score of 0.05, which implies that, in general, there is little improvement over random chance of agreement between the BY2017 PI and the SML-based lists. We also note that there is comparable performance for the SOPHIE, NG2011 and BY2017 gradient-SML lists when they are compared to the Fr2004 auroral list.

Comparing the performance of the SML detection algorithms against the other signatures, we find that the best performing list on average is NG2011 SML, with a mean Heidke Skill Score of 0.21. This is only a marginal improvement over SOPHIE EPT90's score of 0.20. The lowest mean HSSs are achieved by the normalisation detection method, MC2018 SML, and the MLT-filtered gradient method by

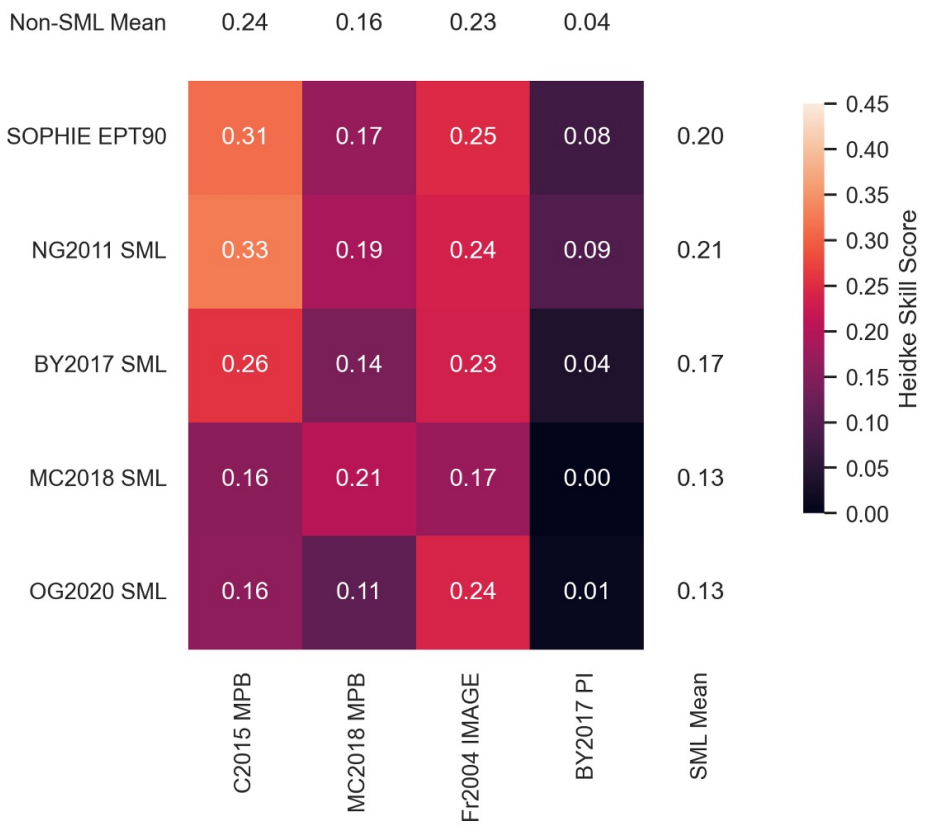

Figure 4.4: A heatmap of the Heidke Skill Scores achieved by the SuperMAG AL-based onset lists vs lists derived from other datasets. Lighter colours indicate a higher level of event coincidence.

OG2020, with a score of 0.13. We also applied the same MLT filter on the NG2011 onset list as was applied for OG2020, only including onsets that the contributing station to SML was within 20 - 03 MLT. In addition, we tested various values for the cutoffs used to restrict possible onset locations within the NG2011 onset list and found that there was no singular value that increased the scores with other onset lists. As such, we present the results of NG2011 using the same cut-off as used by OG2020 SML for best comparison. We find that there is a slight reduction in the Heidke Skill Score obtained by a constrained version of NG2011 with the MPB lists of C2015 and MC2018, while the scores with Fr2004 and BY2017 PI remain the same. Thus, restricting the possible MLTs that an NG2011 SML onset can occur at not only removes false negatives and positives but also true positive coincidences. This is evidence that the lower mean score of the OG2020 SML is not only due to

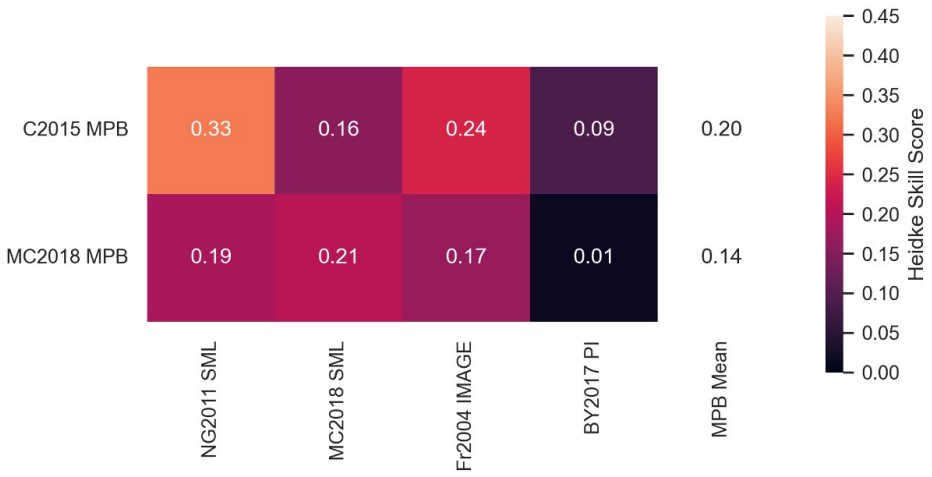

Figure 4.5: A heatmap of the Heidke Skill Scores achieved by the Midlatitude Positive Bay Index-based onset lists vs lists derived from other datasets. Lighter colours indicate a higher level of event coincidence.

the restriction in possible magnetic local times of identification but also due to the other criteria used, such as the requirement for a clear observable growth phase, although it should be noted that Ohtani and Gjerloev (2020) does not assert that their onset list is a complete list of substorm events.

We note that when MC2018 SML was compared with MC2018 MPB, this gave the highest score of all comparisons with MC2018 MPB, however, the improvement in this score over NG2011 SML with MC2018 MPB was marginal. In comparison, there is a much greater difference in score between MC2018 SML and C2015 MPB compared to NG2011 SML and C2015 MPB. As NG2011 was the best performing SML event list, it was the list used for the cross-comparison of distinct signatures only in section 4.3.4 below.

As we also have two methodologies applied to the Midlatitude Positive Bay (MPB) index, we also examine their performance compared to the other lists. To avoid biasing the overall average HSS, we compare these to NG2011 (SML gradient list), MC2018 SML (SML normalised list), as well as Fr2004 IMAGE and BY2017 PI. Figure 4.5 shows a heatmap of the score achieved by C2015 MPB and MC2018 MPB with the algorithms of the other substorm signatures. C2015 MPB outperforms the MC2018 MPB method, with an average score of 0.20 compared to 0.14.

The scores for C2015 MPB are consistently higher, apart from the comparison with MC2018 SML, where C2015 MPB scores 0.16 compared to MC2018 MPB's score of 0.21. In particular, C2015 MPB outperforms MC2018 MPB when compared to lists using features not based on either the westward electrojet or field-aligned currents (Fr2004 IMAGE and BY2017 PI). As such, for further comparison, we used the C2015 MPB as the best performing MPB list.

4.3.4 Relationship between distinct methods

Figure 4.6 shows the Heidke Skill Score (A) and True Positive Rate (B) heatmaps of distinct substorm identification signatures only. This was done by selecting the highest scoring methods of the SML and MPB datasets, shown in the prior figures, to be compared against each other and with the auroral image event list of Fr2004 IMAGE and the particle injection event list of BY2017 PI. We find a very similar performance between NG2011 SML and C2015 MPB, both with a mean HSS of 0.22. The Fr2004 IMAGE list and BY2017 PI lists show some skill in event coincidence with the other signatures, obtaining mean scores of 0.16 and 0.06 respectively. However, our analysis shows that the event coincidence of the auroral onsets and particle injections achieve a score of 0.00, implying that any event coincidence between these two lists is no better than random chance.

When looking at the associated TPR's of these comparisons in Figure 4.6B, we can infer the approximate number of events the pairwise comparison of lists have in common by multiplying the TPR by the total number of events in the reference list (provided in the row headers). From this Figure 4.6B, we see that less than 50% of the events in each list are associated with an event in the other lists. The list with the highest proportion of events associated with another list is C2015 MPB, for which 45% of the 30-minute windows were associated with an event in the NG2011 SML list. In contrast, only 34% of the 30 minute intervals with a NG2011 SML event were associated with a C2015 MPB event. For the Fr2004 IMAGE list, approximately one third of the 30-minute windows were associated with an SML or MPB event, while less than a third of 30-minute windows with an SML or MPB event were associated with an auroral event. Finally, we see that approximately 10%

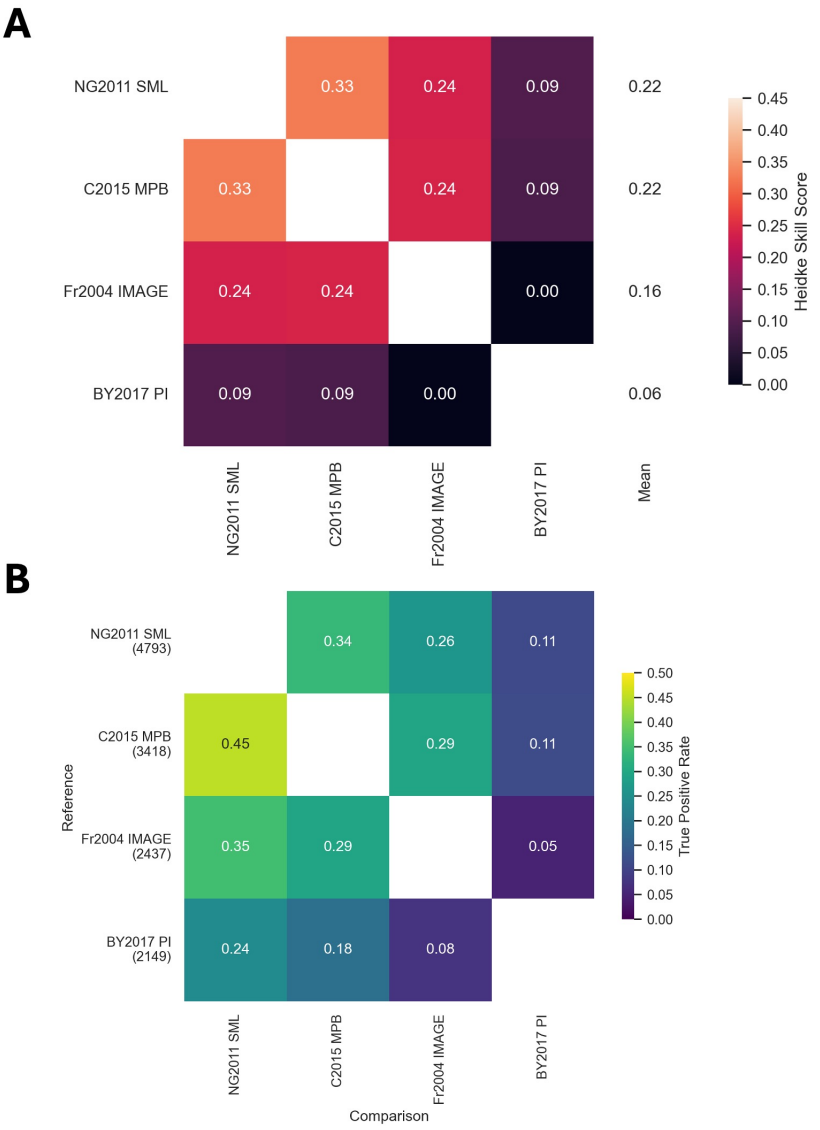

Figure 4.6: (A) Heidke Skill Score heatmap from distinct datasets only (SML, MPB, Auroral Images, Particle Fluxes at Geosynchronous Orbit), (B) The True Positive Rates (TPR) for each cross comparison. The number in parentheses underneath the row labels is the number of events that populate each list. Note that this is asymmetric, as directionality matters in the formulation of TPR.

or less of 30-minute windows with an auroral, MPB, or SML event are associated with a particle injection event.

4.4 Discussion

We evaluated the association between SML-based, MPB-based, auroral-based, and particle injection-based substorm onset lists using metrics used in dichotomous forecast verification. In general, we found that lists based on the SML or MPB index with the time of onset identified from the gradients in these indices showed the greatest association. In contrast, the particle injection list showed a relatively poor association with the other lists, showing marginal or no improvement over random chance associations.

Suprisingly, We found that less than 50% of the events in each list were associated with events in another list using a different substorm signature, that is, they occurred within the same 30-minute time window. This is broadly consistent with a different type of analysis by Forsyth et al. (2015), who examined the probability distribution of the time difference between a SOPHIE onset for various EPT and the nearest onset from another list. They found that only about a third of the onsets of EPT90 occurred within $\pm$30 minutes of the onsets on the Frey and Mende (2006) list and about two-thirds of the onsets of EPT90 occurred within $\pm$30 minutes of the onsets in the Newell and Gjerloev (2011) list.

In our analysis, we show that having event lists with comparable numbers is not necessarily indicative of good agreement between them. To illustrate this, we highlight the comparisons of the SOPHIE technique for variable EPT and hence number of onsets with the SML and MPB lists based on the MC2018 method. MC2018 SML achieves its highest Heidke skill score with SOPHIE EPT 70, but should the HSS be only dependent on comparable numbers, we would expect the best agreement with EPT 60. Furthermore, MC2018 MPB has a similar number of events as MC2018 SML but best associates with SOPHIE EPT 85 which identifies approximately half of the events that MC2018 MPB does. The extreme example of this is that if we create a list of random onsets (i.e. Poisson process with constant probability of occurrence per unit time) with the same number as any observed list, then the occurrence of the random events is independent of the events in the observed list, and the HSS is then zero by definition.

Table 4.3: Results of the pairwise comparison between NG2011 SML and C2015 MPB at different data cadences

NG2011 Data cadence	C2015 Data cadence	Heidke Skill Score	% Change
1-min	1-min	0.327	0.0
1-min	2-min	0.326	0.3
1-min	30-min	0.294	10.1
2-min	1-min	0.328	0.3
2-min	30-min	0.293	10.4
30-min	1-min	0.296	9.5
30-min	2-min	0.292	10.7

We have taken substorm onset lists using techniques and instruments with different data cadences, with the ground magnetometer techniques having the fastest data cadence of 1-minute resolution, the IMAGE spacecraft taking snapshots of the aurora every 2 minutes and the particle injections identifying 30-minute intervals. This can induce artificial delays when identifying events; for example, between an identification method with a 1-minute cadence data source and another method with a 20-minute data source, there can be up to a minute difference in identification even if the event occurred concurrently in both data sources. To examine with this effect, we experimented using different data cadences with the highest scoring comparison from two different data sources, NG2011 SML and C2015 MPB. The results of this numerical experiment are shown in Table 4.3, the top row of this table is the original score achieved by the comparison, now shown in 3 significant figures. As evidenced by the experiments, reducing the data cadence to 2 minutes has a minimal effect on the scores achieved using our method $\pm 0.3\%$. However, the difference when the data cadence is reduced to 30 minutes is more significant, capable of reducing the score achieved by 10%. This reduction affects the comparisons with the particle injections, the lowest scores achieved in our analysis. However, even when accounting for a reduction of 10% in the Heidke skill score, these scores would remain the poorest and as such the data cadence differences have less of an effect on possible misidentification than other factors.

The strongest association that we determined was between SML and MPB-based lists, when the identification of events leveraged gradients in these indices.

For these lists (C2015 MPB and NG2011 SML), we found ~ 1500 coincident events (45% of the MPB list and 34% of the SML list). That these lists showed the strongest associations is to be expected, as they effectively attempt to identify different aspects of the current systems in the substorm current wedge (Kepko et al., 2015). The fact that nearly two-thirds of the SML events are not associated with an apparent enhancement in MPB is intriguing. This may arise from a number of considerations. Firstly, the auroral zone magnetometers are much closer to the current system they are attempting to characterise, since the electrojets are flowing in the ionosphere at ~ 100 km whereas the field-aligned currents that provide the MPB signature are thousands of kilometres from their detecting stations. As such, small-scale features and enhancements may be unresolved by MPB stations, resulting in them missing SML "events". However, the fact that over half of the MPB events do not have an associated SML event means that this cannot be the only explanation.

The index normalisation method by McPherron and Chu (2018) obtains weaker associations compared to gradient identification methods on either index, even when isolating scores against another substorm signature such as Fr2004 IMAGE. The MC2018 method identifies many more events compared to the other non-SOPHIE list, with 7908 and 8601 events for the SML and MPB index, respectively. The next closest method, NG2011 SML only identifies 4793 events during this period, a reduction of $\sim 40-45\%$. The lower levels of association seen then arise from the increased number of false positives in comparison to the other methods. This could be due to the normalisation procedure identifying small perturbations during particularly quiet periods in either index as events, such that non-substorm fluctuations are misclassified as substorm onsets. Further evidence that substorm identification of smaller magnetic fluctuations is a possible cause of the weak association compared to the other lists is that from Figure 4.3, we observe that MC2018 SML's best agreement is with a lower SOPHIE threshold than the other lists, corresponding to requiring smaller gradients in SML to identify substorm onset. It should be noted that the normalisation procedure could also have the effect of suppressing substorm-like perturbations in either index during particularly active times, resolving these in-

tervals as false negatives compared to the other lists, causing the observed reduction in association.

Identification of the substorms by eye from auroral data has been the basis for much of the statistical analysis of substorm phenomenon, and is considered by some to be the most robust identification. Overall, there are far fewer auroral onsets than MPB or SML onsets, even when one considers the viewing restrictions of the IMAGE spacecraft. However, we still find that over two thirds of the identified auroral onsets do not correspond to an event in the MPB or SML lists. This may imply that many of the Fr2004 events are relatively small substorms. In fact, Forsyth et al. (2015) found that the average SML profile of the extended IMAGE onset list (Frey and Mende, 2006) was one of the weakest of the event lists they tested (reaching one of the least negative SML values at peak activity), second only to onsets identified from THEMIS ASIs (Nishimura et al., 2010) (see Figure 4 in Forsyth et al. (2015)). However, we also find that there are comparatively large SML and MPB perturbations that were not associated with auroral events in the Frey et al. (2004) list. These may be expansion phase onsets during or immediately after substorm recovery phases, which may be tricky to identify by eye because of the complex auroral activity already occurring.

Our results show that, in general, there is a poor association between particle injections and auroral, MPB, or SML signatures. This is somewhat surprising, given that substorm particle injections are considered a key driver in radiation belt enhancements (Jaynes et al., 2015; Forsyth et al., 2016). Borovsky and Yakymenko (2017) discuss that the onset times, which mark the beginning of the 30-minute interval in which an injection is observed, may be systematically delayed by 30 minutes from the events they identified from the SML index. This is because particle injections must be detected in situ, whereas all other signatures are detected remotely. More specifically, if there is no Los Alamos National Laboratory (LANL) spacecraft within the vicinity of the injection region and there is an injection at geosynchronous orbit, the injected electrons must drift towards eastward until a spacecraft is encountered. Furthermore, when using the end of the 30-minute in-

terval as the epoch time for the onset of the substorm, the Heidke skill scores for BY2017 PI were improved, in agreement with the hypothesis that there may be a systematic delay between these injections and other signatures. However, the scores achieved were still lower than those attained by other methods, even when accounting for the data cadence effects as described above. As such, spacecraft spacing and electron drifts are not the only considerations for misidentification using injections. It is conceivable that injection events are occurring within the magnetosphere but are sufficiently localised that they pass between spacecraft and are injected further into the inner magnetosphere, or do not reach geosynchronous orbit and thus are not detected by the spacecraft. Rodger et al. (2022a) observes that precipitating flux tends to penetrate further into the inner magnetosphere for larger geomagnetic events (see Figure 1 in Rodger et al. (2022a)), thus leveraging Low Earth Orbit (LEO) spacecraft as an additional data source for injections may be required, as they can cross multiple L-shells quickly.

Most of the onset lists that we have used in this study were developed in isolation to one another. As such, there was little in the way of inter-calibration to indicate that the thresholds used were appropriate and comparable to other substorm identifications. The exception to this was the study by Forsyth et al. (2015), which explicitly compared the results of multiple thresholds with similar results from existing onset lists. We have taken this one step further by determining the thresholds for the SOPHIE algorithm that provide lists with the greatest association to the other lists we have considered. Overall, we find that well-performing SML lists and the C2015 MPB list have the greatest association with the SOPHIE EPT 90 list. However, the Fr2004 IMAGE list has the greatest association with the SOPHIE EPT 85 list, somewhat higher than the EPT 75 found by Forsyth et al. (2015). Although this may imply that there is a certain degree of accidental intercalibration, the differences in peak HSS indicate that different subsets of the event lists agree with the SOPHIE EPT 90 events. Adjusting thresholds to identify a similar set of events will improve the quantified agreement with verification metrics, and the exploration of differences in either onset number of the events that are misidentified

by either list could improve understanding of substorm and magnetotail dynamics.

As part of our analysis, we examined the associations between similar techniques applied to the same datasets and the associations of different techniques applied to the same datasets with lists from different signatures. Typically, we found that the lists that used the normalisation method of McPherron and Chu (2018) had a lesser association with the auroral image and the particle injection lists than the lists that used gradients of SML and MPB. We found that the lists that achieved the highest associations were NG2011 SML and C2015 MPB, as such, we would recommend the use of these onset lists when conducting statistical studies of magnetospheric dynamics surrounding substorm onset. It should be noted that the C2015 MPB list is only available from 1981 - 2015, thus covering missions such as IMAGE, Polar, and Cluster II but missing a large part of the lifetimes of Van Allen Probes, MMS, and any future missions. However, we note that both these lists only provide substorm onset times, whereas the Forsyth et al. (2015) SOPHIE algorithm, which scores only marginally lower than NG2011 SML when compared to non-SML methods, provides complete identification of the time series of substorm phases, in addition to leveraging the SMU dataset to filter out large SML fluctuations that may be due to enhanced convection.

4.5 Summary

In this study, we quantified the coincidence of events identified using various substorm identification methods using a technique derived from contingency tables for the period between May 2000 and December 2002. We found that while there was skill in event association, this varied depending on the method and signature used. The best scoring techniques were gradient methods applied to ground magnetometer data. However, we found that even the methods that obtain the highest levels of association, Newell and Gjerloev (2011) and Chu et al. (2015), have fewer than 50% events common to both lists within the lifetime of the expansion phase. If one were to study the dynamics of the substorm using only one onset list, we recommend using either of the lists by Newell and Gjerloev (2011) or Chu et al. (2015) if the authors are only interested in onset timing, and the SOPHIE technique by (Forsyth et al., 2015) using an EPT of 90 when considering all phases of the substorm. Although it has previously been viewed as a robust signature of substorms, particle injections at geosynchronous orbits obtained the lowest scores in our analysis, showing poor associations with the other lists analysed.

Clearly, there is a need to cross-calibrate these identification methods and narrow the quantitative definition of the substorm, so as not to come to conclusions about magnetospheric dynamics when using just a subset of substorm events or intervals that may not correspond to substorms. Although there have been some efforts to calibrate these onset lists, they have been done such that a similar number of events is identified by a method to some given list, historically the auroral identification onset lists, as they contain the fewest false positives, or to reduce the time differences of the nearest onset identified by a new method to a reference list, for example, Forsyth et al. (2015). Another possible avenue is to define the occurrence of an onset using a combination of datasets, rather than using one signature for substorm onset. The difficulty in this is to account for differences in data cadences, coverage, and time intervals covered by the different datasets that are used.

Chapter 5

Separating the DP1 and DP2 pattern contributions to substorm-like SML bays

This work has been published in C. J. Lao, C. Forsyth, M. P. Freeman, and J. W. Gjerloev. Separating DP1 and DP2 Current Pattern Contributions to Substorm-Like Intensifications in SML. Journal of Geophysical Research: Space Physics*, 130 (4):e2024JA033592, 2025. ISSN 2169-9402. doi: 10.1029/2024JA033592*

5.1 Introduction

From magnetic perturbations measured on the ground, one can estimate the direction and magnitude of the equivalent ionospheric current maps by rotating the magnetic field vectors by 90° clockwise. As such, a positive northward magnetic deflection is produced by an eastward flowing ionospheric current. There must be a degree of care when interpreting these equivalent currents as gradients in conductivity, and the contribution of more distant currents than those in the ionosphere also affects the observed perturbations (Milan et al., 2017). However, from decades of study, the magnetic perturbations produced in the polar regions can be largely decomposed into two main characteristic patterns: the Disturbance Polar (DP) 1 and 2 patterns (Nishida and Kokubun, 1971). The DP1 pattern is associated with substorm-time electrojet (Akasofu et al., 1965), which was later shown to be the

ionospheric leg of the substorm current wedge (McPherron et al., 1973), consisting of a strong westward-directed ionospheric current centred at midnight magnetic local time (MLT). The two-cell DP2 current pattern is produced by the convection of magnetic flux described by the Dungey cycle (Dungey, 1961). Its ground signature is detectable due to the Hall currents that make up the eastward and westward electrojets in the afternoon and morning MLT sectors. It is highly correlated with the southward component of the interplanetary magnetic field (IMF B_z) on short time scales and is associated with general magnetospheric convection (Nishida, 1968a; Friis-Christensen and Wilhjelm, 1975; Shore et al., 2019). Using data-driven methods on SuperMAG data, Shore et al. (2018) were able to decompose these two spatio-temporal patterns, in addition to patterns related to the DPY equivalent current system (Friis-Christensen and Wilhjelm, 1975; Friis-Christensen et al., 1985) and the NBZ field-aligned current system (Maezawa, 1976; Iijima et al., 1984), among the six modes of variation that contribute most to the magnetic field variance throughout Solar Cycle 23. As shown by the Shore et al. (2018) analysis, the DPY spatial pattern is a single vortex that is approximately centred on the magnetic pole and whose polarity and strength is controlled by IMF By. When added to the symmetric component of the DP2 pattern, the DPY component controls the relative strength and shape of the two vortices of the DP2 pattern, creating the so-called "banana" and "orange" convection cells (e.g., Østgaard et al., 2018). The NBZ pattern appears as twin reversed lobe convection cells on the dayside polar cap and is associated with periods of purely northward IMF. Additionally, the reanalysis conducted by Shore et al. (2017) of the single month of February 2001 found that the amplitude of both the DP1 and DP2 modes increased rapidly at substorm onset.

As discussed in Section 3.1, a common way to identify substorms is to detect their ground perturbation due to the ionospheric westward current of the substorm current wedge (DP1 current pattern). By Ampere's law, this creates a southward magnetic deflection observable on the ground at auroral zone latitudes. Other methods of identifying substorms include leveraging auroral imagery, taken from spacecraft (Frey et al., 2004; Liou, 2010) or on the ground using all-sky imagers

(Nishimura et al., 2010), or from particle injections observed by spacecraft at geosynchronous orbit (Borovsky et al., 1993; Borovsky and Yakymenko, 2017). Each method comes with its own advantages and disadvantages, such as identifying substorms from auroral features that currently require these features to be observable from the ground or when a spacecraft is suitably positioned to observe them. The advantage of using magnetic indices is the almost global coverage from the many magnetic observatories and arrays that have been deployed. However, it should be noted that the observation of one signature associated with the substorm does not confirm the occurrence of the phenomena and that any two of different substorm signatures appear together for less than 50% of substorms (Lao et al., 2024) shown and discussed in Chapter 4.

As a reminder, the magnetic indices AU and AL (Davis and Sugiura, 1966), and their SMU and SML generalisation to many stations (Newell and Gjerloev, 2011), were developed to trace the maximum and minimum northward deflections of the northward component of the geomagnetic field across a range of auroral latitude magnetometer stations. At substorm onset, a sharp negative bay is observed in the AL/SML index, indicating an enhancement of the westward auroral electrojet by the substorm. Many automated methods have recently been developed that take advantage of these indices to identify the onset of the expansion phase of the substorm (Newell and Gjerloev (2011); Forsyth et al. (2015); Borovsky and Yakymenko (2017); Ohtani and Gjerloev (2020); McPherron and Chu (2017), see Section 3.1.2 for details of these methods). However, the substorm is not the only magnetospheric phenomenon capable of producing such enhancements of the westward electrojet (Kamide and Kokubun, 1996). In particular, during periods of enhanced convection, DP2 is enhanced, and there is an enhancement in both the eastward and westward electrojets. Thus, SML automated methods may be contaminated with false positive events. Of the techniques mentioned above, it is only the method of Forsyth et al. (2015) that attempts to explicitly separate the DP2 signature of enhanced convection from substorms by assessing periods in which the SML and SMU enhancements are similar.

In this study, we examine the **S**ubstorm **O**nsets and **PH**ases from **I**ndices of the **E**lectrojets (SOPHIE) method developed by Forsyth et al. (2015), where they attempt to distinguish between the ground signatures of substorms, which predominantly enhance the equivalent currents of the DP1 pattern, and periods of enhanced convection due to enhancements of the DP2 current pattern, which are well correlated with periods when the solar wind directly drives the magnetosphere (Nishida, 1968a). We quantify the two current pattern contributions to substorm-like SML intensifications across all magnetic local times. In addition to this, we explore the parameter space used for filtering out these convection enhancements from "true" substorms, to evaluate the effectiveness of auroral indices for substorm identification.

5.2 Data and Method

5.2.1 SOPHIE Identification of Substorm events

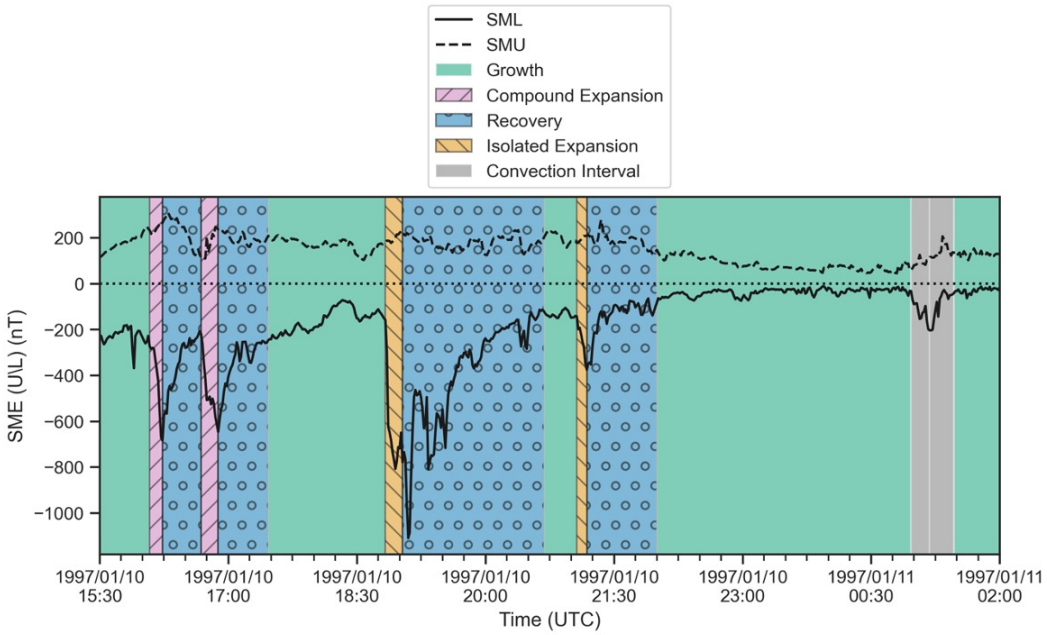

Figure 5.1: The SML (solid black) and SMU (dashed black) indices (nT) plotted as a function of time, with the background colour indicating the substorm phase identified by the Substorm Onsets and Phases from Indices of the Electrojet (SOPHIE) method using an Expansion Percentile Threshold (EPT) of 90 for that period. Green indicates periods of growth, orange \-hatched corresponds to expansion phase that is part of an isolated substorm, pink /-hatched corresponds to an expansion phase that is part of a compound substorm, blue ○-hatched indicates a recovery phase and grey corresponds to periods that have been identified as convection enhancement intervals.

In this study, we make use of the SOPHIE method detailed in Section 3.1.2.1. In particular, we examine the period between January 1997 and December 2019 using the EPT 90 version of SOPHIE. This threshold of SOPHIE has been shown to have the best association with other substorm onset lists, as shown in Chapter 4 (Lao et al., 2024). The SOPHIE method for identifying the phases of the substorm has been used extensively in the literature, particularly in statistical studies of the effects of substorms, including studies of the magnetotail lobes (Coxon et al., 2018), radiation belts (Forsyth et al., 2016; Rodger et al., 2022b,a), ring current (Sandhu et al., 2019), field-aligned currents (Coxon et al., 2017), ground-induced currents (Freeman et al., 2019; Smith et al., 2024), and auroral kilometric radiation (Waters

et al., 2022), as well as the influence of the solar wind and interplanetary magnetic field on substorms (Lockwood, 2023; Laitinen et al., 2024; Walker et al., 2024).

The SOPHIE method does not dictate the ordering of substorm phases; onsets of the expansion phase can occur following growth or recovery phases. In this thesis, we classify an event as an isolated substorm if it follows the phase ordering of Growth-Expansion-Recovery-Growth. In Figure 5.1, two isolated events are shown between 17:30 UT on 1997/01/10 and 02:00 UT on 1997/01/11. Here, the first isolated event has its growth phase begin around 17:30 UT, with the expansion onset occurring at 18:50 UT, followed by a recovery phase at 19:02 UT, transitioning into another growth phase at 20:41 UT. Isolated substorms occur frequently in SOPHIE EPT 90 event identification, compromising 54% of all expansion phase events between January 1997 and December 2019.

The SOPHIE method also resolves periods of compound or recurrent substorm activity (e.g., Rodger et al., 2022b,a; Sandhu et al., 2019). These periods are characterised by multiple expansion and recovery phases, with no intermediate growth phase between them. An example of such a period is shown in Figure 5.1, with the first onset of the compound event occurring at 16:05 UT on 1997/01/10 and the second at 16:41 UT. The period of compound activity is ended by the occurrence of a growth phase at 17:28 UT. In this thesis, all onsets in a compound sequence are classified as individual compound substorms, even though the first onset follows from a growth phase. Between January 1997 and December 2019, 27% of SOPHIE EPT 90 expansion phase events are compound substorms.

Additionally, as described in Section 3.1.2.1, SOPHIE distinguishes between SML bays created by the substorm and those created by magnetospheric convection enhancements. Figure 5.1 shows an example period that has been flagged by the amended SOPHIE method, with the event beginning at 02:07 UT on 1997/01/11 and ending at 02:40 UT. Here, the flagged expansion phase lasted 15 minutes. In the period analysed, 8% of the identified expansion events were flagged as possible convection enhancement intervals.

5.2.2 MLT Distributions of events

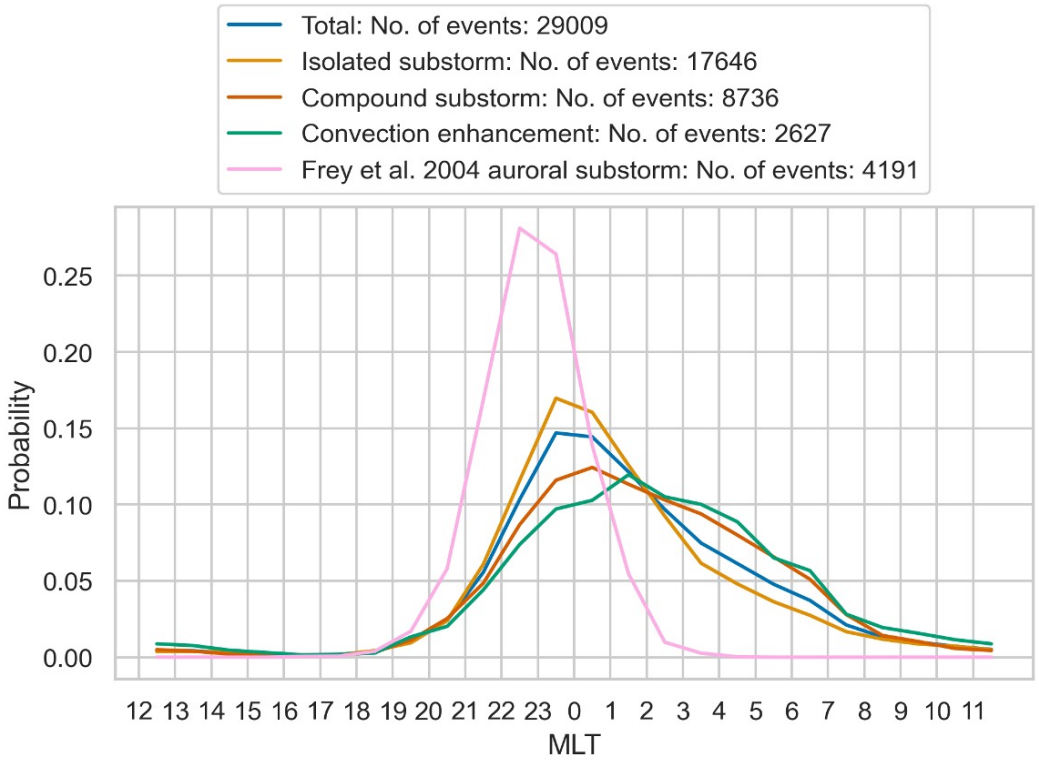

Figure 5.2: The magnetic local time (MLT) probability density (probability per hour MLT) distribution of the contributing station to SML for different event types. The blue indicates the total event distribution, orange corresponds to the isolated substorm events, red corresponds to the compounds substorm events, and green corresponds to the convection enhancements.

Figure 5.2 shows the probability distributions of the onset magnetic local time (MLT) of each SOPHIE EPT 90 event type discussed in Section 5.2.1. That is, from the SOPHIE EPT 90 substorm phase list in the period January 1997 to December 2019 inclusive, we identified the subsets of isolated substorms, compound substorms, and convection enhancements and, for each subset, the MLT of the station that contributes to SML at the time of event onset was sorted into a corresponding 1-hour MLT wide bin. For example, the first compound onset in Figure 5.1 at 16:05 UT has its contributing station at 21.75 MLT at the onset of the expansion phase, and therefore this occurrence would be placed in the 21 - 22 MLT bin. The probability distribution of the onset MLT for each event type was then calculated by dividing the number of events of a given type in each MLT bin by the total number

of events of that type. Similarly, Figure 5.2 also shows the probability distribution of the MLT of substorm onsets identified by Frey et al. (2004) from auroral images in the period from 19 May 2000 to 31 December 2002 inclusive.

Figure 5.2 shows that the probability distributions of different SOPHIE EPT 90 event types are different from each other and to that of the Frey et al. (2004) auroral events. Firstly, the MLT distribution of auroral events (shown in pink) peaks 1 hour of MLT earlier than that of the SOPHIE isolated substorm events (shown in gold). As discussed further in Sections 5.3 and 5.4, this westward displacement is likely explained by the localised auroral brightening signature of substorm onset identified by Frey et al. (2004) being associated with the upward field-aligned current that sits at the western end of the DP1 substorm electrojet detected by SOPHIE.

Secondly, the isolated substorm distribution is asymmetric with a more eastward extended tail than the symmetric auroral distribution. Whilst, as argued above, an eastward shift of the isolated substorm distribution is to be expected, we hypothesise that its MLT asymmetry is because some SOPHIE enhanced convection events are falsely identified as isolated substorms. The convection enhancement distribution (shown in green) is a broad, approximately symmetric, distribution centred later at 01 - 02 MLT. As will be shown in the next section, the MLT extent of this distribution is consistent with the extent of the westward electrojet of the DP2 ionospheric equivalent current pattern, which the SML index is expected to be sampling during periods when magnetospheric convection is enhanced. Thus, if some convection enhancements are misidentified as isolated substorms, then these anomalous events will be predominantly in the post-midnight MLT sector, and the isolated substorm distribution will be erroneously skewed eastward, as observed.

Thirdly, the compound substorm distribution is intermediate between the isolated substorm distribution and the enhanced convection distribution. Thus, the above hypothesis suggests that the compound substorm distribution is even more contaminated by misidentified enhanced convection events than the isolated substorm distribution. This is plausible because the SOPHIE definition of an isolated substorm is most similar to the classic three-phase description of the substorm and is

stricter than that of the compound substorm (i.e. an isolated substorm onset requires a preceding growth phase, whereas each compound substorm onset does not).

In summary, we hypothesise that the isolated substorm distribution in Figure 5.2 is a weighted sum of the MLT distribution of true substorms and the MLT distribution of some misidentified enhanced convection events. In the next section, we attempt to separate out the true substorm distribution.

5.3 Results

5.3.1 Decomposition of MLT distributions

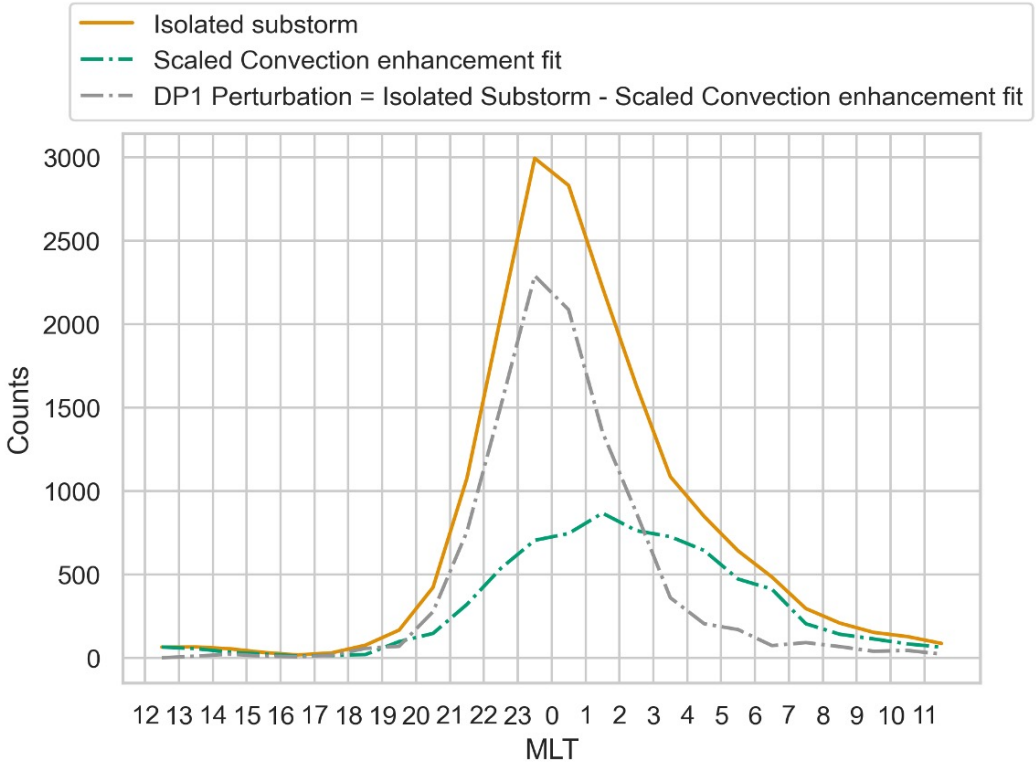

Figure 5.3: The Onset MLT histogram of the isolated substorms (Orange), the Scaled Convection enhancement distribution (Dashed-Dot Green) and the residual distribution when subtracting the Scaled Convection enhancements from the isolated substorms (Dashed-Dot Grey).

As noted above, the probability distribution of the MLT of isolated substorm onsets identified by the SOPHIE EPT 90 method shares some similarities with the probability distribution of the MLT of auroral onsets from Frey et al. (2004) and some similarities with the probability distribution of the MLT of enhanced convection onsets from SOPHIE. We thus postulate that the SOPHIE method has misidentified some enhanced convection events as isolated substorms and thus the histogram of the MLT of SOPHIE isolated substorm onsets is a combination of the histograms of the MLT of true DP1 substorm onsets and DP2 convection enhancements.

We seek to isolate the DP1 histogram by estimating the DP2 histogram and

removing it from the SOPHIE isolated substorm histogram. To estimate the DP2 histogram, we rescale the histogram of the MLT of SOPHIE convection enhancements by multiplying the corresponding probability distribution shown in Figure 5.2 by increasing integer values until the number of convection enhancements in any bin exceeds the number of isolated substorm events from SOPHIE in that bin. The estimated DP2 histogram is shown by the dashed-dot green line in Figure 5.3 and the SOPHIE isolated substorm histogram is shown by the solid gold line. The rescaling assumes that there exists some MLT where DP2 enhancements exclusively occur and no DP1 substorm onsets occur. We then subtract the estimated DP2 histogram from the SOPHIE isolated substorm histogram to yield the estimated histogram of the MLT of true DP1 substorm onsets, shown by the dashed-dotted grey line. It is lacking the post-midnight MLT "bump" and has a shape similar to the Frey et al. (2004) onset distribution but shifted eastward.

5.3.2 Interpretation of the decomposition results

Figure 5.4 (c) shows the resulting probability distributions of the DP1 and DP2 enhancements, with the DP1 distribution transformed into a PDF using the same method of dividing each bin by the total number of events. Additionally, the MLT probability distribution of the Frey et al. (2004) auroral onsets is also plotted. Shown in Figure 5.4 (a) and (b) are the Shore et al. (2018) empirical orthogonal function (EOF) representations of the DP1 and DP2 equivalent current patterns from a reanalysis of the Northern Hemisphere surface external and internal magnetic field during Solar Cycle 23. In these subplots, increasingly red (blue) indicates a larger southward (northward) magnetic deflection observed on the ground due to the DP1 and DP2 current patterns. Below the Onset MLT probability distributions (Figure 5.4 (d)), are the spatial amplitude profiles from auroral latitudes ($65^\circ - 75^\circ$ MLat) of the DP1 pattern and DP2 pattern of Shore et al. (2018), where greater than zero indicates the contribution to a southward magnetic deflection and less than zero indicates the contribution to a northward magnetic deflection; the concentric rings on Figure 5.4 (a) and (b) indicate the latitudes from which we derived the profiles. The spatial amplitude profiles seen in Figure 5.4 (d) are the mean of the latitudinal

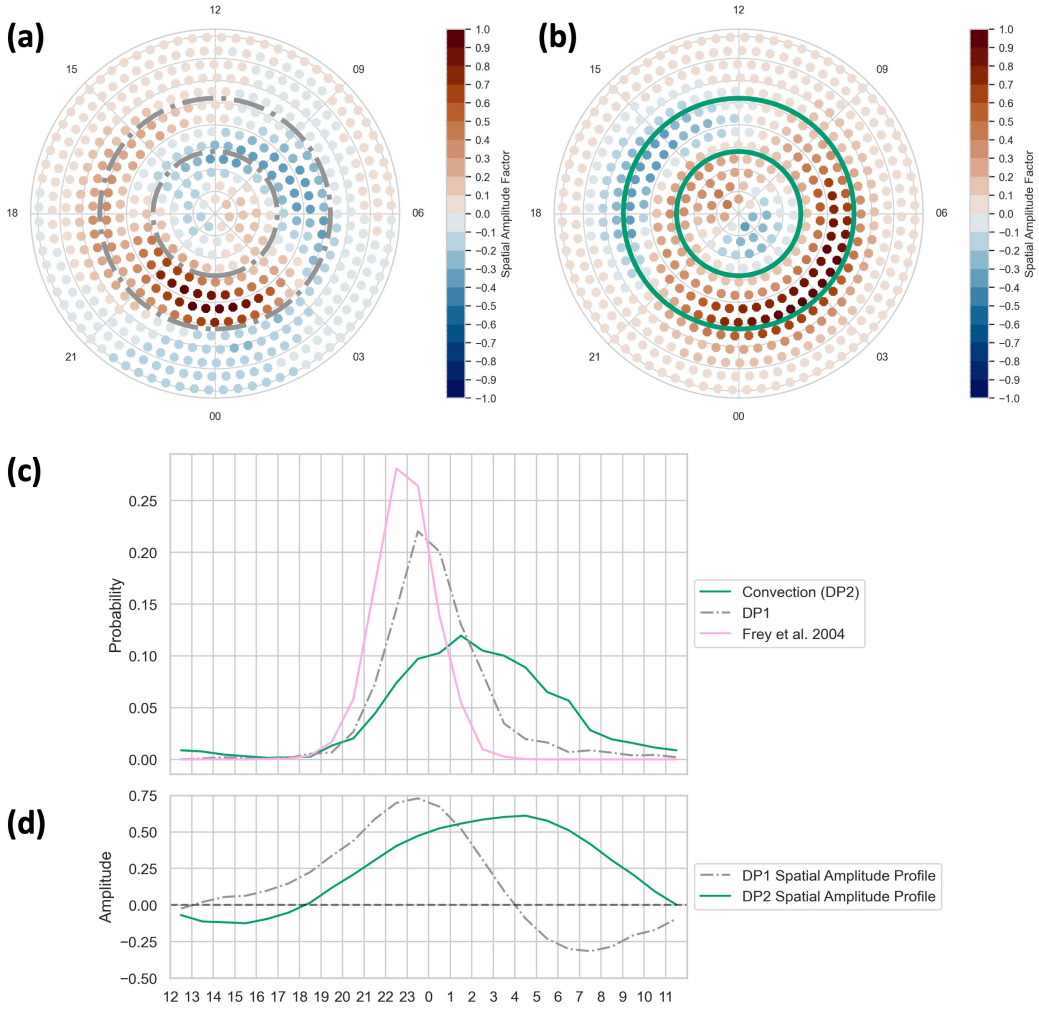

Figure 5.4: The DP1 (a) and DP2 (b) spatial patterns obtained by Shore et al. (2018), in these figures, the darker colour indicates a greater amplitude of the deviation to the north-south component of the ground magnetic field, with red indicating a southward deviation and blue northward. Subplot (c) shows the Onset MLT distributions obtained from the analysis of the SOPHIE method in this study. In addition to the obtained DP1 (Dashed-Dot Grey) and DP2 (Solid Green) perturbation distributions, the Frey et al. (2004) auroral substorm Onset MLT distribution is also plotted in pink. Subplot (d) shows the mean amplitude of the DP1 (Dashed-Dot Grey) and DP2 (Solid Green) patterns at auroral latitudes by MLT, these profiles were obtained by taking longitudinal cuts of the Shore et al. (2018) spatial patterns.

profiles between the two rings in Figure 5.4 (a) and (b). The spatial resolution of the Shore et al. (2018) profiles increases as the latitude decreases, i.e. there are more dots in each concentric ring that go away from the centre; therefore, each latitudinal profile between $65° - 75°$ MLat was resampled to a 1 MLT resolution grid centred

on the half-hours of each MLT before taking the mean.

Figures 5.4 (c-d) show that the extent of the probability distributions for the location of the DP1 and DP2 events is in good agreement with the extent of the southward deflections of the DP1 and DP2 Spatial Amplitude profiles across the auroral latitudes. This result validates the decomposition of SML-bay events into DP1 and DP2 contributions, since the bulk of each event distribution lines up with the region of maximal southward magnetic deflection (that sampled by the SML index) from each spatial pattern. The DP1 Spatial Amplitude profile differs from the DP1 perturbation probability of occurrence on their duskward edge, with a non-zero contribution to southward magnetic deflections from the DP1 patterns still observable around $\sim$ 18MLT. However, since these are spatial profiles of north-south magnetic deflections, we do not expect a one-to-one correspondence to probabilities of event occurrence.

The probability distribution of the DP1 perturbation is more akin to the auroral onsets than the isolated substorms originally identified, sharply peaking before midnight (0.28 at 22 - 23 MLT for Frey et al. (2004) and 0.22 at 23 - 00 MLT for the resolved DP1 perturbations) and rapidly dropping to zero in the afternoon and morning MLTs. We note that there is an offset of 1 hour MLT east for the DP1 probability distribution compared to the Frey et al. (2004) distribution. This is likely due to the auroral signature originating near the westward edge of the Substorm Current Wedge, where the downward-propagating electrons provide the upward field-aligned current, whereas the SML signature originates from a horizontal current connecting the eastward and westward legs of the substorm current wedge. It should be noted that the probability distribution of the onset MLTs and the positive amplitudes of the Spatial Amplitude profiles of the DP1 and DP2 events overlap in the midnight sector. As such, magnetic deflections in this region could be due to enhancements related to either current pattern, complicating the identification of substorms.

5.3.3 Decomposition of other SOPHIE EPT 90 event types

As mentioned in Section 5.2.1, in addition to isolated substorms and enhanced convection events, the SOPHIE method also identifies compound substorms whose onset need not be preceded by a growth phase. Furthermore, as SOPHIE identifies the timing of the recovery phases nonparametrically, similarly to how it identifies expansion phases, and does not enforce that an expansion phase is directly followed by a recovery, other event types are also possible. One of these event types occurs in an order where an identified expansion has no counterpart recovery but instead proceeds immediately into a growth phase, following a Growth-Expansion-Growth regime. Furthermore, recovery phases may be placed before an expansion phase following an isolated substorm regime, following a Growth-Recovery-Expansion-Recovery-Growth order. These events, which we have labelled "Other substorms", account for 3061 additional events between January 1997 and December 2019 (0.09% of all SOPHIE EPT 90 events), or an additional ≈ 130 events per year. The occurrence of these events shows a similar trend to the Solar Cycle (not shown), but their occurrence is not explored in this thesis. Furthermore, SOPHIE-identified substorms may occur recurrently after a SOPHIE-identified convection enhancement similar to the compound example shown in Figure 5.1, where the first expansion phase and associated recovery are instead a convection enhancement and the second event an identified substorm expansion and recovery. We have labelled any expansion phase events occurring directly after a convection enhancement without an intervening growth phase as an "After Convection" substorm. Note that a convection enhancement may occur during a set of compound events, thus splitting the series into two, with the events of the first part labelled as compound substorms and the events after the convection enhancement labelled as After Convection substorm. There are 886 events classified as After Convection Onsets between January 1997 and December 2019 (0.03% of all SOPHIE EPT 90 events).

Using the decomposed MLT probability distributions of DP1 and DP2 determined from above to fit the onset MLT histograms, it is possible to evaluate the contribution of DP1 and DP2 to the different types of events that populate the

SOPHIE EPT 90 phase list. The results of the fitting are shown in Figure 5.5, where we have fit the four different SOPHIE substorm types (isolated substorms (a), compound substorms (b), after convection substorms (c) and other substorms (d)). The fitting was completed by using a linear combination of the DP1 and DP2 probability distribution functions, scaled so that the sum of their scaling must equal the number of events of the fitted SOPHIE event type. For example, when fitting the compound substorms, the combinations that were evaluated were $0 \times pdf(DP1) + 8736 \times pdf(DP2)$, $1 \times pdf(DP1) + 8735 \times pdf(DP2)$, $2 \times pdf(DP1) + 8734 \times pdf(DP2)$, ... , $8736 \times pdf(DP1) + 0 \times pdf(DP2)$. The quality of the fits was evaluated by calculating a goodness-of-fit value for each fit carried out, with the parameter used in this study being the chi-squared value given by

$$\chi^2 = \sum_i^N \frac{\left[y_i^{\text{meas}} - y_i^{\text{model}}(\mathbf{v})\right]^2}{\varepsilon_i^2}$$

where y_i^{meas} is the count observed in each MLT of the original distribution, y_i^{model} is the count evaluated in each MLT bin of the fitted distribution, and ε_i is the estimated uncertainty in the data. In the study conducted, we take ε_i as the standard error of the count in each MLT bin, i.e. it is the square root of the count based on Poisson counting statistics. The combination that had the lowest chi-squared value was selected as the best fit, in the case of the compound substorms, this was the linear combination $1689 \times pdf(DP1) + 7047 \times pdf(DP2)$, which had a chi-squared of 37.

The reconstruction of the distribution for each type of event is shown as a cyan dashed line in each subplot, and with the chi-squared goodness-of-fit value for the reconstruction in the legend of each subplot. There is no desired threshold for this value; however, the "best fit" by the linear combination of DP1 and DP2 probability distributions for each SOPHIE event reconstruction was selected by minimising the chi-squared goodness-of-fit. The distribution that is best fit by a combination of the DP1 and DP2 distributions is the isolated substorms, with a chi-squared goodness-of-fit value of 0.003. However, this is to be expected, as this is the distribution from

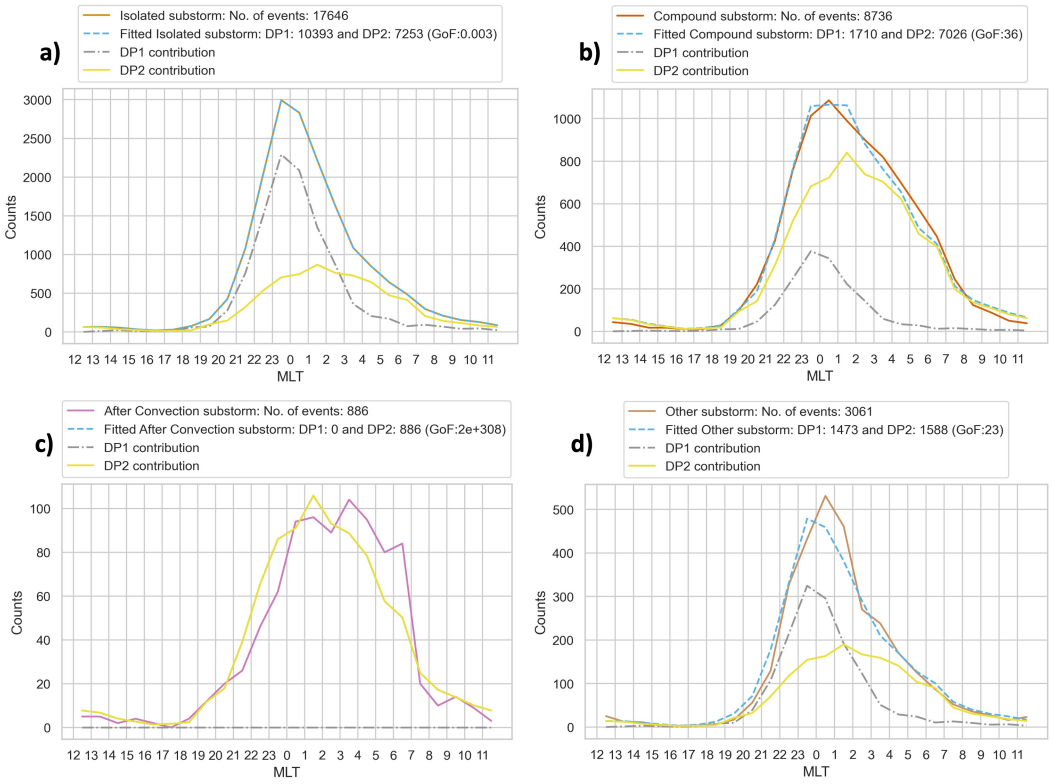

Figure 5.5: The reconstruction of MLT distributions of the full spectrum of SOPHIE event types using the obtained DP1 and DP2 MLT distributions from Figure 5.3. (a) Reconstruction of the isolated substorms, (b) the reconstruction of compound substorms, (c) the reconstruction of substorm expansion phases that directly follow on from a convection enhancement and (d) the reconstruction of substorms that do not fit into the other categories. Note that in panel (c), the line of the fit is obscured by the line of DP2 contribution, as only DP2 contributes towards the best fit.

which we decomposed the DP1 events. The worst fit is to the Onset MLT distribution of After Convection onsets with a chi-squared goodness-of-fit value orders of magnitude larger than the other distributions being fitted and for which the peak at 4 MLT is not reproduced. The anomalously large goodness-of-fit value stems from a zero count for one of the After Convection MLT bins, when ignoring this single bin, the goodness-of-fit value evaluated is ≈ 17, the same order of magnitude as the other fits.

As a result of the fitting, we can distinguish the number of events due to DP1 or DP2 for each SOPHIE event type. For example, of the 17646 isolated substorm events, between January 1997 and December 2019, 10393 were identified due to

enhancements of the DP1 current pattern, and the remaining 7253 due to an enhancement of DP2. Taking the sum of all event types and the DP1 and DP2 current pattern contributions to these, including those originally identified as convection events, we find 32956 westward electrojet enhancement events between January 1997 and December 2019 ($\approx$ 1430 events per year). SOPHIE originally categorised these into 30329 substorms (92% of events) and 2627 convection enhancements (8% of events). With our decomposition, we find that 41% or, 13427 events are due to enhancements of the DP1 current pattern ($\approx$ 590 events per year) and 59% or 19529 are due to enhancements of DP2 ($\approx$ 840 events per year). In comparison, Frey et al. (2004) identified 2437 substorms from observations of the aurora between 18 May 2000 and 31 December 2002, equivalent to $\approx$ 950 substorms per year.

5.3.4 Sensitivity of the decomposition to the detection threshold for convection enhancement events

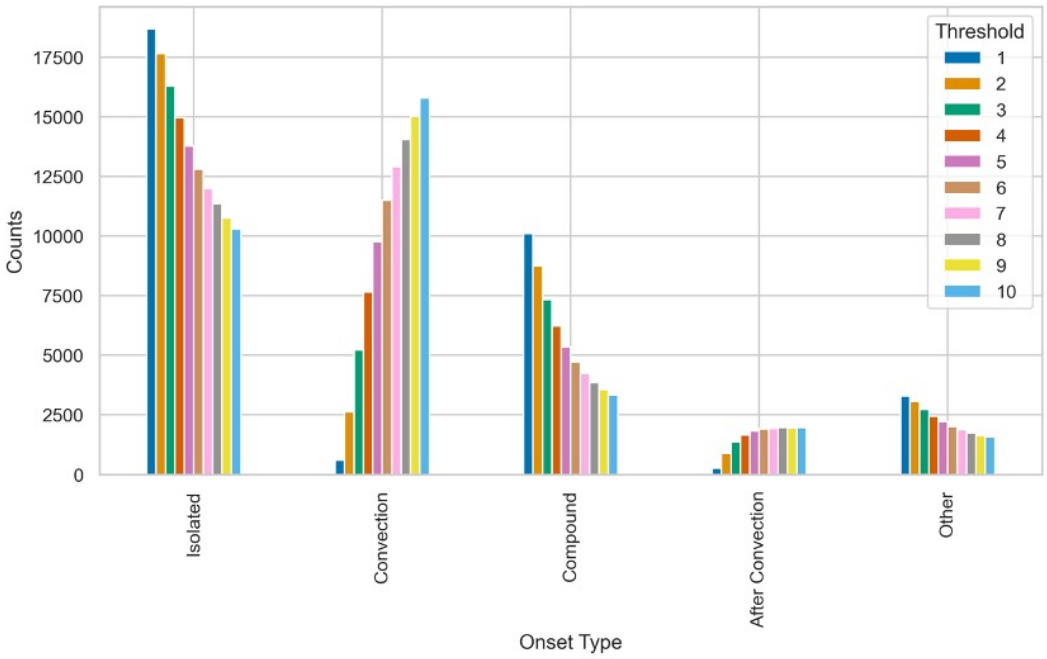

Figure 5.6: Event numbers identified by the SOPHIE method as the threshold value for identifying convection enhancements is modified. A value of 2 means that for a given event, the absolute rate of decrease in SML has to be more than twice that of the rate of increase in SMU to be classed as a substorm rather than a convection enhancement. Previously published SOPHIE lists have used a threshold of 2.

As discussed in Section 3.1.2.1 above, both the original SOPHIE technique and the amended technique used here employ an author-set threshold to decide which SML bays are due to enhanced convection rather than substorm expansion. Currently, this threshold has a value of two based on expert judgement, as discussed above in Section 3.1.2.1, but now we examine the sensitivity of substorm and convection enhancement identification to this value.

Figure 5.6 shows the breakdown of SOPHIE event types for integer values of the convection event threshold between unity and ten. We observe that 32956 SML bay events are identified between January 1997 and December 2019, invariant of the convection event threshold used. The division of these 32956 events identified into the five types of events varies significantly as the threshold increases. Note that

Threshold 2 corresponds to the MLT distributions plotted in Figure 5.2, without the After Convection and Other substorms. As expected, more events are classified as convection enhancements than substorms as the convection event threshold increases, since the magnitude of the change in SML required for an event to be labelled as a substorm becomes greater. We observe that convection events make up less than 2% of the events when using a Threshold value of 1. This increases to 48% when using a Threshold value of 10. Similarly, the number of After Convection substorms increases as the convection event threshold is increased, although this number seemingly saturates at 6% of events at a Threshold of 7 and above. As the number of identified substorms decreases as the threshold increases, this does not happen homogeneously across isolated and compound substorms that reduce at different rates. Compared to their Threshold 1 value, isolated substorms have reduced by 45% when using a Threshold of 10, whereas compound substorms have reduced by 67%, an indication that compound events have a higher degree of DP2 contamination than isolated substorms.

Figure 5.7 shows the Onset MLT probability distributions for isolated substorms identified using different convection enhancement thresholds. We observe that these probability distributions continue to show additional events in the morning MLTs as the threshold for the convection enhancement classification increases, though there is a marginal increase in the peak at 23 - 00 MLT (≈ 0.01 difference between Thresholds 1 and 10). This implies that varying the convection enhancement threshold is insufficient to reduce the proportion of isolated substorms that arise from DP2 type activity.

The decomposition of events into contributions from DP1 and DP2 described above in Section 5.3.1 was applied to the distributions of each threshold. This was completed using the isolated substorm and convection enhancement MLT probability distributions evaluated for each threshold (not shown). Similarly to Section 5.3.1, the four substorm event types (isolated substorm, compound substorm, after convection substorm, and other substorm) were divided into their underlying DP1 and DP2 current pattern contributions. Figure 5.8 shows the split of the events

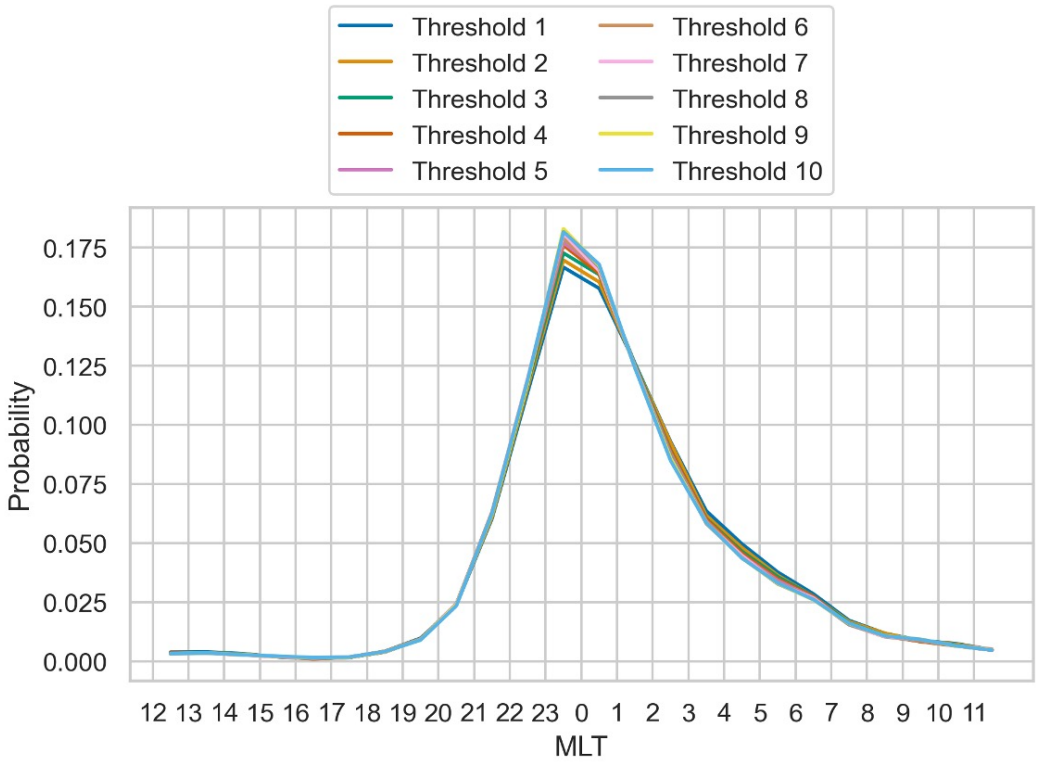

Figure 5.7: Isolated substorm probability distribution for various convection event filtering thresholds used.

identified by the SOPHIE method into originally identified substorms and convection enhancements. We also show the relative contributions of DP1 and DP2 that result from the fitting described above reapplied to the subsets of substorm and convection events for each threshold. Note that previously published event lists derived from the SOPHIE method correspond to the SML/SMU Threshold of 2. As discussed above, we observe the trend of more events being classed as convection enhancements rather than substorms as the threshold value increases. Additionally, as the threshold increases, more events are classified as DP2 rather than DP1.

We observe that the number of SOPHIE identified substorms and DP1 perturbations do not intersect or converge for any value of the convection enhancement threshold. The number of events due to enhancements of the DP1 equivalent pattern is always less than the number of SOPHIE identified substorms; as such, the contributions of DP1 and DP2 can always be decomposed from the MLT distribution of SOPHIE substorm events. This implies that SOPHIE identified substorms

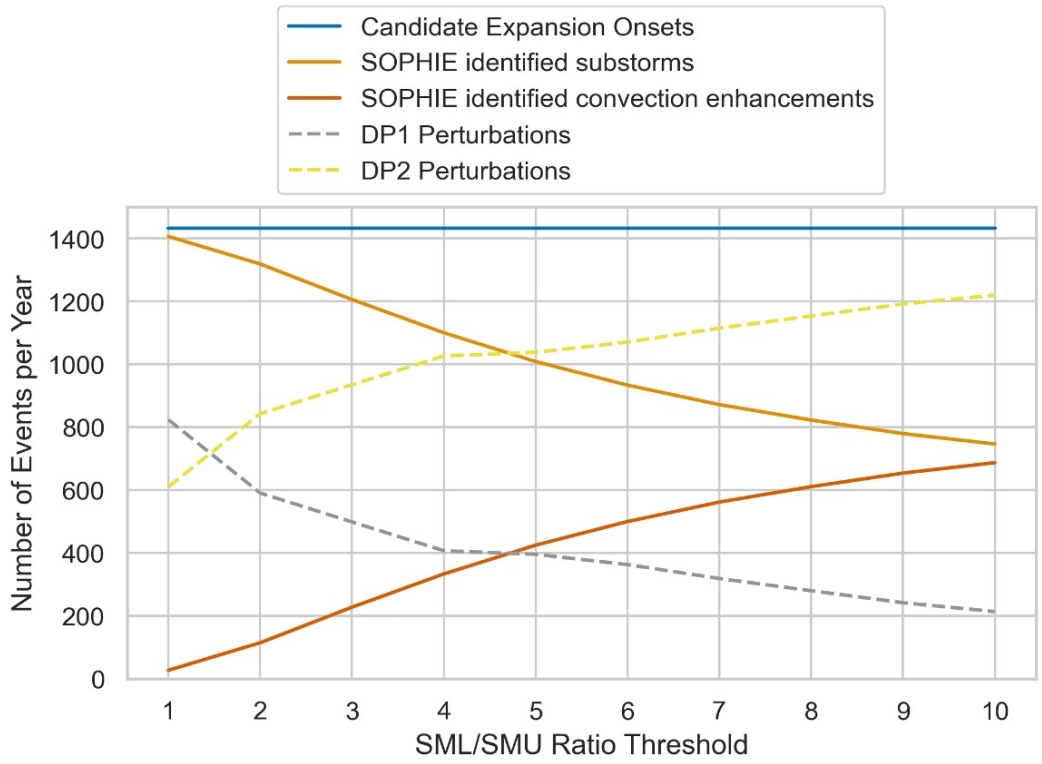

Figure 5.8: Numbers of substorms and convection enhancements originally identified by SOPHIE (Solid) and also their breakdown into DP1 or DP2 (Dashed) as a function of threshold used for convection enhancement filtering. Blue corresponds to the number of candidate expansion phases identified i.e. all periods which satisfy the SOPHIE EPT 90 condition of a decrease in SML that exceeds that 90th percentile of the yearly decrease in SML. Orange corresponds to the number that were identified as a substorm, red corresponds to the number of candidate events identified as a convection enhancement interval, dashed grey corresponds to the number of all candidate events that were due to the DP1 pattern, and dashed yellow corresponds to the number of all events that were due to the DP2 pattern.

are not solely due to enhancements of the DP1 current (or the closure of the Substorm Current Wedge through the ionosphere), regardless of the threshold value used. However, while there is some contamination of SOPHIE identified substorms by convection enhancement events, this contamination is likely greater for other methods that make no attempt to identify events with enhancements in SMU.

5.4 Discussion

In this study, we have examined the contribution of enhancements of the DP1 and DP2 current patterns to substorm-like SML bays by inspecting event MLT distributions as identified by the SOPHIE method (Forsyth et al., 2015). Our results indicate that there is a notable contribution to substorm-like SML bays due to enhancements of the DP2 current pattern. Moreover, as SOPHIE is only one of many techniques applied to the AL/SML index for substorm identification, albeit one that attempts to filter by leveraging the SMU index also, any method using these indices will be populated with "DP2 events".

To decompose the contribution of the DP1 pattern to SOPHIE identified substorms, we have assumed that SOPHIE convection enhancement events are a good proxy for enhancements of only the DP2 equivalent current pattern. The enhancement of the westward electrojet related to the DP2 pattern is largely expected to occur at morning MLTs; however, the work of Shore et al. (2018) shows that the enhancement of the westward electrojet due to DP2 can also occur in the midnight MLT sector. In agreement with this, Figure 5.3 shows that both the DP1 and DP2 events have non-zero probabilities of occurrence at night-side MLTs, with the extent of the SOPHIE convection events (green line of Fig 5.4c) matching the extent of the spatial amplitude profile of DP2 resolved by Shore et al. (2018) at auroral latitudes. Moreover, SOPHIE makes use of the SMU index sampling the eastward electrojet to identify convection enhancements and, as it is unlikely for the formation and closure of the SCW to produce an enhancement of current in an eastward direction, we can be confident that the convection enhancements are due to enhancements of DP2 only and are minimally "contaminated" DP1-type events.

We have also assumed that substorms would primarily cause magnetic perturbations consistent with those of equivalent currents of the DP1 current pattern, with the formation of the substorm current wedge that closes through the ionosphere driving the enhancement of the westward electrojet (McPherron et al., 1973). This assumption is evidenced by the similarity of the decomposed DP1 distribution to that of auroral substorm onsets, as identified by Frey et al. (2004) and the extent

of this distribution that matches the extent of the spatial profile of the Shore et al. (2018) DP1 pattern from auroral latitudes. The work of Shore et al. (2018) found that this pattern showed a sharp increase in amplitude at the onset of the substorm, was poorly correlated with the IMF B_z and was never the dominant spatial mode contributing to ground magnetic field variance over a whole month during Solar Cycle 23 consistent with the interpretation of the substorm being a loading-unloading phenomenon of the magnetosphere.

There is a systematic shift between the observed MLT distributions, with the auroral onsets peaking 1 MLT westward of the SML identified onsets. This is consistent with the aurora being colocated with the upward FAC of the SCW, with the current carried by downward travelling electrons, while the peak southward ground magnetic perturbation is due to the westward flowing ionospheric current. Recent studies have indicated that the onset of auroral beads, one of the first auroral signatures of substorms (Kalmoni et al., 2017; Nishimura et al., 2016), coincides with ULF magnetic pulsations on the ground (Rae et al., 2012; Smith et al., 2020). However, these pulsations appear to be distinct from the large-scale perturbations that result in negative bays in AL/SML.

As we would expect the enhancement of the eastward electrojet to be correlated with that of the westward electrojet during periods of enhanced convection and uncorrelated during a substorm expansion, we explored the capability of the using SMU index within the SOPHIE method to distinguish between non-substorm and substorm-related changes in SML. In Section 5.3.4, we tested various thresholds to filter out convection enhancements from substorms. Figure 5.8 indicates that regardless of the value of the threshold used to classify convection enhancement intervals or DP2 events, the number of identified substorms and DP1 events do not converge, which means that there is still a contribution of the DP2 pattern regardless of the selected threshold. This has two significant implications: 1) even when leveraging SMU/AU, the auroral indices alone are unable to distinguish the substorm from other magnetospheric phenomena; 2) the substorm can produce enhancements of the westward electrojet, at MLTs much different from the expected

location of DP1. This could be due to localised conductivity enhancements in the ionosphere, either from the propagation of precipitated particles superposing with solar illumination (particularly during the Northern Hemisphere summer) or increased precipitation at these locations, further complicating the identification of true positive substorm events.

Isolated substorm studies using the Polar Ionospheric X-ray Imaging Experiment (PIXIE) by Østgaard et al. (1999) observed that the precipitation of the high-energy electrons that cause the X-ray aurora has a localised maximum towards morning magnetic local times (5 - 9 MLT). The authors noted that this localised maximum was delayed in response to the onset of the substorm, with the physical interpretation that these precipitating electrons have drifted from the injection region in the midnight sector before being scattered into the loss cone in the dawn sector. This precipitation will lead to an increased conductivity in the ionosphere, and as the westward convection electrojet is already colocated at morning MLTs, one can imagine a situation where the current flowing is increased and as a result producing a magnetic signature similar to the substorm negative bay in SML at a location unusual for a true positive identification from ground magnetometer data. However, since the precipitation was due to the substorm process, it would be misleading not to identify such an event as a substorm, although the enhancement of SML was not due to the closure of the substorm current wedge via the ionosphere. This resultant signature would be dependent on the timing and rate of ionisation, and as such there is more to be explored between the relationship of the substorm X-ray aurora and ground magnetic perturbations.

Since it is possible to identify convection enhancements as shown here and in previous work (Shore et al., 2017, 2018) at MLTs where we expect substorms, they cannot simply be filtered out by using the MLT location of the contributing station to SML. Therefore, lists using the SML index alone (Newell and Gjerloev, 2011; Borovsky and Yakymenko, 2017; Ohtani and Gjerloev, 2020) will be populated with false positives, events identified as substorms, but the enhancement in SML is due to convection enhancements or other magnetospheric phenomena. Figure 5.9 shows

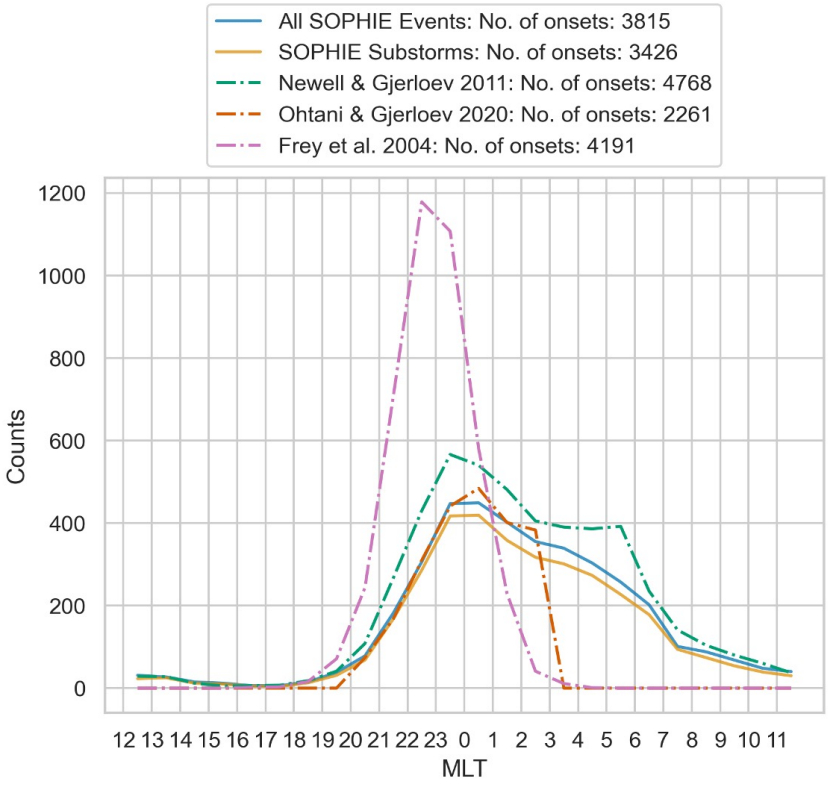

Figure 5.9: Onset MLT distributions from various event lists. SOPHIE (All Events in Blue, substorms in Orange) Newell and Gjerloev (2011) (Green Dashed-Dot) and Ohtani and Gjerloev (2020) (Orange Dashed-Dot) events were from 1997 - 2020, while Frey et al. (2004) (Pink Dashed-Dot) were from 19th May 2000 to 31st December 2002.

the onset MLT distributions from the Frey et al. (2004), Newell and Gjerloev (2011), Ohtani and Gjerloev (2020) and SOPHIE (All events and Only Substorms) from the interval 19 May 2000 and 31 December 2002. In Figure 5.9, we observe that the MLT distributions of the SML identified events are more similar to each other than to the Frey et al. (2004) MLT distribution. This is in part due to the Frey et al. (2004) events being identified from auroral images, therefore unlikely to be contaminated with DP2 events which do not have the accompanying auroral features that a "true" substorm does. It should also be noted that the MLT distribution of substorm-related Pi2 pulsations (Yeoman et al., 1994) is more similar to that of auroral onsets and our decomposed DP1 distribution, being symmetric and centred on midnight MLT.

As we have shown above that SOPHIE is contaminated with DP2 events and that these can occur within the MLT window of Ohtani and Gjerloev (2020), there-

fore it is probable that these onset lists are also contaminated with DP2 events. This issue is one possible source of ambiguity in conducting statistical substorm studies, as the dynamics of other magnetospheric phenomena could be included in with "true" substorms, particularly when relating localised effects throughout the magnetosphere with respect to the substorm. As such, despite considerable progress being made in understanding the characteristic features and consequent effects of the substorm, some conclusions from studies using substorm lists built from magnetic indices may be incomplete as these studies may be considering non-substorm intervals, including other phenomena that are capable of enhancing the electrojets. This ranges from the importance of the phenomenon in the energization and variability of the ring current (Sandhu et al., 2019) and the radiation belts (Forsyth et al., 2016; Rodger et al., 2022a) to its influence on ground-induced currents (Freeman et al., 2019).

One possible route to improve our confidence in identifying substorm intervals could be the use of additional datasets to supplement the auroral indices. One such way of achieving this is by including the behaviour of the driver, i.e. the solar wind, when identifying substorms. Previous studies have indicated that substorms typically occur after the solar wind has been southward for 22 of the preceding 30 minutes (Morley and Freeman, 2007). Moreover, the work of Shore et al. (2018) showed that the amplitude of the DP2 pattern is much better correlated with shorter time responses to the IMF than the DP1 pattern. However, taking this approach may have the effect of increasing the number of missed substorm identifications from auroral indices, due to the underlying assumption that substorms cannot occur during strong steady driving.

Another approach integrating other data sets than just the auroral indices was taken by Milan et al. (2021), where they distinguish the AL enhancements due to the substorm from other magnetospheric phenomena by applying the Expanding and Contracting Polar Cap (ECPC) paradigm (Siscoe and Huang, 1985; Lockwood et al., 1990; Cowley and Lockwood, 1992) to event identification. They made use of proxies for the dayside reconnection rate, cross-polar cap potential, as well

as the auroral indices to identify the magnetospheric convection state in the year 2010, evaluating between periods of quiet, substorm interval (including the separate phases) and directly driven periods. This approach led to the finding a rate of occurrence of substorms of approximately 550 events per year, lower than that found by Borovsky et al. (1993) or Frey et al. (2004) from injections and auroral intensifications, which identified approximately 1500 events per year. For reference, during the period analysed, SOPHIE identified $\approx$ 1430 SML enhancement events per year, of which $\approx$ 1320 per year were initially identified as substorms; however, our reanalysis showed that only $\approx$ 590 of these per year were due to enhancements of the DP1 pattern, similar to the number identified by (Milan et al., 2021). In the same period, Newell and Gjerloev (2011) identify $\approx$ 1700 substorms per year and Ohtani and Gjerloev (2020) identify $\approx$ 950 isolated substorms per year using the SML index, still many more than the proposed number of DP1 events from our reanalysis.

There is also the approach taken by Haiducek et al. (2020) to integrate multiple datasets. In this case, they combined multiple already existing substorm lists, based on the AL index, MPB index (Chu et al., 2015), auroral images and particle injections, to more robustly identify events for the month of January 2005. They achieved this by convolving each onset list with Gaussian kernels, i.e. they turned an onset time (a unit impulse in time) into a Gaussian onset window centred at the onset time. A substorm onset period was then identified as when a combination of different signatures identified at approximately the same time. This was integrated in the Haiducek et al. (2020) method in a way such that a threshold value was required to be surpassed for a substorm to be identified, but the height of the peak of the Gaussian window from a single signature would not break this threshold. As such, this method requires overlap of multiple detection signatures to indicate a substorm. A full mathematical of the convolution and combination is available in the full text (Haiducek et al., 2020), where they also compare against an MHD model's ability to reproduce substorm characteristics. Although a promising pathway for robust identification, a major limitation of this route is the lack of a common

description of the substorm by the community or a set of "true" substorms to compare against and tune the parameters for the threshold and kernel width. We also note that the level of co-occurrence of onsets identified from MPB, AL, particle injections and auroral enhancements within 30 minutes between different substorm signatures is remarkably low, with less than a 50% overlap between pairs of lists based on these identifiers (Lao et al., 2024).

This study highlights some important considerations when conducting studies of substorms. Firstly, it indicates the importance of the separation of AL/SML bays that are due to the substorm and other magnetospheric phenomena. Currently, only SOPHIE (Forsyth et al., 2015) and Milan et al. (2021) attempt to do this by comparing the AL/SML bay with another feature. Ohtani and Gjerloev (2020) makes an attempt at this by limiting identifications to within 23 - 03 MLT, but our results show there are still a large number of DP2 driven magnetic bays in this local time sector. However, leveraging the SMU index, as the SOPHIE method does, is inadequate to completely isolate the DP1 and DP2 modes of magnetospheric response. Auroral indices are a simplification of a diverse set of observations related to a multitude of processes across multiple scales. This simplification may discard critical data that means that auroral indices do not have enough information to be used to robustly identify substorms. Highlighted above are some possible pathways that could result in a more robust substorm identification schema by including multiple datasets. However, while a promising idea, this is not simple as one must account for the differences in data cadences, coverage, and the time interval covered by the different datasets being used. Moreover, we showed in Chapter 4 that in the period when there were the auroral indices, midlatitude indices, auroral imagery, and geosynchronous particle observations available, for a given substorm there is a less than 50% chance that two or more methods will identify it as one (Lao et al., 2024). Our study also highlights that caution must be observed when identifying substorms in the dawn sector. Although it is more likely for these events to be DP2 related, it is possible that "true substorms" are detected in this region, highlighting the limitations of a blunt approach such as the one by Ohtani and Gjerloev (2020).

When conducting case studies of events identified in this region, we recommend the verification of a true substorm occurrence using another indicator.

Lists of "substorms" are inherently useful in solar terrestrial physics, providing a common baseline for both case and statistical studies of a variety of processes that are part of or result from the phenomena associated with substorms. However, all of these lists have their limitations. Firstly, there is no quantifiable consensus within the solar terrestrial physics community as to what a substorm is, but rather a set of qualitative descriptions of substorm effects, such as the rapid closure of open flux in the magnetotail, brightening and westward expansion of the auroral, injections of energetic particles at geosynchronous orbit, and the formation of magnetic bays at high and midlatitudes. These effects are not necessarily unique to substorms and may arise from other activity, such as pseudobreakups and steady magnetospheric convection events, and thus may appear in substorm identification lists. SOPHIE attempts to mitigate one of these effects (enhanced magnetospheric convection) and does remove a large number of potential substorms by comparing SML and SMU, but our work shows that this is not perfect. However, we would contend that it provides a better mitigation than limiting identifications to a set of MLT sectors, given the large overlap between the MLT distributions of DP1 and DP2 driven effects. In truth, any list of "substorms" is, in fact, a list of magnetic enhancements, auroral enhancements, particle enhancements, etc. which may or may not align with substorm activity and should, ultimately, be treated in that way.

5.5 Summary

In this study, we have used the SOPHIE method (Forsyth et al., 2015) to quantify the respective contributions of the DP1 and DP2 current patterns to the formation of substorm-like SML bays. This was achieved by evaluating and manipulating the onset MLT, defined as the location of the station that contributes to SML at onset, of various classes of events identified in the SOPHIE phase list. Using the onset MLT distribution of convection enhancements identified by SOPHIE as an indicator of the DP2 event distribution, we were able to decompose a contribution from both DP1 and DP2 to the onset MLT distribution of isolated substorms. We find that although the SOPHIE method attempts to filter out convection enhancements, 59% of the events originally identified as substorms are instead due to enhancements of the DP2 current pattern, rather than DP1 which is associated with the ionospheric leg of the Substorm Current Wedge. Finally, we explored different values for the threshold used to distinguish between convection enhancements and "true" substorm events, and found that no value can distinguish convection events entirely.

We come to the conclusion that the auroral indices, even when filtering events by magnetic local time, are unable to provide sufficient information to robustly identify substorms from enhancements of magnetospheric convection. There is still an invaluable use case for substorm lists using auroral indices in finding events for case studies, which can then be verified as true substorms via other substorm signatures, e.g., particle injections, auroral enhancements. However, caution must be exercised when conducting statistical studies related to the substorm phenomena when using these lists, as the effects of other magnetospheric modes and phenomena are not entirely removed.

Chapter 6

Case studies of typical and atypical substorms and magnetospheric convection enhancements

6.1 Introduction

In Chapter 5, using the convection enhancement events identified by the SOPHIE method (Forsyth et al., 2015) as a proxy for the DP2 events, we showed that the substorms identified by SOPHIE are composed of DP2 events (non-substorms) and DP1 events (substorms) (Nishida and Kokubun, 1971; Kamide and Kokubun, 1996). Using the expansion phase threshold (EPT) 90 version of SOPHIE, we found that up to 59% of substorms are possibly misidentified DP2 events. We showed that while it was possible to statistically decompose these two event types using their onset locations, additional information to the auroral indices is required to remove the false DP2 identifications on a case by case basis. SOPHIE is the only method that attempts to filter out falsely identified substorms, by integrating information from the SMU index, hence, all other substorm identification methods based on the SML index are likely to be equally or even greater filled with false substorm events, contributing to the low association observed between SML-based identification methods and other proxies of the substorm in Chapter 4. In order to address these failings, it is informative to examine identified substorms on a case by case

basis in an effort to identify other signatures which may uniquely identify non-substorm events.

In this study, we present the observations of four events: two substorms, one which was identified in SML at the most typical location of pre-midnight magnetic local time (MLT) and one identified in SML at an atypical location of dawn MLT, and two convection enhancements, one at a typical location for a DP2 event at dawn MLT, and one whose location is more typical of a substorm in pre-midnight. The categorisation of in terms of the event location is based on where the ground magnetic signature was observed, rather than the location of any auroral brightening. We compare and contrast these events to evaluate whether there are any significant differences in the prior conditions that could lead to better filtering of the substorm events identified by SOPHIE and other SML-based algorithms. The solar wind and interplanetary magnetic field (IMF) observations during these events are presented, as well as the geomagnetic indices.

6.2 Data

The events analysed in this study were selected using SOPHIE (Section 3.1.2.1) for the identification of substorm and convection intervals using an expansion percentage threshold (EPT) of 90 and a convection enhancement ratio threshold of 2. Similar to Chapter 5, we consider only isolated substorms and convection enhancements (a single "expansion" and "recovery phase" preceded by a "growth phase"). We filter the events in SOPHIE for those occurring approximately at either the spring or autumn equinox to minimise any seasonal effect on our events. At these times, the terminator is approximately spanning across the 18 - 06 meridian so that our events have similar levels of solar conductance. In addition, we also filter for substorm and convection enhancements which occur between 01:00 UT to 05:00 UT so that the events analysed were identified with a similar SuperMAG network layout. An example period, without an event occurring, is shown in Figure 6.1[1]. This network layout was selected because it has North America in the dusk sector and Europe in

[1]This image was generated using the SuperMAG polar plotting tool at `https://supermag.jhuapl.edu/rBrowse/`.

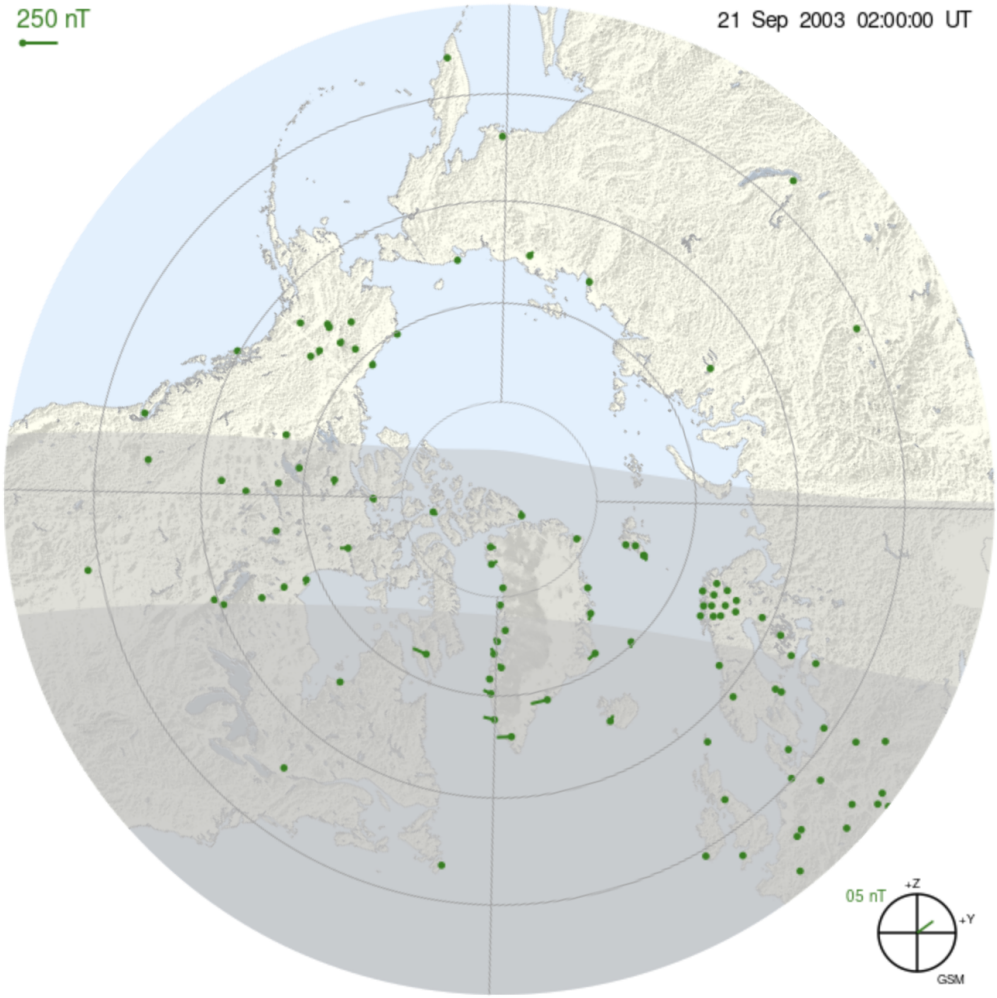

Figure 6.1: Example configuration of the SuperMAG network at 02:00 UT on 21 Sep 2003 that we filter our onset times for. Each concentric ring indicates 10° away from the Northern Magnetic Pole. Also shown are the solar terminators on the ground (spanning approximately at the 18 - 06 MLT meridian) and in the ionosphere (the terminator closer to magnetic midnight) indicating the portion of the Northern Hemisphere which is in darkness and which is sunlit. Each green dot is the location of SuperMAG data contributing station, with the tail emanating from each showing the magnetic deflection at that location rotated 90° clockwise. In this configuration, we have a high density of stations in the longitudinal direction in the dusk and dawn sectors at all latitudes, and a high density of stations in the midnight sector at high latitudes.

the dawn sector, maximising the number of stations and therefore coverage of the nightside auroral region.

We used solar wind plasma and interplanetary magnetic field measurements from the OMNI HRO dataset (King and Papitashvili, 2005) to evaluate the state

of magnetospheric driving during the intervals analysed. A brief description of the collection and preprocessing of this dataset is outlined in Section 3.4. During the intervals analysed, the data sources were the Wind and ACE spacecraft at L1-orbit. In addition to the raw measurements themselves, we also use the ε parameter derived by Perreault and Akasofu (1978) given by

$$\varepsilon = \frac{4\pi}{\mu_0} v_{sw} B^2 \sin^4 \frac{\theta}{2} \tag{6.1}$$

which has units of $\mathrm{W/m^2}$, to quantify the energy input from the solar wind to the magnetosphere. In this equation, all variables are in SI units, with v_{sw} the solar wind flow speed, B the magnitude of the solar wind magnetic field, θ the IMF clock angle given by $\theta = \arctan \frac{B_y}{B_z}$, with B_y and B_z the y and z components of the IMF in the GSM coordinate frame, and finally μ_0 is the permeability of free space. Various measures of solar wind driving of the magnetosphere, coupling functions, have been presented in the literature since the discovery of the solar wind and magnetosphere (Perreault and Akasofu, 1978; Kan and Lee, 1979; Newell et al., 2007; Lockwood and McWilliams, 2021), and their correlation with various geomagnetic indices studied. In this study, we choose the coupling function developed by Perreault and Akasofu (1978), but ultimately, we analyse the trends in energy addition to magnetosphere rather than the exact values of ε, so it is largely interchangeable with the other measures available. The mean value of the Perreault and Akasofu (1978) ε parameter (dashed black) between January 1997 and December 2019 is 7.33×10^{-5} $\mathrm{W/m^2}$.

To evaluate the geomagnetic response, we used four different magnetic indices: the PC index, the SMU and SML indices, and the MPB index, all outlined in Chapter 3. We also make use of SMU and SML subdivided by MLT. In this dataset, the 24 magnetic local time values of SML and SMU are derived using a 3-hour MLT window and are attainable because there is generally at least one station in each MLT sector in the SuperMAG collaboration of networks. Thus, at a given time, there are 24 SMU-LT and 24 SML-LT values. The 3-hour window is centred on the half-hour of the MLT sector for which the data are being recorded, for example,

SML12 is centred at 1230 MLT and uses the MLT window 1100 MLT to 1400 MLT (Newell and Gjerloev, 2014).

In addition to these datasets, for two of the events analysed, we also used IMAGE Burch (2000) observations of the aurora. Specifically, we used images taken by the WIC instrument Mende et al. (2000b) onboard IMAGE, the details of which are discussed in Section 3.2. For the remaining two events, these occurred beyond the primary mission phase of IMAGE when it was taking observations of the Northern Hemisphere, and therefore no observations were available to be analysed.

6.3 Observations

The substorms events studied are identified by the SOPHIE EPT 90 method at 04:30 UT on 12 August 2001 and 02:36 UT on 26 September 2000. Both of these events occur within the IMAGE primary mission phase timeframe. For the first substorm event presented, the contributing station at onset was in the midnight MLT sector, typically where we would expect a substorm to occur, as shown in Chapter 5, while for the second event, the contributing station to SML at the time of onset was in the dawn MLT sector, which is more typical for a convection enhancement.

The convection enhancements analysed in this study were identified by SOPHIE EPT90 at 01:35 UT on 14 April 2006 and 01:41 UT on 6 April 2004. The first of these events occurred outside the IMAGE primary mission phase timeframe, and therefore no FUV auroral observations were available, while for the second event FUV observations were not available as IMAGE was not located over either pole. For the first convection enhancement, the contributing station at onset was in the dawn sector, more typical of a convection enhancement event. For the second convection enhancement, the station that contributed to SML at the onset of the event was in the midnight sector, where predominantly substorms are observed.

6.3.1 Substorm in the midnight sector

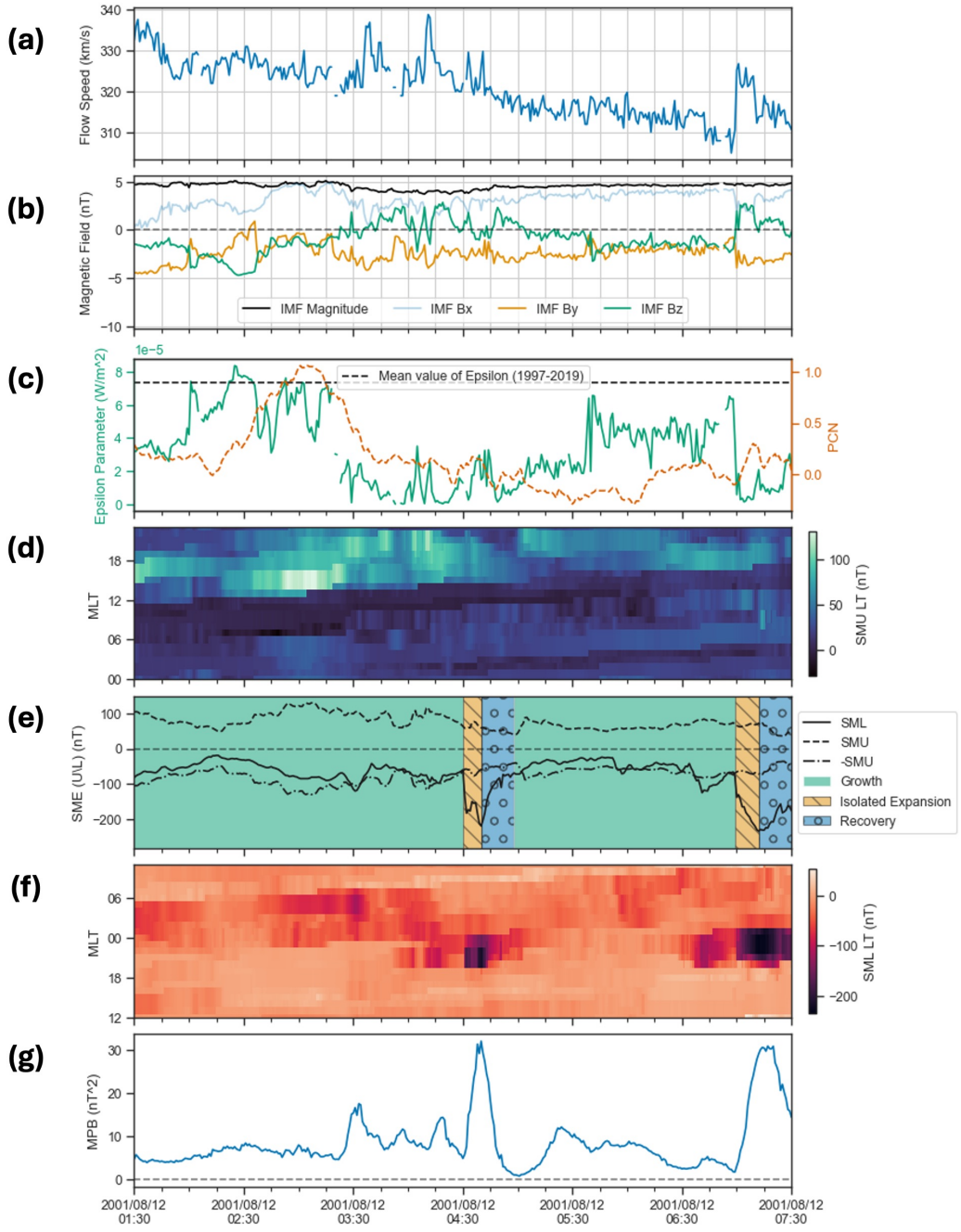

Figure 6.2: Solar wind and magnetometer observations for 6 hours around the substorm at 04:30 UT on 12 August 2001.

Figures 6.2 and 6.3 show the observations for the 6 hours surrounding the substorm that occurred at 04:30 UT on 12 August 2001. This substorm had its magnetic and auroral signature in the typical location of pre-midnight magnetic

local times, with the contributing station to SML at SOPHIE EPT 90 identified onset being at 23.57 MLT and an auroral onset identified by Frey et al. (2004) at 22.54 MLT. Substorm onsets from Frey et al. (2004); Chu et al. (2015) and Forsyth et al. (2015) all occurred within 2 minutes of each other, and thus the identification is consistent across these lists.

The top two panels (a and b) of Figure 6.2 show the solar wind and interplanetary magnetic field conditions around the time of this event, with panel a showing the solar wind flow speed in km/s, panel b showing the magnitude of the IMF in black and its X (light blue), Y (orange), and Z (green) components in the geocentric solar magnetic (GSM) coordinate frame. Panel c shows the Perreault and Akasofu (1978) ε parameter (green) in W/m^2, its mean value (dashed black) between January 1997 and December 2019 and the PCN index (red). The bottom 4 panels show the high-latitude and midlatitude magnetospheric response during the interval. Panels d and f show the SMU and SML indices by magnetic local time (SMU-LT and SML-LT), respectively. In these plots, a lighter (darker) colour indicates a higher (lower) value of SMU-LT (SML-LT). Panel e shows the SML (solid black) and SMU (dashed black) indices. Additionally, -SMU (SMU reflected across the x-axis) (dashed-dot black) is plotted. Panel e is colour coded by the SOPHIE identified phases of the substorm during the interval. Finally, panel g shows the magnitude of the MPB index (Chu et al., 2015) during the time interval analysed. In addition to our selected event, another isolated substorm is identified afterward our event, occurring at approximately 07:00 UT.

The period around the time of the selected substorm event is typified by slow solar wind, with the observed flow speeds below the 20th percentile of flow speeds observed between January 1997 and December 2019. The IMF magnitude of ≈ 5 nT during the analysed interval remains relatively constant and is typical of the period between January 1997 and December 2019 (the median value during this period being 5.12 nT).

The IMF distribution in the 3 components varies significantly throughout the period shown in Figure 6.7. At the beginning of the interval, the IMF is dominated

by a negative B_y component. At approximately 02:00 UT, there is a rotation in the IMF such that the dominant component is in the negative B_z direction. This rotation in the IMF also results in an increase in ε (panel c) from 4×10^{-5} W/m^2 to $\approx 7 \times 10^{-5}$ W/m^2. This rotation in the IMF continues until the IMF is almost perfectly southward at 02:15 UT, corresponding to the maximum of ε during this interval at $> 8 \times 10^{-5}$ W/m^2. The increased level of driving of the magnetosphere by the solar wind continues until 03:15 UT, when the north-south component of the IMF tends to zero or even northward, with the value of ε decreasing sharply from $\approx 7 \times 10^{-5}$ W/m^2 to below 3×10^{-5} W/m^2.

In terms of magnetospheric response, there is a 15-minute delay from the increase in ε to be observed in the PC index, possibly indicating the time for the IMF change to propagate through the magnetosphere and couple to the ionosphere. The PC index is observed to have reached a minimum of below 0 mV/m at 02:15 UT before increasing to above 1 mV/m at 02:50 UT, and this is maintained for approximately 15 - 20 minutes. This is indicative of an increase in magnetospheric convection as energy and flux are transferred to the magnetosphere during the period of southward IMF and dayside reconnection. The PC index then begins to reduce at 03:10 UT until it is back to its prior level at 03:45 UT. The increase in magnetospheric convection can also be inferred from the SML and SMU indices. Beginning at 02:15 UT, we observe the SMU and SML indices increasing in strength (higher absolute values for both indices); it is most obvious when observing that although their values are different, the SML and -SMU traces follow the same trend from 02:15 UT to 03:20 UT. The decrease in SML and increase in SMU, which are well-matched, are indicative of the strengthening of the Hall currents associated with the Disturbance Polar (DP) 2 pattern associated with magnetospheric convection. Another indicator of a DP2 type enhancement are the locations of the SML and SMU enhancements. Panel d shows that during this interval the most positive values of SMU-LT, and therefore the contributing stations to the SMU index are in the post-noon sector at 13 - 17 MLT, while panel f shows that the most negative values of SML-LT, and therefore the contributing stations to the SML index are in the dawn

sector at 03 - 07 MLT.

There is a small negative deviation of the SML index at 03:24 UT of the order of ~ 50 nT (-60 nT to -110 nT) that lasts 7 minutes from the beginning to the minima. It then takes 9 minutes to recover from this minima to above the previous level (-40 nT) at 03:41 UT. The gradient and length of the event were insufficient to trigger the SOPHIE method to identify it as either a substorm or a convection enhancement. However, at the same time, a pulse is observed in the MPB index, reaching a maximum of 20 nT at 03:32 UT before decreasing to the background level at 03:45 UT. Again, the size of the event was insufficient for it to be identified as a substorm by the Chu et al. (2015) method, which requires that MPB pulses be greater than 25 nT to be identified as a substorm. Observing the SML-LT "heatmap" of Figure 6.4f, the "darkest" region at this time and therefore the most negative values are in the dawn sector between 04 - 07 MLT. For the SML contributing station to be within this region, but for a pulse to be observed in the MPB index is highly unusual, due to the derivation of the MPB index subselecting only for midlatitude stations within 5 hours of 23.5 MLT. The further analysis of this event does not fall within the scope of this study; however, it may provide the opportunity to understand other causes of substorm-like intensifications of the auroral current systems.

The highlighted substorm event was identified by SOPHIE EPT 90 at 04:30 UT, with the contributing station to SML at the time of onset at 23.57 MLT. The somewhat shorter than average expansion phase was identified to last 10 minutes, during which SML decreased by 163 nT from -54 nT to -217 nT. The recovery phase of this event was evaluated by SOPHIE to have lasted 18 minutes, with SML increasing by 152 nT to -65 nT at the end of the recovery phase. As can be seen in panel f, the most negative values of SML-LT are observable across a range of MLTs in the pre-midnight sector, with the darkest region between 20 - 23 MLT during the expansion phase. The region of maximal negative values spreads dawnward as the substorm transitions to the recovery phase. For SMU, a small increase is observed, but only on the order of ~ 10 nT and occurs for a shorter period than the expansion

phase. However, the general trend of SMU and SMU-LT throughout the expansion and recovery phase of the substorm is a decrease in value. Inspecting panel g, this event also satisfies the criteria of Chu et al. (2015) MPB substorm (Section 3.1.3.1), with the onset of the event occurring at the same time as the SOPHIE identified onset and a maximum MPB value of > 30 nT. In particular, the MPB index returns to low values in concert with the end of the SML recovery phase.

Looking at the solar wind and IMF observations prior to the substorm occurrence, it can be seen that there is a small but sudden increase in flow speed 30 to 15 minutes prior to the onset observed in geomagnetic data. This results in a marginal increase in ε from $\approx .1 \times 10^{-5}$ W/m^2 to $3-4 \times 10^{-5}$ W/m^2, which could have provided the additional energy to instigate the substorm. Additionally, around this time, approximately 15 minutes prior to onset, a northward turning of the IMF is observed, although studies have shown that although the occurrence of a northward IMF turning and substorm may coincide, northward turnings themselves are not required to trigger the magnetospheric instability associated with the substorm (Freeman and Morley, 2009; Wild et al., 2009).

Figure 6.3 shows the auroral observations of the selected event using the FUV-WIC instrument (Mende et al., 2000b) onboard the IMAGE spacecraft (Gibson et al., 2000). The nine panels (a-i) cover 18 minutes of UV observations between 04:26 UT and 04:42 UT on 12 August 2001 around the selected substorm event. Whereas the substorm is identified at 04:30 by the SOPHIE EPT 90 method, its auroral features occur after this time with the WIC observation at 04:30 UT (panel c) showing quiet-time auroral activity and the first features of an auroral substorm observable in the observation taken at 04:32 UT, additionally, it is at 04:32 UT that is selected by the Frey et al. (2004) method as the onset time for the auroral substorm. In this observation, a clear brightening of the aurora is visible spanning 21 - 23 MLT and $65^\circ - 70^\circ$ MLat. It is possible that the auroral substorm onset occurred between these two observations, however, due to the data cadence of IMAGE the earliest possible time that the onset could be confirmed is the 04:32 UT observation. The implications this has for the temporal agreement between pairwise comparisons

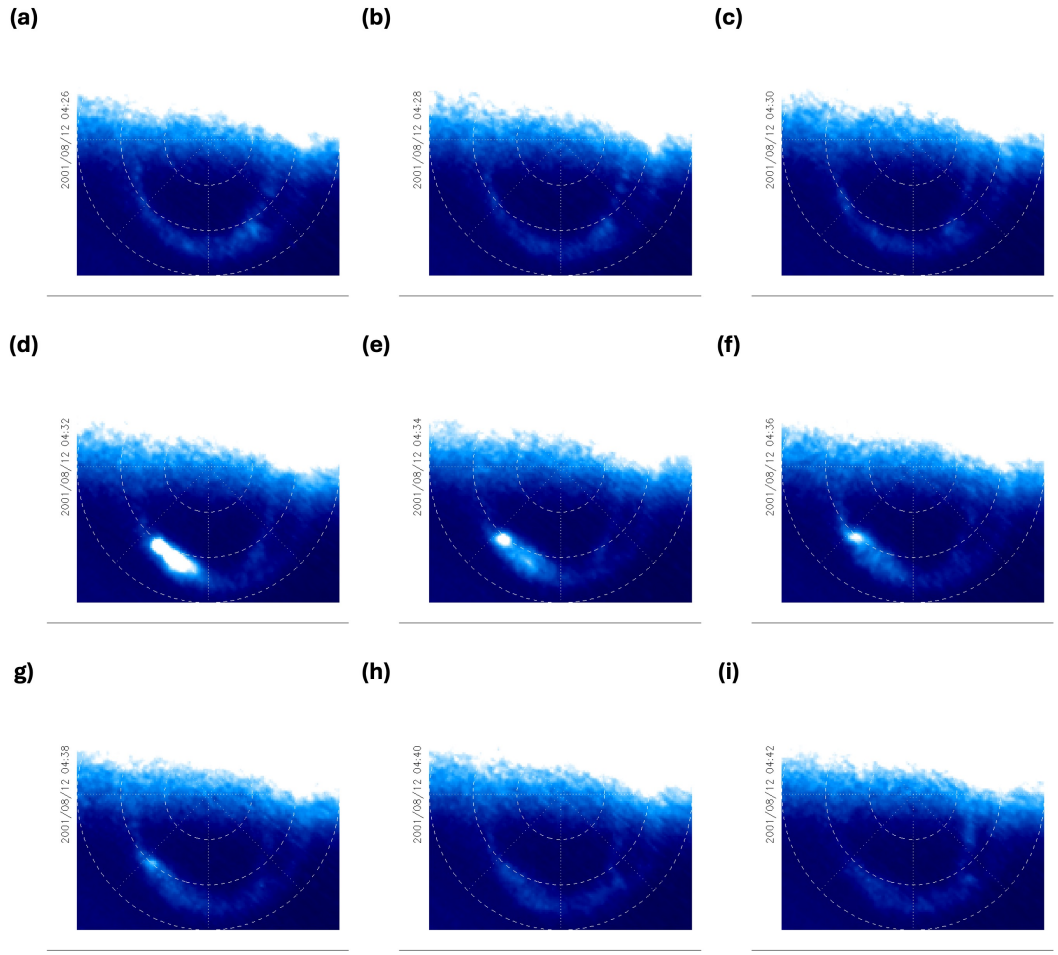

Figure 6.3: IMAGE FUV observations of an 18-minute period (04:26 UT - 04:42 UT 12 August 2001) around our selected substorm event. Panels a-g show the observations transformed onto a regular MLT by MLat grid. Here, each dashed concentric ring indicates 10° of MLat away from the geomagnetic pole and each radial dotted line 3 hours of MLT. The auroral onset, as seen in panel d, is first observed at 04:32 UT as a large intensification of the aurora across 21 - 23 MLT. The poleward-western edge of this auroral feature continues to show a high level of activity until the observation at 04:40 where auroral activity returns back to the background level.

of substorm lists were discussed in Chapter 4 in Section 4.4.

An anomalous observation of this substorm is that its location of occurrence is somewhat in contradiction to the expected effect of B_y. When the IMF has a negative B_y component, Østgaard et al. (2011) showed that auroral substorm onsets are more likely to be dawnward, particularly of 23 MLT. Furthermore, Ruohoniemi and Greenwald (2005) presented convection flows derived from SuperDARN radars for different magnitudes and clock angles of the IMF. Their results show that the

expected location of the westward electrojet of the substorm is more likely to be shifted dawnward after a period of negative IMF B_y. Therefore, our selected event presents a statistical anomaly to the results of Ruohoniemi and Greenwald (2005).

6.3.2 Substorm in the dawn sector

Figures 6.4 and 6.5 show the observations of the substorm identified by SOPHIE EPT 90 at 02:36 UT on 26 September 2000, and the 3 hours before and after this substorm event. This substorm had its magnetic and auroral signature in an atypical location at dawn and post-midnight magnetic local times, respectively, with the contributing station to SML at SOPHIE EPT 90 identified onset being at 04.81 MLT and the auroral onset identified by Frey et al. (2004) at 00.62 MLT. Despite this, the event was identified by Frey et al. (2004); Chu et al. (2015) and Forsyth et al. (2015) to within a few minutes of each other.

The observations in Figure 6.4 are organised in the same format as those in Figure 6.2. It should be noted that although the panels show the same quantities as in Figure 6.2, the axes values differ, for example, the values of ε in Figure 6.4c are a magnitude greater than those in Figure 6.2c.

Compared to the event studied in Section 6.3.1, this event occurs under much stronger solar wind driving. First, the solar wind flow speed is $\approx$ 150 km/s faster (the minimum flow speed observed during this interval is 480 km/s), but it is also more variable with changes observed during the interval on the order of $\approx$ 100 km/s. The maximum flow speed during the interval is $>$ 600 km/s and the maximum before the substorm $\approx$ 560 km/s. The IMF magnitude at the beginning of the interval of Figure 6.4b is twice that observed throughout Figure 6.2b, at 10 nT, although around the time of our event this decreases to $\approx$ 6 nT. From the beginning of our interval up to shortly before the substorm event at 02:36 UT, the IMF B_z is predominantly directed southward, although its value varies significantly from -7 to $+5$ nT. We also observe that B_y is positive throughout this period before the selected substorm event, with its value between 1 and 9.5 nT. The difference in solar wind driving is best captured by ε in panel c, where the value of ε for this substorm interval is approximately an order of magnitude greater than for the previous substorm event, peaking at $\approx 6 \times 10^{-4}\mathrm{W/m^2}$, approaching the top percentile ε observed between 1997 and 2019 ($\approx 7 \times 10^{-4}\mathrm{W/m^2}$).

The strength of solar wind driving is reflected in the response of the magneto-

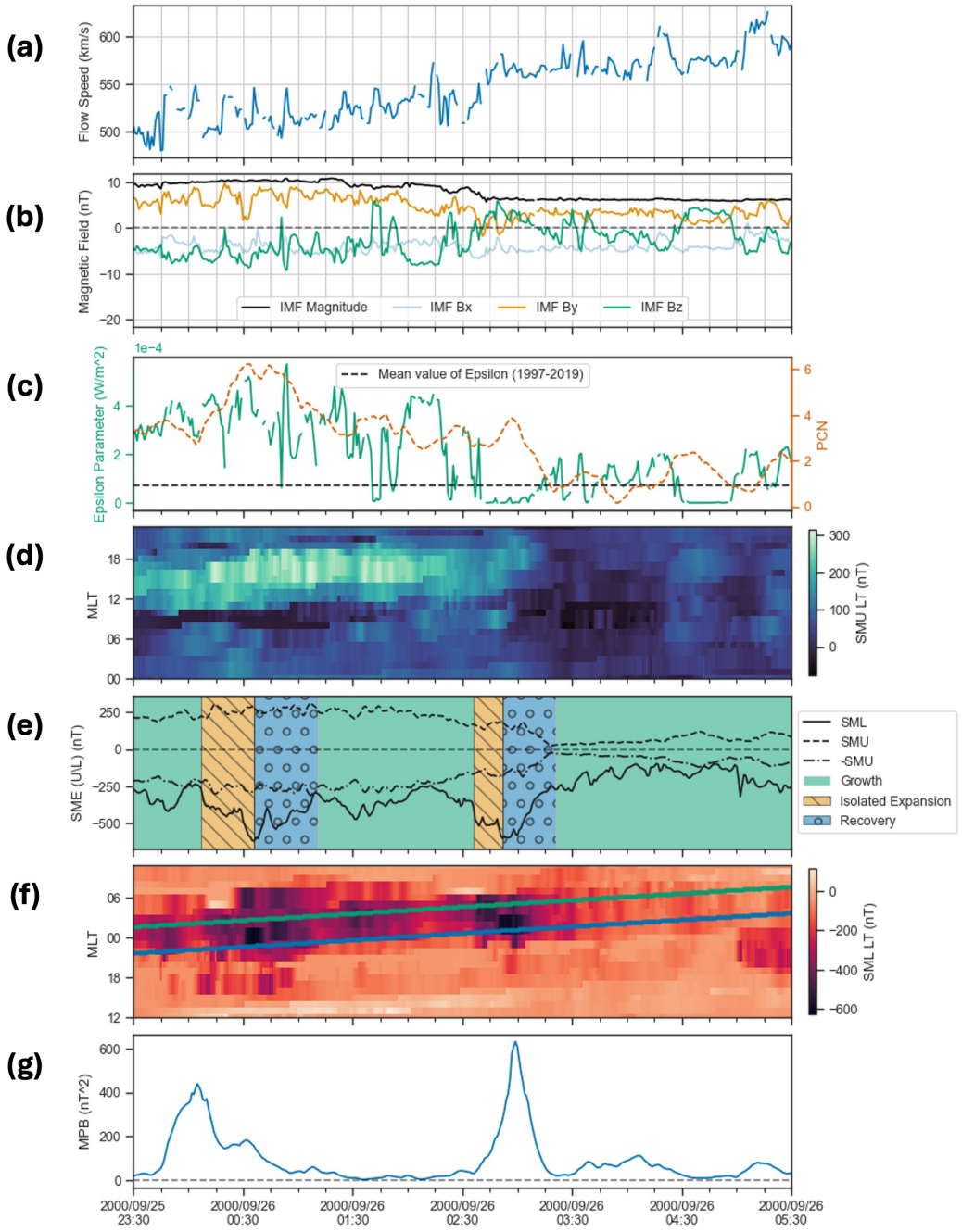

Figure 6.4: Solar wind and magnetometer observations for 6 hours around the substorm at 02:36 UT on 26 September 2000. On Panel f the location of Narsarsuaq (blue) and Tromso (green) magnetometer stations are displayed.

sphere. Two hours before the onset, the PC index peaks at a value of 6 mV/m, and does not fall below a value of 2 mV/m before onset. The electrojet strengths are elevated, and another substorm is identified by both SOPHIE EPT 90 and the MPB index within 2 hours of the event selected, with the value of SML at or below -200

nT throughout the period prior. In terms of SMU, in the 3 hours before the selected substorm, its value fluctuates around 250nT before decreasing in the 30 minutes prior to onset. After the first substorm of the interval, SML and SMU follow similar trends, with the variations in -SMU and SML relatively well-matched, although with the absolute value of SML $\sim 10-100$ nT larger than SMU, highlighting the asymmetry of the westward and eastward electrojet strengths. However, this relationship breaks down ≈ 20 minutes before the onset of the selected event, with the absolute value of SMU decreasing and the absolute value of SML increasing.

The highlighted substorm event was identified by SOPHIE EPT 90 at 02:36 UT, with the contributing station to SML at the time of onset located at 04.81 MLT. As with the last event, the shorter than average expansion phase was identified to last 16 minutes, during which SML decreased by 241 nT from -364 nT to -605 nT. The recovery phase of this event was evaluated by SOPHIE to have lasted 29 minutes, with SML increasing by 328 nT to -277 nT at the end of the recovery phase. There is a possible argument to be made that SOPHIE misidentified the beginning of this event, with a noticeable but shallower SML gradient observable beginning at 02:13 UT. Observing panels d and f, although the SML-LT "hotspot" is widespread from 23 - 07 MLT at the time of onset, the most negative values come from the dawn sector, specifically between 02 - 05 MLT. Late in the expansion phase and during the recovery phase, the most negative values instead come from the midnight sector, indicative of the evolution of the substorm. The value of SMU remains relatively constant throughout the expansion phase, with the contributing region in SMU-LT at the time of substorm onset widespread throughout the dayside MLTs. However, in the recovery phase of the substorm, we see a steady decrease in SMU during it to almost 0 nT, with the contributing region ambiguous. Inspecting panel g, we observe that this event is also identifiable in the MPB index, with a value of > 600 nT^2 observed. Observing the solar wind conditions immediately before the selected event, there is a northward turning of the IMF ≈ 20 minutes prior to the event, although it is southward directed again after 10 minutes. This variation in the IMF is also observable in ε, with its value decreasing to ≈ 0 15 minutes before our

event before increasing to $3 \times 10^{-4}\mathrm{W/m^2}$ again.

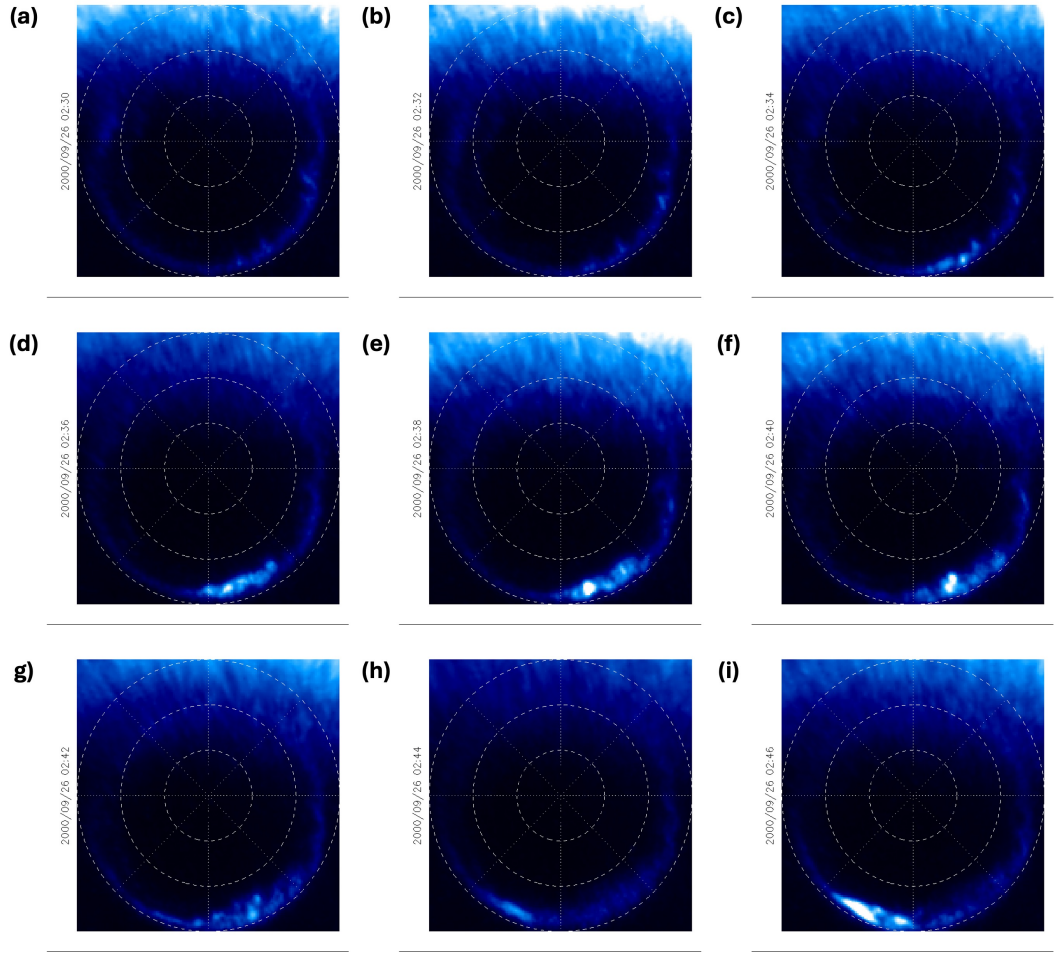

Figure 6.5: IMAGE FUV observations of an 18-minute period (02:30 UT - 02:46 UT 26 September 2000) around our selected substorm event. Shown the in same format as Figure 6.5. The auroral onset, as seen in panel d, is first observed at 02:36 UT as an intensification of the aurora at $\approx$ 01 MLT. This feature continues to be enhanced and propagates poleward in the 2 subsequent observations at 02:38 UT and 02:40 UT, before reducing to the background level. In panel i, at 02:46 UT another intensification of the aurora is observed.

Figure 6.5 shows the UV auroral observations from IMAGE-FUV of the substorm event identified at 02:36 UT by SOPHIE EPT 90. The nine panels (a-i) cover 18 minutes of UV observations between 02:30 UT and 02:46 UT on 12 August 2001 around the selected substorm event. For this substorm event, its auroral onset occurs seemingly simultaneously with onset on the ground, with the observation at 02:36 UT (panel d) showing the clear brightening associated with the auroral substorm. Again, it is possible that the "true" onset occurred between 02:34 UT and 02:36 UT.

In panel d, the brightening of the aurora occurs in the post-midnight sector at ≈ 01 MLT and ≈ 65 MLat before spreading poleward and azimuthally in subsequent observations in panel e and panel f. A notable qualitative difference with the substorm in the midnight sector is the disjointness of the onset arc. The level of auroral activity reduces in panels g and h before another intensification occurs at 02:46 UT in the pre-midnight sector (panel i) and is spread over a range of MLT.

We have highlighted the location of two SuperMAG contributing magnetometer stations on panel f. The blue line indicates the location of the Narsarsuaq (NAQ) station in southern Greenland, at geographic coordinates of 61.17° N 314.57° E. The green line indicates the location of the Tromso (TRO) station in northern Norway, at the geographic coordinates of 69.66° N 18.94° E. Around the time of onset, NAQ is approximately at 0.80 MLT while TRO is approximately at 4.80 MLT (likely the contributing station at onset). Although NAQ is closer to the auroral onset, the SML signature at this location is weaker than that at TRO. We would expect some displacement between the auroral intensification and the peak magnetic signature. However, the difference shown in this event, on the order of $\approx 2-3$ MLT, is much greater than the 1 MLT displacement typically observed. Note that NAQ is at a lower latitude than TRO and thus may be below the equatorward boundary of the auroral oval. The western edge of the "hotspot" in panel f at onset of the selected substorm is at approximately at 2 MLT which is likely one of the Icelandic magnetometer stations, which are at 64° GLat, still more northern than NAQ. Finally, this substorm event is another not well described by the statistical effect of the IMF B_y, with B_y positive for the period prior and during our event but the substorm occurring towards dawn MLTs contrary to the expected effect.

6.3.3 Convection enhancement in the dawn sector

Figure 6.6 shows the observations of the convection enhancement that was identified at 01:35 UT on 14 April 2006 by SOPHIE EPT 90. For the time interval of this event, the IMAGE mission had already ended when communication with the spacecraft was lost in December 2005 and before the implementation of the THEMIS ASI network. Therefore, a global view of the aurora at high time resolution was not available for this event. The magnetic signature of this convection event came from the typical location for a DP2 signature at dawn MLTs, with the contributing station to SML at onset located at 04.00 MLT. There is a Chu et al. (2015) identified event that coincides with the enhancement of convection, with its onset identified at 01:48 UT from the MPB index, which indicates a discrepancy between these two techniques in identifying substorms.

The observations in Figure 6.6 are organised in the same format as those in Figure 6.2. It should be noted that although the panels show the same quantities as in Figure 6.2, the axes values differ, for example, the values of ε in Figure 6.6c are more than a magnitude greater than those in Figure 6.2c. Additionally, there is a black band in the SMU-LT plot shown in panel d, i.e. values at the lowest end of the colour scale $0-5$ nT with little or no variation, which rotates in MLT with the rotation of the Earth. We suspect that these stations, which are in the Siberian region that has the lowest station density in the SuperMAG network, may be outputting erroneous values for the maximum northward deflection. This means that the global SMU value may be an underestimate of the true SMU value.

The convection enhancement was identified during a period of steady and strong driving from the solar wind. During the interval, we observe solar wind flow speeds of ≈ 500 km/s, greater than the average of 430 km/s between 1997 and 2019, which steadily drops by 50 km/s over the first 4 hours, then returns more rapidly towards the initial values, but the variation is small ($\approx 10\%$). The period is characterised by a strong and relatively steady IMF at ≈ 20 nT, which is in the top percentile of the IMF magnitudes observed between January 1997 and December 2019. The IMF magnitude is dominated by its B_y component, which is ≈ -13 nT

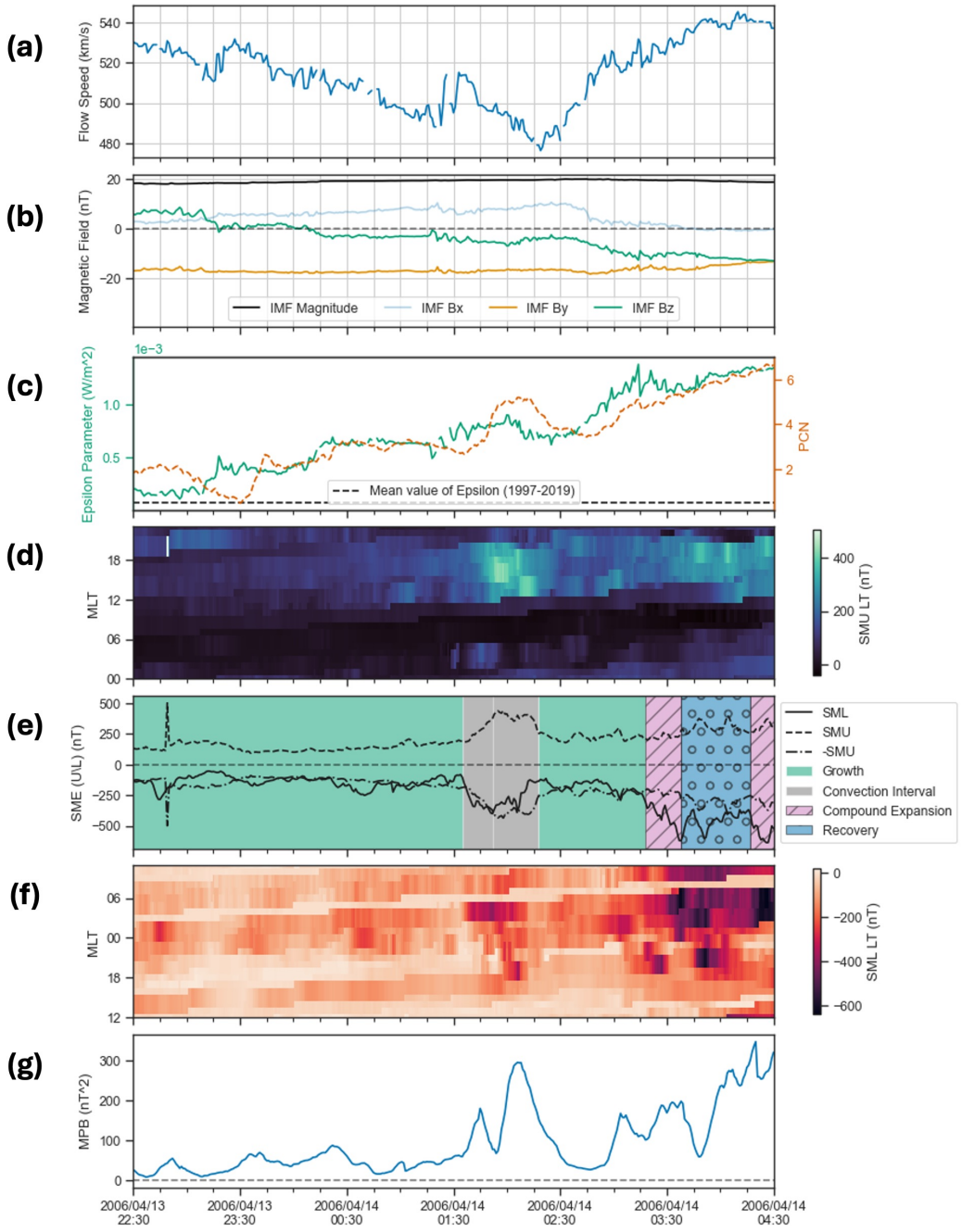

Figure 6.6: Solar wind and magnetometer observations for 6 hours around the magnetospheric convection enhancement at 01:35 UT on 14 April 2006.

throughout the interval. The IMF is northward, although weakly, until ≈ 1 hour before the convection interval, after which it is weakly southward. This results in values of ε for the interval analysed in Figure 6.6 that are in the top decile of ε ($> 0.1 \times 10^{-3}$ W/m^2) observed between January 1997 and December 2019. In the

hour before the convection enhancement onset, ε increases to $> 0.5 \times 10^{-3}$ W/m^2 and continues to increase to $> 1 \times 10^{-3}$ W/m^2 30 minutes after the end of the convection enhancement. The changes in ε are a result of the north to south turning of the IMF B_z as the solar wind velocity is reducing and the IMF B_y is constant.

Observing the response of the magnetosphere, the PC index follows the trends of ε. There is a minimum in PC observed 2 hours before the onset of the convection enhancement, followed by a steady growth in the PC index over the next 4 hours. The strength of driving is reflected in the SMU and SML indices: they are well-matched in the period prior to the convection interval, with their magnitudes in the range $150 - 200$ nT. This is indicative of the westward and eastward electrojets being dominated by a DP2 equivalent current system. Although they are relatively well-matched, there are minor deviations during the period before the convection enhancement in both the SML and SMU indices. The first example is the SML bay at ≈22:40 UT on 13 April 2006 where a drop of -100 nT was observed. However, this is not sustained for a long period of time, and SML recovers in $\approx$ 15 minutes. This is accompanied by a Chu et al. (2015) substorm identification from the MPB index at 22:34 UT. This indicates that there is an enhancement of field-aligned current structures, although whether this is substorm-related requires other data sources, such as in-situ spacecraft, to be fully explored. There are other SML bay structures, such as at 00:15 UT, before the convection enhancement, but they are neither strong deviations nor sustained, although their SML signature comes from the pre-midnight sector.

The highlighted convection enhancement was identified by SOPHIE EPT 90 at 01:35 UT, with the contributing station to SML at the time of onset located at 04.00 MLT. The "expansion" phase of this convection enhancement was identified to last 17 minutes, during which the SML decreased by 292 nT from -105 nT to -397 nT. The "recovery" phase of this event was evaluated by SOPHIE EPT 90 to have lasted 26 minutes with SML increasing by 256 nT to –141 nT at the end of the recovery phase. The convection enhancement lasted 43 minutes in total. During this interval, the magnitude of SMU changes in a similar manner, satisfying the

criteria for the identification of convection enhancement. This is observed in panel f, as the reflection of SMU over the x-axis (-SMU) largely follows the trace of the SML index, albeit taking slightly longer to recover to the background level. At approximately the same time as the convection enhancement in SML, the PC index also increases over a period of ≈ 10 minutes to a value of 5.5 $\mathrm{mV/m}$. This value is maintained for approximately the same period of time as the "expansion" phase of convection enhancement in the SML/SMU indices before reducing to 4 $\mathrm{mV/m}$. After a small delay, the PC index once again follows the trend of solar wind driving, as seen by the increase in ε, increasing to the maximum of the period of > 6 $\mathrm{mV/m}$ at the end of the interval analysed. This convection interval is accompanied by a Chu et al. (2015) substorm identification from the MPB index at 01:48 UT, as the minima between the two peaks at 01:44 UT (≈ 200 $\mathrm{nT^2}$) and 02:05 UT (≈ 300 $\mathrm{nT^2}$). There is an argument that these two peaks consist of two distinct events, as they are both significant MPB pulses. However, the criteria of Chu et al. (2015) mean that only the MPB pulse which has a higher value is identified as a potential substorm since they occur within the temporal vicinity of each other.

After the convection event, a series of compound substorms began. These show further enhancements in MPB and show a distinct difference between the SMU and SML variations.

The event presented demonstrates traits associated with convection enhancements (SMU and SML are well-matched with steady high solar wind driving). The enhancement in MPB is puzzling but does indicate that the enhanced convection requires an enhanced field-aligned current. This may indicate that MPB is sensitive to non-SCW structures.

6.3.4 Convection enhancement in the midnight sector

Figure 6.7 shows the observations of the convection enhancement that was identified at 01:41 UT on 06 April 2004 by SOPHIE EPT 90. For the time interval of this event, no IMAGE observations were available, again before the implementation of the THEMIS ASI network. Therefore, a global view of the aurora at high time resolution was not available for this event. The magnetic signature of this convection event came from an atypical location for a DP2 signature at pre-midnight MLT, with the contributing station to SML at SOPHIE EPT 90 identified onset located at 23.76 MLT. There was no associated Chu et al. (2015) MPB identification with this event, and thus both lists agree that this is not a substorm event.

The observations in Figure 6.7 are organised in the same format as those in Figure 6.2. It should be noted that although the panels show the same quantities as in Figure 6.2, the axes values differ, for example, the values of ε in Figure 6.7c are a magnitude greater than those in Figure 6.2c. Additionally, the continuity of the plasma parameter observations before the onset of the convection enhancement is limited compared to the other intervals analysed. This results in data gaps in both the solar wind flow speed (panel a) and the ε parameter (panel c). Similar to Figure 6.6d, there is a black band in the SMU-LT plot shown in panel d, that is, values at the lowest end of the colour scale $0-5$ nT with little or no variation with the end of its period in each MLT sector punctuated by a fill value (transparent box in panel D), which rotates in MLT with rotation of the Earth. We suspect that these stations, which are in the Siberian region that has the lowest station density in the SuperMAG network, may be outputting erroneous values for the maximum northward deflection.

The convection enhancement was identified during a period of strong driving from the solar wind. At the beginning of the interval, we observe typical solar wind flow speeds of ≈ 450 km/s. This gradually increases to 550 km/s over 5 hours. The period is characterised by a relatively steady IMF at ≈ 10 nT. The magnitude of the IMF before the enhancement of convection is dominated by its GSM B_x component, which is ≈ 9 nT until $\approx 15-20$ minutes after the onset of the

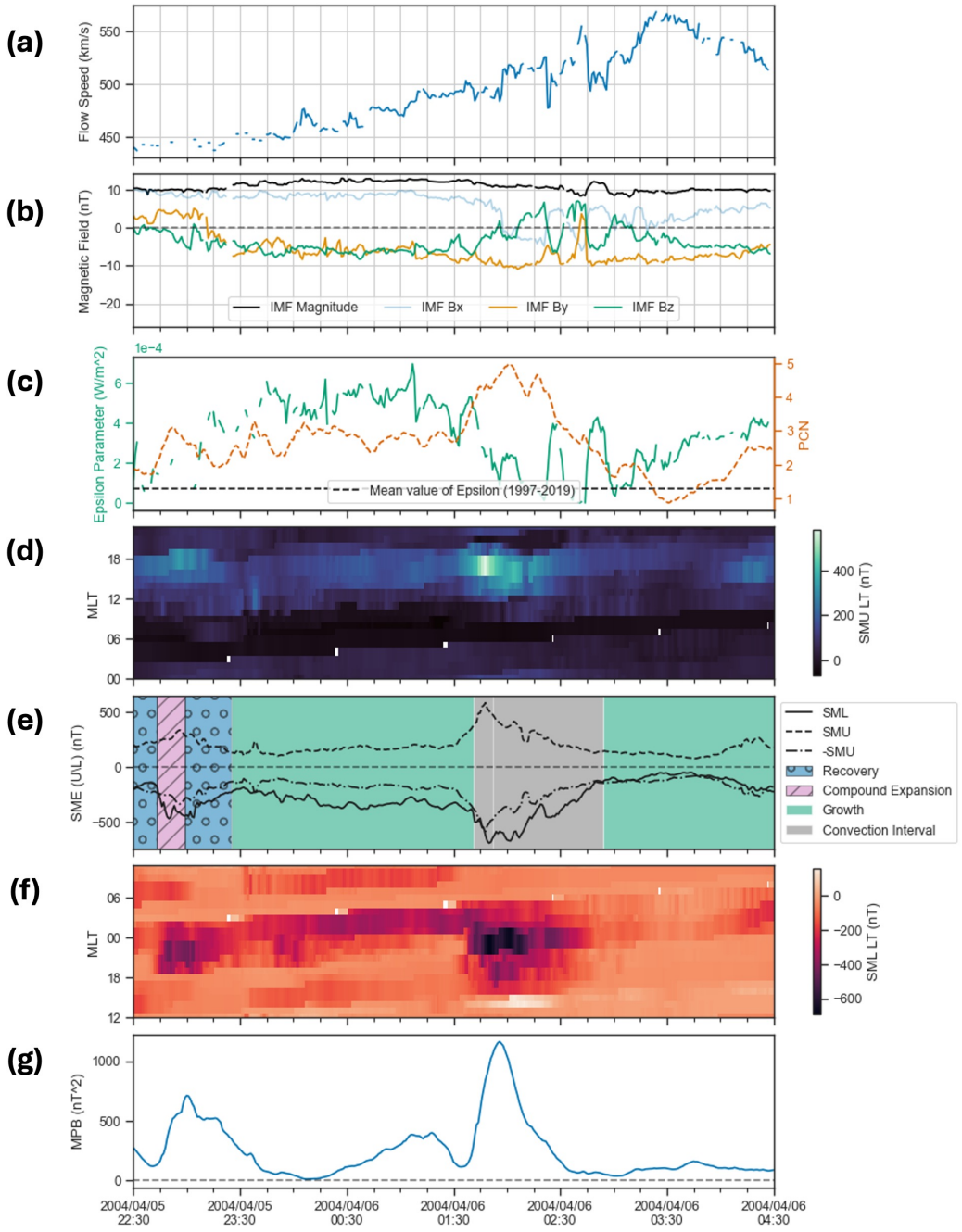

Figure 6.7: Solar wind and magnetometer observations for 6 hours around the magnetospheric convection enhancement at 01:41 UT on 6 April 2004.

convection enhancement when it turns negative. Although initially northward, in the $\approx$ 2 hour period before onset, the IMF B_z component is directed southward, in the same order of magnitude as the negative B_y component. Similar to the dawnside convection enhancement interval, this results in values of ε that are in the top decile

of ε ($> 0.1 \times 10^{-3}$ W/m^2) observed between January 1997 and December 2019. In the 2 hours before the start of the convection enhancement, ε increases to $> 0.5 \times 10^{-3}$ W/m^2. Approximately 15 minutes before onset, the value of ε begins to decrease, as the magnitude of B_z also begins to decrease. In general, after the event the driving of the magnetosphere is weaker. However, there are 2 $\approx$ 10-minute pulses where ε increases to $\approx 0.4 \times 10^{-3}$ W/m^2, one during the "recovery" phase of the convection enhancement.

Observing the state of the magnetosphere, the PC index largely follows the trends of ε prior to the convection enhancement. The minimum in PC prior to the event occurs at the beginning of the interval when the driving is weakest. In the 90 minutes before the onset of the convection enhancement, PC stays relatively steady at a value of ≈ 2.5 mV/m. In terms of the SML and SMU indices, there is a set of compound substorm events that occurs at the beginning of the interval, with the last expansion phase of this "chain" of events occurring 2 hours and 45 minutes prior to the convection enhancement. This substorm is also identified by the Chu et al. (2015) MPB method, with its MPB peak at ≈ 700 nT^2. After the recovery phase of this compound substorm, the SMU and SML indices are relatively steady prior to the convection enhancement, showing a small increase in magnitude. However, an offset in the SML and SMU magnitudes is observed, possibly an effect of the increased conductivity in the morning sector due to substorm precipitation.

The highlighted convection enhancement was identified by SOPHIE EPT 90 at 01:41 UT, with the contributing station to SML at the time of onset located at 23.76 MLT. The "expansion" phase of this convection enhancement was identified to last 11 minutes, during which the SML decreased by 235 nT from -410 nT to -645 nT. The "recovery" phase of this event was evaluated by SOPHIE EPT 90 to have lasted 62 minutes, with SML increasing by 530 nT to -115 nT at the end of the recovery phase. The convection enhancement lasted 73 minutes in total. During this interval, SMU changes magnitude in a similar manner, satisfying the criteria for convection enhancement identification, although reaching its peak magnitude earlier than SML. This is observed in panel f, since the reflection of SMU over the

x-axis, -SMU, largely follows the trace of the SML index. Approximately the same time as the convection enhancement in SML, the PC index also increases over a period of ≈ 10 minutes to a value of $4-5$ mV/m. This value is maintained for approximately 30 minutes before gradually decreasing to below that observed before convection enhancement at < 1 mV/m 30 minutes after the end of convection enhancement. This convection interval is not accompanied by a Chu et al. (2015) substorm identification from the MPB index, although a significant MPB pulse is observed that peaks at > 1000 nT^2 at the same time. This is immediately preceded by another pulse that peaks at > 500 nT^2, whose onset is at 00:15 UT. Interestingly, there is a Chu et al. (2015) identification at 03:31 UT, where a significantly smaller change in MPB is observed and in SML there is a possible signature of another convection enhancement (well-matched SMU and SML magnitudes).

This event presents an anomaly in the statistical picture of the effect of the IMF B_y on the ionospheric convection pattern and therefore magnetic perturbations. As with the convection enhancement in the dawn sector, this event occurs in a period of strong IMF B_y. Ruohoniemi and Greenwald (1998) showed that typically this acts to rotate the Northern Hemisphere convection pattern anticlockwise when looking down onto the pole, acting to shift the magnetic perturbations related to it towards dawn. However, in contrast to this, in the current event presented the magnetic perturbations have been shifted toward dusk, this could be as a result of lingering conductance in the pre-midnight sector due to precipitation from the compound substorms 2 hours before the convection enhancement, however this needs further investigation.

6.4 Discussion

In this study, we examine four events in detail in terms of their solar wind and ground magnetometer measurements. Two of these events were substorms that are related to DP1 magnetic perturbations, one where the maximum ground magnetic perturbation is observed at a typical location for DP1, and the other where the maximum ground magnetic perturbation is observed at an atypical location. In addition to ground magnetometer measurements of these events, observations of the aurora from a global imager are presented around the time of substorm onset. The other two events analysed were what have been termed convection enhancements in Chapter 5, which are related to DP2 magnetic perturbations, one where the maximum ground magnetic perturbation is observed at a typical location for DP2, and the other where the maximum ground magnetic perturbation is observed at an atypical location.

Although the events presented in this study occur after periods of strong driving (in the upper deciles of ε observed between 1997 and 2019), apart from the substorm presented in Section 6.3.1, it is not necessarily a requirement. As the substorm is a loading-unloading phenomenon, there is a requirement that energy and magnetic flux are added to the magnetosphere prior to onset, this is simply the growth phase of the substorm. However, there appears to be no set threshold for what this driving has to be, other than prior to the substorm there has to be a prolonged period of southward IMF (Morley and Freeman, 2007; Freeman and Morley, 2009; Wild et al., 2009).

Our observations in Section 6.3.1 seem in contrast to this hypothesis, with the last prolonged period of southward IMF observed approximately 2 hours before onset. However, these observations can be explained within the paradigm of the Minimal Substorm Model of Freeman and Morley (2004). It has been proposed that the energy budget of the substorm is analogous to a sand pile model, in which the addition of energy and mass to the magnetosphere is akin to adding grains of sand to a sand pile, before a threshold is crossed and the system reconfigures, for the sand pile this is its collapse and reconfiguration to a lower height, and for the magnetosphere

it is the onset of the substorm expansion phase during which reconnection closes the open magnetic flux in the tail lobes before it is recirculated. In this framework, the prolonged period of southward IMF 2 hours prior to onset drove the magnetosphere to just below the point of criticality, such that any other addition of energy would force the instability of the substorm to occur. In line with this hypothesis, there are two short periods of southward IMF and therefore increased ε in the 30 - 15 minutes immediately before the SML onset. We assume there was the required energy input to push the magnetosphere beyond its critical threshold. Although this period is well explained qualitatively by the Freeman and Morley (2004) model, it leads to natural follow-up questions such as what the threshold may be (i.e. is it quantifiable to effectively explain and forecast substorm occurrence), how it varies, and what its internal and external influences may be. There is also the question of how well the convection enhancements, and the interplay of the directly driven (DP2) and loading-unloading (DP1) response modes (Kamide, 1982; Kamide and Kokubun, 1996) of the magnetosphere, are explained by the paradigm.

For the convection enhancement intervals, both events in this study occur under strong driving from the solar wind, one sustained throughout the interval (Section 6.3.3) and the other where the driving is periodically stronger and weaker throughout its lifetime (Section 6.3.4). Note that these are definitionally different from Steady Magnetospheric Convection (SMC) events (Sergeev et al., 1996a; Kissinger et al., 2011; Walach and Milan, 2015), as the convection enhancements are short-lived intensifications, in this study identified from the westward and eastward electrojets. Both of the convection enhancements presented are preceded by relatively long (> 2 hours) of steady but elevated levels of magnetospheric convection, indicated by the PC index and the SMU and SML indices, which could be interpreted as SMCs. Although many varying criteria have been set to identify SMCs, like substorms there is no consensus on the definition of an SMC event (Sergeev et al., 1996b, 1998; O'Brien et al., 2002; McWilliams et al., 2008; Kissinger et al., 2010). Although we have presented only two events, neither show signs that the impulsive increase in convection has an external trigger. The further study of con-

vection enhancement intervals with in-situ spacecraft could reveal if there are any internal changes in the magnetosphere that are causal to the impulsive increase of convection. This was not achievable in this study because coverage in the far- and near-Earth magnetotail was limited for the intervals selected. The intervals presented in this study were chosen to have similar conditions as the substorms selected, minimising the seasonal effect of the moving terminator (events were identified in the vicinity of the equinoxes).

In the events chosen, there seem to be no other clear differentiators apart from the "correlated" changes in the SMU and SML magnitudes for convection enhancements compared to substorm intervals. It could be argued that the IMF conditions are qualitatively more chaotic prior to the substorm events than for the convection intervals. However, statistical studies that use a larger number of events need to be conducted to confirm whether this is true. In terms of geomagnetic indices, there appears to be no obvious additional differentiator, as even the MPB index shows significant increases during these intervals. This is particularly interesting because this index was hypothesised to respond only to enhancements of the field-aligned currents of the substorm current wedge (Chu et al., 2015). The MPB index therefore could be reflecting the enhancement in the Region 1 and Region 2 field-aligned currents when magnetospheric convection is enhanced (Coxon et al., 2014a), particularly since the MPB index integrates data from the whole nightside ($\pm$5 hours from 23.30 MLT) for its calculation. As stated in Section 3.1.3, only stations that show significant deviations in this region are included for the MPB calculation. Therefore, the addition of an extent or a width parameter (in MLT or MLon) of the stations included for the calculation of MPB could indicate if MPB enhancements are created by a structure that is more localised (such as the SCW) or more global (R1/R2 currents).

One indicator that could be used to distinguish between these two event types, is their auroral signature. For this study, there were no global imagers available for the convection enhancement events and the all-sky imager array observations were disrupted with cloud cover, and therefore, we were unable to present any auroral

observations for the convection intervals. Although local observations of the aurora from the ground using all-sky imagers have been fruitful (Nishimura et al., 2010, 2011; Murphy et al., 2014; Kalmoni et al., 2018), the global view of the aurora provides a unique perspective of meso-to-large-scale structures and their relationship to various magnetospheric phenomena, not just the substorm.

In the substorms presented, the locations where their signatures are observed contradict the expected effect of the influence of IMF B_y. Using substorm onsets identified using the Polar and IMAGE spacecraft, Østgaard et al. (2011) showed that under positive IMF B_y, the onset of the auroral substorm preferentially occurred towards dusk MLTs and under negative IMF B_y they preferentially occurred further towards dawn MLTs. Although Østgaard et al. (2011) clearly shows the effect of an ongoing dominant B_y component, it should be noted that it is relatively minor, such that the mean location of auroral onset is -0.5 MLT for 90° clock angle and +0.5 MLT for 270° clock angle with standard deviations of the order 0.1 MLT. The substorms presented in this study are therefore well outside of this statistical picture, with the event in Section 6.3.1 under negative B_y identified from the aurora at 22.52 MLT and the event in Section 6.3.2 under positive B_y identified from the aurora at 0.62 MLT. It is unclear from the other observations presented, why this departure from the statistical effect occurred.

The magnetic signature of the substorm event described in Section 6.3.2, occurs significantly further dawnward than its auroral counterpart. Some displacement is expected, as the auroral intensification is expected to be conjugate with the upward FAC of the SCW, where the downward-directed electrons which intensify the aurora are the current carriers. We expect this displacement to be of the order of 1 MLT, e.g., the displacement between Frey et al. (2004) onset peaks and the DP1 peak in Chapter 5. However, the difference in location of the station that contributed to SML at the time of onset and where the auroral onset was identified was $\approx 2-3$ MLT. This can be explained in part by the station coverage of the SuperMAG network, as the auroral onset occurred over the east coast of Greenland. However, stations located much closer to the location of auroral onset were contributing to

SML at the time, including those located in Iceland. We hypothesise that these stations were below the equatorward boundary at the time of onset and thus observed weaker geomagnetic fluctuations compared to the Tromso station (located at higher latitudes) which contributed to SML at the time of onset. This is in part supported by Dimitrakoudis et al. (2022), where they showed that geomagnetic fluctuations are stronger within the auroral zone.

6.5 Summary

Table 6.1: Summary statistics of the events presented in this study

Event type	ΔSML (nT)	Mean (Std dev) of ε (1 hr prior) (W/m^2)	ΔMPB (nT^2)	Duration (min)
Substorm in the midnight sector	163	9.1×10^{-6} (7.7×10^{-6})	≈ 25	28
Substorm in the dawn sector	241	2.5×10^{-4} (1.5×10^{-4})	≈ 600	45
Convection enhancement in the dawn sector	292	6.4×10^{-4} (4.0×10^{-5})	≈ 250	43
Convection enhancement in the midnight sector	235	5.3×10^{-4} (5.9×10^{-5})	≈ 1000	73

Four event studies identified using the SOPHIE EPT 90 method (Forsyth et al., 2015) are presented: two substorms and two convection enhancements. Six-hour observations of the solar wind and interplanetary magnetic field measured at L1, the PC index, the SMU and SML index and their local time partitioned counterparts, and the MPB index are presented for each event. Table 1 shows a summary of the events presented in this chapter. Specifically, the change in SML of each event, the mean and standard deviation of ε 1 hour before each event, the change in MPB of each event, and their durations are presented. In addition, auroral observations are presented when available, specifically for the two substorm events. From our analysis of the events, we conclude the following:

- The substorm and convection enhancement events presented in this study occur under strong driving. For 3 of the events shown, the ε values are in the top decile for the period between 1997 and 2019.
- The substorms presented in this study have their signatures occurring in locations contrary to the expected effect of the IMF B_y component. In addition to this, the magnetic signature of one event is especially displaced from its auroral signature, a possible effect of non-uniform station density of magnetometer networks.

- There is no other obvious differentiator between the convection enhancements and substorms apart from coupled changes in SMU and SML magnitudes for convection enhancements. The IMF conditions appear to be steadier prior to the convection enhancements than for the substorms. With the standard deviations of ε in Table 6.1 an order of magnitude smaller than the mean value in the hour before the event occurrence, but a further statistical study is required to evaluate whether this is always the case. Furthermore, even the MPB index, which is thought to sample the occurrence and strength FACs of the substorm current wedge, is also elevated during convection enhancements.

- Our results also imply that the act of simplifying data to indices may remove crucial information that cannot be simply recovered by including more indices.

Chapter 7

Final Remarks and Future Work

> Yesterday is history, Tomorrow is a mystery, but Today is a gift. That is why it is called the present.
>
> Master Oogway, Kung Fu Panda (2008)

Ever since its first description from auroral observations more than 60 years ago by Akasofu (1964), the substorm has been a topic of significant research. However, despite this, the space physics community still lacks a consensus on what constitutes as a substorm event, with many questions remaining regarding this fundamental magnetospheric process. The substorm is a key element in the flow of energy and mass in the coupled solar wind-magnetosphere-ionosphere system, therefore the lack of understanding of this important physical process hinders our ability to understand and predict the magnetospheric response to external driving.

In this thesis, we investigated the temporal relationship between different substorm onset lists that have been provided in the literature. These lists are essential to explain or predict substorm dynamics and effects, as a sufficiently extensive catalogue of events is required to validate any model or statistical result. However, we found that there is a significant divergence in the events identified, with less than 50% agreement between any pair of catalogues within a 30-minute window. Following this, we decomposed the substorm and magnetospheric convection contributions to magnetic perturbations at high latitudes. We found that a significant

number $> 50\%$ of these perturbations that were originally identified as related to the substorm were misidentified. Moreover, we postulate that the auroral indices as they are constructed today do not contain the information required to fully resolve the two components of the auroral electrojets (Kamide and Kokubun, 1996). Following this result, we investigated a set of four events, two substorms and two impulsive magnetospheric convection enhancements, in search of further differentiators between these two event types.

In Chapter 4, we applied statistical techniques traditionally used in model validation and verification (Mooney et al., 2021; Smith et al., 2021; Mooney et al., 2024; Smith et al., 2024), but have also seen use in other studies (Forsyth et al., 2016, 2020b), namely contingency tables. The method we used was detailed in Chapter 3. Using this framework, we quantified the coincidence of events identified using various substorm identification methods for the period between May 2000 and December 2002, i.e. during the initial mission lifetime of the IMAGE spacecraft. We found that while in general there was a greater than chance association between detections from different substorm signatures, this varied depending on the method and signature used.

A significant revelation of this study was that particle injections at geosynchronous orbits displayed an almost random association with other features of the substorm, in particular a random relationship with substorms identified from the aurora. The substorm signature that showed the greatest association with other features was the ground magnetic perturbations, namely the methods developed by Newell and Gjerloev (2011) and Chu et al. (2015). This led us to recommend these catalogues for community use, or the catalogue by Forsyth et al. (2015) if substorm phases were required. However, the work given in chapter 5 showed us that these lists are still likely contaminated with non-substorm events. Thus, we would like to highlight that although we recommended these catalogues, caution should still be exercised against over-interpreting any results derived using them, as only a 50% overlap in events was observed, showing that the effects of other phenomena could be folded into those of the substorm.

In Chapter 5, we quantified the contributions of substorms and impulsive convection enhancements to substorm-like features in the SML index. This was achieved by statistically analysing the onset MLT of the two types of events identified using the SOPHIE technique of Forsyth et al. (2015). We found that although the SOPHIE method attempts to filter out convection enhancements, 59% of the events originally identified as substorms are instead due to impulsive magnetospheric convection enhancements or enhancements of the DP2 current pattern, rather than DP1, which is associated with the ionospheric leg of the Substorm Current Wedge. Additionally, we showed that this false positive identification affects compound substorms much more significantly, approximately 8 in 10 compound events are falsely identified, though they are half as common as the traditional isolated substorm event. The results of this work indicate the importance of the separation of AL/SML bays that are due to the substorm and other magnetospheric phenomena.

Moreover, when we explored thresholds to distinguish between impulsive magnetospheric convection enhancements and "true" substorm events, we found that no single value can distinguish convection events entirely. Thus, we came to the conclusion that the auroral indices do not have the required information to perfectly identify substorm events, as they inherently allow the identification of false positives. This does not mean that methodologies built on them are fruitless, as they provide invaluable resources in finding events efficiently, which can then be verified as "true" substorms via the occurrence of other substorm signatures.

In Chapter 6, we built on top of the work completed in Chapter 5, investigating four events, two substorms, and two impulsive magnetospheric convection enhancements, identified using the SOPHIE technique by (Forsyth et al., 2015). For all events, the solar wind (measurements from L1 spacecraft) and magnetospheric (geomagnetic indices) conditions in the surrounding 6 hours ($\pm$3 hours) around the onset of each event were analysed. The events analysed all occurred under strong driving from the solar wind. However, in analysing both the magnetospheric and solar wind conditions prior to the event, there was no other obvious differentia-

tor between the impulsive magnetospheric convection enhancements and substorms apart from coupled changes in SMU and SML magnitudes that SOPHIE leverages for the identification of convection enhancements. It seems that impulsive magnetospheric convection enhancements appear to occur after periods of steadier solar wind driving compared to substorms, but whether this is the case for a larger set of events needs to be further studied.

In the process of completing this thesis and answering some of the uncertainties regarding the signatures of the substorm, there were pathways which were not pursued and provide a course for future work. In Chapter 4, we showed that the particle injections showed a poor association with other substorm signatures, which improved when using the end of the injection interval as the onset time. An avenue not explored in this thesis but could provide fruitful for substorm research is the evaluation of whether this was a result of automated method of Borovsky and Yakymenko (2017) or a true systematic delay between an injection at geosynchronous orbit and any ground effect. In Chapter 5, we discussed the ordering of substorm phases to classify SOPHIE (Forsyth et al., 2015) events, one class of these events which we labelled "Other" does not fit into the traditional framework of isolated substorms (Growth into Expansion into Recovery into Growth) and compound substorms (Growth into multiple Expansion and Recovery cycles into Growth). We showed that these events were $\sim 50\%$ due to DP1 and $\sim 50\%$ due to DP2, and discussed that they were more likely to occur during Solar maximum. The further examination of these events, including the solar wind and magnetotail conditions at the time of their occurrence, would build upon our understanding of magnetospheric response modes and could result in more robust identification of substorms from auroral indices. In Chapter 6, we suggest that the current understanding of the structure of the field-aligned currents between nightside magnetosphere and ionosphere during substorm intervals still requires work, as the MPB index, which has been constructed such that it should only respond to the substorm, shows significant variations during convection enhancements. Additionally, there are various contrasting phenomenological models of the FAC and substorm electrojet structure

(e.g. McPherron, 1970; Gjerloev and Hoffman, 2014; Kepko et al., 2015; Liu et al., 2015), highlighting the further work required in this area of substorm research.

Lists of "substorms" are inherently useful in solar terrestrial physics, providing a common baseline for both case and statistical studies of various processes that are part of or result from the phenomena associated with substorms. However, this thesis has shown that despite considerable progress being made in understanding the characteristic features and consequent effects of the substorm, some conclusions from studies using substorm lists may be incomplete, as these studies may be considering non-substorm intervals. This ranges from the importance of the phenomenon in the energization and variability of the ring current (Sandhu et al., 2019) and the radiation belts (Forsyth et al., 2016; Rodger et al., 2022a) to its influence on ground-induced currents (Freeman et al., 2019). As discussed throughout the thesis, our studies highlight that currently these individual "substorm" lists are not fully representative of the phenomena. In reality, they are lists of phenomena associated with the substorm, for example a list of magnetic enhancements, auroral enhancements, particle enhancements, etc. which may or may not align with substorm activity and should, ultimately, be treated in that way.

The work in this thesis highlights some major issues regarding substorm identification and its implications for the study of the phenomena. However, there are many pathways in the short- and long-term to resolve these issues. As has been recommended throughout this thesis, the development of identification using multiple datasets and ideally those using different substorm signatures, e.g., ground magnetic perturbations and the aurora, will improve our confidence in identifying "true" substorm intervals. Moreover, the data from new and upcoming missions such as NASA EZIE which will use Zeeman effect to "image" the electrojets and ESA/CAS SMILE will provide an invaluable resource to validate our methods against. NASA EZIE will provide another view in addition to our ground magnetometer arrays on the structure of the auroral electrojets, to further understand the relationship between its two components (directly driven and loading-unloading). ESA/CAS SMILE will provide a global view of the aurora that has not been available since

the end of the Polar mission in 2008. This thesis has focussed primarily on the false identification of events in ground magnetometer data; similar work must be completed on the other substorm signatures for us to have confidence in combined datasets. This will contribute towards a community consensus on a quantitative description of the substorm from which we can identify events, and thus improve our understanding of this still enigmatic phenomenon.

Bibliography

A. T. Aikio, V. A. Sergeev, M. A. Shukhtina, L. I. Vagina, V. Angelopoulos, and G. D. Reeves. Characteristics of pseudobreakups and substorms observed in the ionosphere, at the geosynchronous orbit, and in the midtail. *Journal of Geophysical Research: Space Physics*, 104(A6):12263–12287, 1999. ISSN 2156-2202. doi: 10.1029/1999JA900118.

S. I. Akasofu. The development of the auroral substorm. *Planetary and Space Science*, 12(4):273–282, Apr. 1964. ISSN 0032-0633. doi: 10.1016/0032-0633(64)90151-5.

S.-I. Akasofu. *Polar and Magnetospheric Substorms*, volume 11 of *Astrophysics and Space Science Library*. Springer Netherlands, Dordrecht, 1968. ISBN 978-94-010-3463-0 978-94-010-3461-6. doi: 10.1007/978-94-010-3461-6.

S.-I. Akasofu and S. Chapman. The ring current, geomagnetic disturbance, and the Van Allen radiation belts. *Journal of Geophysical Research (1896-1977)*, 66(5):1321–1350, 1961. ISSN 2156-2202. doi: 10.1029/JZ066i005p01321.

S. I. Akasofu, S. Chapman, and C. I. Meng. The polar electrojet. *Journal of Atmospheric and Terrestrial Physics*, 27(11):1275–1305, Nov. 1965. ISSN 0021-9169. doi: 10.1016/0021-9169(65)90087-5.

H. Alfvén. Existence of Electromagnetic-Hydrodynamic Waves. *Nature*, 150(3805):405–406, Oct. 1942. ISSN 1476-4687. doi: 10.1038/150405d0.

O. Amm and R. Fujii. Separation of Cowling channel and local closure currents

in the vicinity of a substorm breakup spiral. *Journal of Geophysical Research: Space Physics*, 113(A6), 2008. ISSN 2156-2202. doi: 10.1029/2008JA013021.

V. Angelopoulos, W. Baumjohann, C. F. Kennel, F. V. Coronti, M. G. Kivelson, R. Pellat, R. J. Walker, H. Luehr, and G. Paschmann. Bursty Bulk Flows in the Inner Central Plasma Sheet. *Journal of Geophysical Research*, 97:4027–4039, Apr. 1992. ISSN 0148-0227. doi: 10.1029/91JA02701.

V. Angelopoulos, C. F. Kennel, F. V. Coroniti, R. Pellat, M. G. Kivelson, R. J. Walker, C. T. Russell, W. Baumjohann, W. C. Feldman, and J. T. Gosling. Statistical characteristics of bursty bulk flow events. *Journal of Geophysical Research: Space Physics*, 99(A11):21257–21280, 1994. ISSN 2156-2202. doi: 10.1029/94JA01263.

R. L. Arnoldy and K. W. Chan. Particle substorms observed at the geostationary orbit. *Journal of Geophysical Research (1896-1977)*, 74(21):5019–5028, 1969. ISSN 2156-2202. doi: 10.1029/JA074i021p05019.

Y. Asano, T. Mukai, M. Hoshino, Y. Saito, H. Hayakawa, and T. Nagai. Current sheet structure around the near-Earth neutral line observed by Geotail. *Journal of Geophysical Research: Space Physics*, 109(A2), 2004. ISSN 2156-2202. doi: 10.1029/2003JA010114.

M. P. Aubry, C. T. Russell, and M. G. Kivelson. Inward motion of the magnetopause before a substorm. *Journal of Geophysical Research (1896-1977)*, 75(34):7018–7031, 1970. ISSN 2156-2202. doi: 10.1029/JA075i034p07018.

W. I. Axford. The interaction between the solar wind and the Earth's magnetosphere. *Journal of Geophysical Research (1896-1977)*, 67(10):3791–3796, 1962. ISSN 2156-2202. doi: 10.1029/JZ067i010p03791.

W. I. Axford. Magnetospheric convection. *Reviews of Geophysics*, 7(1-2):421–459, 1969. ISSN 1944-9208. doi: 10.1029/RG007i001p00421.

D. N. Baker, P. R. Higbie, E. W. Hones Jr., and R. D. Belian. High-resolution energetic particle measurements at 6.6 RE 3. Low-energy electron anisotropies and short-term substorm predictions. *Journal of Geophysical Research: Space Physics*, 83(A10):4863–4868, 1978. ISSN 2156-2202. doi: 10.1029/JA083iA10p04863.

D. N. Baker, T. I. Pulkkinen, V. Angelopoulos, W. Baumjohann, and R. L. McPherron. Neutral line model of substorms: Past results and present view. *Journal of Geophysical Research: Space Physics*, 101(A6):12975–13010, 1996. ISSN 2156-2202. doi: 10.1029/95JA03753.

S. J. Bame, J. R. Asbridge, H. E. Felthauser, E. W. Hones, and I. B. Strong. Characteristics of the plasma sheet in the Earth's magnetotail. *Journal of Geophysical Research (1896-1977)*, 72(1):113–129, 1967. ISSN 2156-2202. doi: 10.1029/JZ072i001p00113.

S. J. Bame, D. J. McComas, M. F. Thomsen, B. L. Barraclough, R. C. Elphic, J. P. Glore, J. T. Gosling, J. C. Chavez, E. P. Evans, and F. J. Wymer. Magnetospheric plasma analyzer for spacecraft with constrained resources. *Review of Scientific Instruments*, 64(4):1026–1033, Apr. 1993. ISSN 0034-6748, 1089-7623. doi: 10.1063/1.1144173.

W. Baumjohann and R. A. Treumann. *Basic Space Plasma Physics*. 1996. doi: 10.1142/p015.

W. Baumjohann, G. Paschmann, and C. A. Cattell. Average plasma properties in the central plasma sheet. *J. Geophys. Res.*, 94(A6):6597–6606, June 1989. ISSN 01480227. doi: 10.1029/JA094iA06p06597.

W. Baumjohann, M. Blanc, A. Fedorov, and K.-H. Glassmeier. Current Systems in Planetary Magnetospheres and Ionospheres. *Space Sci Rev*, 152(1):99–134, May 2010. ISSN 1572-9672. doi: 10.1007/s11214-010-9629-z.

R. D. Belian, D. N. Baker, P. R. Higbie, and E. W. Hones Jr. High-resolution energetic particle measurements at 6.6 RE, 2. High-energy proton drift echoes.

Journal of Geophysical Research: Space Physics, 83(A10):4857–4862, 1978. ISSN 2156-2202. doi: 10.1029/JA083iA10p04857.

R. D. Belian, G. R. Gisler, T. Cayton, and R. Christensen. High- Z energetic particles at geosynchronous orbit during the Great Solar Proton Event Series of October 1989. *J. Geophys. Res.*, 97(A11):16897–16906, Nov. 1992. ISSN 0148-0227. doi: 10.1029/92JA01139.

R. D. Belian, T. E. Cayton, and G. D. Reeves. Quasi-Periodic Global Substorm Generated Flux Variations Observed at Geosynchronous Orbit. In *Space Plasmas: Coupling Between Small and Medium Scale Processes*, pages 143–148. American Geophysical Union (AGU), 1995. ISBN 978-1-118-66405-6. doi: 10.1029/GM086p0143.

A. Bergin, S. C. Chapman, and J. W. Gjerloev. AE, D, and Their SuperMAG Counterparts: The Effect of Improved Spatial Resolution in Geomagnetic Indices. *Journal of Geophysical Research: Space Physics*, 125(5):e2020JA027828, 2020. ISSN 2169-9402. doi: 10.1029/2020JA027828.

K. Birkeland. *The Norwegian Aurora Polaris Expedition, 1902-1903*, volume 1. Christiania, H. Aschelhoug, 1908-, 1908.

J. Birn, M. F. Thomsen, J. E. Borovsky, G. D. Reeves, D. J. McComas, and R. D. Belian. Characteristic plasma properties during dispersionless substorm injections at geosynchronous orbit. *Journal of Geophysical Research*, 102:2309–2324, Feb. 1997. ISSN 0148-0227. doi: 10.1029/96JA02870.

T. Bloch, C. E. J. Watt, M. J. Owens, R. L. Thompson, and O. Agiwal. Constraining the Location of the Outer Boundary of Earth's Outer Radiation Belt. *Earth and Space Science*, 8(6):e2020EA001610, 2021. ISSN 2333-5084. doi: 10.1029/2020EA001610.

P. D. Boakes, S. E. Milan, G. A. Abel, M. P. Freeman, G. Chisham, and B. Hubert. A superposed epoch investigation of the relation between magnetospheric solar

wind driving and substorm dynamics with geosynchronous particle injection signatures. *Journal of Geophysical Research: Space Physics*, 116(A1), 2011. ISSN 2156-2202. doi: 10.1029/2010JA016007.

J. E. Borovsky. What magnetospheric and ionospheric researchers should know about the solar wind. *Journal of Atmospheric and Solar-Terrestrial Physics*, 204: 105271, Aug. 2020. ISSN 1364-6826. doi: 10.1016/j.jastp.2020.105271.

J. E. Borovsky and K. Yakymenko. Substorm occurrence rates, substorm recurrence times, and solar wind structure. *Journal of Geophysical Research: Space Physics*, 122(3):2973–2998, 2017. ISSN 2169-9402. doi: 10.1002/2016JA023625.

J. E. Borovsky, R. J. Nemzek, and R. D. Belian. The occurrence rate of magnetospheric-substorm onsets: Random and periodic substorms. *Journal of Geophysical Research: Space Physics*, 98(A3):3807–3813, 1993. ISSN 2156-2202. doi: 10.1029/92JA02556.

R. Boström. A model of the auroral electrojets. *Journal of Geophysical Research (1896-1977)*, 69(23):4983–4999, 1964. ISSN 2156-2202. doi: 10.1029/JZ069i023p04983.

J. Burch. IMAGE mission overview. *Space Science Reviews*, 91(1):1–14, Jan. 2000. ISSN 1572-9672. doi: 10.1023/A:1005245323115.

J. L. Burch, P. H. Reiff, J. D. Menietti, R. A. Heelis, W. B. Hanson, S. D. Shawhan, E. G. Shelley, M. Sugiura, D. R. Weimer, and J. D. Winningham. IMF B_y - dependent plasma flow and Birkeland currents in the dayside magnetosphere: 1. Dynamics Explorer observations. *J. Geophys. Res.*, 90(A2):1577–1593, Feb. 1985. ISSN 0148-0227. doi: 10.1029/JA090iA02p01577.

M. N. Caan, R. L. McPherron, and C. T. Russell. Substorm and interplanetary magnetic field effects on the geomagnetic tail lobes. *Journal of Geophysical Research (1896-1977)*, 80(1):191–194, 1975. ISSN 2156-2202. doi: 10.1029/JA080i001p00191.

M. N. Caan, R. L. McPherron, and C. T. Russell. The statistical magnetic signature of magnetospheric substorms. *Planetary and Space Science*, 26(3):269–279, Mar. 1978. ISSN 0032-0633. doi: 10.1016/0032-0633(78)90092-2.

L. J. Cahill and P. G. Amazeen. The boundary of the geomagnetic field. *Journal of Geophysical Research (1896-1977)*, 68(7):1835–1843, 1963. ISSN 2156-2202. doi: 10.1029/JZ068i007p01835.

X. Cai and C. R. Clauer. Investigation of the period of sawtooth events. *Journal of Geophysical Research: Space Physics*, 114(A6), 2009. ISSN 2156-2202. doi: 10.1029/2008JA013764.

X. Cai, M. G. Henderson, and C. R. Clauer. A statistical study of magnetic dipolarization for sawtooth events and isolated substorms at geosynchronous orbit with GOES data. *Annales Geophysicae*, 24(12):3481–3490, Dec. 2006. ISSN 0992-7689. doi: 10.5194/angeo-24-3481-2006.

X. Cai, J.-C. Zhang, C. R. Clauer, and M. W. Liemohn. Relationship between sawtooth events and magnetic storms. *Journal of Geophysical Research: Space Physics*, 116(A7), 2011. ISSN 2156-2202. doi: 10.1029/2010JA016310.

T. E. Cayton, R. D. Belian, S. P. Gary, T. A. Fritz, and D. N. Baker. Energetic electron components at geosynchronous orbit. *Geophysical Research Letters*, 16 (2):147–150, 1989. ISSN 1944-8007. doi: 10.1029/GL016i002p00147.

S. Chapman and V. C. A. Ferraro. A new theory of magnetic storms. *Terrestrial Magnetism and Atmospheric Electricity*, 36(2):77–97, 1931. ISSN 0096-8013. doi: 10.1029/TE036i002p00077.

F. F. Chen. *Introduction to Plasma Physics and Controlled Fusion: Volume 1: Plasma Physics*. Springer Science & Business Media, Mar. 2013. ISBN 978-1-4757-5595-4.

C. Cheng. Physics of Substorm Growth Phase, Onset, and Dipolarization. *Space*

Science Reviews, 113(1):207–270, Oct. 2004. ISSN 1572-9672. doi: 10.1023/B:SPAC.0000042943.59976.0e.

C. Z. Cheng and A. T. Y. Lui. Kinetic ballooning instability for substorm onset and current disruption observed by AMPTE/CCE. *Geophysical Research Letters*, 25 (21):4091–4094, 1998. ISSN 1944-8007. doi: 10.1029/1998GL900093.

X. Chu, T.-S. Hsu, R. L. McPherron, V. Angelopoulos, Z. Pu, J. J. Weygand, K. Khurana, M. Connors, J. Kissinger, H. Zhang, and O. Amm. Development and validation of inversion technique for substorm current wedge using ground magnetic field data. *Journal of Geophysical Research: Space Physics*, 119(3): 1909–1924, 2014. ISSN 2169-9402. doi: 10.1002/2013JA019185.

X. Chu, R. L. McPherron, T.-S. Hsu, and V. Angelopoulos. Solar cycle dependence of substorm occurrence and duration: Implications for onset. *Journal of Geophysical Research: Space Physics*, 120(4):2808–2818, 2015. ISSN 2169-9402. doi: 10.1002/2015JA021104.

C. R. Clauer and Y. Kamide. DP 1 and DP 2 current systems for the March 22, 1979 substorms. *Journal of Geophysical Research: Space Physics*, 90(A2):1343–1354, 1985. ISSN 2156-2202. doi: 10.1029/JA090iA02p01343.

C. R. Clauer and R. L. McPherron. Mapping the local time-universal time development of magnetospheric substorms using mid-latitude magnetic observations. *J. Geophys. Res.*, 79(19):2811–2820, July 1974a. ISSN 01480227. doi: 10.1029/JA079i019p02811.

C. R. Clauer and R. L. McPherron. Variability of mid-latitude magnetic parameters used to characterize magnetospheric substorms. *Journal of Geophysical Research (1896-1977)*, 79(19):2898–2900, 1974b. ISSN 2156-2202. doi: 10.1029/JA079i019p02898.

L. B. N. Clausen, J. B. H. Baker, J. M. Ruohoniemi, S. E. Milan, J. C. Coxon, S. Wing, S. Ohtani, and B. J. Anderson. Temporal and spatial dynamics of the

regions 1 and 2 Birkeland currents during substorms. *Journal of Geophysical Research: Space Physics*, 118(6):3007–3016, 2013. ISSN 2169-9402. doi: 10.1002/jgra.50288.

J. Cohen. A Coefficient of Agreement for Nominal Scales. *Educational and Psychological Measurement*, 20(1):37–46, Apr. 1960. ISSN 0013-1644. doi: 10.1177/001316446002000104.

F. V. Coroniti and C. F. Kennel. Changes in magnetospheric configuration during the substorm growth phase. *Journal of Geophysical Research (1896-1977)*, 77 (19):3361–3370, 1972a. ISSN 2156-2202. doi: 10.1029/JA077i019p03361.

F. V. Coroniti and C. F. Kennel. Polarization of the auroral electrojet. *Journal of Geophysical Research (1896-1977)*, 77(16):2835–2850, 1972b. ISSN 2156-2202. doi: 10.1029/JA077i016p02835.

V. Coumans, C. Blockx, J.-C. Gérard, B. Hubert, and M. Connors. Global morphology of substorm growth phases observed by the IMAGE-SI12 imager. *Journal of Geophysical Research: Space Physics*, 112(A11), 2007. ISSN 2156-2202. doi: 10.1029/2007JA012329.

S. W. H. Cowley. Plasma populations in a simple open model magnetosphere. *Space Sci Rev*, 26(3):217–275, July 1980. ISSN 1572-9672. doi: 10.1007/BF00167825.

S. W. H. Cowley. Magnetosphere-Ionosphere Interactions: A Tutorial Review. In *Magnetospheric Current Systems*, pages 91–106. American Geophysical Union (AGU), 2000. ISBN 978-1-118-66900-6. doi: 10.1029/GM118p0091.

S. W. H. Cowley and M. Lockwood. Excitation and decay of solar wind-driven flows in the magnetosphere-ionosphere system. *Annales Geophysicae*, 10:103–115, Feb. 1992. ISSN 0992-76891432-0576.

S. W. H. Cowley, J. P. Morelli, and M. Lockwood. Dependence of convective flows and particle precipitation in the high-latitude dayside ionosphere on the

X and Y components of the interplanetary magnetic field. *Journal of Geophysical Research: Space Physics*, 96(A4):5557–5564, 1991. ISSN 2156-2202. doi: 10.1029/90JA02063.

T. G. Cowling. The Electrical Conductivity of an Ionised Gas in the Presence of a Magnetic Field. *Monthly Notices of the Royal Astronomical Society*, 93(1): 90–97, Nov. 1932. ISSN 0035-8711. doi: 10.1093/mnras/93.1.90.

J. C. Coxon, S. E. Milan, L. B. N. Clausen, B. J. Anderson, and H. Korth. The magnitudes of the regions 1 and 2 Birkeland currents observed by AMPERE and their role in solar wind-magnetosphere-ionosphere coupling. *Journal of Geophysical Research: Space Physics*, 119(12):9804–9815, 2014a. ISSN 2169-9402. doi: 10.1002/2014JA020138.

J. C. Coxon, S. E. Milan, L. B. N. Clausen, B. J. Anderson, and H. Korth. A superposed epoch analysis of the regions 1 and 2 Birkeland currents observed by AMPERE during substorms. *Journal of Geophysical Research: Space Physics*, 119(12):9834–9846, 2014b. ISSN 2169-9402. doi: 10.1002/2014JA020500.

J. C. Coxon, I. J. Rae, C. Forsyth, C. M. Jackman, R. C. Fear, and B. J. Anderson. Birkeland currents during substorms: Statistical evidence for intensification of Regions 1 and 2 currents after onset and a localized signature of auroral dimming. *Journal of Geophysical Research: Space Physics*, 122(6):6455–6468, 2017. ISSN 2169-9402. doi: 10.1002/2017JA023967.

J. C. Coxon, M. P. Freeman, C. M. Jackman, C. Forsyth, I. J. Rae, and R. C. Fear. Tailward Propagation of Magnetic Energy Density Variations With Respect to Substorm Onset Times. *Journal of Geophysical Research: Space Physics*, 123 (6):4741–4754, 2018. ISSN 2169-9402. doi: 10.1029/2017JA025147.

N. U. Crooker. The magnetospheric boundary layers: A geometrically explicit model. *Journal of Geophysical Research (1896-1977)*, 82(25):3629–3633, 1977. ISSN 2156-2202. doi: 10.1029/JA082i025p03629.

W. D. Cummings and P. J. Coleman Jr. Simultaneous Magnetic Field Variations at the Earth's Surface and at Synchronous, Equatorial Distance. Part I. Bay-Associated Events. *Radio Science*, 3(7):758–761, 1968. ISSN 1944-799X. doi: 10.1002/rds196837758.

I. A. Daglis, R. M. Thorne, W. Baumjohann, and S. Orsini. The terrestrial ring current: Origin, formation, and decay. *Reviews of Geophysics*, 37(4):407–438, 1999. ISSN 1944-9208. doi: 10.1029/1999RG900009.

L. Dai, M. Zhu, Y. Ren, W. Gonzalez, C. Wang, D. Sibeck, A. Samsonov, P. Escoubet, B. Tang, J. Zhang, and G. Branduardi-Raymont. Global-scale magnetosphere convection driven by dayside magnetic reconnection. *Nat Commun*, 15(1):639, Jan. 2024. ISSN 2041-1723. doi: 10.1038/s41467-024-44992-y.

T. N. Davis and M. Sugiura. Auroral electrojet activity index AE and its universal time variations. *Journal of Geophysical Research (1896-1977)*, 71(3):785–801, 1966. ISSN 2156-2202. doi: 10.1029/JZ071i003p00785.

S. E. DeForest and C. E. McIlwain. Plasma clouds in the magnetosphere. *Journal of Geophysical Research (1896-1977)*, 76(16):3587–3611, 1971. ISSN 2156-2202. doi: 10.1029/JA076i016p03587.

A. D. DeJong, A. J. Ridley, X. Cai, and C. R. Clauer. A statistical study of BRIs (SMCs), isolated substorms, and individual sawtooth injections. *Journal of Geophysical Research: Space Physics*, 114(A8), 2009. ISSN 2156-2202. doi: 10.1029/2008JA013870.

G. L. Delzanno, J. E. Borovsky, M. G. Henderson, P. A. Resendiz Lira, V. Roytershteyn, and D. T. Welling. The impact of cold electrons and cold ions in magnetospheric physics. *Journal of Atmospheric and Solar-Terrestrial Physics*, 220: 105599, Sept. 2021. ISSN 1364-6826. doi: 10.1016/j.jastp.2021.105599.

M. H. Denton, J. E. Borovsky, and T. E. Cayton. A density-temperature description of the outer electron radiation belt during geomagnetic storms. *Journal of*

Geophysical Research: Space Physics, 115(A1), 2010. ISSN 2156-2202. doi: 10.1029/2009JA014183.

A. Dessler and J. A. Fejer. INTERPRETATION OF K, INDEX AND M-REGION GEOMAGNETIC STORMS. *Planetary and Space Science*, 1963.

S. Dimitrakoudis, D. K. Milling, A. Kale, and I. R. Mann. Sensitivity of Ground Magnetometer Array Elements for GIC Applications I: Resolving Spatial Scales With the BEAR and CARISMA Arrays. *Space Weather*, 20(1):e2021SW002919, 2022. ISSN 1542-7390. doi: 10.1029/2021SW002919.

I. Doxas, W. Horton, W. Lin, S. Seibert, and M. Mithaiwala. A dynamical model for the coupled inner magnetosphere and tail. *IEEE Transactions on Plasma Science*, 32(4):1443–1448, Aug. 2004. ISSN 1939-9375. doi: 10.1109/TPS.2004.833388.

J. W. Dungey. Interplanetary Magnetic Field and the Auroral Zones. *Phys. Rev. Lett.*, 6(2):47–48, Jan. 1961. doi: 10.1103/PhysRevLett.6.47.

J. W. Dungey. Interactions of solar plasma with the geomagnetic field. *Planetary and Space Science*, 10:233–237, Jan. 1963. ISSN 0032-0633. doi: 10.1016/0032-0633(63)90020-5.

T. E. Eastman, L. A. Frank, W. K. Peterson, and W. Lennartsson. The plasma sheet boundary layer. *Journal of Geophysical Research: Space Physics*, 89(A3):1553–1572, 1984. ISSN 2156-2202. doi: 10.1029/JA089iA03p01553.

M. El-Alaoui, R. J. Walker, and R. L. McPherron. Effects of the Ionospheric Conductance on the Dynamics of the Magnetotail. *Journal of Geophysical Research: Space Physics*, 128(1):e2022JA030259, 2023. ISSN 2169-9402. doi: 10.1029/2022JA030259.

R. Elhawary, K. M. Laundal, J. P. Reistad, and S. M. Hatch. Possible Ionospheric Influence on Substorm Onset Location. *Geophysical Research Letters*, 49(4):e2021GL096691, 2022. ISSN 1944-8007. doi: 10.1029/2021GL096691.

R. D. Elphinstone, J. S. Murphree, D. J. Hearn, L. L. Cogger, I. Sandahl, P. T. Newell, D. M. Klumpar, S. Ohtani, J. A. Sauvaud, T. A. Potemra, K. Mursula, A. Wright, and M. Shapshak. The double oval UV auroral distribution: 1. Implications for the mapping of auroral arcs. *Journal of Geophysical Research: Space Physics*, 100(A7):12075–12092, 1995. ISSN 2156-2202. doi: 10.1029/95JA00326.

D. H. Fairfield. Average and unusual locations of the Earth's magnetopause and bow shock. *Journal of Geophysical Research (1896-1977)*, 76(28):6700–6716, 1971. ISSN 2156-2202. doi: 10.1029/JA076i028p06700.

D. H. Fairfield. Advances in magnetospheric storm and substorm research: 1989–1991. *Journal of Geophysical Research: Space Physics*, 97(A7):10865–10874, 1992. ISSN 2156-2202. doi: 10.1029/92JA00326.

M. H. Farris and C. T. Russell. Determining the standoff distance of the bow shock: Mach number dependence and use of models. *Journal of Geophysical Research: Space Physics*, 99(A9):17681–17689, 1994. ISSN 2156-2202. doi: 10.1029/94JA01020.

U. Feldman, E. Landi, and N. A. Schwadron. On the sources of fast and slow solar wind. *Journal of Geophysical Research: Space Physics*, 110(A7), 2005. ISSN 2156-2202. doi: 10.1029/2004JA010918.

Ya.I. Feldstein. Magnetic field variations in the polar region during magnetically quiet periods and interplanetary magnetic fields. *Space Sci Rev*, 18(5-6), 1976. ISSN 0038-6308, 1572-9672. doi: 10.1007/BF00169523.

L. A. Fisk. Motion of the footpoints of heliospheric magnetic field lines at the Sun: Implications for recurrent energetic particle events at high heliographic latitudes. *Journal of Geophysical Research: Space Physics*, 101(A7):15547–15553, 1996. ISSN 2156-2202. doi: 10.1029/96JA01005.

V. Formisano, G. Moreno, F. Palmiotto, and P. C. Hedgecock. Solar wind interaction with the Earth's magnetic field: 1. Magnetosheath. *Journal of Geophys-*

ical Research (1896-1977), 78(19):3714–3730, 1973. ISSN 2156-2202. doi: 10.1029/JA078i019p03714.

C. Forsyth, A. N. Fazakerley, I. J. Rae, C. E. J. Watt, K. Murphy, J. A. Wild, T. Karlsson, R. Mutel, C. J. Owen, R. Ergun, A. Masson, M. Berthomier, E. Donovan, H. U. Frey, J. Matzka, C. Stolle, and Y. Zhang. In situ spatiotemporal measurements of the detailed azimuthal substructure of the substorm current wedge. *Journal of Geophysical Research: Space Physics*, 119(2):927–946, 2014a. ISSN 2169-9402. doi: 10.1002/2013JA019302.

C. Forsyth, C. E. J. Watt, I. J. Rae, A. N. Fazakerley, N. M. E. Kalmoni, M. P. Freeman, P. D. Boakes, R. Nakamura, I. Dandouras, L. M. Kistler, C. M. Jackman, J. C. Coxon, and C. M. Carr. Increases in plasma sheet temperature with solar wind driving during substorm growth phases. *Geophysical Research Letters*, 41 (24):8713–8721, 2014b. ISSN 1944-8007. doi: 10.1002/2014GL062400.

C. Forsyth, I. J. Rae, J. C. Coxon, M. P. Freeman, C. M. Jackman, J. Gjerloev, and A. N. Fazakerley. A new technique for determining Substorm Onsets and Phases from Indices of the Electrojet (SOPHIE). *Journal of Geophysical Research: Space Physics*, 120(12):10,592–10,606, 2015. ISSN 2169-9402. doi: 10.1002/2015JA021343.

C. Forsyth, I. J. Rae, K. R. Murphy, M. P. Freeman, C.-L. Huang, H. E. Spence, A. J. Boyd, J. C. Coxon, C. M. Jackman, N. M. E. Kalmoni, and C. E. J. Watt. What effect do substorms have on the content of the radiation belts? *Journal of Geophysical Research: Space Physics*, 121(7):6292–6306, 2016. ISSN 2169-9402. doi: 10.1002/2016JA022620.

C. Forsyth, M. Shortt, J. C. Coxon, I. J. Rae, M. P. Freeman, N. M. E. Kalmoni, C. M. Jackman, B. J. Anderson, S. E. Milan, and A. G. Burrell. Seasonal and Temporal Variations of Field-Aligned Currents and Ground Magnetic Deflections During Substorms. *Journal of Geophysical Research: Space Physics*, 123(4): 2696–2713, 2018. ISSN 2169-9402. doi: 10.1002/2017JA025136.

C. Forsyth, V. A. Sergeev, M. G. Henderson, Y. Nishimura, and B. Gallardo-Lacourt. Physical Processes of Meso-Scale, Dynamic Auroral Forms. *Space Sci Rev*, 216(4):46, Apr. 2020a. ISSN 1572-9672. doi: 10.1007/s11214-020-00665-y.

C. Forsyth, C. E. J. Watt, M. K. Mooney, I. J. Rae, S. D. Walton, and R. B. Horne. Forecasting GOES 15 >2 MeV Electron Fluxes From Solar Wind Data and Geomagnetic Indices. *Space Weather*, 18(8):e2019SW002416, 2020b. ISSN 1542-7390. doi: 10.1029/2019SW002416.

L. A. Frank and J. D. Craven. Imaging results from Dynamics Explorer 1. *Reviews of Geophysics*, 26(2):249–283, 1988. ISSN 1944-9208. doi: 10.1029/RG026i002p00249.

M. P. Freeman and S. K. Morley. A minimal substorm model that explains the observed statistical distribution of times between substorms. *Geophysical Research Letters*, 31(12), 2004. ISSN 1944-8007. doi: 10.1029/2004GL019989.

M. P. Freeman and S. K. Morley. No evidence for externally triggered substorms based on superposed epoch analysis of IMF Bz. *Geophysical Research Letters*, 36(21), 2009. ISSN 1944-8007. doi: 10.1029/2009GL040621.

M. P. Freeman, C. Forsyth, and I. J. Rae. The Influence of Substorms on Extreme Rates of Change of the Surface Horizontal Magnetic Field in the United Kingdom. *Space Weather*, 17(6):827–844, 2019. ISSN 1542-7390. doi: 10.1029/2018SW002148.

H. U. Frey and S. B. Mende. Substorm onsets as observed by IMAGE-FUV. page 6, 2006.

H. U. Frey, S. B. Mende, V. Angelopoulos, and E. F. Donovan. Substorm onset observations by IMAGE-FUV. *Journal of Geophysical Research: Space Physics*, 109(A10), 2004. ISSN 2156-2202. doi: 10.1029/2004JA010607.

E. Friis-Christensen and J. Wilhjelm. Polar cap currents for different directions of the interplanetary magnetic field in the Y-Z plane. *Journal of Geophysical Research (1896-1977)*, 80(10):1248–1260, 1975. ISSN 2156-2202. doi: 10.1029/JA080i010p01248.

E. Friis-Christensen, Y. Kamide, A. D. Richmond, and S. Matsushita. Interplanetary magnetic field control of high-latitude electric fields and currents determined from Greenland Magnetometer Data. *Journal of Geophysical Research: Space Physics*, 90(A2):1325–1338, 1985. ISSN 2156-2202. doi: 10.1029/JA090iA02p01325.

N. Fukushima. Equivalence in ground geomagnetic effect of chapman–vestine's and birkeland–alfven's electric current-systems for polar magnetic storms. *Rep. Ionosphere Space Res. Jap. 23: 219-27(1969).*, Jan. 1969.

N. Fukushima. Some topics and historical episodes in geomagnetism and aeronomy. *Journal of Geophysical Research: Space Physics*, 99(A10):19113–19142, 1994. ISSN 2156-2202. doi: 10.1029/94JA00102.

S. Fuselier, J. L. Burch, W. Lewis, and P. Reiff. Overview of the image science objectives and mission phases. *Space Science Reviews*, 91(1):51–66, Jan. 2000. ISSN 1572-9672. doi: 10.1023/A:1005255224024.

C. Gabrielse, V. Angelopoulos, A. Runov, and D. L. Turner. The effects of transient, localized electric fields on equatorial electron acceleration and transport toward the inner magnetosphere. *Journal of Geophysical Research: Space Physics*, 117 (A10), 2012. ISSN 2156-2202. doi: 10.1029/2012JA017873.

C. Gabrielse, T. Nishimura, M. Chen, J. H. Hecht, S. R. Kaeppler, D. M. Gillies, A. S. Reimer, L. R. Lyons, Y. Deng, E. Donovan, and J. S. Evans. Estimating Precipitating Energy Flux, Average Energy, and Hall Auroral Conductance From THEMIS All-Sky-Imagers With Focus on Mesoscales. *Front. Phys.*, 9, Oct. 2021. ISSN 2296-424X. doi: 10.3389/fphy.2021.744298.

J.-C. Gérard, B. Hubert, A. Grard, M. Meurant, and S. B. Mende. Solar wind control of auroral substorm onset locations observed with the IMAGE-FUV imagers. *Journal of Geophysical Research: Space Physics*, 109(A3), 2004. ISSN 2156-2202. doi: 10.1029/2003JA010129.

W. Gibson, J. Burch, J. Scherrer, M. Tapley, R. Killough, F. Volpe, W. Davis, D. Vaccarello, G. Grismore, D. Sakkas, and S. Housten. The IMAGE Observatory. *Space Science Reviews*, 91(1):15–50, Jan. 2000. ISSN 1572-9672. doi: 10.1023/A:1005203207186.

J. W. Gjerloev. The SuperMAG data processing technique. *Journal of Geophysical Research: Space Physics*, 117(A9), 2012. ISSN 2156-2202. doi: 10.1029/2012JA017683.

J. W. Gjerloev and R. A. Hoffman. The large-scale current system during auroral substorms. *Journal of Geophysical Research: Space Physics*, 119(6):4591–4606, 2014. ISSN 2169-9402. doi: 10.1002/2013JA019176.

J. W. Gjerloev, R. A. Hoffman, J. B. Sigwarth, and L. A. Frank. Statistical description of the bulge-type auroral substorm in the far ultraviolet. *Journal of Geophysical Research: Space Physics*, 112(A7), 2007. ISSN 2156-2202. doi: 10.1029/2006JA012189.

J. D. Haiducek, D. T. Welling, S. K. Morley, N. Y. Ganushkina, and X. Chu. Using Multiple Signatures to Improve Accuracy of Substorm Identification. *Journal of Geophysical Research: Space Physics*, 125(4):e2019JA027559, 2020. ISSN 2169-9402. doi: 10.1029/2019JA027559.

J. K. J. K. Hargreaves. *The Solar-Terrestrial Environment : An Introduction to Geospace–the Science of the Terrestrial Upper Atmosphere, Ionosphere, and Magnetosphere*. Cambridge University Press, 1992. ISBN 978-0-521-32748-0 978-0-521-42737-1.

M. G. Henderson. The May 2–3, 1986 CDAW-9C interval: A sawtooth event.

Geophysical Research Letters, 31(11), 2004. ISSN 1944-8007. doi: 10.1029/2004GL019941.

M. G. Henderson. Association of Mesoscale Auroral Structures and Breakups With Energetic Particle Injections at Geosynchronous Orbit. *Frontiers in Astronomy and Space Sciences*, 9, 2022. ISSN 2296-987X. doi: 10.3389/fspas.2022.742246.

M. G. Henderson, G. D. Reeves, R. Skoug, M. F. Thomsen, M. H. Denton, S. B. Mende, T. J. Immel, P. C. Brandt, and H. J. Singer. Magnetospheric and auroral activity during the 18 April 2002 sawtooth event. *Journal of Geophysical Research: Space Physics*, 111(A1), 2006a. ISSN 2156-2202. doi: 10.1029/2005JA011111.

M. G. Henderson, R. Skoug, E. Donovan, M. F. Thomsen, G. D. Reeves, M. H. Denton, H. J. Singer, R. L. McPherron, S. B. Mende, T. J. Immel, J. B. Sigwarth, and L. A. Frank. Substorms during the 10–11 August 2000 sawtooth event. *Journal of Geophysical Research: Space Physics*, 111(A6), 2006b. ISSN 2156-2202. doi: 10.1029/2005JA011366.

J. P. Heppner. Time sequences and spatial relations in auroral activity during magnetic bays at College, Alaska. *Journal of Geophysical Research (1896-1977)*, 59 (3):329–338, 1954. ISSN 2156-2202. doi: 10.1029/JZ059i003p00329.

M. Hesse and P. A. Cassak. Magnetic Reconnection in the Space Sciences: Past, Present, and Future. *Journal of Geophysical Research: Space Physics*, 125(2): e2018JA025935, 2020. ISSN 2169-9402. doi: 10.1029/2018JA025935.

R. J. Hogan and I. B. Mason. Deterministic Forecasts of Binary Events. In *Forecast Verification*, chapter 3, pages 31–59. John Wiley & Sons, Ltd, 2011. ISBN 978-1-119-96000-3. doi: 10.1002/9781119960003.ch3.

R. E. Holzer and J. A. Slavin. Magnetic flux transfer associated with expansions and contractions of the dayside magnetosphere. *Journal of Geophysical Research: Space Physics*, 83(A8):3831–3839, 1978. ISSN 2156-2202. doi: 10.1029/JA083iA08p03831.

E. W. Hones Jr. Observations in the Earth's Magnetotail Relating to Magnetic Merging (Invited paper). *Solar Physics*, 47:101–113, Mar. 1976. ISSN 0038-0938. doi: 10.1007/BF00152248.

E. W. Hones Jr. Plasma Sheet Behavior During Substorms. In *Magnetic Reconnection in Space and Laboratory Plasmas*, pages 178–184. American Geophysical Union (AGU), 1984. ISBN 978-1-118-66422-3. doi: 10.1029/GM030p0178.

E. W. Hones Jr., T. A. Fritz, J. Birn, J. Cooney, and S. J. Bame. Detailed observations of the plasma sheet during a substorm on April 24, 1979. *Journal of Geophysical Research: Space Physics*, 91(A6):6845–6859, 1986. ISSN 2156-2202. doi: 10.1029/JA091iA06p06845.

C.-S. Huang. Evidence of periodic (2–3 hour) near-tail magnetic reconnection and plasmoid formation: Geotail observations. *Geophysical Research Letters*, 29 (24):42–1–42–4, 2002. ISSN 1944-8007. doi: 10.1029/2002GL016162.

C.-S. Huang, J. C. Foster, G. D. Reeves, G. Le, H. U. Frey, C. J. Pollock, and J.-M. Jahn. Periodic magnetospheric substorms: Multiple space-based and ground-based instrumental observations. *Journal of Geophysical Research: Space Physics*, 108(A11), 2003. ISSN 2156-2202. doi: 10.1029/2003JA009992.

C.-S. Huang, A. D. DeJong, and X. Cai. Magnetic flux in the magnetotail and polar cap during sawteeth, isolated substorms, and steady magnetospheric convection events. *Journal of Geophysical Research: Space Physics*, 114(A7), 2009. ISSN 2156-2202. doi: 10.1029/2009JA014232.

T. Iijima and T. A. Potemra. The amplitude distribution of field-aligned currents at northern high latitudes observed by Triad. *Journal of Geophysical Research (1896-1977)*, 81(13):2165–2174, 1976a. ISSN 2156-2202. doi: 10.1029/JA081i013p02165.

T. Iijima and T. A. Potemra. Field-aligned currents in the dayside cusp observed by Triad. *Journal of Geophysical Research (1896-1977)*, 81(34):5971–5979, 1976b. ISSN 2156-2202. doi: 10.1029/JA081i034p05971.

T. Iijima and T. A. Potemra. Large-scale characteristics of field-aligned currents associated with substorms. *Journal of Geophysical Research: Space Physics*, 83 (A2):599–615, 1978. ISSN 2156-2202. doi: 10.1029/JA083iA02p00599.

T. Iijima, T. A. Potemra, L. J. Zanetti, and P. F. Bythrow. Large-scale Birkeland currents in the dayside polar region during strongly northward IMF: A new Birkeland current system. *Journal of Geophysical Research: Space Physics*, 89(A9): 7441–7452, 1984. ISSN 2156-2202. doi: 10.1029/JA089iA09p07441.

T. Iyemori. Time Delay of the Substorm Onset from the IMF Southward Turning. *Journal of geomagnetism and geoelectricity*, 32(5):267–273, 1980. doi: 10.5636/jgg.32.267.

A. N. Jaynes, D. N. Baker, H. J. Singer, J. V. Rodriguez, T. M. Loto'aniu, A. F. Ali, S. R. Elkington, X. Li, S. G. Kanekal, S. G. Claudepierre, J. F. Fennell, W. Li, R. M. Thorne, C. A. Kletzing, H. E. Spence, and G. D. Reeves. Source and seed populations for relativistic electrons: Their roles in radiation belt changes. *Journal of Geophysical Research: Space Physics*, 120(9):7240–7254, 2015. ISSN 2169-9402. doi: 10.1002/2015JA021234.

N. M. E. Kalmoni, I. J. Rae, K. R. Murphy, C. Forsyth, C. E. J. Watt, and C. J. Owen. Statistical azimuthal structuring of the substorm onset arc: Implications for the onset mechanism. *Geophysical Research Letters*, 44(5):2078–2087, 2017. ISSN 1944-8007. doi: 10.1002/2016GL071826.

N. M. E. Kalmoni, I. J. Rae, C. E. J. Watt, K. R. Murphy, M. Samara, R. G. Michell, G. Grubbs, and C. Forsyth. A diagnosis of the plasma waves responsible for the explosive energy release of substorm onset. *Nat Commun*, 9(1):4806, Nov. 2018. ISSN 2041-1723. doi: 10.1038/s41467-018-07086-0.

Y. Kamide. The two-component auroral electrojet. *Geophysical Research Letters*, 9(10):1175–1178, 1982. ISSN 1944-8007. doi: 10.1029/GL009i010p01175.

Y. Kamide and S. Kokubun. Two-component auroral electrojet: Importance for

substorm studies. *Journal of Geophysical Research: Space Physics*, 101(A6): 13027–13046, 1996. ISSN 2156-2202. doi: 10.1029/96JA00142.

Y. Kamide and C. E. McIlwain. The onset time of magnetospheric substorms determined from ground and synchronous satellite records. *Journal of Geophysical Research (1896-1977)*, 79(31):4787–4790, 1974. ISSN 2156-2202. doi: 10.1029/JA079i031p04787.

Y. Kamide, W. Sun, and S.-I. Akasofu. The average ionospheric electrodynamics for the different substorm phases. *Journal of Geophysical Research: Space Physics*, 101(A1):99–109, 1996. ISSN 2156-2202. doi: 10.1029/95JA02990.

J. R. Kan and L. C. Lee. Energy coupling function and solar wind-magnetosphere dynamo. *Geophysical Research Letters*, 6(7):577–580, 1979. ISSN 1944-8007. doi: 10.1029/GL006i007p00577.

P. J. Kellogg. Flow of plasma around the Earth. *Journal of Geophysical Research (1896-1977)*, 67(10):3805–3811, 1962. ISSN 2156-2202. doi: 10.1029/JZ067i010p03805.

L. Kepko, R. L. McPherron, O. Amm, S. Apatenkov, W. Baumjohann, J. Birn, M. Lester, R. Nakamura, T. I. Pulkkinen, and V. Sergeev. Substorm Current Wedge Revisited. *Space Sci Rev*, 190(1):1–46, July 2015. ISSN 1572-9672. doi: 10.1007/s11214-014-0124-9.

K. K. Khurana, R. J. Walker, and T. Ogino. Magnetospheric convection in the presence of interplanetary magnetic field B : A conceptual model and simulations. *Journal of Geophysical Research: Space Physics*, 101(A3):4907–4916, 1996. ISSN 2156-2202. doi: 10.1029/95JA03673.

J. H. King and N. E. Papitashvili. Solar wind spatial scales in and comparisons of hourly Wind and ACE plasma and magnetic field data. *Journal of Geophysical Research: Space Physics*, 110(A2), 2005. ISSN 2156-2202. doi: 10.1029/2004JA010649.

J. Kissinger, R. L. McPherron, V. Angelopoulos, T.-S. Hsu, and J. P. McFadden. An investigation of the association between steady magnetospheric convection and CIR stream interfaces. *Geophysical Research Letters*, 37(4), 2010. ISSN 1944-8007. doi: 10.1029/2009GL041541.

J. Kissinger, R. L. McPherron, T.-S. Hsu, and V. Angelopoulos. Steady magnetospheric convection and stream interfaces: Relationship over a solar cycle. *Journal of Geophysical Research: Space Physics*, 116(A5), 2011. ISSN 2156-2202. doi: 10.1029/2010JA015763.

J. Kissinger, R. L. McPherron, T.-S. Hsu, V. Angelopoulos, and X. Chu. Necessity of substorm expansions in the initiation of steady magnetospheric convection. *Geophysical Research Letters*, 39(15), 2012. ISSN 1944-8007. doi: 10.1029/2012GL052599.

M. G. Kivelson and C. T. Russell. *Introduction to Space Physics*. Cambridge University Press, Cambridge, 1995.

S. Kokubun and T. Iijima. Time-sequence of polar magnetic substorms. *Planetary and Space Science*, 23:1483–1494, Nov. 1975.

H. E. J. Koskinen, R. E. Lopez, R. J. Pellinen, T. I. Pulkkinen, D. N. Baker, and T. Bösinger. Pseudobreakup and substorm growth phase in the ionosphere and magnetosphere. *Journal of Geophysical Research: Space Physics*, 98(A4):5801–5813, 1993. ISSN 2156-2202. doi: 10.1029/92JA02482.

A. Kullen and T. Karlsson. On the relation between solar wind, pseudobreakups, and substorms. *Journal of Geophysical Research: Space Physics*, 109(A12), 2004. ISSN 2156-2202. doi: 10.1029/2004JA010488.

J. Laitinen, L. Holappa, and H. Vanhamäki. The Polarity of IMF B Strongly Modulates Particle Precipitation During High-Speed Streams. *Geophysical Research Letters*, 51(17):e2024GL110877, 2024. ISSN 1944-8007. doi: 10.1029/2024GL110877.

C. J. Lao, C. Forsyth, M. P. Freeman, A. W. Smith, and M. K. Mooney. On the Association of Substorm Identification Methods. *Journal of Geophysical Research: Space Physics*, 129(9):e2024JA032762, 2024. ISSN 2169-9402. doi: 10.1029/2024JA032762.

C. J. Lao, C. Forsyth, M. P. Freeman, and J. W. Gjerloev. Separating DP1 and DP2 Current Pattern Contributions to Substorm-Like Intensifications in SML. *Journal of Geophysical Research: Space Physics*, 130(4):e2024JA033592, 2025. ISSN 2169-9402. doi: 10.1029/2024JA033592.

D.-Y. Lee, L. R. Lyons, and K. Yumoto. Sawtooth oscillations directly driven by solar wind dynamic pressure enhancements. *Journal of Geophysical Research: Space Physics*, 109(A4), 2004. ISSN 2156-2202. doi: 10.1029/2003JA010246.

J. F. Lemaire and K. I. Gringauz. *The Earth's Plasmasphere*. Cambridge Atmospheric and Space Science Series. Cambridge University Press, Cambridge, 1998. ISBN 978-0-521-43091-3. doi: 10.1017/CBO9780511600098.

T. W. Lezniak, R. L. Arnoldy, G. K. Parks, and J. R. Winckler. Measurement and Intensity of Energetic Electrons at the Equator at 6.6 Re. *Radio Science*, 3(7): 710–714, 1968. ISSN 1944-799X. doi: 10.1002/rds196837710.

H. Li, C. Wang, and Z. Peng. Solar wind impacts on growth phase duration and substorm intensity: A statistical approach. *Journal of Geophysical Research: Space Physics*, 118(7):4270–4278, 2013. ISSN 2169-9402. doi: 10.1002/jgra.50399.

W. Li and M. Hudson. Earth's Van Allen Radiation Belts: From Discovery to the Van Allen Probes Era. *Journal of Geophysical Research: Space Physics*, 124 (11):8319–8351, 2019. ISSN 2169-9402. doi: 10.1029/2018JA025940.

X. Li, D. N. Baker, M. Temerin, G. D. Reeves, and R. D. Belian. Simulation of dispersionless injections and drift echoes of energetic electrons associated with substorms. *Geophysical Research Letters*, 25(20):3763–3766, 1998. ISSN 1944-8007. doi: 10.1029/1998GL900001.

M. W. Liemohn, A. D. Shane, A. R. Azari, A. K. Petersen, B. M. Swiger, and A. Mukhopadhyay. RMSE is not enough: Guidelines to robust data-model comparisons for magnetospheric physics. *Journal of Atmospheric and Solar-Terrestrial Physics*, 218:105624, July 2021. ISSN 1364-6826. doi: 10.1016/j.jastp.2021.105624.

K. Liou. Polar Ultraviolet Imager observation of auroral breakup. *Journal of Geophysical Research: Space Physics*, 115(A12), 2010. ISSN 2156-2202. doi: 10.1029/2010JA015578.

K. Liou and P. T. Newell. On the azimuthal location of auroral breakup: Hemispheric asymmetry. *Geophysical Research Letters*, 37(23), 2010. ISSN 1944-8007. doi: 10.1029/2010GL045537.

K. Liou, P. T. Newell, D. G. Sibeck, C.-I. Meng, M. Brittnacher, and G. Parks. Observation of IMF and seasonal effects in the location of auroral substorm onset. *Journal of Geophysical Research: Space Physics*, 106(A4):5799–5810, 2001. ISSN 2156-2202. doi: 10.1029/2000JA003001.

J. Liu, V. Angelopoulos, A. Runov, and X.-Z. Zhou. On the current sheets surrounding dipolarizing flux bundles in the magnetotail: The case for wedgelets. *Journal of Geophysical Research: Space Physics*, 118(5):2000–2020, 2013. ISSN 2169-9402. doi: 10.1002/jgra.50092.

J. Liu, V. Angelopoulos, X. Chu, X.-Z. Zhou, and C. Yue. Substorm current wedge composition by wedgelets. *Geophysical Research Letters*, 42(6):1669–1676, 2015. ISSN 1944-8007. doi: 10.1002/2015GL063289.

M. Lockwood. Universal Time Effects on Substorm Growth Phases and Onsets. *Journal of Geophysical Research: Space Physics*, 128(11):e2023JA031671, 2023. ISSN 2169-9402. doi: 10.1029/2023JA031671.

M. Lockwood and K. A. McWilliams. On Optimum Solar Wind-Magnetosphere Coupling Functions for Transpolar Voltage and Planetary Geomagnetic Activ-

ity. *Journal of Geophysical Research: Space Physics*, 126(12):e2021JA029946, 2021. ISSN 2169-9402. doi: 10.1029/2021JA029946.

M. Lockwood, S. W. H. Cowley, and M. P. Freeman. The excitation of plasma convection in the high-latitude ionosphere. *Journal of Geophysical Research: Space Physics*, 95(A6):7961–7972, 1990. ISSN 2156-2202. doi: 10.1029/JA095iA06p07961.

A. Lui. Potential Plasma Instabilities For Substorm Expansion Onsets. *Space Sci Rev*, 113(1):127–206, July 2004. ISSN 1572-9672. doi: 10.1023/B:SPAC.0000042942.00362.4e.

A. T. Y. Lui. Characteristics of the Cross-Tail Current in the Earth's Magnetotail. In *Magnetospheric Currents*, pages 158–170. American Geophysical Union (AGU), 1984. ISBN 978-1-118-66413-1. doi: 10.1029/GM028p0158.

A. T. Y. Lui. A synthesis of magnetospheric substorm models. *Journal of Geophysical Research: Space Physics*, 96(A2):1849–1856, 1991. ISSN 2156-2202. doi: 10.1029/90JA02430.

A. T. Y. Lui. Current disruption in the Earth's magnetosphere: Observations and models. *Journal of Geophysical Research: Space Physics*, 101(A6):13067–13088, 1996. ISSN 2156-2202. doi: 10.1029/96JA00079.

A. T. Y. Lui, C.-L. Chang, A. Mankofsky, H.-K. Wong, and D. Winske. A cross-field current instability for substorm expansions. *Journal of Geophysical Research: Space Physics*, 96(A7):11389–11401, 1991. ISSN 2156-2202. doi: 10.1029/91JA00892.

K. Maezawa. Magnetospheric convection induced by the positive and negative Z components of the interplanetary magnetic field: Quantitative analysis using polar cap magnetic records. *Journal of Geophysical Research (1896-1977)*, 81(13):2289–2303, 1976. ISSN 2156-2202. doi: 10.1029/JA081i013p02289.

M. Maimaiti, B. Kunduri, J. M. Ruohoniemi, J. B. H. Baker, and L. L. House. A Deep Learning-Based Approach to Forecast the Onset of Magnetic Substorms. *Space Weather*, 17(11):1534–1552, 2019. ISSN 1542-7390. doi: 10.1029/2019SW002251.

B. H. Mauk and C.-I. Meng. Characterization of geostationary particle signatures based on the 'Injection Boundary' Model. *Journal of Geophysical Research: Space Physics*, 88(A4):3055–3071, 1983. ISSN 2156-2202. doi: 10.1029/JA088iA04p03055.

H. McCreadie and M. Menvielle. The PC index: Review of methods. *Annales Geophysicae*, 28(10):1887–1903, Oct. 2010. ISSN 0992-7689. doi: 10.5194/angeo-28-1887-2010.

C. E. McIlwain. Substorm injection boundaries. In B. M. McCormac, editor, *Magnetospheric Physics*, pages 143–154, Dordrecht, 1974. Springer Netherlands. ISBN 978-94-010-2214-9.

R. L. McPherron. Growth phase of magnetospheric substorms. *Journal of Geophysical Research (1896-1977)*, 75(28):5592–5599, 1970. ISSN 2156-2202. doi: 10.1029/JA075i028p05592.

R. L. McPherron and X. Chu. The Mid-Latitude Positive Bay and the MPB Index of Substorm Activity. *Space Sci Rev*, 206(1):91–122, Mar. 2017. ISSN 1572-9672. doi: 10.1007/s11214-016-0316-6.

R. L. McPherron and X. Chu. The Midlatitude Positive Bay Index and the Statistics of Substorm Occurrence. *Journal of Geophysical Research: Space Physics*, 123 (4):2831–2850, 2018. ISSN 2169-9402. doi: 10.1002/2017JA024766.

R. L. McPherron, C. T. Russell, and M. P. Aubry. Satellite studies of magnetospheric substorms on August 15, 1968: 9. Phenomenological model for substorms. *Journal of Geophysical Research (1896-1977)*, 78(16):3131–3149, 1973. ISSN 2156-2202. doi: 10.1029/JA078i016p03131.

R. L. McPherron, T. P. O'Brien, and S. Thompson. Solar wind drivers for steady magnetospheric convection. 2005.

R. L. McPherron, J. M. Weygand, and T.-S. Hsu. Response of the Earth's magnetosphere to changes in the solar wind. *Journal of Atmospheric and Solar-Terrestrial Physics*, 70(2-4):303–315, Feb. 2008. ISSN 13646826. doi: 10.1016/j.jastp.2007.08.040.

K. A. McWilliams, J. B. Pfeifer, and R. L. McPherron. Steady magnetospheric convection selection criteria: Implications of global SuperDARN convection measurements. *Geophysical Research Letters*, 35(9), 2008. ISSN 1944-8007. doi: 10.1029/2008GL033671.

M. M. Meier, R. D. Belian, T. E. Cayton, R. A. Christensen, B. Garcia, K. M. Grace, J. C. Ingraham, J. G. Laros, and G. D. Reeves. The energy spectrometer for particles (ESP): Instrument description and orbital performance. In *AIP Conference Proceedings*, volume 383, pages 203–210, Taos, New Mexico (USA), 1996. AIP. doi: 10.1063/1.51533.

S. Mende, H. Heetderks, H. Frey, M. Lampton, S. Geller, R. Abiad, O. Siegmund, A. Tremsin, J. Spann, H. Dougani, S. Fuselier, A. Magoncelli, M. Bumala, S. Murphree, and T. Trondsen. Far ultraviolet imaging from the IMAGE spacecraft. 2. Wideband FUV imaging. *Space Science Reviews*, 91(1):271–285, Jan. 2000a. ISSN 1572-9672. doi: 10.1023/A:1005227915363.

S. Mende, H. Heetderks, H. Frey, M. Lampton, S. Geller, S. Habraken, E. Renotte, C. Jamar, P. Rochus, J. Spann, S. Fuselier, J.-C. Gerard, R. Gladstone, S. Murphree, and L. Cogger. Far ultraviolet imaging from the IMAGE spacecraft. 1. System design. *Space Science Reviews*, 91(1):243–270, Jan. 2000b. ISSN 1572-9672. doi: 10.1023/A:1005271728567.

S. Mende, H. Heetderks, H. Frey, J. Stock, M. Lampton, S. Geller, R. Abiad, O. Siegmund, S. Habraken, E. Renotte, C. Jamar, P. Rochus, J.-C. Gerard, R. Sigler, and H. Lauche. Far ultraviolet imaging from the IMAGE spacecraft. 3.

Spectral imaging of Lyman-α and OI 135.6 nm. *Space Science Reviews*, 91(1): 287–318, Jan. 2000c. ISSN 1572-9672. doi: 10.1023/A:1005292301251.

S. B. Mende, S. E. Harris, H. U. Frey, V. Angelopoulos, C. T. Russell, E. Donovan, B. Jackel, M. Greffen, and L. M. Peticolas. The THEMIS Array of Ground-based Observatories for the Study of Auroral Substorms. *Space Sci Rev*, 141(1-4):357–387, Dec. 2008. ISSN 0038-6308, 1572-9672. doi: 10.1007/s11214-008-9380-x.

C.-I. Meng. Polar cap variations and the interplanetary magnetic field. In S.-I. Akasofu, editor, *Dynamics of the Magnetosphere*, pages 23–46, Dordrecht, 1980. Springer Netherlands. ISBN 978-94-009-9519-2.

S. E. Milan, G. Provan, and B. Hubert. Magnetic flux transport in the Dungey cycle: A survey of dayside and nightside reconnection rates. *Journal of Geophysical Research: Space Physics*, 112(A1), 2007. ISSN 2156-2202. doi: 10.1029/2006JA011642.

S. E. Milan, J. Hutchinson, P. D. Boakes, and B. Hubert. Influences on the radius of the auroral oval. *Annales Geophysicae*, 27(7):2913–2924, July 2009. ISSN 0992-7689. doi: 10.5194/angeo-27-2913-2009.

S. E. Milan, L. B. N. Clausen, J. C. Coxon, J. A. Carter, M.-T. Walach, K. Laundal, N. Østgaard, P. Tenfjord, J. Reistad, K. Snekvik, H. Korth, and B. J. Anderson. Overview of Solar Wind–Magnetosphere–Ionosphere–Atmosphere Coupling and the Generation of Magnetospheric Currents. *Space Sci Rev*, 206(1):547–573, Mar. 2017. ISSN 1572-9672. doi: 10.1007/s11214-017-0333-0.

S. E. Milan, J. A. Carter, H. Sangha, G. E. Bower, and B. J. Anderson. Magnetospheric Flux Throughput in the Dungey Cycle: Identification of Convection State During 2010. *Journal of Geophysical Research: Space Physics*, 126(2): e2020JA028437, 2021. ISSN 2169-9402. doi: 10.1029/2020JA028437.

V. Mishin and Y. Karavaev. Saturation of the magnetosphere during superstorms: New results from the magnetogram inversion technique. *Solar-Terrestrial Physics*, 3(3):28–36, Oct. 2017. doi: 10.12737/stp-33201704.

M. D. Montgomery, J. R. Asbridge, and S. J. Bame. Vela 4 plasma observations near the Earth's bow shock. *Journal of Geophysical Research (1896-1977)*, 75 (7):1217–1231, 1970. ISSN 2156-2202. doi: 10.1029/JA075i007p01217.

M. K. Mooney, C. Forsyth, I. J. Rae, G. Chisham, J. C. Coxon, M. S. Marsh, D. R. Jackson, S. Bingham, and B. Hubert. Examining Local Time Variations in the Gains and Losses of Open Magnetic Flux During Substorms. *Journal of Geophysical Research: Space Physics*, 125(4):e2019JA027369, 2020. ISSN 2169-9402. doi: 10.1029/2019JA027369.

M. K. Mooney, M. S. Marsh, C. Forsyth, M. Sharpe, T. Hughes, S. Bingham, D. R. Jackson, I. J. Rae, and G. Chisham. Evaluating Auroral Forecasts Against Satellite Observations. *Space Weather*, 19(8):e2020SW002688, 2021. ISSN 1542-7390. doi: 10.1029/2020SW002688.

M. K. Mooney, C. Forsyth, M. S. Marsh, L. Bradley, T. Finnigan, F. Forde, F. Garrigan, C. Mancini-Tuffier, T. Mancini-Tuffier, E. Roberts, P. Vessoni, J. Powell, S. Clark, C. J. Lao, A. Smith, D. R. Jackson, S. Bingham, M. Sharpe, T. Hughes, G. Chisham, and S. Milan. Evaluating Auroral Forecasts Against Satellite Observations Under Different Levels of Geomagnetic Activity. *Journal of Geophysical Research: Space Physics*, 129(8):e2023JA031478, 2024. ISSN 2169-9402. doi: 10.1029/2023JA031478.

T. E. Moore, R. L. Arnoldy, J. Feynman, and D. A. Hardy. Propagating substorm injection fronts. *Journal of Geophysical Research: Space Physics*, 86(A8):6713–6726, 1981. ISSN 2156-2202. doi: 10.1029/JA086iA08p06713.

S. K. Morley and M. P. Freeman. On the association between northward turnings of the interplanetary magnetic field and substorm onsets. *Geophysical Research Letters*, 34(8), 2007. ISSN 1944-8007. doi: 10.1029/2006GL028891.

S. K. Morley, M. P. Freeman, and E. I. Tanskanen. A comparison of the probability distribution of observed substorm magnitude with that predicted by a minimal

substorm model. *Annales Geophysicae*, 25(11):2427–2437, Nov. 2007. ISSN 0992-7689. doi: 10.5194/angeo-25-2427-2007.

K. R. Murphy, D. M. Miles, C. E. J. Watt, I. J. Rae, I. R. Mann, and H. U. Frey. Automated determination of auroral breakup during the substorm expansion phase using all-sky imager data. *Journal of Geophysical Research: Space Physics*, 119 (2):1414–1427, 2014. ISSN 2169-9402. doi: 10.1002/2013JA018773.

K. R. Murphy, S. N. Bentley, D. M. Miles, J. K. Sandhu, and A. W. Smith. Imaging the magnetosphere–ionosphere system with ground-based and in-situ magnetometers. In *Magnetospheric Imaging*, pages 287–340. Elsevier, 2022. ISBN 978-0-12-820630-0. doi: 10.1016/B978-0-12-820630-0.00002-7.

R. Nakamura, D. N. Baker, T. Yamamoto, R. D. Belian, E. A. Bering III, J. R. Benbrook, and J. R. Theall. Particle and field signatures during pseudobreakup and major expansion onset. *Journal of Geophysical Research: Space Physics*, 99 (A1):207–221, 1994. ISSN 2156-2202. doi: 10.1029/93JA02207.

R. Nakamura, W. Baumjohann, Y. Asano, A. Runov, A. Balogh, C. J. Owen, A. N. Fazakerley, M. Fujimoto, B. Klecker, and H. Rème. Dynamics of thin current sheets associated with magnetotail reconnection. *Journal of Geophysical Research: Space Physics*, 111(A11), 2006. ISSN 2156-2202. doi: 10.1029/2006JA011706.

N. F. Ness. The Earth's magnetic tail. *Journal of Geophysical Research (1896-1977)*, 70(13):2989–3005, 1965. ISSN 2156-2202. doi: 10.1029/JZ070i013p02989.

M. Neugebauer and C. W. Snyder. Mariner 2 observations of the solar wind: 1. Average properties. *Journal of Geophysical Research (1896-1977)*, 71(19):4469–4484, 1966. ISSN 2156-2202. doi: 10.1029/JZ071i019p04469.

P. T. Newell and J. W. Gjerloev. Evaluation of SuperMAG auroral electrojet indices as indicators of substorms and auroral power. *Journal of Geophysical Research: Space Physics*, 116(A12), 2011. ISSN 2156-2202. doi: 10.1029/2011JA016779.

P. T. Newell and J. W. Gjerloev. Local geomagnetic indices and the prediction of auroral power. *Journal of Geophysical Research: Space Physics*, 119(12):9790–9803, 2014. ISSN 2169-9402. doi: 10.1002/2014JA020524.

P. T. Newell, C.-I. Meng, and K. M. Lyons. Suppression of discrete aurorae by sunlight. *Nature*, 381(6585):766–767, June 1996. ISSN 0028-0836, 1476-4687. doi: 10.1038/381766a0.

P. T. Newell, T. Sotirelis, K. Liou, C.-I. Meng, and F. J. Rich. A nearly universal solar wind-magnetosphere coupling function inferred from 10 magnetospheric state variables. *Journal of Geophysical Research: Space Physics*, 112(A1), 2007. ISSN 2156-2202. doi: 10.1029/2006JA012015.

A. Nishida. Coherence of geomagnetic DP 2 fluctuations with interplanetary magnetic variations. *Journal of Geophysical Research (1896-1977)*, 73(17):5549–5559, 1968a. ISSN 2156-2202. doi: 10.1029/JA073i017p05549.

A. Nishida. Geomagnetic Dp 2 fluctuations and associated magnetospheric phenomena. *Journal of Geophysical Research (1896-1977)*, 73(5):1795–1803, 1968b. ISSN 2156-2202. doi: 10.1029/JA073i005p01795.

A. Nishida and Y. Kamide. Magnetospheric processes preceding the onset of an isolated substorm: A Case study of the March 31, 1978, substorm. *Journal of Geophysical Research: Space Physics*, 88(A9):7005–7014, 1983. ISSN 2156-2202. doi: 10.1029/JA088iA09p07005.

A. Nishida and S. Kokubun. New polar magnetic disturbances: S , SP, DPC, and DP 2. *Reviews of Geophysics*, 9(2):417–425, 1971. ISSN 1944-9208. doi: 10.1029/RG009i002p00417.

Y. Nishimura, L. Lyons, S. Zou, V. Angelopoulos, and S. Mende. Substorm triggering by new plasma intrusion: THEMIS all-sky imager observations. *Journal of Geophysical Research: Space Physics*, 115(A7), 2010. ISSN 2156-2202. doi: 10.1029/2009JA015166.

Y. Nishimura, L. R. Lyons, V. Angelopoulos, T. Kikuchi, S. Zou, and S. B. Mende. Relations between multiple auroral streamers, pre-onset thin arc formation, and substorm auroral onset. *Journal of Geophysical Research: Space Physics*, 116 (A9), 2011. ISSN 2156-2202. doi: 10.1029/2011JA016768.

Y. Nishimura, J. Yang, P. L. Pritchett, F. V. Coroniti, E. F. Donovan, L. R. Lyons, R. A. Wolf, V. Angelopoulos, and S. B. Mende. Statistical properties of substorm auroral onset beads/rays. *Journal of Geophysical Research: Space Physics*, 121 (9):8661–8676, 2016. ISSN 2169-9402. doi: 10.1002/2016JA022801.

T. Obayashi. The interaction of the solar wind with the geomagnetic field during disturbed conditions. *Solar-terrestrial physics*, page 107, 1967.

T. P. O'Brien, S. M. Thompson, and R. L. McPherron. Steady magnetospheric convection: Statistical signatures in the solar wind and AE. *Geophysical Research Letters*, 29(7):34–1–34–4, 2002. ISSN 1944-8007. doi: 10.1029/2001GL014641.

S. Ohtani and J. W. Gjerloev. Is the Substorm Current Wedge an Ensemble of Wedgelets?: Revisit to Midlatitude Positive Bays. *Journal of Geophysical Research: Space Physics*, 125(9):e2020JA027902, 2020. ISSN 2169-9402. doi: 10.1029/2020JA027902.

S. Ohtani, B. J. Anderson, D. G. Sibeck, P. T. Newell, L. J. Zanetti, T. A. Potemra, K. Takahashi, R. E. Lopez, V. Angelopoulos, R. Nakamura, D. M. Klumpar, and C. T. Russell. A multisatellite study of a pseudo-substorm onset in the near-Earth magnetotail. *Journal of Geophysical Research: Space Physics*, 98(A11):19355–19367, 1993. ISSN 2156-2202. doi: 10.1029/93JA01421.

H. J. Opgenoorth, M. a. L. Persson, T. I. Pulkkinen, and R. J. Pellinen. Recovery phase of magnetospheric substorms and its association with morning-sector aurora. *Journal of Geophysical Research: Space Physics*, 99(A3):4115–4129, 1994. ISSN 2156-2202. doi: 10.1029/93JA01502.

N. Østgaard, J. Stadnes, J. Bjordal, R. R. Vondrank, S. A. Cummer, D. L. Chenette, G. K. Parks, M. J. Brittnacher, and D. L. McKenzie. Global-scale electron precip-

itation features seen in UV and X rays during substorms. *Journal of Geophysical Research: Space Physics*, 104(A5):10191–10204, 1999. ISSN 2156-2202. doi: 10.1029/1999JA900004.

N. Østgaard, S. B. Mende, H. U. Frey, T. J. Immel, L. A. Frank, J. B. Sigwarth, and T. J. Stubbs. Interplanetary magnetic field control of the location of substorm onset and auroral features in the conjugate hemispheres. *Journal of Geophysical Research: Space Physics*, 109(A7), 2004. ISSN 2156-2202. doi: 10.1029/2003JA010370.

N. Østgaard, N. A. Tsyganenko, S. B. Mende, H. U. Frey, T. J. Immel, M. Fillingim, L. A. Frank, and J. B. Sigwarth. Observations and model predictions of substorm auroral asymmetries in the conjugate hemispheres. *Geophysical Research Letters*, 32(5), 2005. ISSN 1944-8007. doi: 10.1029/2004GL022166.

N. Østgaard, K. M. Laundal, L. Juusola, A. Åsnes, S. E. Håland, and J. M. Weygand. Interhemispherical asymmetry of substorm onset locations and the interplanetary magnetic field. *Geophysical Research Letters*, 38(8), 2011. ISSN 1944-8007. doi: 10.1029/2011GL046767.

N. Østgaard, J. P. Reistad, P. Tenfjord, K. M. Laundal, T. Rexer, S. E. Haaland, K. Snekvik, M. Hesse, S. E. Milan, and A. Ohma. The asymmetric geospace as displayed during the geomagnetic storm on 17 August 2001. *Annales Geophysicae*, 36(6):1577–1596, Nov. 2018. ISSN 0992-7689. doi: 10.5194/angeo-36-1577-2018.

E. Parker. Extension of the solar corona into interplanetary space. *Journal of Geophysical Research (1896-1977)*, 64(11):1675–1681, 1959. ISSN 2156-2202. doi: 10.1029/JZ064i011p01675.

E. N. Parker. Sweet's mechanism for merging magnetic fields in conducting fluids. *Journal of Geophysical Research (1896-1977)*, 62(4):509–520, 1957. ISSN 2156-2202. doi: 10.1029/JZ062i004p00509.

E. N. Parker. Dynamics of the Interplanetary Gas and Magnetic Fields. *ApJ*, 128: 664, Nov. 1958. ISSN 0004-637X, 1538-4357. doi: 10.1086/146579.

G. K. Parks, B. Mauk, C. Gurgiolo, and C. S. Lin. Observations of plasma injection. In S.-I. Akasofu, editor, *Dynamics of the Magnetosphere*, pages 371–383, Dordrecht, 1980. Springer Netherlands. ISBN 978-94-009-9519-2.

N. Partamies, T. I. Pulkkinen, R. L. McPherron, K. McWilliams, C. R. Bryant, E. Tanskanen, H. J. Singer, G. D. Reeves, and M. F. Thomsen. Different magnetospheric modes: Solar wind driving and coupling efficiency. *Annales Geophysicae*, 27(11):4281–4291, Nov. 2009. ISSN 0992-7689. doi: 10.5194/angeo-27-4281-2009.

G. Paschmann. Recent in-situ observations of magnetic reconnection in near-Earth space. *Geophysical Research Letters*, 35(19), 2008. ISSN 1944-8007. doi: 10.1029/2008GL035297.

P. Perreault and S.-I. Akasofu. A study of geomagnetic storms. *Geophys J Int*, 54(3): 547–573, Sept. 1978. ISSN 0956-540X, 1365-246X. doi: 10.1111/j.1365-246X.1978.tb05494.x.

S. M. Petrinec and C. T. Russell. Near-Earth magnetotail shape and size as determined from the magnetopause flaring angle. *Journal of Geophysical Research: Space Physics*, 101(A1):137–152, 1996. ISSN 2156-2202. doi: 10.1029/95JA02834.

T. D. Phan, G. Paschmann, W. Baumjohann, N. Sckopke, and H. Lühr. The magnetosheath region adjacent to the dayside magnetopause: AMPTE/IRM observations. *Journal of Geophysical Research: Space Physics*, 99(A1):121–141, 1994. ISSN 2156-2202. doi: 10.1029/93JA02444.

A. Piel. *Plasma Physics: An Introduction to Laboratory, Space, and Fusion Plasmas*. Springer, Berlin, Heidelberg, 2010. ISBN 978-3-642-10490-9 978-3-642-10491-6. doi: 10.1007/978-3-642-10491-6.

T. I. Pulkkinen, D. N. Baker, R. J. Pellinen, J. Büchner, H. E. J. Koskinen, R. E. Lopez, R. L. Dyson, and L. A. Frank. Particle scattering and current sheet stability in the geomagnetic tail during the substorm growth phase. *Journal of Geophysical Research: Space Physics*, 97(A12):19283–19297, 1992. ISSN 2156-2202. doi: 10.1029/92JA01189.

T. I. Pulkkinen, D. N. Baker, P. K. Toivanen, R. J. Pellinen, R. H. W. Friedel, and A. Korth. Magnetospheric field and current distributions during the substorm recovery phase. *Journal of Geophysical Research: Space Physics*, 99(A6):10955–10966, 1994. ISSN 2156-2202. doi: 10.1029/93JA02718.

T. I. Pulkkinen, D. N. Baker, R. J. Pellinen, J. S. Murphree, and L. A. Frank. Mapping of the auroral oval and individual arcs during substorms. *Journal of Geophysical Research: Space Physics*, 100(A11):21987–21994, 1995. ISSN 2156-2202. doi: 10.1029/95JA01632.

T. I. Pulkkinen, D. N. Baker, M. Wiltberger, C. Goodrich, R. E. Lopez, and J. G. Lyon. Pseudobreakup and substorm onset: Observations and MHD simulations compared. *Journal of Geophysical Research: Space Physics*, 103(A7):14847–14854, 1998. ISSN 2156-2202. doi: 10.1029/97JA03244.

T. I. Pulkkinen, M. Palmroth, H. E. J. Koskinen, T. V. Laitinen, C. C. Goodrich, V. G. Merkin, and J. G. Lyon. Magnetospheric modes and solar wind energy coupling efficiency. *Journal of Geophysical Research: Space Physics*, 115(A3), 2010. ISSN 2156-2202. doi: 10.1029/2009JA014737.

T. Pytte, R. L. McPherron, E. W. Hones Jr., and H. I. West Jr. Multiple-satellite studies of magnetospheric substorms: Distinction between polar magnetic substorms and convection-driven negative bays. *Journal of Geophysical Research: Space Physics*, 83(A2):663–679, 1978. ISSN 2156-2202. doi: 10.1029/JA083iA02p00663.

I. J. Rae, C. E. J. Watt, K. R. Murphy, H. U. Frey, L. G. Ozeke, D. K. Milling, and I. R. Mann. The correlation of ULF waves and auroral intensity before, during

and after substorm expansion phase onset. *Journal of Geophysical Research: Space Physics*, 117(A8), 2012. ISSN 2156-2202. doi: 10.1029/2012JA017534.

D. Rasinskaite, C. E. J. Watt, C. Forsyth, A. W. Smith, C. J. Lao, S. Chakraborty, J. C. Holmes, and G. L. Delzanno. Estimating Electron Temperature and Density Using Van Allen Probe Data: Typical Behavior of Energetic Electrons in the Inner Magnetosphere. *Journal of Geophysical Research: Space Physics*, 130(4): e2024JA033443, 2025. ISSN 2169-9402. doi: 10.1029/2024JA033443.

G. D. Reeves, M. G. Henderson, P. S. McLachlan, R. D. Belian, R. H. W. Friedel, and A. Korth. Radial propagation of substorm injections. 389:579, Oct. 1996.

G. D. Reeves, M. G. Henderson, R. M. Skoug, M. F. Thomsen, J. E. Borovsky, H. O. Funtsen, P. C:Son Brandt, D. J. Mitchell, J.-M. Jahn, C. J. Pollock, D. J. McComas, and S. B. Mende. IMAGE, POLAR, and Geosynchronous Observations of Substorm and Ring Current Ion Injection. In *Disturbances in Geospace: The Storm-Substorm Relationship*, pages 91–101. American Geophysical Union (AGU), 2003. ISBN 978-1-118-66577-0. doi: 10.1029/142GM09.

A. J. Ridley, G. Lu, C. R. Clauer, and V. O. Papitashvili. Ionospheric convection during nonsteady interplanetary magnetic field conditions. *Journal of Geophysical Research: Space Physics*, 102(A7):14563–14579, 1997. ISSN 2156-2202. doi: 10.1029/97JA00940.

C. J. Rodger, M. A. Clilverd, A. T. Hendry, and C. Forsyth. Examination of Radiation Belt Dynamics During Substorm Clusters: Magnetic Local Time Variation and Intensity of Precipitating Fluxes. *Journal of Geophysical Research: Space Physics*, 127(12):e2022JA030750, 2022a. ISSN 2169-9402. doi: 10.1029/2022JA030750.

C. J. Rodger, A. T. Hendry, M. A. Clilverd, C. Forsyth, and S. K. Morley. Examination of Radiation Belt Dynamics During Substorm Clusters: Activity Drivers and Dependencies of Trapped Flux Enhancements. *Journal of Geophysical Re-*

search: Space Physics, 127(1):e2021JA030003, 2022b. ISSN 2169-9402. doi: 10.1029/2021JA030003.

G. Rostoker. Geomagnetic indices. *Reviews of Geophysics*, 10(4):935–950, 1972. ISSN 1944-9208. doi: 10.1029/RG010i004p00935.

G. Rostoker. On the place of the pseudo-breakup in a magnetospheric substorm. *Geophysical Research Letters*, 25(2):217–220, 1998. ISSN 1944-8007. doi: 10.1029/97GL03583.

G. Rostoker. The evolving concept of a magnetospheric substorm. *Journal of Atmospheric and Solar-Terrestrial Physics*, 61(1-2):85–100, Jan. 1999. ISSN 13646826. doi: 10.1016/S1364-6826(98)00119-9.

A. Roux, S. Perraut, P. Robert, A. Morane, A. Pedersen, A. Korth, G. Kremser, B. Aparicio, D. Rodgers, and R. Pellinen. Plasma sheet instability related to the westward traveling surge. *Journal of Geophysical Research*, 96:17697–17714, Oct. 1991. ISSN 0148-0227. doi: 10.1029/91JA01106.

J. M. Ruohoniemi and R. A. Greenwald. The response of high-latitude convection to a sudden southward IMF turning. *Geophysical Research Letters*, 25(15):2913–2916, 1998. ISSN 1944-8007. doi: 10.1029/98GL02212.

J. M. Ruohoniemi and R. A. Greenwald. Dependencies of high-latitude plasma convection: Consideration of interplanetary magnetic field, seasonal, and universal time factors in statistical patterns. *Journal of Geophysical Research: Space Physics*, 110(A9), 2005. ISSN 2156-2202. doi: 10.1029/2004JA010815.

T. Saito, K. Yumoto, and Y. Koyama. Magnetic pulsation Pi2 as a sensitive indicator of magnetospheric substorm. *Planetary and Space Science*, 24(11):1025–1029, Nov. 1976. ISSN 00320633. doi: 10.1016/0032-0633(76)90120-3.

T. Sakurai and T. Saito. Magnetic pulsation Pi2 and substorm onset. *Planetary and Space Science*, 24(6):573–575, June 1976. ISSN 00320633. doi: 10.1016/0032-0633(76)90135-5.

J. K. Sandhu, I. J. Rae, M. P. Freeman, C. Forsyth, M. Gkioulidou, G. D. Reeves, H. E. Spence, C. M. Jackman, and M. M. Lam. Energization of the Ring Current by Substorms. *Journal of Geophysical Research: Space Physics*, 123(10):8131–8148, 2018. ISSN 2169-9402. doi: 10.1029/2018JA025766.

J. K. Sandhu, I. J. Rae, M. P. Freeman, M. Gkioulidou, C. Forsyth, G. D. Reeves, K. R. Murphy, and M.-T. Walach. Substorm-Ring Current Coupling: A Comparison of Isolated and Compound Substorms. *Journal of Geophysical Research: Space Physics*, 124(8):6776–6791, Aug. 2019. ISSN 2169-9402. doi: 10.1029/2019JA026766.

R. Schunk and A. Nagy. *Ionospheres: Physics, Plasma Physics, and Chemistry*. Cambridge Atmospheric and Space Science Series. Cambridge University Press, Cambridge, 2 edition, 2009. ISBN 978-0-521-87706-0. doi: 10.1017/CBO9780511635342.

V. Sergeev, D. Yahnin, K. Liou, M. Thomsen, and G. Reeves. Narrow Plasma Streams as a Candidate to Populate the Inner Magnetosphere. In *The Inner Magnetosphere: Physics and Modeling*, pages 55–60. American Geophysical Union (AGU), 2005. ISBN 978-1-118-66609-8. doi: 10.1029/155GM07.

V. A. Sergeev, R. J. Pellinen, and T. I. Pulkkinen. Steady magnetospheric convection: A review of recent results. *Space Sci Rev*, 75(3):551–604, Feb. 1996a. ISSN 1572-9672. doi: 10.1007/BF00833344.

V. A. Sergeev, T. I. Pulkkinen, and R. J. Pellinen. Coupled-mode scenario for the magnetospheric dynamics. *Journal of Geophysical Research: Space Physics*, 101 (A6):13047–13065, 1996b. ISSN 2156-2202. doi: 10.1029/95JA03192.

V. A. Sergeev, L. I. Vagina, R. D. Elphinstone, J. S. Murphree, D. J. Hearn, L. L. Cogger, and M. L. Johnson. Comparison of UV optical signatures with the substorm current wedge as predicted by an inversion algorithm. *Journal of Geophysical Research: Space Physics*, 101(A2):2615–2627, 1996c. ISSN 2156-2202. doi: 10.1029/95JA00537.

V. A. Sergeev, Y. Kamide, S. Kokubun, R. Nakamura, C. S. Deehr, T. J. Hughes, R. P. Lepping, T. Mukai, A. A. Petrukovich, J.-H. Shue, K. Shiokawa, O. A. Troshichev, and K. Yumoto. Short-duration convection bays and localized interplanetary magnetic field structures on November 28, 1995. *Journal of Geophysical Research: Space Physics*, 103(A10):23593–23609, 1998. ISSN 2156-2202. doi: 10.1029/98JA01747.

V. A. Sergeev, N. A. Tsyganenko, M. V. Smirnov, A. V. Nikolaev, H. J. Singer, and W. Baumjohann. Magnetic effects of the substorm current wedge in a "spread-out wire" model and their comparison with ground, geosynchronous, and tail lobe data. *Journal of Geophysical Research: Space Physics*, 116(A7), 2011. ISSN 2156-2202. doi: 10.1029/2011JA016471.

R. M. Shore, M. P. Freeman, J. A. Wild, and J. W. Gjerloev. A high-resolution model of the external and induced magnetic field at the Earth's surface in the Northern Hemisphere. *Journal of Geophysical Research: Space Physics*, 122(2): 2440–2454, 2017. ISSN 2169-9402. doi: 10.1002/2016JA023682.

R. M. Shore, M. P. Freeman, and J. W. Gjerloev. An Empirical Orthogonal Function Reanalysis of the Northern Polar External and Induced Magnetic Field During Solar Cycle 23. *Journal of Geophysical Research: Space Physics*, 123(1):781–795, 2018. ISSN 2169-9402. doi: 10.1002/2017JA024420.

R. M. Shore, M. P. Freeman, and J. W. Gjerloev. Interplanetary Magnetic Field Control of Polar Ionospheric Equivalent Current System Modes. *Space Weather*, 17(7):976–988, 2019. ISSN 1542-7390. doi: 10.1029/2019SW002161.

J.-H. Shue, J. K. Chao, H. C. Fu, C. T. Russell, P. Song, K. K. Khurana, and H. J. Singer. A new functional form to study the solar wind control of the magnetopause size and shape. *Journal of Geophysical Research: Space Physics*, 102 (A5):9497–9511, 1997. ISSN 2156-2202. doi: 10.1029/97JA00196.

D. G. Sibeck, R. E. Lopez, and E. C. Roelof. Solar wind control of the magne-

topause shape, location, and motion. *Journal of Geophysical Research: Space Physics*, 96(A4):5489–5495, 1991. ISSN 2156-2202. doi: 10.1029/90JA02464.

S. F. Singer. A new model of magnetic storms and aurorae. *Eos, Transactions American Geophysical Union*, 38(2):175–190, 1957. ISSN 2324-9250. doi: 10.1029/TR038i002p00175.

G. L. Siscoe and T. S. Huang. Polar cap inflation and deflation. *Journal of Geophysical Research: Space Physics*, 90(A1):543–547, 1985. ISSN 2156-2202. doi: 10.1029/JA090iA01p00543.

J. A. Slavin and R. E. Holzer. Solar wind flow about the terrestrial planets 1. Modeling bow shock position and shape. *Journal of Geophysical Research: Space Physics*, 86(A13):11401–11418, 1981. ISSN 2156-2202. doi: 10.1029/JA086iA13p11401.

A. W. Smith, I. J. Rae, C. Forsyth, C. E. J. Watt, and K. R. Murphy. On the Magnetospheric ULF Wave Counterpart of Substorm Onset. *Journal of Geophysical Research: Space Physics*, 125(4):e2019JA027573, 2020. ISSN 2169-9402. doi: 10.1029/2019JA027573.

A. W. Smith, C. Forsyth, I. J. Rae, T. M. Garton, T. Bloch, C. M. Jackman, and M. Bakrania. Forecasting the Probability of Large Rates of Change of the Geomagnetic Field in the UK: Timescales, Horizons, and Thresholds. *Space Weather*, 19(9):e2021SW002788, 2021. ISSN 1542-7390. doi: 10.1029/2021SW002788.

A. W. Smith, I. J. Rae, C. Forsyth, J. C. Coxon, M.-T. Walach, C. J. Lao, D. S. Bloomfield, S. A. Reddy, M. K. Coughlan, A. Keesee, and S. Bentley. Space Weather Forecasts of Ground Level Space Weather in the UK: Evaluating Performance and Limitations. *Space Weather*, 22(11):e2024SW003973, 2024. ISSN 1542-7390. doi: 10.1029/2024SW003973.

T. W. Speiser and N. F. Ness. The neutral sheet in the geomagnetic tail: Its motion, equivalent currents, and field line connection through it. *Journal of Geophysical*

Research (1896-1977), 72(1):131–141, 1967. ISSN 2156-2202. doi: 10.1029/JZ072i001p00131.

N. A. Stepanov, V. A. Sergeev, M. A. Shukhtina, Y. Ogawa, X. Chu, and D. D. Rogov. Ionospheric Electron Density and Conductance Changes in the Auroral Zone During Substorms. *Journal of Geophysical Research: Space Physics*, 126 (7):e2021JA029572, 2021. ISSN 2169-9402. doi: 10.1029/2021JA029572.

L. Svalgaard. Polar cap magnetic variations and their relationship with the interplanetary magnetic sector structure. *Journal of Geophysical Research (1896-1977)*, 78(13):2064–2078, 1973. ISSN 2156-2202. doi: 10.1029/JA078i013p02064.

E. Tanskanen, T. I. Pulkkinen, H. E. J. Koskinen, and J. A. Slavin. Substorm energy budget during low and high solar activity: 1997 and 1999 compared. *Journal of Geophysical Research: Space Physics*, 107(A6):SMP 15–1–SMP 15–11, 2002. ISSN 2156-2202. doi: 10.1029/2001JA900153.

P. Tenfjord, N. Østgaard, K. Snekvik, K. M. Laundal, J. P. Reistad, S. Haaland, and S. E. Milan. How the IMF B induces a B component in the closed magnetosphere and how it leads to asymmetric currents and convection patterns in the two hemispheres. *Journal of Geophysical Research: Space Physics*, 120(11):9368–9384, 2015. ISSN 2169-9402. doi: 10.1002/2015JA021579.

O. Troshichev and V. Andrezen. The relationship between interplanetary quantities and magnetic activity in the southern polar cap. *Planetary and Space Science*, 33 (4):415–419, Apr. 1985. ISSN 00320633. doi: 10.1016/0032-0633(85)90086-8.

O. Troshichev, B. Kuznetsov, and M. Pudovkin. The current systems of the magnetic substorm growth and explosive phases. *Planetary and Space Science*, 22(10):1403–1412, Oct. 1974. ISSN 00320633. doi: 10.1016/0032-0633(74)90037-3.

O. Troshichev, V. Andrezen, S. Vennerstrøm, and E. Friis-Christensen. Magnetic activity in the polar cap—A new index. *Planetary and Space Science*, 36(11): 1095–1102, Nov. 1988. ISSN 00320633. doi: 10.1016/0032-0633(88)90063-3.

O. Troshichev, A. Janzhura, and P. Stauning. Unified PCN and PCS indices: Method of calculation, physical sense, and dependence on the IMF azimuthal and northward components. *Journal of Geophysical Research: Space Physics*, 111(A5), 2006. ISSN 2156-2202. doi: 10.1029/2005JA011402.

O. Troshichev, A. Janzhura, and P. Stauning. Correction to "Unified PCN and PCS indices: Method of calculation, physical sense, and dependence on the IMF azimuthal and northward components". *Journal of Geophysical Research: Space Physics*, 114(A11), 2009. ISSN 2156-2202. doi: 10.1029/2009JA014937.

N. A. Tsyganenko. Modeling of twisted/warped magnetospheric configurations using the general deformation method. *Journal of Geophysical Research: Space Physics*, 103(A10):23551–23563, 1998. ISSN 2156-2202. doi: 10.1029/98JA02292.

J. A. Van Allen, G. H. Ludwig, E. C. Ray, and C. E. McILWAIN. Observation of High Intensity Radiation by Satellites 1958 Alpha and Gamma. *Journal of Jet Propulsion*, 28(9):588–592, Sept. 1958. doi: 10.2514/8.7396.

S. Vennerstrøm, E. Friis-Christensen, O. A. Troshichev, and V. G. Andersen. Comparison between the polar cap index, PC, and the auroral electrojet indices AE, AL, and AU. *Journal of Geophysical Research: Space Physics*, 96(A1):101–113, 1991. ISSN 2156-2202. doi: 10.1029/90JA01975.

I. O. Voronkov, E. F. Donovan, and J. C. Samson. Observations of the phases of the substorm. *Journal of Geophysical Research: Space Physics*, 108(A2), 2003. ISSN 2156-2202. doi: 10.1029/2002JA009314.

M.-T. Walach and S. E. Milan. Are steady magnetospheric convection events prolonged substorms? *Journal of Geophysical Research: Space Physics*, 120(3): 1751–1758, 2015. ISSN 2169-9402. doi: 10.1002/2014JA020631.

S. J. Walker, K. M. Laundal, J. P. Reistad, S. M. Hatch, A. Ohma, and J. Gjerloev. The Ionospheric Leg of the Substorm Current Wedge: Combining Iridium and

Ground Magnetometers. *Journal of Geophysical Research: Space Physics*, 129 (7):e2024JA032414, 2024. ISSN 2169-9402. doi: 10.1029/2024JA032414.

D. D. Wallis and E. E. Budzinski. Empirical models of height integrated conductivities. *Journal of Geophysical Research: Space Physics*, 86(A1):125–137, 1981. ISSN 2156-2202. doi: 10.1029/JA086iA01p00125.

A. P. Walsh. *New Perspectives on Magnetotail Dynamic Processes from Combined Cluster and Double Star Observations*. Doctoral, UCL (University College London), Sept. 2009.

A. P. Walsh, S. Haaland, C. Forsyth, A. M. Keesee, J. Kissinger, K. Li, A. Runov, J. Soucek, B. M. Walsh, S. Wing, and M. G. G. T. Taylor. Dawn–dusk asymmetries in the coupled solar wind–magnetosphere–ionosphere system: A review. *Annales Geophysicae*, 32(7):705–737, July 2014. ISSN 0992-7689. doi: 10.5194/angeo-32-705-2014.

H. Wang, H. Lühr, S. Y. Ma, and P. Ritter. Statistical study of the substorm onset: Its dependence on solar wind parameters and solar illumination. *Annales Geophysicae*, 23(6):2069–2079, Sept. 2005. ISSN 0992-7689. doi: 10.5194/angeo-23-2069-2005.

H. Wang, H. Lühr, S. Y. Ma, and H. U. Frey. Interhemispheric comparison of average substorm onset locations: Evidence for deviation from conjugacy. *Annales Geophysicae*, 25(4):989–999, May 2007. ISSN 0992-7689. doi: 10.5194/angeo-25-989-2007.

S. Watanabe, D. Bilitza, F. Tsuchiya, A. Kumamoto, Y. Miyoshi, Y. Kasahara, T. Hori, A. Shinbori, A. Matsuoka, and I. Shinohara. Satellite observations and modeling of the plasmapause structure and dynamics. *Advances in Space Research*, 75(5):4230–4244, Mar. 2025. ISSN 02731177. doi: 10.1016/j.asr.2024.10.015.

J. E. Waters, C. M. Jackman, D. K. Whiter, C. Forsyth, A. R. Fogg, L. Lamy, B. Cecconi, X. Bonnin, and K. Issautier. A Perspective on Substorm Dynamics Using

10 Years of Auroral Kilometric Radiation Observations From Wind. *Journal of Geophysical Research: Space Physics*, 127(9):e2022JA030449, 2022. ISSN 2169-9402. doi: 10.1029/2022JA030449.

D. R. Weimer. Substorm time constants. *Journal of Geophysical Research: Space Physics*, 99(A6):11005–11015, 1994. ISSN 2156-2202. doi: 10.1029/93JA02721.

J. M. Weygand, R. L. McPherron, K. Kauristie, H. U. Frey, and T. S. Hsu. Relation of auroral substorm onset to local AL index and dispersionless particle injections. *Journal of Atmospheric and Solar-Terrestrial Physics*, 70(18):2336–2345, Dec. 2008. ISSN 1364-6826. doi: 10.1016/j.jastp.2008.09.030.

J. A. Wild, E. E. Woodfield, and S. K. Morley. On the triggering of auroral substorms by northward turnings of the interplanetary magnetic field. *Annales Geophysicae*, 27(9):3559–3570, Sept. 2009. ISSN 0992-7689. doi: 10.5194/angeo-27-3559-2009.

J. Wilhjelm, E. Friis-Christensen, and T. A. Potemra. The relationship between ionospheric and field-aligned currents in the dayside cusp. *Journal of Geophysical Research: Space Physics*, 83(A12):5586–5594, 1978. ISSN 2156-2202. doi: 10.1029/JA083iA12p05586.

T. K. Yeoman, M. P. Freeman, G. D. Reeves, M. Lester, and D. Orr. A comparison of midlatitude Pi 2 pulsations and geostationary orbit particle injections as substorm indicators. *Journal of Geophysical Research: Space Physics*, 99(A3):4085–4093, 1994. ISSN 2156-2202. doi: 10.1029/93JA03233.

X.-J. Zhang, V. Angelopoulos, A. Runov, X.-Z. Zhou, J. Bonnell, J. P. McFadden, D. Larson, and U. Auster. Current carriers near dipolarization fronts in the magnetotail: A THEMIS event study. *Journal of Geophysical Research: Space Physics*, 116(A5), 2011. ISSN 2156-2202. doi: 10.1029/2010JA015885.

J. B. Zirker. Coronal holes and high-speed wind streams. *Reviews of Geophysics*, 15(3):257–269, 1977. ISSN 1944-9208. doi: 10.1029/RG015i003p00257.